Eurotherm 103

Nanoscale and Microscale Heat Transfer IV

October 15-17, 2014

Lyon, France

Organized by

The Centre for Energy and Thermal Sciences of Lyon

(CETHIL, CNRS – INSA Lyon – University Lyon 1)

ISBN: 978-2-9539515-9-2

Edited by the Centre for Energy and Thermal Sciences of Lyon (CETHIL), Villeurbanne, France.

Printed by AGG Print, Villeurbanne, France.

October 2014.

The **Eurotherm seminar 103** "**Nanoscale and Microscale Heat Transfer IV**" is a follow-up of Eurotherm seminars 57, 75 and 91 « Nanoscale and Microscale Heat Transfer » held in Poitiers, Reims and Poitiers (France) in 1998, 2003 and 2011. This seminar aims at presenting the state of the art and the modern trends in nanoscale and microscale heat transfer. It focuses on heat transfer at short length and time scales where the physical laws used in classical heat transfer are not valid anymore. Thermal radiation at subwavelength scales or heat conduction driven by the mesoscopic transport of electrons and phonons are the typical topics tackled by the seminar as well as applications of these concepts to nano-objects.

Chairs

R. Vaillon, CETHIL, Villeurbanne, France

C.M. Sotomayor Torres, ICN2, Barcelona, Spain

P.-O. Chapuis, CETHIL, Villeurbanne, France

Scientific Committee

P. Ben-Abdallah, Institut d'Optique, Palaiseau, France

O. Bourgeois, Institut Néel, Grenoble, France

G. Casati, University of Insubria, Italy

D.G. Cahill, University of Illinois at Urbana-Champaign, USA

G. Chen, MIT, Cambridge, USA

C. Dames, University of California Berkeley, USA

C. Fu, Peking University, China

B. Gotsmann, IBM Zürich, Switzerland

J.-J. Greffet, Institut d'Optique, Palaiseau, France

C. Henkel, Universität Potsdam, Germany

K. Joulain, Institut P', Poitiers-Futuroscope, France

A. Kittel, Universität Oldenburg, Germany

O. Kolosov, University of Lancaster, UK

D. Lacroix, LEMTA, Nancy, France

J.R. Lukes, University of Pennsylvania, U.S.A.

I. Maasilta, Jyväskylä University, Finland

M.P. Mengüç, Özyegin University, Istanbul, Turkey

B. Perrin, INSP – University Paris 6, France

M. Rubi, University of Barcelona, Spain

L. Shi, The University of Texas at Austin, USA

N. Trannoy, GRESPI, Reims, France

S. Volz, EM2C, Châtenay-Malabry, France

Z. Zhang, Georgia Institute of Technology, USA

Local organizers

R. Vaillon & P.-O. Chapuis, CETHIL, Villeurbanne, France

with the continuous help of the “Micro and Nanoscale Heat Transfer” group members:

A. Assy, E. Blandre, M. Chamtouri*, A. Darwiche, O. Dupré, S. Gomès, W. Jaber, S. Lefèvre, M. Massoud, E. Nefzaoui*, T. Nghiem, O. Merchiers, S. Rault, D. Renahy.

* until September 1st.

Sponsors

Société Française de Thermique

GDRe CNRS 250

Thermal NanoSciences and NanoEngineering

ARC Energies

Rhône-Alpes

Conseil Régional

Rhône-Alpes

INSA de Lyon

Délégation Rhône-Auvergne

Université Claude Bernard Lyon 1

The local organizers are also very thankful to

Faculté des Sciences et Technologies

for funding the registration of three Master students

Club NANO-MICROTECHNOLOGIE

38 de SCIENCES nanoSCIENCES FONDATION

for advertising the conference in their networks

For providing the local organizers specific and valuable help, special thanks to

Paul VALLETTE, "Société Française de Thermique",

Solange PERREL, ''Cellule Congrès'' of University Lyon 1,

The Communication Division of INSA de Lyon,

The Communication Division of CNRS – Délégation Rhône-Auvergne,

Secretary staff of CETHIL,

GEN, TC and Humanities Departments of INSA de Lyon.

Conference program in a glance

Tutorials' timetable

October 14		
TIME	INSA Lyon - René Char	INSA Lyon - Chappe
08:30	*Registration opening - Agora*	
09:00	**RAD-1** J-J. Greffet	**COND-1** J. Lukes
10:30	*Break - Agora*	
11:00	**RAD-1** J-J. Greffet	**COND-1** J. Lukes
12:15	*Lunch - Agora*	
13:30	**RAD-2** A. Kittel	**COND-2** O. Bourgeois
15:00	*Break - Agora*	
15:30-16:45	**RAD-2** A. Kittel	**COND-2** O. Bourgeois
18:30-20:00	Ice breaker	

Conference program

October 15		October 16		October 17	
TIME	ISC		ISC		ISC
08:15	*Registration cont'd*				
08:45	*Welcome address*				
09:00	**Keynote lecture 1**	D.G. Cahill	**Session 5**	V. Jean et al.	**Session 10**	J. Mayo et al.
09:20	Chair: C. Sotomayor Torres		Constrictions and wires	X. Zianni	Subwavelength radiation (2)	R. Incardone et al.
09:40	**Session 1**	S. Xiong et al.	Chair: S. Merabia	J. Larroque et al.	Chair: M. Rubi	L. Tranchant et al.
10:00	Atomic simulations	E. Lampin et al.	*Break*			V. Kubytskyi et al.
10:20	Chair: D. Lacroix	M.B. Zanjani et al.	**Poster session 2** (Work-in-progress posters included)			K. Joulain et al.
10:40	*Break*				*Break*	
11:10	**Session 2**	P. Ben-Abdallah et al.			**Keynote lecture 3** Chair: P-O. Chapuis	B. Gotsmann
11:30	Subwavelength radiation (1)	A. Didari & M.P. Mengüç	**Session 6**	O. Lozan et al.		
11:50	Chair: Y. Ezzahri	E. Blandre et al.	Surface modes	S. Lang et al.	*Lunch*	
12:10		D. Costantini et al.	Chair: K. Joulain	J. Ordonnez-Miranda et al.		
12:30	*Lunch*		*Lunch*			
13:20					**Session 11**	N. Könne et al.
13:40					Phonons and vibrations	E. Chavez-Angel et al.
14:00	**Session 3**	M. Massoud et al.	**Session 7**	K. Kloppstech et al.	Chair: S. Volz	S. Pailhes et al.
14:20	Experimental heat conduction (1)	N. Zen et al.	Experimental heat conduction (2)	J. Bodzenta et al.		M. Grossmann et al.
14:40	Chair: S. Reparaz	V. Lacatena et al.	Chair: I. Maasilta	J. Jaramillo-Fernandez et al.		B. Graczykowski et al.
15:00		C. Quintero et al.	**Session 8** Phonon simulations	J-P. Crocombette	*Closing remarks*	
15:20	**Poster session 1**		Chair: K. Termentzidis	H. Han et al.	*Break*	
15:40			*Break*			
16:10			**Keynote lecture 2** Chair: R. Vaillon	S. Fan		
16:30	*Break*					
16:50	**Session 4**	T. Puurtinen & I. Maasilta	**Session 9**	G. Benenti & G. Casati		
17:10	Numerical heat transfer	S. Merabia et al.	Energy conversion	I. Latella et al.		
17:30	Chair: E. Lampin	K. Termentzidis & D. Lacroix	Chair: P. Ben-Abdallah	R. Couderc et al.		
17:50-18:10		J. Alotaibi & G.P. Srivastava		M. Shimizu et al.		
20:00-23:30			Conference dinner			

Poster session 1	
PS1-01	J. Drevillon et al.
PS1-02	T.T.T. Nghiem et al.
PS1-03	S. Gluchko et al.
PS1-04	J. Randrianalisoa & N. Trannoy
PS1-05	W. Jaber et al.
PS1-06	N. Zhong et al.
PS1-07	H-C. Zhang et al.
PS1-08	A. Assy et al.
PS1-09	G. Kane et al.
PS1-10	M. Amara & A. Vossier
PS1-11	Y. Liu et al.
PS1-12	C.D.S. Brites et al.
PS1-13	S. Park
PS1-14	A. Bontempi et al.
PS1-15	A. Saci et al.

Poster session 2	
PS2-01	T. Stoll et al.
PS2-02	T.T.T. Nghiem & P-O. Chapuis
PS2-03	G. Okyay et al.
PS2-04	K. Horne et al.
PS2-05	Y. Ezzahri & K. Joulain
PS2-06	G. Degliame et al.
PS2-07	C. He et al.
PS2-08	E. Nefzaoui & P-O. Chapuis

Work-In-Progress posters
communicated in a separate booklet

Tutorials' program

Tuesday, October 14th, 2014

INSA de Lyon

Introductory sessions: concepts and state-of-the-art methods in nanoscale thermal radiation and heat conduction, both from the theory and modeling, and experimental points of view.

RAD- 1	**Jean-Jacques GREFFET**, Institut d'Optique, France
9h – 12h15 Coffee break: 10h30-11h	Nanoscale thermal radiation: theory and modelling

COND- 1	**Jennifer R. LUKES**, University of Pennsylvania, USA
9h – 12h15 Coffee break: 10h30-11h	Nanoscale thermal conduction: theory and modelling

RAD- 2	**Achim KITTEL**, Universität Oldenburg, Germany
13h30 – 16h45 Coffee break: 15h-15h30	Nanoscale thermal radiation: experimental methods

COND- 2	**Olivier BOURGEOIS**, Institut Néel, France
13h30 – 16h45 Coffee break: 15h-15h30	Nanoscale thermal conduction: experimental methods

Conference program

Wednesday, October 15th, 2014

Institut des Sciences Cognitives

Keynote lecture 1	**David G. CAHILL**, University of Illinois at Urbana-Champaign, USA	
Chair: C. Sotomayor Torres		
9h-9h40	D.G. CAHILL, G.T. HOHENSEE and G.-M. CHOI	Coupling of heat and spin currents at the nanoscale in cuprates and metallic multilayers

Session 1	Atomic simulations	
Chair: D. Lacroix		
9h40-10h00	S. XIONG, Y.A. KOSEVICH, K. SÄÄKILAHTI, Y. NI and S. VOLZ	Low thermal conductivity design with Si twinning superlattice nanowires
10h00-10h20	E. LAMPIN, P.L. PALLA, P.-A. FRANCIOSO and F. CLERI	Approach-to-equilibrium molecular dynamics: thermal properties from temperature transient
10h20-10h40	M.B. ZANJANI, A.R. DAVOYAN, A.M. MAHMOUD, N. ENGHETA and J.R. LUKES	One-way phonon transport in modulated acoustic waveguides

Session 2	Subwavelength radiation (1)	
Chair: Y. Ezzahri		
11h10-11h30	P. BEN-ABDALLAH, S.-A. BIEHS, K. JOULAIN and C. HENKEL	Superdiffusive heat transport in nanoparticle networks
11h30-11h50	A. DIDARI and M.P. MENGÜÇ	Near-field thermal emission between corrugated surfaces separated by nano-gaps
11h50-12h10	E. BLANDRE, P.-O. CHAPUIS, M. FRANCOEUR and R. VAILLON	Near-field thermal radiation absorbed by a flat film in the vicinity of a semi-infinite emitter
12h10-12h30	D. COSTANTINI, G. BRUCOLI, H. BENISTY, F. MARQUIER and J.-J. GREFFET	Thermal emission control with surface waves

Session 3	Experimental heat conduction (1)	
Chair: S. Reparaz		
14h00-14h20	M. MASSOUD, P.-O. CHAPUIS, B. CANUT , P. NEWBY, L.G. FRECHETTE and J.-M. BLUET	Thermal conductivity of porous silicon irradiated with swift heavy ions
14h20-14h40	N. ZEN, T.A. PUURTINEN, T.J. ISOTALO, S. CHAUDHURI and	Coherent control of thermal conduction in two-dimensional phononic crystals

	I.J. MAASILTA	
14h40-15h00	V. LACATENA, M. HARAS, J.-F. ROBILLARD, S. MONFRAY, T. SKOTNICKI, E. DUBOIS	Reduction of thermal conductivity in silicon thin film membranes by phononic engineering
15h00-15h20	C.M. QUINTERO, O. KRAIEVA, E.M. HERNÁNDEZ, F. CARCENAC, D. LAGRANGE, G. MOLNÁR and C. BERGAUD	Joule heated micro- and nanowires: A versatile platform for high spatial and temporal resolution thermal investigations

Poster session 1 15h20-16h30	
J. DREVILLON, E. NEFZAOUI, Y. EZZAHRI and K. JOULAIN	Radiative thermal rectification using superconducting materials
T.T.T. NGHIEM, J. SAINT-MARTIN and P. DOLLFUS	Analysis of thermal conductance of ballistic point contacts using Boltzmann Transport Equation
S. GLUCHKO, J. ORDONEZ-MIRANDA, L. TRANCHANT, Thomas ANTONI and S. VOLZ	Focusing of surface phonon-polaritons along conical and wedge polar structures
J. RANDRIANALISOA and N. TRANNOY	Modeling of heat transfer through gas molecules between a hot SThM probe and a cold sample surface
W. JABER, C. CHEVALIER and P.-O. CHAPUIS	Thermal conductances across silicon sub-mean free path sources measured with a four-probe electrical setup
N. ZHONG, S.J. GARCIA and S. VAN DER ZWAAG	Thermal conductivity restoration by disulfide-based self-healing polymers
H.-C. ZHANG, Y. ZHAO, H.-P. TAN, Y. LI and H.-Y. YU	Optimizing design of a thermal protection structure with PCs meta-material considering micro-scale transfer characteristics
A. ASSY, S. LEFEVRE, P.-O. CHAPUIS and S. GOMES	Heat transfer through the water meniscus at the tip-sample contact investigated with Scanning Thermal Microscopy
G. KANE, N. VAST and J. SJAKSTE	Thermoelectric coefficients: coupling transport equations and *ab initio* calculation
M. AMARA and A. VOSSIER	Thermal and electrical behavior of photon enhanced thermionic conversion
Y. LIU, D. TAINOFF, M. BOUKHARI, J. RICHARD, A. BARSKI, P. BAYLE-GUILLEMAUD, E. HADJI, A. ASSY, S. GOMES and O. BOURGEOIS	Thermal properties of a nanostructured Ge:Mn thin film for thermoelectricity
C.D.S. BRITES, P.P. LIMA, N.J.O. SILVA, A. MILAN, V.S. AMARAL, F. PALACIO and L.D. CARLOS	Heat transfer studies using Ln^{3+} based nanothermometers
S. PARK	Xe-Arc Flash Lamp Crystallization of Amorphous Silicon Thin-Film for Large-Scale Displays
A. BONTEMPI, L. THIERY, D. TEYSSIEUX and P. VAIRAC	2ω/3ω SThM: improvements and perspectives
A. SACI, J.-L. BATTAGLIA, A. KUSIAK, R. FALLICA and M. LONGO	SThM measurement of thermal conductivity of a nanowire Sb_2Te_3 crystal along the c-axis

Session 4	Numerical heat transfer	
Chair: E. Lampin		
16h50-17h10	T. PUURTINEN and I. MAASILTA	Calculation of ballistic and Casimir-limit phonon thermal conduction in thin membranes
17h10-17h30	S. MERABIA, J. LOMBARD, T. BIBEN and A. ALKURDI	Interfacial heat transport in liquids and nanobubble dynamics
17h30-17h50	K. TERMENTZIDIS and D. LACROIX	Thermal conductivity of modulated nanowires
17h50-18h10	J. AL-OTAIBI and G.P. SRIVASTAVA	A comparative study of the anharmonicity of the transverse optical phonons in lead chalcogenides

Thursday, October 16th, 2014

Institut des Sciences Cognitives

Session 5	Constrictions and wires	
Chair: S. Merabia		
9h00-9h20	V. JEAN, K. TERMENTZIDIS, S. FUMERON and D. LACROIX	Phonon transport through constrictions in silicon nanowires
9h20-9h40	X. ZIANNI	Heat transfer in modulated nanowires with variable thickness
9h40-10h00	J. LARROQUE, J. SAINT-MARTIN and P. DOLLFUS	Phonon transport in silicon nanowires using a full-band Monte Carlo approach

Poster session 2 10h20-11h30	
T. STOLL, P. MAIOLI, A. CRUT, N. DEL FATTI and F VALLEE	Time-resolved measurements and quantitative analysis of the cooling dynamics of gold and gold-silica nanospheres in liquid environment
T.T.T. NGHIEM and P.-O. CHAPUIS	Heat transfer through a triangular phononic crystal column
G. OKYAY, Y. JOUMANI, C. BERTAIL and F. ENGUEHARD	Morphologies and radiative properties of soot particles issued from partial oxidation combustions
K. HORNE, M. CHIRTOC, N. HORNY, T. ANTONI, S. VOLZ and H. BAN	Thermal properties of chirped superlattice structures through molecular dynamics and photothermal radiometry
Y. EZZAHRI and K. JOULAIN	Vacuum phonon coupling through Casimir force between two solid dielectric materials
G. DEGLIAME, N. TRANNOY, J-P. JOUART, M. DIAF, T. DUVAUT and D. CARON	Submicrometric scale thermometry: coupling of a thermal-resistive probe and a photoluminescent microcrystal
C. HE, M. DANIEL, M. GROSSMANN, O. RISTOW, D. BRICK, M. SCHUBERT, M. ALBRECHT and T. DEKORSY	Coherent acoustic phonons in thin films of $CoSb_3$ and partially filled $Yb_xCo_4Sb_{12}$ skutterudites
E. NEFZAOUI & P.-O. CHAPUIS	A comparative study of different numerical approaches to the Boltzmann Transport Equation for phonons

Abstracts of the **''Work-In-Progress'' poster session** are not part of the proceedings. They are provided separately.

Session 6	Surface modes	
Chair: K. Joulain		
11h30-11h50	O. LOZAN, M. PERRIN, B. EA-KIM, J.-M. RAMPNOUX, S. DILHAIRE and P. LALANNE	Ultrafast plasmon heat transfer around subwavelength structures
11h50-12h10	S. LANG, M. TSCHIKIN, S-A. BIEHS, P. BEN-ABDALLAH, A. PETROV and M. EICH	Large penetration depth in hyperbolic metamaterials

12h10-12h30	J. ORDONEZ-MIRANDA, L. TRANCHANT, T. ANTONI and S. VOLZ	Fresnel-like formulas for the reflection and transmission of surface phonon-polaritons at a dielectric interface

Session 7	Experimental heat conduction (2)	
Chair: I. Maasilta		
14h00-14h20	K. KLOPPSTECH, N. KÖNNE and A. KITTEL	In-situ calibration of thermal sensors to measure absolute heat fluxes at the nano-scale
14h20-14h40	J. BODZENTA, M. CHIRTOC and J. JUSZCZYK	Quantitative thermal conductivity measurement by scanning thermal microscopy with nanofabricated thermal probes - methodology and modeling
14h40-15h00	J. JARAMILLO-FERNANDEZ, W. KASSEM, V. REMONDIERE, U. SOUPREMANIEN, E. OLLIER and S. VOLZ	Strain based thermal conductivity tuning on nanoscale polycrystalline AlN thin-films

Session 8	Phonon simulations	
Chair: K. Termentzidis		
15h00-15h20	J.-P. CROCOMBETTE	High temperature increase of the thermal conductivity of zirconium carbide explained by atomistic simulations
15h20-15h40	H. HAN, Y.A. KOSEVICH and S. VOLZ	Phonon interference and thermal conductance reduction in atomic-scale metamaterials

Keynote lecture 2	**Shanhui FAN**, Stanford University, USA	
Chair: R. Vaillon		
16h10-16h50	S. FAN, A. RAMAN, L. ZHU, M. ANOMA and E. REPHAELI	Nanophotonic control of thermal radiation: maximal violation of detailed balance, and experimental demonstration of daytime radiative cooling

Session 9	Energy conversion	
Chair: P. Ben Abdallah		
16h50-17h10	G. BENENTI and G. CASATI	Increasing thermoelectric efficiency: dynamical models unveil microscopic mechanisms
17h10-17h30	I. LATELLA, A. PÉREZ-MADRID, L.C. LAPAS and J.M. RUBI	Near-field thermodynamics and nanoscale energy harvesting
17h30-17h50	R. COUDERC, M. LEMITI and M. AMARA	Detailed analysis of heat generation in silicon solar cells
17h50-18h10	M. SHIMIZU, A. KOHIYAMA, F. IGUCHI and H. YUGAMI	Low concentration solar-thermophotovoltaic system using high-temperature photonics

Friday, October 17th, 2014

Institut des Sciences Cognitives

Session 10	Subwavelength radiation (2)	
Chair: M. Rubi		
9h00-9h20	J. MAYO, Y. TSURIMAKI, P.-O. CHAPUIS, J. OKAJIMA, A. KOMIYA, S. MARUYAMA, A. NARAYANASWAMY and R. VAILLON	Thermal radiation between two plates: regime map and analytical expressions for the net radiative heat flux from far to near field
9h20-9h40	R. INCARDONE, T. EMIG and M. KRÜGER	Heat transfer between anisotropic nanoparticles: enhancement and switching
9h40-10h00	L. TRANCHANT, J. ORDONEZ-MIRANDA, T. ANTONI and S. VOLZ	Far field diffraction of thermal Surface Phonon-Polaritons at the tip of micrometric glass tubes
10h00-10h20	V. KUBYTSKYI, S.-A. BIEHS and P. BEN-ABDALLAH	Radiative thermal memory
10h20-10h40	K. JOULAIN, Y. EZZAHRI and J. DREVILLON	Super Planckian thermal emission of subwavelength disks

Keynote lecture 3	**Bernd GOTSMANN**, IBM Research Zürich, Switzerland	
Chair: P.-O. Chapuis		
11h10-11h50	F. MENGES, P. MENSCH, S. KARG, A. STEMMER, H. RIEL and B. GOTSMANN	Nanoscale thermometry using scanning thermal microscopy

Session 11	Phonons and vibrations	
Chair: S. Volz		
13h20-13h40	N. KÖNNE, K. KLOPPSTECH and A. KITTEL	Experimental investigation of single molecule thermal conductance
13h40-14h00	E. CHÁVEZ-ÁNGEL, R.A. ZARATE, D. NAVARRO-URRIOS, J. GOMIS-BRESCO, F. ALZINA and C.M. SOTOMAYOR TORRES	Modification of Akhieser mechanism in Si nanoresonators
14h00-14h20	S. PAILHES, V.M. GIORDANO, H. EUCHNER, R. DEBORD and M. DE BOISSIEU	The low thermal conductivity of clathrates: a phononic filter effect
14h20-14h40	M. GROSSMANN, M. KLINGELE, P. SCHEEL, O. RISTOW, M. HETTICH, C. HE, R. WAITZ, M. SCHUBERT, A. BRUCHHAUSEN, V. GUSEV, E. SCHEER and T. DEKORSY	Acoustic frequency combs as a tool for measuring adhesion in a thin two-layer system
14h40-15h00	B. GRACZYKOWSKI, J. GOMIS-BRESCO, F. ALZINA, J.S. REPARAZ, A. SHCHEPETOV, M. PRUNNILA, J. AHOPELTO and C.M. SOTOMAYOR TORRES	Acoustic phonon dispersion in ultra-thin Si membranes under static stress field

Contents

Keynote lectures 1

K1: Coupling of heat and spin currents at the nanoscale in cuprates and metallic multilayers 3
D.G. CAHILL, G.T. HOHENSEE and G.-M. CHOI

K2: Nanophotonic control of thermal radiation: maximal violation of detailed balance, and experimental demonstration of daytime radiative cooling 7
S. FAN, A. RAMAN, L. ZHU, M. ANOMA and E. REPHAELI

K3: Nanoscale thermometry using scanning thermal microscopy 9
F. MENGES, P. MENSCH, S. KARG, A. STEMMER, H. RIEL and B. GOTSMANN

Oral presentations 13

Session 1: Atomic simulations 14

S1-01: Low thermal conductivity design with Si twinning superlattice nanowires 15
S. XIONG, Y.A. KOSEVICH, K. SÄÄKILAHTI, Y. NI and S. VOLZ

S1-02: Approach-to-equilibrium molecular dynamics: thermal properties from temperature transient 18
E. LAMPIN, P.L. PALLA, P.-A. FRANCIOSO and F. CLERI

S1-03: One-way phonon transport in modulated acoustic waveguides 21
M.B. ZANJANI, A.R. DAVOYAN, A.M. MAHMOUD, N. ENGHETA and J.R. LUKES

Session 2: Subwavelength radiation (1) 24

S2-01: Superdiffusive heat transport in nanoparticle networks 25
P. BEN-ABDALLAH, S.-A. BIEHS, K. JOULAIN and C. HENKEL

S2-02: Near-field thermal emission between corrugated surfaces separated by nano-gaps 28
A. DIDARI and M.P. MENGÜÇ

S2-03: Near-field thermal radiation absorbed by a flat film in the vicinity of a semi-infinite emitter 32
E. BLANDRE, P.-O. CHAPUIS, M. FRANCOEUR and R. VAILLON

S2-04: Thermal emission control with surface waves 36
D. COSTANTINI, G. BRUCOLI, H. BENISTY, F. MARQUIER and J.-J. GREFFET

Session 3: Experimental heat conduction (1) 38

S3-01: Thermal conductivity of porous silicon irradiated with swift heavy ions 39
M. MASSOUD, P.-O. CHAPUIS, B. CANUT , P. NEWBY, L.G. FRECHETTE and J.-M. BLUET

S3-02: Coherent control of thermal conduction in two-dimensional phononic crystals 42
N. ZEN, T.A. PUURTINEN, T.J. ISOTALO, S. CHAUDHURI and I.J. MAASILTA

S3-03: Reduction of thermal conductivity in silicon thin film membranes by phononic engineering .. 44
V. LACATENA, M. HARAS, J.-F. ROBILLARD, S. MONFRAY, T. SKOTNICKI, E. DUBOIS

S3-04: Joule heated micro- and nanowires: A versatile platform for high spatial and temporal resolution thermal investigations 47
C.M. QUINTERO, O. KRAIEVA, E.M. HERNÁNDEZ, F. CARCENAC, D. LAGRANGE, G. MOLNÁR and C. BERGAUD

Session 4: Numerical heat transfer 51

S4-01: Calculation of ballistic and Casimir-limit phonon thermal conduction in thin membranes 52
T. PUURTINEN and I. MAASILTA

S4-02: Interfacial heat transport in liquids and nanobubble dynamics 55
S. MERABIA, J. LOMBARD, T. BIBEN, A. ALKURDI

S4-03: Thermal conductivity of modulated nanowires 59
K. TERMENTZIDIS and D. LACROIX

S4-04: A comparative study of the anharmonicity of the transverse optical phonons in lead chalcogenides 61
J. AL-OTAIBI and G.P. SRIVASTAVA

Session 5: Constrictions and wires 64

S5-01: Phonon transport through constrictions in silicon nanowires 65
V. JEAN, K. TERMENTZIDIS, S. FUMERON and D. LACROIX

S5-02: Heat transfer in modulated nanowires with variable thickness 68
X. ZIANNI

S5-03: Phonon transport in silicon nanowires using a full-band Monte Carlo approach 72
J. LARROQUE, J. SAINT-MARTIN and P. DOLLFUS

Session 6: Surface modes 76

S6-01: Ultrafast plasmon heat transfer around subwavelength structures 77
O. LOZAN, M. PERRIN, B. EA-KIM, J.-M. RAMPNOUX, S. DILHAIRE and P. LALANNE

S6-02: Large penetration depth in hyperbolic metamaterials 80
S. LANG, M. TSCHIKIN, S.-A. BIEHS, P. BEN-ABDALLAH, A. PETROV and M. EICH

S6-03: Fresnel-like formulas for the reflection and transmission of surface phonon-polaritons at a dielectric interface 83
J. ORDONEZ-MIRANDA, L. TRANCHANT, T. ANTONI and S. VOLZ

Session 7: Experimental heat conduction (2) 86

S7-01: In-situ calibration of thermal sensors to measure absolute heat fluxes at the nano-scale 87

K. KLOPPSTECH, N. KÖNNE and A. KITTEL

S7-02: Quantitative thermal conductivity measurement by scanning thermal microscopy with nanofabricated thermal probes - methodology and modeling 90
J. BODZENTA, M. CHIRTOC and J. JUSZCZYK

S7-03: Strain based thermal conductivity tuning on nanoscale polycrystalline AlN thin-films..... 93
J. JARAMILLO-FERNANDEZ, W. KASSEM, V. REMONDIERE, U. SOUPREMANIEN, E. OLLIER and S. VOLZ

Session 8: Phonon simulations 97

S8-01: High temperature increase of the thermal conductivity of zirconium carbide explained by atomistic simulations 98
J.-P. CROCOMBETTE

S8-02: Phonon interference and thermal conductance reduction in atomic-scale metamaterials 102
H. HAN, Y.A. KOSEVICH and S. VOLZ

Session 9: Energy conversion 106

S9-01: Increasing thermoelectric efficiency: dynamical models unveil microscopic mechanisms 107
G. BENENTI and G. CASATI

S9-02: Near-field thermodynamics and nanoscale energy harvesting..... 109
I. LATELLA, A. PÉREZ-MADRID, L.C. LAPAS and J.M. RUBI

S9-03: Detailed analysis of heat generation in silicon solar cells 112
R. COUDERC, M. LEMITI and M. AMARA

S9-04: Low concentration solar-thermophotovoltaic system using high-temperature photonics 116
M. SHIMIZU, A. KOHIYAMA, F. IGUCHI and H. YUGAMI

Session 10: Subwavelength radiation (2) 120

S10-01: Thermal radiation between two plates: regime map and analytical expressions for the net radiative heat flux from far to near field 121
J. MAYO, Y. TSURIMAKI, P.-O. CHAPUIS, J. OKAJIMA, A. KOMIYA, S. MARUYAMA, A. NARAYANASWAMY and R. VAILLON

S10-02: Heat transfer between anisotropic nanoparticles: enhancement and switching..... 124
R. INCARDONE, T. EMIG and M. KRÜGER

S10-03: Far field diffraction of thermal Surface Phonon-Polaritons at the tip of micrometric glass tubes 126
L. TRANCHANT, J. ORDONEZ-MIRANDA, T. ANTONI and S. VOLZ

S10-04: Radiative thermal memory 129

V. KUBYTSKYI, S.-A. BIEHS and P. BEN-ABDALLAH

S10-05: Super Planckian thermal emission of subwavelength disks 132
K. JOULAIN, Y. EZZAHRI and J. DREVILLON

Session 11: Phonons and vibrations 136

S11-01: Experimental investigation of single molecule thermal conductance 137
N. KÖNNE, K. KLOPPSTECH and A. KITTEL

S11-02: Modification of Akhieser mechanism in Si nanoresonators 139
E. CHÁVEZ-ÁNGEL, R.A. ZARATE, D. NAVARRO-URRIOS, J. GOMIS-BRESCO, F. ALZINA and C.M. SOTOMAYOR TORRES

S11-03: The low thermal conductivity of clathrates: a phononic filter effect 143
S. PAILHES, V.M. GIORDANO, H. EUCHNER, R. DEBORD and M. DE BOISSIEU

S11-04: Acoustic frequency combs as a tool for measuring adhesion in a thin two-layer system 145
M. GROSSMANN, M. KLINGELE, P. SCHEEL, O. RISTOW, M. HETTICH, C. HE, R. WAITZ, M. SCHUBERT, A. BRUCHHAUSEN, V. GUSEV, E. SCHEER and T. DEKORSY

S11-05: Acoustic phonon dispersion in ultra-thin Si membranes under static stress field 147
B. GRACZYKOWSKI, J. GOMIS-BRESCO, F. ALZINA, J.S. REPARAZ, A. SHCHEPETOV, M. PRUNNILA, J. AHOPELTO and C.M. SOTOMAYOR TORRES

Poster contributions 149

Poster session 1 150

PS1-01: Radiative thermal rectification using superconducting materials 151
J. DREVILLON, E. NEFZAOUI, Y. EZZAHRI and K. JOULAIN

PS1-02: Analysis of thermal conductance of ballistic point contacts using Boltzmann Transport Equation 155
T.T.T. NGHIEM, J. SAINT-MARTIN and P. DOLLFUS

PS1-03: Focusing of surface phonon-polaritons along conical and wedge polar structures 159
S. GLUCHKO, J. ORDONEZ-MIRANDA, L. TRANCHANT, T. ANTONI and S. VOLZ

PS1-04: Modeling of heat transfer through gas molecules between a hot SThM probe and a cold sample surface 162
J. RANDRIANALISOA and N. TRANNOY

PS1-05: Thermal conductances across silicon sub-mean free path sources measured with a four-probe electrical setup 164
W. JABER, C. CHEVALIER and P.-O. CHAPUIS

PS1-06: Thermal conductivity restoration by disulfide-based self-healing polymers 167
N. ZHONG, S.J. GARCIA and S. VAN DER ZWAAG

PS1-07: Optimizing design of a thermal protection structure with PCs meta-material considering micro-scale transfer characteristics....169
H.-C. ZHANG, Y. ZHAO, H.-P. TAN, Y. LI and H.-Y. YU

PS1-08: Heat transfer through the water meniscus at the tip-sample contact investigated with Scanning Thermal Microscopy....173
A. ASSY, S. LEFEVRE, P.-O. CHAPUIS and S. GOMES

PS1-09: Thermoelectric coefficients: coupling transport equations and *ab initio* calculation....176
G. KANE, N. VAST and J. SJAKSTE

PS1-10: Thermal and electrical behavior of photon enhanced thermionic conversion....178
M. AMARA and A. VOSSIER

PS1-11: Thermal properties of a nanostructured Ge:Mn thin film for thermoelectricity....182
Y. LIU, D. TAINOFF, M. BOUKHARI, J. RICHARD, A. BARSKI, P. BAYLE-GUILLEMAUD, E. HADJI, A. ASSY, S. GOMES and O. BOURGEOIS

PS1-12: Heat transfer studies using Ln^{3+} based nanothermometers....186
C.D.S. BRITES, P.P. LIMA, N.J.O. SILVA, A. MILAN, V.S. AMARAL, F. PALACIO and L.D. CARLOS

PS1-13: Xe-Arc Flash Lamp Crystallization of Amorphous Silicon Thin-Film for Large-Scale Displays....189
S. PARK

PS1-14: 2ω/3ω SThM: improvements and perspectives....193
A. BONTEMPI, L. THIERY, D. TEYSSIEUX and P. VAIRAC

PS1-15: SThM measurement of thermal conductivity of a nanowire Sb_2Te_3 crystal along the c-axis....197
A. SACI, J.-L. BATTAGLIA, A. KUSIAK, R. FALLICA and M. LONGO

Poster session 2 200

PS2-01: Time-resolved measurements and quantitative analysis of the cooling dynamics of gold and gold-silica nanospheres in liquid environment....201
T. STOLL, P. MAIOLI, A. CRUT, N. DEL FATTI and F VALLEE

PS2-02: Heat transfer through a triangular phononic crystal column....204
T.T.T. NGHIEM and P.-O. CHAPUIS

PS2-03: Morphologies and radiative properties of soot particles issued from partial oxidation combustions....207
G. OKYAY, Y. JOUMANI, C. BERTAIL and F. ENGUEHARD

PS2-04: Thermal Properties of Chirped Superlattice Structures through Molecular Dynamics and Photothermal Radiometry....211
K. HORNE, M. CHIRTOC, N. HORNY, T. ANTONI, S. VOLZ and H. BAN

PS2-05: Vacuum phonon coupling through Casimir force between two solid dielectric materials 214
Y. EZZAHRI and K. JOULAIN

PS2-06: Submicrometric scale thermometry: coupling of a thermal-resistive probe and a photoluminescent microcrystal.....218
G. DEGLIAME, N. TRANNOY, J.-P. JOUART, M. DIAF, T. DUVAUT and D. CARON

PS2-07: Coherent acoustic phonons in thin films of $CoSb_3$ and partially filled $Yb_xCo_4Sb_{12}$ skutterudites.....220
C. HE, M. DANIEL, M. GROSSMANN, O. RISTOW, D. BRICK, M. SCHUBERT, M. ALBRECHT and T. DEKORSY

PS2-08: A comparative study of different numerical approaches to the Boltzmann Transport Equation for phonons.....222
E. NEFZAOUI and P.-O. CHAPUIS

Index of authors.....225

Nanoscale and Microscale Heat Transfer IV

Keynote lectures

Coupling of heat and spin currents at the nanoscale in cuprates and metallic multilayers

David G. CAHILL*, Gregory T. HOHENSEE, and Gyung-Min CHOI

Department of Materials Science and Engineering and Materials Research Laboratory, University of Illinois, Urbana, Illinois 61801

**corresponding author: d-cahill@illinois.edu*

Keywords: thermal conductivity, magnons, ultrafast heat transfer, spin current, spin Seebeck

A. Thermal transport by magnons and magnon-phonon coupling in cuprates.

Heat conduction in materials is typically mediated by thermal excitations of atomic vibrations (i.e., phonons) or thermal excitations of the electronic degrees of freedom (i.e., electrons and holes in metals and heavily doped semiconductors). However, any thermal excitation of the solid can, in principle, contribute significantly to the thermal conductivity if the heat capacity of the excitations is significant, the excitations have a large dispersion so that the group velocity is large, and the lifetime of the excitation is not too short. These conditions are met by the spin degrees of freedom in low-dimensional quantum magnets based on copper oxides ($Sr_{14}Cu_{24}O_{41}$, La_2CuO_4, $CaCu_2O_3$). These materials have a seemingly unique large magnon thermal conductivity: near room temperature, the magnon thermal conductivities are comparable to the electronic thermal conductivities of metal alloys. A fundamental question then arises: what limits the magnon lifetimes and therefore limits the magnon thermal conductivity? We are studying the exchange of thermal energy between the magnon and phonon systems as a first step toward answering that question.

We use time-domain thermoreflectance (TDTR) to measure the thermal conductivity of cuprate single crystals as a function of the frequency of thermal fields. In a time-domain thermoreflectance measurement, a laser oscillator, typically a Ti :sapphire laser operating at a 80 MHz repetition rate, is used as a pulsed source of light. The output is split into a pump and probe beam. The pump beam is modulated at a high frequency (between 1 and 20 MHz). The time of arrival of the pump and probe beams at the sample surface is adjusted by a mechanical delay line with picosecond precision. The time dependence of the temperature excursions induced by the pump provide useful information about heat capacity of thin metal films and thermal conductance of interfaces; most of the sensitivity to the thermal conductivity of the sample, however, comes from the out-of-phase response at the modulation frequency of the pump beam [1]. Approximately 10 years ago, we introduced an exact analytical solution of the diffusion equation (the analytical solution must be evaluated numerically) for an arbitrary multilayer sample in a TDTR experiment [2]. Anisotropy of high symmetry (a thermal conductivity tensor with only in-plane and through plane values) is easily incorporated. These solutions have been recently extended to the situation where the pump and probe beams are displaced with respect to each other [3].

Phenomenological two-temperature models have been used for many years to describe the coupled transport of heat by electrons and phonons in metals. Here, we apply this concept to the coupled transport of heat by magnons and phonons in the spin ladder compound $Ca_9La_5Cu_{24}O_{41}$. In this type of two-temperature modeling, the magnons and phonons separately satisfy a diffusion equation while the two diffusion equations are coupled to each other through a coupling parameter that has units of a thermal conductance per unit volume. Microscopically, the problem is, of course, much more

complicated than this single parameter can capture. The single-parameter model will work best if the magnon occupation numbers can be approximated by a single magnon temperature and the phonon occupation by a single phonon temperature. We recently described how our conventional solution for the heat diffusion equation in the TDTR geometry can be extended to multiple channels [4].

Because phonons can carry heat across the Al/sample interface but magnons cannot (there are no

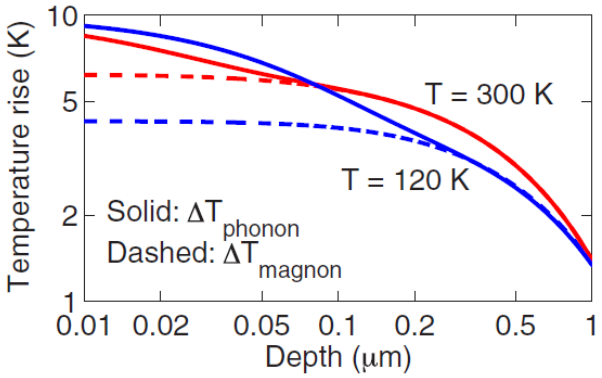

Figure 1 : Model calculation of the amplitudes of the magnon and phonon temperature oscillations near the surface of a Al/spin-ladder sample during a time-domain thermoreflectance measurement with a pump modulation frequency of 10 MHz. Near room temperature, 300 K, the region of non-equilibrium is much thinner than the thermal penetration depth. At low temperatures, 120 K, the non-equilibrium region starts to overlap with the thermal penetration depth.

magnon excitations in the Al film transducer), the Al/sample interface creates a strong non-equilibrium between the magnon and phonon temperatures [5]. This region of non-equilibrium extends over a distance of nanoscale dimensions, approximately 50 nm at room temperature and 200 nm at 120 K, see Fig. 1. At low temperatures and high modulation frequencies, the region of non-equilibrium approaches the thermal penetration depth in the experiment and, as a consequence, the apparent thermal conductivity is strongly suppressed. We use comparisons between measured apparent thermal conductivity at different modulation frequencies and the predictions of the 2-channel model [4] to determine the magnon-phonon coupling parameter g from 80 to 300 K. Near the peak in the magnon thermal conductivity, $g \approx 10^{15}$ W m^{-3} K^{-1}, approximately two orders of magnitude smaller than a typical electron-phonon coupling parameter in a metal [5].

B. Generation of spin currents by heat currents in metallic multilayers

Cross terms of the electrical and thermal transport coefficients, i.e., the Seebeck and Peltier coefficients, have been a topic of sustained study for many decades because of their applications in sensing, solid-state cooling, and energy harvesting. There are also cross-terms that involve spin and charge currents, and cross terms for spin and heat currents. The cross-terms of spin and charge are a key topic of study in the field of spintronics. The cross-terms of spin and heat are a core consideration of an emerging discipline, often referred to as spin caloritronics.

One of the most challenging problems in the field of spin caloritronics is the detection of the spin density or spin current in a sample: the experimentalist does not have the meter for spin that is analogous to of a thermometer or a voltmeter. Often, measurements are based on the so-called inverse spin Hall effect (ISHE) where a spin current entering a normal (nonferromagnetic) metal with strong

spin-orbit coupling generates an electric field that can be measured as a transverse voltage. The voltages generated by the ISHE effect are extremely small and, controversially, a susceptibile to systematic errors generated by conventional magneto-thermoelectric effects driven by heat currents flowing through the electrical contact leads. We have taken an alternative approach for detecting spin that also provides high time resolution: we detect the spin density in a normal metal using the magneto-optic Kerr effect (MOKE). By performing MOKE measurements with a pump probe apparatus, we can generate enormous heat currents (surpassing 100 GW m^{-2} K^{-1}) on picosecond time-scales and simultaneously detect spin accumulation with picosecond time resolution [6].

We are working to better constrain the calibration of the Kerr rotation as a function of spin accumulation in Cu and Au. This is a challenging process because we do not have a calibrated source of spin. Our initial experiments and analysis suggest that the Kerr rotation is determined by the strength of the spin-orbit coupling in the conduction band and is approximately 5 times stronger in Au than in Cu.

We study two types of samples that are shown schematically as Fig. 2. In the first type of sample, the spin accumulation in the normal metal is detected by time-resolved MOKE (TR-MOKE). In the second type of sample, the transfer of spin angular momentum (the so-called spin transfer torque) is detected by the amplitude of the magnetic precession that is induced into a very thin (2 nm thick) in-plane magnet made of CoFeB [6].

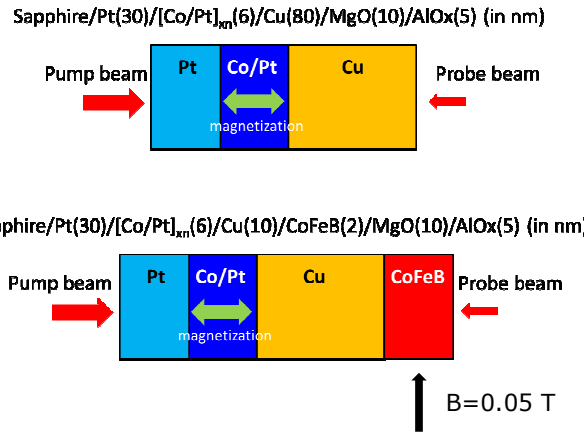

Figure 2: Schematic diagrams of the two types of samples used in the studies of thermally-driven spin currents. The numbers in the sample descriptions are thicknesses in nm. The pump beam is incident on the left and heat flows from left-to-right. (Top) Sample design for spin accumulation. The spin density in the thick Cu layer is detected by the magneto-optic Kerr effect (MOKE). (Bottom) Sample design for spin-transfer torque. The spin transfer torque is measured through the amplitude of the magnetization precession of the CoFeB ferromagnetic layer, also detected optically via MOKE.

We are working to constrain the many parameters in the models of heat transport, spin generation and spin diffusion that we use to analyze the experiments. In the initial experiments, we have found that the spin currents are predominately generated by the fast thermal demagnetization of the (Co,Pt) ferromagnetic layer. Essentially, raising the temperature decreases the equilibrium magnetization and the non-equilibrium between electrons and magnons transfer a fraction of the spin angular momentum to the conduction electrons which then diffuse into the adjacent layers. A smaller amount of spin current is generated by the spin-dependent Seebeck effect (SDSE) of the ferromagnetic layer. The SDSE is due to the fact that the product of the Seebeck coefficients and conductivities of the up and

down spin sub-bands are not equal; therefore, a heat current passing through a ferromagnet produces a spin accumulation near the surfaces or interfaces of the ferromagnetic layer that can diffuse into adjacent layers [6].

We argue that the experimental design illustrated by Fig. 2 will provide a rich platform for studies of the coupling of heat and spin in metallic multilayers. With some advances, we will soon have calibrated sources of spin and calibrated detectors of spin, both with picosecond time resolution. This platform can be used to quantitatively study thermal generation of spin currents by the spin-dependent Seebeck effect and ultrafast demagnetization, as well as transport physics of spin such as the transport and mixing of spin at interfaces.

References

[1] D. G. Cahill *et al*., "Nanoscale Thermal Transport II: 2003-2012," *Appl. Phys. Rev*. **1**, 011305, 2014.

[2] D. G. Cahill, "Analysis of heat flow in layered structures for time-domain thermoreflectance," *Rev. Sci. Instrum*. **75**, 5119, 2004.

[3] J. P. Feser and David G. Cahill, "Probing anisotropic heat transport using time-domain thermoreflectance with offset laser spots," *Rev. Sci. Instrum.* **83**, 104901, 2012.

[4] R. B. Wilson, J. P. Feser, G. T. Hohensee, D. G. Cahill, "Analysis of two-channel heat flow in pump-probe studies of non-equilibrium thermal transport," *Phys. Rev. B* **88**, 144305, 2013.

[5] G. T. Hohensee, R. B. Wilson, J. P. Feser, and D. G. Cahill, "Magnon-phonon coupling in Ca9La5Cu24O41 spin ladders measured by time-domain thermoreflectance," *Phys. Rev. B* **89**, 024422, 2014.

[6] Gyung-Min Choi, Byoung-Chul Min, Kyung-Jin Lee, and David G. Cahill, "Spin current generated by thermally-driven ultrafast demagnetization," *Nature Communications* **5**, 4334, 2014.

Nanophotonic control of thermal radiation: maximal violation of detailed balance, and experimental demonstration of daytime radiative cooling

Shanhui FAN[a*], Aaswath RAMAN[a], Linxiao ZHU[a], Marc ANOMA[a] and Eden REPHAELI[a]

[a]*Ginzton Laboratory, Department of Electrical Engineering, Stanford University, Stanford, CA 94305*

Keywords: nanophotonc structure, thermal radiation, radiative-cooling, detailed balance, non-reciprocity

The use of nanophotonic structure opens significant new possibilities to control thermal radiation, both in enabling new thermal physics effects, and in creating new application opportunities. In this talk, we will review some of our recent efforts in nanophotonics-enabled thermal radiation control. In particular, we will discuss the possibility of using non-reciprocal nanophotonic structures to maximally violate detailed balance. We will also report some of our recent experimental efforts in the successful demonstration of passive radiative cooling under direct sunlight.

1. Maximal violation of detailed balance in non-reciprocal nanophotonic structures

For thermal radiation, the principle of detailed balance leads to the general form of the Kirchhoff's law which states that

$$e(\omega,\theta,\phi) = \alpha(\omega,\theta,\phi) \tag{1}$$

where $e(\omega,\theta,\phi)$ is the directional spectral emissivity, $\alpha(\omega,\theta,\phi)$ is the directional spectral absorptivity, Microscopically, Eq. 1 can be proven using the fluctuation-dissipation theorem, but only for emitters consisting of materials satisfying Lorentz reciprocity [1]. It has been noted theoretically that non-reciprocal materials, such as magneto-optical materials, may not obey detailed balance [2] and hence may not satisfy Eq. 1, without violating the second law of thermodynamics. However, there has not been any direct experimental measurement or theoretical design of actual physical structures that violate detailed balance.

In recent years, significant recent efforts have been devoted to the use of engineered photonic structures, including photonic crystals, optical antennas, and meta-materials, for the control of thermal radiation properties. Photonic structures can exhibit thermal radiation properties that are significantly different from naturally occurring materials. Notable examples include the creation of thermal emitters with narrow spectrum or enhanced coherence. All previous works on the thermal radiation properties of photonic structures, however, consider only reciprocal materials. Here, using the formalism of fluctuational electrodynamics, we present a direct numerical calculation of thermal emission from non-reciprocal photonic structures, and introduce the theoretical conditions for such structures to maximally violate detailed balance, i.e. to achieve a unity difference between directional spectral emissivity and absorptivity [3].

Non-reciprocal photonic structures represent an important emerging direction for the control of thermal radiation. From a fundamental point of view, significant numbers of theoretical approaches for the calculations of far-field thermal radiation use the Kirchhoff's law of Eq. 1 by computing the

absorption properties. Such an approach is no longer applicable for non-reciprocal thermal emitters, and direct calculations using the formalism of fluctuational electrodynamics become essential. From a practical point of view, creating non-reciprocal thermal emitters can have important implications for the enhancement of the efficiency for solar cells [4] and thermophotovoltaic systems.

2. Experimental demonstration of daytime radiative cooling

Cooling is a significant end-use of energy globally and a major driver of peak electricity demand. Air conditioning of buildings, for example, accounts for 15% of the primary energy used to generate electricity in the United States. A passive cooling strategy that cools without any electricity input could therefore have a significant impact on global energy consumption.

To achieve cooling one needs to be able to reach and maintain a temperature below the ambient air. At night, passive cooling below ambient air temperature has been demonstrated using a technique known as radiative cooling, where one uses a device exposed to the sky to radiatively emit heat to outer space through a transparency window in the atmosphere between 8-13 μm [5][6]. Peak cooling demand however occurs during the daytime. Daytime radiative cooling below ambient under direct sunlight [7][8] was never achieved, because sky access during the day results in heating of the radiative cooler by the sun.

Here, using a thermal nanophotonic approach [9], we introduce an integrated nanophotonic solar reflector and thermal emitter that reflects 97% of incident sunlight while emitting strongly and selectively in the atmospheric transparency window. When exposed to direct solar irradiance of greater than 850 W/m^2 on a rooftop, the nanophotonic radiative cooler achieves 4.9^{o}C below ambient air temperature, and has a cooling power of 40.1 W/m^2 at ambient. These results demonstrate that a tailored, nanophotonic approach can fundamentally enable new technological possibilities for energy efficiency, and further indicate that the cold darkness of the universe can be used as a renewable thermodynamic resource, even during the hottest hours of the day.

References

[1] M. Kruger, G. Bimonte, T. Emig and M. Kardar, “Trace formulae for non-equilibrium Casimir interactions, heat radiation and heat transfer for arbitrary objects”, *Physical Review B* **86**, 115423, 2012.

[2] W. C. Snyder, Z. Wan, X. Li, “Thermodynamic constraints on reflectance reciprocity and Kirchhoff’s law”, *Applied Optics* **37**, 3464, 1995.

[3] L. Zhu and S. Fan, “Near-complete violation of detailed balance in thermal radiation”, (submitted, 2014).

[4] M. A. Green, “Time-Asymmetric Photovoltaics”, *Nano Letters*, **12**, 5985, 2012.

[5] C.G. Granqvist, A. Hjortsberg, “Radiative cooling to low temperatures: General considerations and application to selectively emitting SiO films”, *Journal of Applied Physics*, **52**, 4205, 1981.

[6] A.R. Gentle, G.B. Smith, “Radiative Heat Pumping from the Earth Using Surface Phonon Resonant Nanoparticles”, *Nano Letters*, **10**, 373, 2010.

[7] S. Catalanotti, V. Cuomo, G. Piro, D. Ruggi, V. Silvestrini, G. Troise, “The radiative cooling of selective surfaces”, *Solar Energy*, **17**, 83, 1975.

[8] E. Rephaeli, A. Raman, and S. Fan, “Ultrabroadband photonic structures to achieve high-performance daytime radiative cooling”, *Nano Letters*, **13**, 1457, 2013.

[9] A. P. Raman, M. A. Anoma, L. Zhu, E. Rephaeli, and S. Fan, “Passive radiative cooling below ambient air temperature under direct sunlight”, (submitted, under external review, 2014).

Nanoscale thermometry using scanning thermal microscopy

Fabian MENGES[a,b], Philipp MENSCH[a], Siegfried KARG[a], Andreas STEMMER[b], Heike RIEL[a], and Bernd GOTSMANN[a*]

[a]*IBM Research - Zurich, Säumerstrasse, 8803 Rüschlkion, Switzerland*

[b]*Nanotechnology Group, ETH Zurich, Säumerstrasse 4, CH-8803 Rüschlikon, Switzerland*

**corresponding author: bgo@zurich.ibm.com www.zurich.ibm.com/~bgo*

Keywords: Scanning thermal microscopy, self-heating, nanoscale hot spots, thermometry, nanowire

Regions of increased heat generation, so-called hot spots, deteriorate the performance and reliability of nanoelectronic devices [1], while experimental characterization is restricted by limited spatial resolution in thermometry. Since local self-heating is of increasing importance for future devices, where scaling, integration of novel materials and structures tend to impede heat conduction, new methods and instrumentations are needed to study the coupling between thermal, electrical and structural properties at the level of individual operating devices.

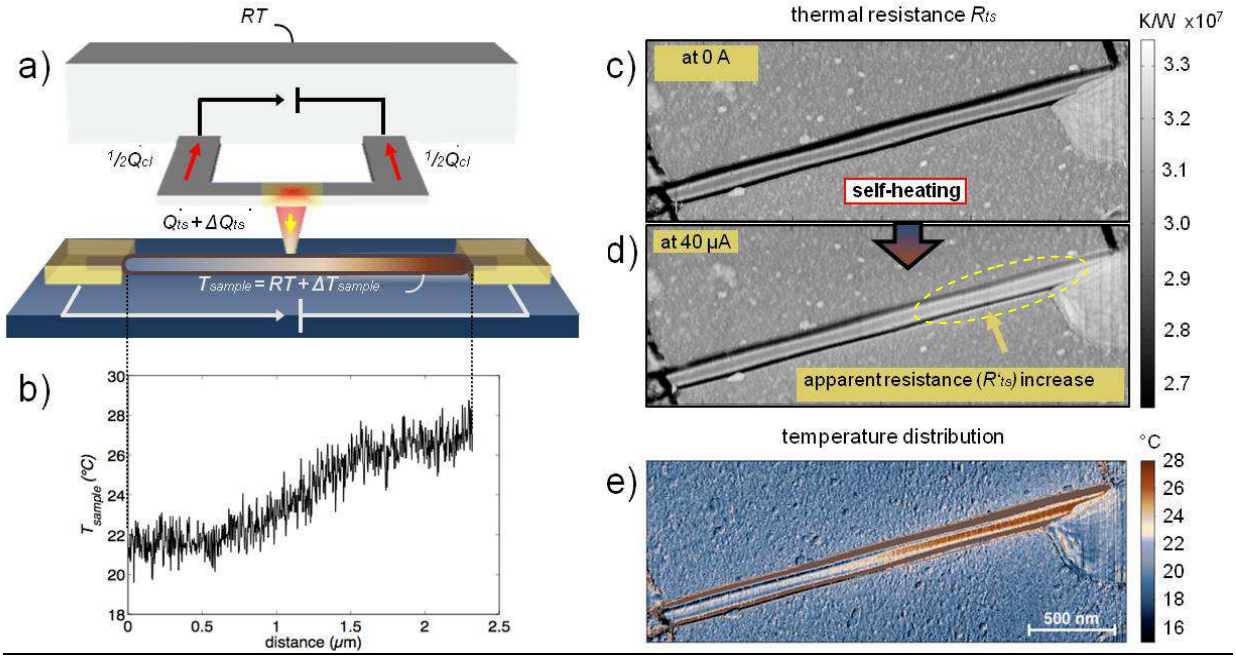

Figure 1: Scanning thermal microscopy for thermometry of nanoscale temperature distribution. a) Schematic of the experiment including cantilevered SThM tip with integrated heater/sensor and active nanowire (NW) device (InAs NW with Au contacts). b) Temperature distribution along the NW extracted from SThM data. c) Reference measurement of the position dependent thermal resistance of the tip-sample contact R_{ts} using an idle sample at RT. d) Repeated measurement with self-heated NW showing an apparent increase of R_{ts} locally along the NW. e) Extracted temperature distribution map.

With decreasing size of microelectronic devices, the thermal hot spots can reach dimensions below 10 nm. On this length scales thermometry is not yet very advanced. Scanning Thermal Microscopy (SThM) [2] appears to be an ideal method to address the challenge. By moving a sharp tip attached to

a heater/sensor in contact with a device of interest, thermal signals relating to thermal conductance and temperature distribution within a sample can be inferred.

Despite recent progress using the method [3-6], however, it remains a challenge to extract quantitative data from measured SThM images on the nanoscale. One of the reasons for this is the fact that a large thermal resistance separates the sample region to be measured from the integrated heater/sensor. Sensor and sample do therefore not equilibrate. This poses several calibration challenges and systematic errors to the SThM method. In this presentation the most important systematic errors of the method are discussed and the efforts to eliminate them will be described. Application examples and measurements on nanoscale test structures will be shown.

The large thermal resistance between the SThM sensor tip and the sample is expected to increase strongly when scaling down to the nanoscale due to surface-to-volume scaling. Consider, for example, the case of an anticipated lateral resolution of 10 nm at an accuracy of ΔT_{sample} = 1 K. The thermal resistance of the contact between the contacting tip and the sample can then be dominated by the interface thermal resistance and fall in the range of $R_{ts} = 10^7 - 10^9$ K/W leading to a heat flux down to 1 nW. In contrast, the electrical leads leading to the temperature sensor within the cantilevered SThM tip have a thermal resistance R_{sensor} of typically 2 to 4 orders of magnitude smaller, leading to temperature rises in the sensor of $\Delta T_{sensor} < 1$ mK. Furthermore, R_{int} varies strongly as a function of tip position while scanning the sample surface, i.e. $R_{ts} = R_{ts}(x,y)$. Reasons for this are topography artifacts caused by a varying contact diameter between the tip and the sample surface, the variation of the local sample thermal conductivity, and the load force between tip and sample [7]. For the quantitative interpretation of the data therefore $R_{ts}(x,y)$, $\Delta T_{sensor}(x,y)$ and R_{sensor} have to be determined experimentally.

A two-pass method [5] serves to quantify these signals: The thermal resistance of the tip-sample contact R_{ts} (consisting mainly of R_{int}, and the spreading resistances in tip and sample) are determined from the heat flux from the sensor into the sample Q_{ts} and the temperature difference between the sensor temperature T_{sensor} and room temperature RT:

$$\dot{Q}_{ts} = (T_{sensor} - RT)/R_{ts} \quad (1)$$

For a sample at temperature $RT+\Delta T_{sample}$ we therefore have:

$$\dot{Q}'_{ts} = \left(T_{sensor} - \{RT + \Delta T_{sample}\}\right)/R_{ts} \quad (2)$$

The measurement process is illustrated in Fig. 1. First, we measure R_{ts} for each image pixel using an unheated sample ($R_{ts}(x,y)$) from the measured tip-sample heat flux using Eq. (1), as shown in Fig. 1c. Next, the measurement is repeated on the self-heated sample to determine a modified heat flux Q_{ts}' from which the sample temperature ΔT can be determined using Eq. (2). Self heating effects can be directly seen plotting the *apparent* thermal resistance $R_{ts} = (T_{sensor} - RT)/\dot{Q}_{ts}$, see Fig. 1d. The resulting ΔT is plotted in Fig. 1b and e.

Recently, the proposed method was developed further to reach a resolution of ΔT_{sample} in the mK-range at a lateral resolution of below 10 nm [8]. The talk will describe examples of isolated hot-spots in nanowire devices (Figure 2) and metal interconnect structures. Furthermore, effects of Peltier and Joule heating will be discussed.

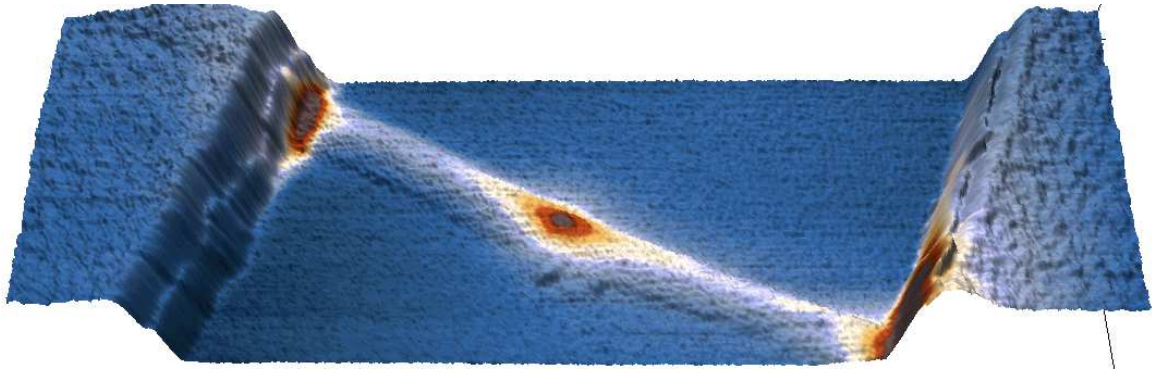

Figure 2: Hot spots in self-heated single vanadium oxide nanowire as measured using SThM.
The image shows a topography image of a vanadium oxide nanowire contacted using gold electrodes and supported by a silicon nitride substrate. The image size is 2.5 x 0.8 μm^2 and the height of the electrodes is 40 nm. The color scale denotes the thermal signal overlayed onto the topography. A local hotspot at the center of the wire is caused by local defects, two more hot spots can be observed at the contacts to the metal electrodes.

.

The experimental results shown in the talk were obtained with generous support from Heinz Schmid, Pratyush Das Kanungo, Ute Drechsler, Emanuel Loertscher, Mark Lantz, Kirsten Moselund, Christos Dimitrakopoulos and Meinrad Tschudy.

This work was supported in part by the Swiss National Science Foundation (Project No. 134777) and **t**he European Union FP7 Project Nanoheat under Grant Agreement No. 318625.

References

[1] E. Pop, "Energy Dissipation and Transport in Nanoscale Devices", *Nano Res.* **3**, 147−169, 2010.

[2] A. Majumdar, "Scanning Thermal Microscopy", *Annu. Rev. Mat. Sci.* **29**, 505, 1999.

[3] S. Gomès, O. Chapuis, F. Nepveu, N. Trannoy, S. Volz, B. Charlot, G. Tessier, S. Dilhaire, B. Cretin and P. Vairac, "Temperature Study of Sub-Micrometric ICs by Scanning Thermal Microscopy", *IEEE Trans. CPMT* **30,** 424, 2007.

[4] K. Kim, J. Chung, J. Won, O. Kwon, J. S. Lee, S. H. Park, and Y. K. Choi, "Quantitative scanning thermal microscopy using double scan technique", *Appl. Phys. Lett.* **93**, 203115, 2008.

[5] F. Menges, A. Stemmer, H. Riel, B. Gotsmann, "Quantitative Thermometry of Nanoscale Hot Spots", *Nano Lett.* **12**, 596, 2012.

[6] K. Kim, W. Jeong, W. Lee, P. Reddy, "Ultra-High Vacuum Scanning Thermal Microscopy for Nanometer Resolution Quantitative Thermometry", ACS Nano **6**, 4248, 2012.

[7] B. Gotsmann, M.A. Lantz, "Quantized thermal transport across contacts of rough surfaces", *Nature Materials* **12**, 59-65, 2013.

[8] F. Menges, A. Stemmer, H. Riel, B. Gotsmann, "Thermal Transport into Graphene through Nanoscopic Contacts", *Phys. Rev. Lett.* **111**, 205901, 2013.

Nanoscale and Microscale Heat Transfer IV

Oral presentations

Session 1

Atomic simulations

Low thermal conductivity design with Si twinning superlattice nanowires

Shiyun XIONG[a,b], Yuriy A. KOSEVICH[a,b,c], K. SÄÄKILAHTI[a,b,d], Yuxiang NI[a,b], and Sebastian VOLZ[a,b,*]

[a]*CNRS, UPR 288 Laboratoire d'Energétique Moléculaire et Macroscopique, Combustion (EM2C), Grande Voie des Vignes, 92295 Châtenay-Malabry, France*

[b]*Ecole Centrale Paris, Grande Voie des Vignes, 92295 Châtenay-Malabry, France*

[c]*Semenov Institute of Chemical Physics, Russian Academy of Sciences, 119991 Moscow, Russia*

[d]*Department of Biomedical Engineering and Computational Science, Aalto University, FI-00076 Aalto, Finland*

**corresponding author: sebastian.volz@ecp.fr*

Keywords: Thermal conductivity, Twinning superlattice, Molecular dynamics, Mode polarization.

Due to the unique thermal transport properties, heterostructure superlattices (SLs) have been widely studied [1-6]. It has been shown that, for a crystalline superlattice (SL), the cross-plane thermal conductivity can be one order of magnitude smaller than the one of bulk materials with a single component, and in some cases, even smaller than the value of a random alloy with the same elements due to the numerous interface scatterings. On the other hand, geometric SLs composed by the same component have rarely been studied [7]. Nevertheless, this kind of SLs has also vital importance as they involve nontrivial consequences on the electronic and phonon properties of the materials. Twinning, also known as the planar stacking fault, is one of the most important defects in materials science and it is most often related to mechanical properties [8,9]. The impact of twinning on mechanical [8,9], electronic [10,11], as well as on optical properties [11] has been widely studied while this impact remains unexplored concerning thermal properties. In this work, we perform nonequilibrium molecular dynamics (NEMD) simulations to calculate the thermal conductivity of the Si NWs with twinning SLs. We show that the thermal conductivity of the twinning SL NWs can be remarkably reduced up to 65% at room temperature compared to their pristine counterpart. A minimum thermal conductivity due to a geometric effect is found with a specific SL period.

Fig. 1 shows the structure of the twinning SL with the diameter D and period L_p. For a close-packing structure, there are usually three types of stacking sites with exactly the same configuration but having a shift one from another in a specific direction. The three stacking sites are usually labelled as A, B, and C. The B and C sites can be obtained from the A site with a shift of $(1+3n)b_v$ and $(2+3n)b_v$, respectively, where b_v is the minimum shift length and n is an integer. For Si having a FCC diamond lattice, b_v =2.217 Å. The wire firstly grows according to a FCC structure, i.e., following a stacking in the ABCABC sequence with the same shift given by the vector b_v between the neighboring layers. After several ABC periods, a stacking fault is introduced, instead of stacking a A layer, a B layer is directly introduced after the C layer with a shift of b_v in the opposite direction. After the stacking fault, the stacking sequence changes to CBACBA, which is purely symmetrical to the previous stacking. As a result, a kink is formed with the angle θ= 109.4°.

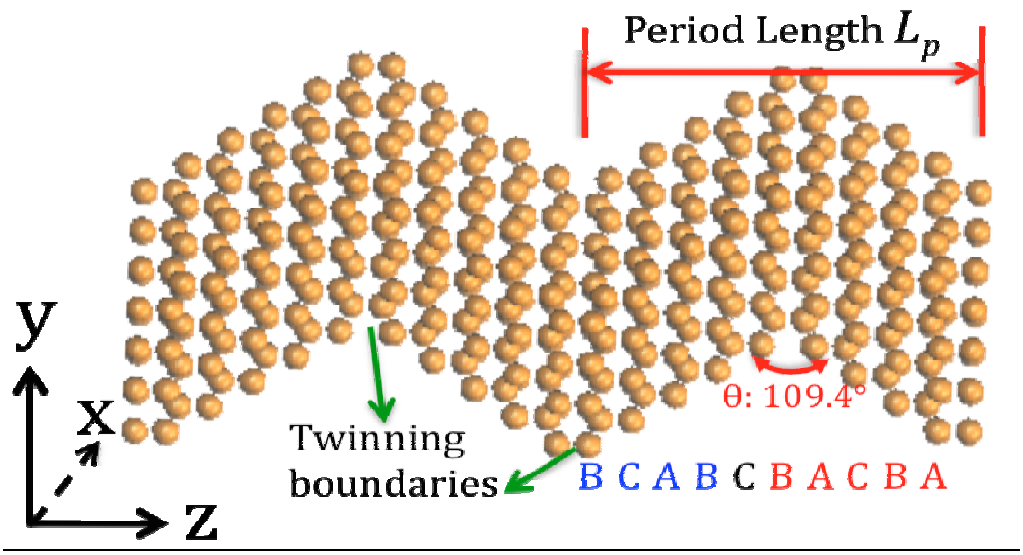

Figure 1: Schematic of a twinning superlattice structure with period length L_p .

All the thermal conductivities are carried out with NEMD simulations using the LAMMPS software [12]. The commonly adopted Stillinger-Weber potential [13,14] is used to describe the interactions between atoms. With the help of the Nosé-Hoover thermostat [15,16], several layers of atoms at the two ends of wire were coupled to a hot and a cold baths having temperatures $\boldsymbol{T_0}+\boldsymbol{\Delta}/2$ and $\boldsymbol{T_0}-\boldsymbol{\Delta}/2$, respectively. 5 ns runs were performed to reach non-equilibrium steady state, and another 5 ns to timeaverage the local temperature $\boldsymbol{T}$ and the microscopic heat flux $\boldsymbol{j}$ along the z direction. All the NWs thermal conductivities were measured with the same kink leg length of 34.5 nm.

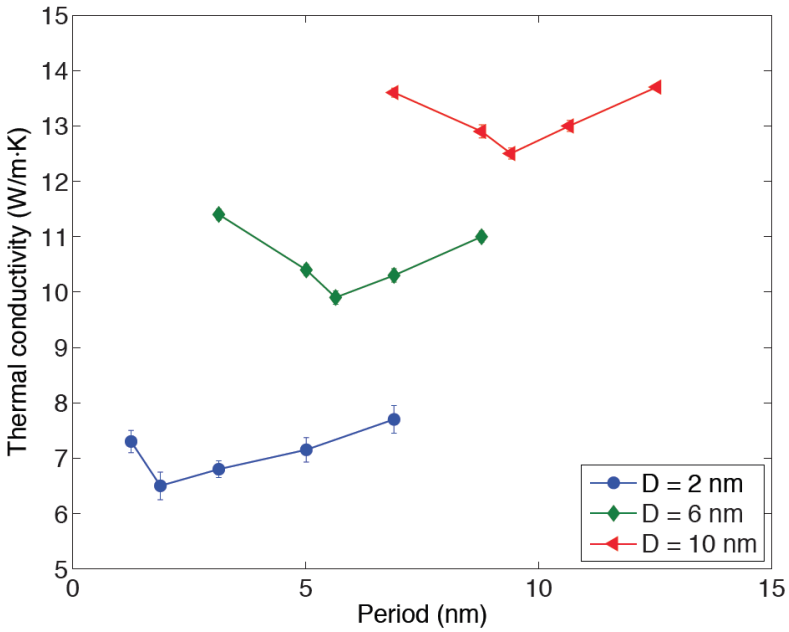

Figure 2: Thermal conductivity variation with period length for different diameters at 300 K.

Fig. 2 represents the thermal conductivities of the Si twinning SL NWs as a function of period $\boldsymbol{L_p}$ and specified diameter D at 300 K. The thermal conductivities of pristine NWs with 2, 6, and 10 nm in diameter are 18.4±0.15, 21±0.1, and 24.5±0.11 W/mK. As it is shown in Fig. 2, the thermal conductivities of the NWs with twinning SL are largely decreased compared to the one of the pristine NW. When the diameter remains invariant, the increase in SL period leads the thermal conductivity to decrease first, reaching a minimum value, and then progressively to an increase. The minimum

thermal conductivity observed here seems similar to that observed in the hetereostructure SLs [1-4]. However, the mechanism taking place in the twinning SL NWs completely differs from the one observed in heterostructure SL. In this latter situation, the minimum thermal conductivity is attributed to the interplay between the phonon coherence and the interface scattering. For the twinning SL NWs, thermal conductivity change is fully ascribed to the twinning induced zigzag geometric effect. This can be confirmed from the diameter dependent SL periods corresponding to the minimum thermal conductivities. The period length of minimal thermal conductivity increases with the diameter. It has been experimentally demonstrated that the twinning boundary has almost no effect on the electrical conductivity in both bulk [17] and nanowire [18] cases. As a result, the thermoelectric figure of merit of Si can be notably enhanced with the twinning SL NWs thanks to the significant thermal conductivity decrease.

To explain the large thermal conductivity decrease as well as the minimal thermal conductivities, we checked the normal mode polarization vectors [19]. We found that at the period with minimum thermal conductivity, the polarization vectors are randomly distributed on an arc, showing no favored polarization direction. Consequently, the decrease of thermal conductivity originates from the loss of preferential atom polarization orientation and the minimal thermal conductivity arises due to the disappearance of favored atom polarization directions.

References

[1] P. Hyldgaard, G.D. Mahan, *Phys. Rev. B* **56**, 10754-10757, 1997.

[2] M.D. Simkin, G.D. Mahan, *Phys. Rev. Lett.* **84**, 927-930, 2000.

[3] Y.K. Koh, Y. Cao, D.G. Cahill, D. Jena, *Adv. Funct. Mater.* **19**,610-615, 2009.

[4] M.L. Lee, R. Venkatasubramanian, *Appl. Phys. Lett.* **92**, 053112, 2008.

[5] S. Volz, J. Saulnier, G. Chen, P. Beauchamp, *Microelectron J.* **31**, 815, 2000.

[6] A. Rajabpour, S. Volz, *J. Appl. Phys.* **108**, 094324, 2010.

[7] K. Termentzidis, T. Barreteau, Y. Ni, S. Merabia, X . Zianni, Y. Chalopin, P. Chantrenne, S. Volz, *Phys. Rev. B* **87**, 125410, 2013.

[8] J. Wang, H. Huang, *Appl. Phys. Lett*. **88**, 203112, 2006.

[9] Z. Lin, L. Wang, J. Zhang, X.-Y. Guo, W. Yang, H.-K. Mao, Y. Zhao, *Scripta Mater*. **63**, 981- 984, 2010.

[10] Z. Ikonic, G.P. Srivastava, J.C. Inkson, *Phys. Rev. B* **48**, 17181-17193, 1993.

[11] Z. Ikonic, G.P. Srivastava, J.C. Inkson, *Phys. Rev. B* **52**, 14078-14085, 1995.

[12] S. Plimpton, *J. Comput. Phys*. **117**, 1-19, 1995.

[13] F.H. Stillinger, T.A. Weber, *Phys. Rev. B* **31**, 5262-5271, 1985.

[14] K. Ding, H.C. Andersen, *Phys. Rev. B* **34**, 6987-6991, 1986.

[15] S. Nosé, *Mol. Phys.* **53**, 255, 1984.

[16] W.G. Hoover, *Phys. Rev. A* **31**, 1695-1697, 1985.

[17] L. Lu, Y. Shen, X. Chen, L. Qian, K. Lu, K. *Science* **304**, 422-426, 2004.

[18] S. Zhong, T. Koch, M. Wang, T. Scherer, S. Walheim, H. Hahn, T. Schimmel, *Small* **5**, 2265- 2270, 2009.

[19] P.K. Schelling, S.R. Phillpot, *J. Am. Ceram. Soc*. **84**, 2997-3007, 2001.

Approach-to-equilibrium molecular dynamics: thermal properties from temperature transient

Evelyne LAMPIN*, Pier Luca PALLA, Pierre-Arnaud FRANCIOSO and Fabrizio CLERI

IEMN, UMR CNRS 8520 and Université de Lille I, F-59652, Villeneuve d'Ascq, France

**corresponding author: evelyne.lampin@univ-lille1.fr*

Keywords: computational physics, heat transport.

Molecular dynamics (MD) is a statistical mechanics computational approach that provides the opportunity to access basics phenomena involved in the heat transfer at the nanoscale. MD is generally used either to extract bulk conductivities from the heat current fluctuations during a NVE simulation (Green-Kubo or EMD approach [1]), or bulk conductivities and interface resistances from the temperature profile once the stationary regime between a hot and a cold reservoir is reached (direct method or NEMD [2]). We have developed an alternative framework of MD simulations for the study of thermal conductivities and interface resistances. The method, called approach-to-equilibrium MD (AEMD), relies on i) the creation of a transient heat current and the extraction of the transient decay time and ii) an original exploitation of the decay time to obtain bulk conductivities and/or interface resistances in a range of configuration from bulks to interfaces, nanostructures and constrictions, therefore extending the use of transients to the determination of thermal properties.

AEMD starts with the equilibration of the system in NVT under two temperature constraints to obtain a box like temperature profile (Fig. 1).

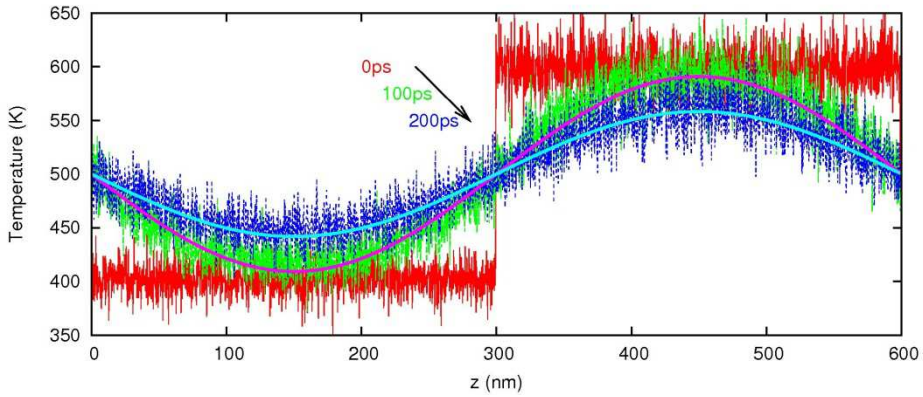

Figure 1: Temperature profiles at the initial state (red) and during approach-to-equilibrium (green and blue).

The system is afterwards let free to approach equilibrium during a transient of typically a few hundreds of picoseconds. The temperature decay during the transient is monitored, it is exponential (Fig. 2), while the temperature profile (Fig. 1) is sinusoidal. These forms are also the solutions of the 1D heat equation solution [3] although a length dependent conductivity has to be introduced.

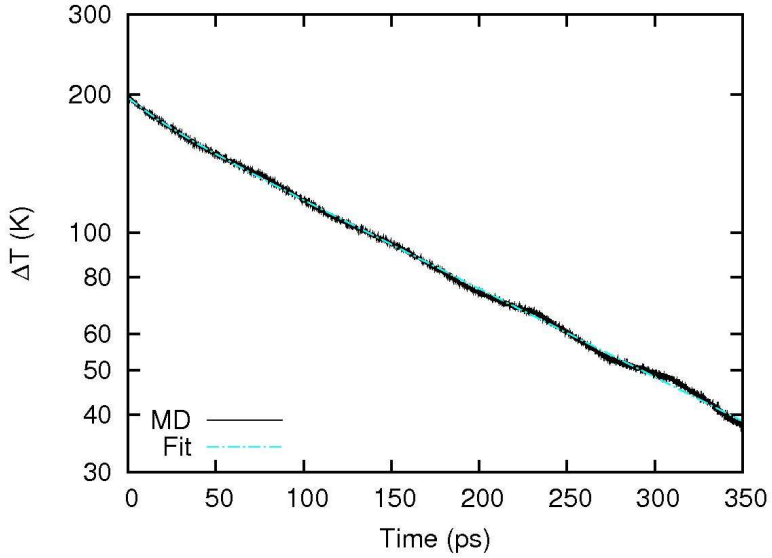

Figure 2: Temperature difference between initial blocks as a function of time.

The length dependent thermal conductivity is given in Fig. 3 for a range of good to poor conductors is given in Fig. 3. Although systems with size over the micrometers were studied thanks to the efficiency of the method, the convergence is not reached for silicon. A Matthiessen rule is used to extrapolate to infinite length.

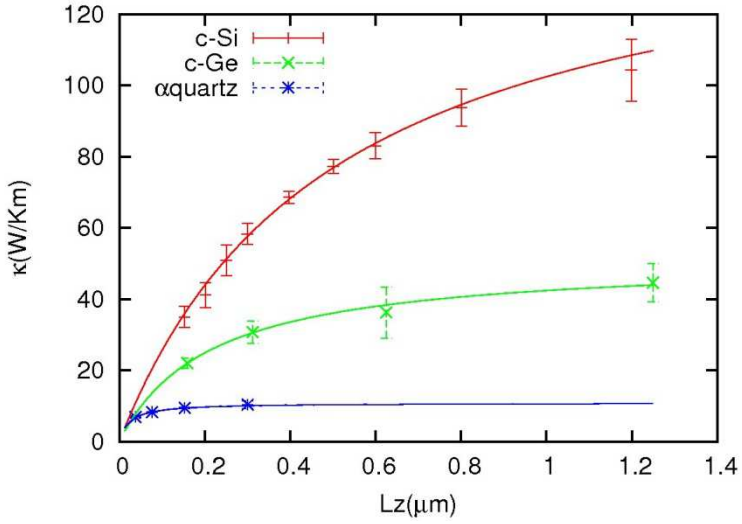

Figure 3: Bulk conductivities as a function of length[3].

The method has also been applied to interfaces such as crystalline silicon (cSi) / amorphous silica ($aSiO_2$), a more challenging system because of the contrast between bulk conductivities. The total resistance is given in Fig. 4. Several calculations are combined to extract the interface resistance from the intercept at origin of the linear evolution at larger $aSiO_2$ thickness. The interface resistance is low but for advanced technologies using an ultra-thin buried oxide (20nm), it will contribute significantly to the total resistance on the heat path from active layer to back-side [4].

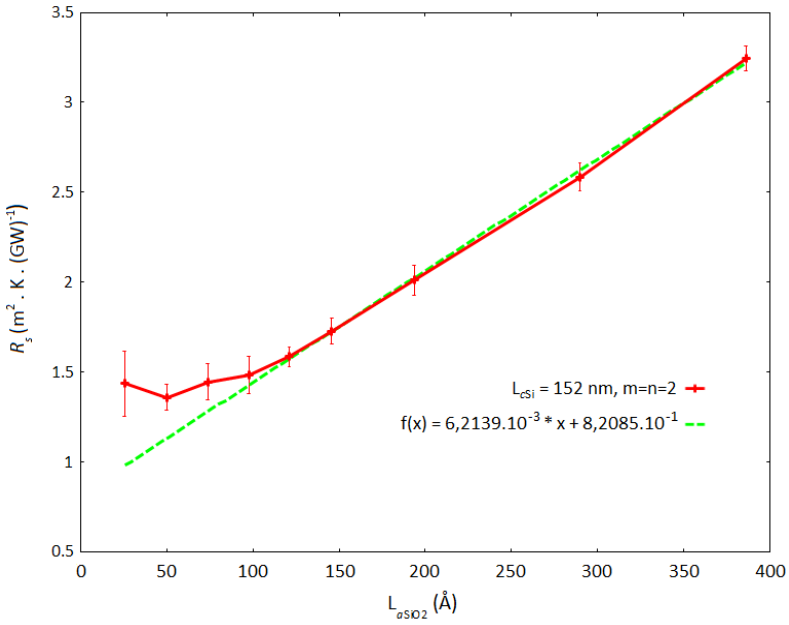

Figure 4: Total resistance of a cSi/aSiO_2 system. The crystalline thickness is fixed at 152 nm, the amorphous thickness is varied in x axis.

References

[1] R. Zwanzig, "Time-correlation functions and transport coefficients in statistical mechanics", *Ann. Rev. Phys. Chem.* **16**, 67, 1965.

[2] P. K. Schelling, S. R. Phillpot and P. Keblinski, "Comparison of atomic-level simulation methods for computing thermal conductivity", *Phys. Rev. B* **65**, 144306, 2002.

[3] E. Lampin, P. L. Palla, P.-A. Francioso and F. Cleri, "Thermal conductivity from approach-to-equilibrium molecular dynamics", *J. Appl. Phys.* **114**, 033525, 2013.

[4] E. Lampin, Q.-H. Nguyen, P. A. Francioso and F. Cleri, "Thermal boundary resistance at silicon-silica interfaces by molecular dynamics simulations", *Appl. Phys. Lett.* **100**, 131906, 2012.

One-way phonon transport in modulated acoustic waveguides

Mehdi B. ZANJANI[a], Arthur R. DAVOYAN[b], Ahmed M. MAHMOUD[b], Nader ENGHETA[b], and Jennifer R. LUKES[a*]

[a]*University of Pennsylvania, Department of Mechanical Engineering and Applied Mechanics, Philadelphia, Pennsylvania 19104, USA*

[b]*University of Pennsylvania, Department of Electrical and Systems Engineering, Philadelphia, Pennsylvania 19104, USA*

**corresponding author: jrlukes@seas.upenn.edu*

Keywords: acoustic isolation, spatio-temporal modulation, mode conversion.

Introduction

Pathbreaking theoretical and experimental advances in one-dimensional nonlinear lattices [1] and asymmetrically mass-loaded nanotubes [2] have led to a surge in interest in thermal rectification in the last decade [3]. Thermal rectification, in which the heat current flowing through a system under the same thermal bias is different in forward and backward directions, opens up new possibilities for controlling heat transport in materials and enables a critical first step toward phononic circuits for information processing [4].

A related but less-studied problem than thermal rectification is one-way phonon isolation, which is concerned with the forward and backward transport of *individual phonons* as opposed to the entire phonon spectrum. In one-way phonon isolation, an individual phonon mode incident on a system from one direction is transmitted while the same phonon incident on the system from the opposite direction is blocked. In the example given in Fig. 1, components to the right of the waveguide are isolated from the rightward traveling mode, enabling one-way transport of the mode in the leftward direction only. Such isolation would be of interest for the interconnects in MEMS acoustic wave signal processing devices, in which the waveguide in Fig. 1 represents the transmission line used to guide waves between transmitter and receiver modules [5]. Additionally, it may be useful in low temperature heat transfer applications, where the phonon energy density is close to Planckian with a well defined peak that could potentially be targeted to control a significant portion of the heat flow.

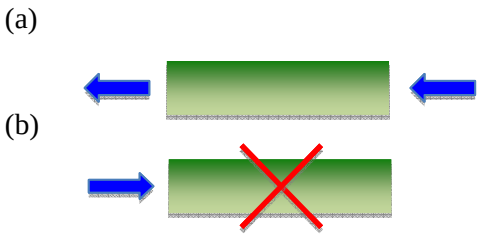

Figure 1: Principle of one-way phonon isolation. (a) Phonon mode incident on waveguide from right is transmitted; (b) phonon mode incident from left is blocked

Previous studies have demonstrated acoustic rectification in systems with nonlinearity and structural asymmetry [6-7]. An analogous isolation mechanism employing a combination of nonlinearity and structural asymmetry has also been achieved in optical systems [8-9]. The low efficiency of frequency conversion in the above acoustic systems leads to low transmission properties, pointing to the need for different approaches to isolation. Here we pursue a conceptually different approach for efficient phonon isolation that works for *linear*, structurally symmetric systems [10]. The main idea of the approach is to use spatio-temporal modulations of waveguide properties to break the symmetry of wave propagation in forward and backward directions. This approach was first proposed by Yu and

Fan [11-12] for optical waveguides; here we apply it to acoustic waveguides in the long-wavelength (continuum) limit.

Approach

To do this, we study shear horizontal wave propagation in a two dimensional plate acoustic waveguide with free boundaries. The governing equation for the SH waves is [13]

$$\rho \frac{\partial^2 u}{\partial t^2} = c_{44} \frac{\partial^2 u}{\partial x^2} + c_{44} \frac{\partial^2 u}{\partial y^2}, \tag{1}$$

where ρ is density, c_{44} is a component of the elastic stiffness tensor for a cubic crystal, and u is out-of-plane displacement. To achieve symmetry breaking, the density in the lower half of the waveguide is modulated using a simple harmonic form:

$$\rho = \rho_o + \delta\rho \cos(\Omega t - Kx). \tag{1}$$

Here Ω is the frequency at which the density within the domain is modulated and K is the modulation wavenumber describing the spatial density variation along the wave propagation direction.

Results

Numerical simulations using the finite element method indicate that one-way phonon transport is achieved via spatio-temporal modulation of density [10]. Figure 2(a) shows the out-of-plane material displacements generated by a lowest order symmetric shear horizontal mode ("mode 1") incident on the modulation domain from the right; Fig. 2(b) shows the corresponding displacements for mode 1 incident from the left. In Fig. 2(a), complete conversion of the incident mode to the lowest order antisymmetric mode ("mode 2") occurs within the domain. Mode 1 cannot transmit through the domain and thus complete isolation of this mode occurs. In the bottom figure, mode 1 transmits

Figure 2: Modal displacements for (a) mode 1 incident from the left, and (b) mode 1 incident from the right. In (a), mode 1 (blue) is not transmitted through the waveguide; it instead converts to mode 2 (red).

unimpeded through the domain.

Discussion

Inspired by the work of Yu and Fan in optical waveguides [11-12], we have applied spatio-temporal modulation to an acoustic waveguide to break time and spatial inversion symmetry [10]. Using numerical simulations, we demonstrated that this approach led to one-way transport via conversion of the rightward traveling lowest order symmetric mode (mode 1) to the lowest order antisymmetric mode (mode 2). In essence, the modulation triggers an inter-band transition between the two modes. It is important to note that mode 2 still carries energy through the waveguide; to block all energy transport the above isolator could be combined with a filter centered at the mode 2 frequency

$\omega_2=\omega_1+\Omega$. While only the shear horizontal modes have been treated in this work, the approach is general and can be applied to other waveguide vibrational modes.

Acknowledgments

We acknowledge support from the National Science Foundation (Grant No. DMR-1120901). We are also thankful to D. Cheney for useful discussions.

References

[1] M. Terraneo, M. Peyrard, G. Casati, "Controlling the energy flow in non-linear lattices: a model for a thermal rectifier", *Phys. Rev. Lett.* **88**, 094302, 2002.

[2] C.W. Chang, D. Okawa, A. Majumdar, A. Zettl, "Solid-state thermal rectifier", *Science* **314,** 1121, 2006.

[3] N.A. Roberts, D. G. Walker, "A review of thermal rectification observations and models in solid materials", *Int. J. Therm. Sci.* **50**, 648, 2011.

[4] N. Li, J. Ren, L. Wang, G. Zhang, P. Hänggi, B. Li, "Colloquium: Phononics: Manipulating heat flow with electronic analogs and beyond", *Rev. Mod. Phys.* **84**, 1045, 2012.

[5] I. Voiculescu, A. N. Nordin, "Acoustic wave based MEMS devices for biosensing applications", *Biosens. Bioelectron.* **33**, 1, 2012.

[6] B. Liang, B. Yuan, J. C. Cheng, "Acoustic diode: rectification of acoustic energy flux in one-dimensional systems", *Phys. Rev. Lett.* **103**, 104301, 2009.

[7] X. S. Guo, Z. Lin, J. Tu, B. Liang, J. Cheng, D. Zhang, "Modeling and optimization of an acoustic diode based on micro-bubble nonlinearity", *J. Acoust. Soc. Am.* **133**, 1119, 2013.

[8] A. E. Miroshnichenko, E. Brasselet, Y. S. Kivshar, "Reversible optical nonreciprocity in periodic structures with liquid crystals", *Appl. Phys. Lett.* **96**, 063302, 2010.

[9] A. Alberucci, G. Assanto, "All-optical isolation by directional coupling", *Opt. Lett.* **33**, 1641, 2008.

[10] M. B. Zanjani, A. R. Davoyan, A. M. Mahmoud, N. Engheta, J. R. Lukes, "One-way phonon isolation in acoustic waveguides", *Appl. Phys. Lett.* **104**, 081905, 2014.

[11] Z. Yu, S. Fan, "Complete optical isolation created by indirect interband photonic transitions", *Nat. Photonics* **3**, 91, 2009.

[12] H. Lira, Z. Yu, S. Fan, M. Lipson, "Electrically Driven Nonreciprocity Induced by Interband Photonic Transition on a Silicon Chip", *Phys. Rev. Lett.* **109**, 033901, 2012.

[13] B. Auld, *Acoustic Fields and Waves in Solids*, Krieger Publishing Company, 1990.

Session 2

Subwavelength radiation (1)

Superdiffusive heat transport in nanoparticle networks

Philippe BEN-ABDALLAH[a*], Svend-Age BIEHS[b], Karl JOULAIN[c] and Carsten HENKEL[d]

[a]*Laboratoire Charles Fabry, UMR 8501, Institut d'Optique, CNRS, Université Paris-Sud 11, 2, Avenue Augustin Fresnel, 91127 Palaiseau Cedex, France*

[b]*Institut für Physik, Carl von Ossietzky Universität, D-26111 Oldenburg, Germany*

[c]*Institut PPrime, CNRS-Universite´ de Poitiers-ENSMA, UPR 3346, 2, Rue Pierre Brousse, Boîte Postale 633, 86022 Poitiers Cedex, France*

[d]*Institute of Physics and Astronomy, University of Potsdam, Karl-Liebknecht-Straße 24/25, 14476 Potsdam, Germany*

**corresponding author: pba@institutoptique.fr*

Keywords: Near-field, surface phonon-polariton, anomalous transport

It is commonly admitted since the pioneer work of Fourier that the heat conduction in a bulk solid is governed by a normal diffusion process.

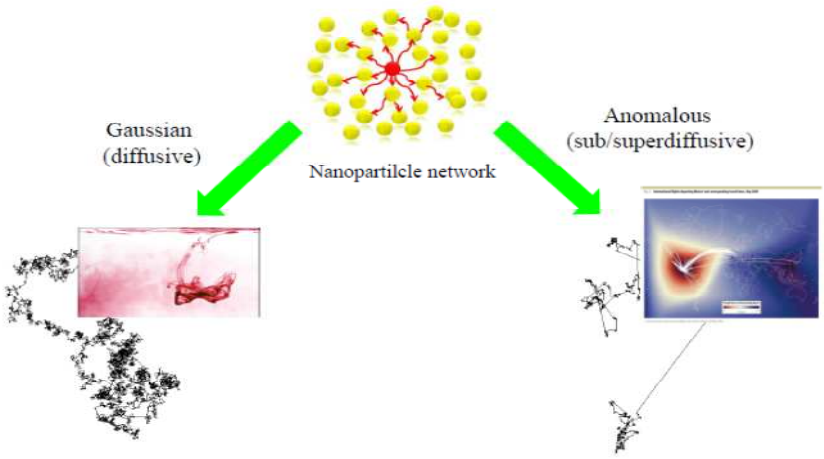

Figure 1: Two different transport regimes. (left) Classical diffusion of a ink drop in water. The ink particles follow a random diffusion process governed by a Gaussian probability distribution function of step length. (right) Anomalous (superdiffusive) spreading of a flu pendemic . Each contaminated personn can travel using different types (walk, car, train, plane) of transport with different transport length. The pdf of step length is algebraic.

Microscopically speaking heat carriers (phonons or electrons) move through the atomic lattice of materials following a random walk [1] with a step length probability density which is a Gaussian and the heat spatial spreading is limited both by the speed of heat carriers and by the distance covered by them between two successive collision events. Numerous transport mechanisms, such as the pollution dispersion (see Fig. 1-left), obey to diffusive processes. Nevertheless, many transport mechanisms are

governed by long range interactions such as those that exist in generalized random walks (GRW), processes where the step length probability is broadband. Lévy flights [2,3] are probably the most famous class of GRW (see Fig. 1-right) in which extremely long jumps can occur as well as very short ones.

In the present work it is shown (Fig. 2) that, if such media contain plasmonic structures networks such as polar-nanoparticle networks, heat can be transported by collective interactions mechanims of non-radiative photons (near-field transport) though these networks. We consider a distribution of N particles at temperature T_i separated by distances which are assumed to be small compared with the thermal wavelengths $\lambda_i = ch/(2\pi k_B T_i)$. Then, this network can be modeled by a set of pointlike dipoles in mutual interaction. Given an initial temperature distribution, the time evolution of this field is governed (at least at the beginning of relaxtion process) by the following balance energy equation

$$\rho_i C_i V_i \frac{dT_i}{dt} \approx \sum_j G(|r_i - r_j|)(T_j - T_i) \tag{1}$$

where ρ_i, C_i and V_i denote the density, the heat capacity and the volume of the i^{th} particle while G is the radiative thermal conductance between two point which can be calculated using the many-body radiative heat transfer theory [4-6]. This equation is a discrete form of the Chapman-Kolmogorov master equation

$$\frac{\partial T_i}{\partial t} = \int_{R^d} p(\mathbf{r_i}, \mathbf{r}) \frac{T(\mathbf{r}, t)}{\tau(\mathbf{r})} d\mathbf{r} - \frac{T(\mathbf{r_i}, t)}{\tau(\mathbf{r_i})} \tag{2}$$

which formally describes a system which is driven by a Markov process (here d is the space dimension).

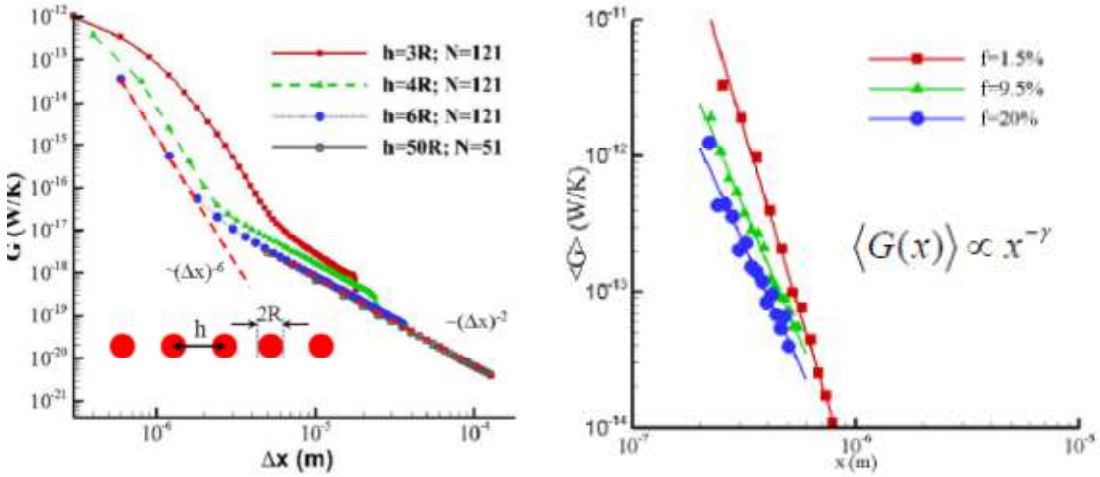

(a) **(b)**

Figure 2: Thermal conductance at T=300 K between two particles in (a) a linear chain of spherical SiC nanoparticles of radius R=100 nm for different separation distances h inside a (b) in a ramdom distribution of SiC particles (R=100 nm). The statistical averaging is performed with m = 250 realizations generated with a uniform random distribution probability. Particles are immerged in vacuum.

The temperature distribution T(r,t) evolves in the same way as a generalized random walk, where jumps between positions r and r' occur with a probability distribution function of step length

proportional to $p(r,r')=(1/C\Delta V)\ \tau(r)G(r-r')$ at a rate $\tau^{-1}(r)= (1/C\Delta V)\ \int dr'G(r-r')$. Thus, to analyze the transport of heat throughout the network, we just have to investigate the probability distribution of step lengths x that is to say the spatial evolution of the thermal conductance. These evolutions are plotted in Fig. 2 both for 1D and 3D systems. In linear and ordered chains of particles (d=1) we see (Fig. 2-a), at long separation distances, that the thermal conductance decays algebraically with the separation distance following a power law scaling in $G \sim(\Delta x)^{-2}$ demonstrating so that the moments of the pdf p(x) of higher order than two are divergent. This proves the superdiffusive behavior of these chains for the transport of heat by near-field interaction. More generally a detailed analysis of heat transport (Fig. 2-b) shows that the transport of heat still is superdiffusive [6] in random networks of nanoparticles.

The ability to design nanocomposite materials able to transport heat faster than with phonons in solids opens new practical perspectives. In particular, it could find broad applications in the domain of ultrafast thermal management.

References

[1] A. Einstein, "Über die von der molekularkinetischen Theorie der Wärme geforderte Bewegung von in ruhenden Flüssigkeiten suspendierten Teilchen", *Ann. Phys. (Berlin)* **322**, 549, 1905.

[2] P. Lévy, "Théorie de l'Addition des Variables Aléatoires" (Gauthier-Villars, Paris, 1937)

[3] M. F. Shlesinger, G.M. Zaslavsky, and U. Frisch , "Lévy Flights and Related Topics in Physics", *Lecture Notes in Physics* Vol. 450 (Springer-Verlag, Berlin, 1995).

[4] P. Ben-Abdallah, S.-A. Biehs, and K. Joulain, "Many-body radiative heat transfer theory", *Phys. Rev. Lett.* **107**, 114301, 2011.

[5] R. Messina, M. Tschikin, S.-A. Biehs, and P. Ben-Abdallah, "Fluctuation-electrodynamic theory and dynamics of heat transfer in systems of multiple dipoles", *Phys. Rev. B* **88**, 104307, 2013.

[6] P. Ben-Abdallah, R. Messina, S. A. Biehs, M. Tschikin, K. Joulain and C. Henkel, "Heat superdiffusion in plasmonics nanostructure networks", *Phys. Rev. Lett.* **111**, 17, 174301, 2013.

Near-field thermal emission between corrugated surfaces separated by nano-gaps

Azadeh DIDARI* and M. Pinar MENGÜÇ**

Center for Energy, Environment and Economy (CEEE) and Faculty of Engineering, Özyeğin University, Istanbul, 34794 Turkey

**Corresponding author: azadeh.didari@ozu.edu.tr*
***Corresponding author: pinar.menguc@ozyegin.edu.tr*

Keywords: near-field thermal emission, local density of electromagnetic states, corrugated surfaces, finite difference time domain method, energy-harvesting nanodevices.

Abstract

Near-field thermal radiation with its many potential applications in different fields such as energy harvesting to nano-scale manufacturing is proved to be crucial in the development of new devices. Modeling near-field thermophotovoltaics via computational techniques has been one of the main focuses of our research group. In the present study, we show that near-field thermal emission between two parallel SiC thin films separated by a nano-gap can be modeled via Finite Difference Time Domain Method (FDTD) when arbitrary-size nanoparticles are present on the surfaces of the emitting film. We compare different nano-particle shapes and discuss the configurations which have the highest impact on the enhancement of near-field thermal emission. Convolutional Perfectly Matched Layer (CPML) is used as it was determined to be the optimum boundary condition that gives the most accurate results compared against the other methodologies for similar configurations. We also discuss possible future extensions of this work.

1. Introduction

TPV power generation has significant potential for applications in industrial energy conversion technologies and in principle is similar to solar photovoltaic energy conversion. In [1] we have presented the results obtained for the near-field thermal emission calculations via FDTD method for perfectly flat, parallel, thin SiC films supporting surface phonon polaritons and separated by a nano-gap. We showed a good agreement with analytical results presented in [2].

FDTD method is a computational approach with which modeling wave propagation in complex media, such as time-varying, anisotropic, lossy, dispersive and non-linear media is possible. Having computational techniques such as FDTD method when working with arbitrary sub-wavelength structures is very helpful as analytical solutions may not be easily found for such geometries due to geometry asperity.

We present here the results based on calculations of near-field thermal emission at nano-gaps formed between two thin films made of SiC, with the presence of structured arbitrary-shaped, nano-particles (gratings) on the surface of the emitting film. The additional results are currently obtained to show the potential of the analysis to real-time applications. The extension of this idea is indeed applicable to nano-scale detection and nano-manufacturing principles [3-7].

2. Methodology

The near-field thermal emission is studied through finite difference time domain method between two thin SiC films by calculations of local density of electromagnetic state (LDOS), where one film has a

temperature of 300 K (emitting layer) and a thickness of 100 nm and nano-structured gratings of arbitrary (e.g. ellipses, triangles, squares, etc.) are placed upon it and have perfect contact with the layer. The other film is kept at 0 K (non-emitting layer) and has a thickness of 10 nm and is separated by a vacuum gap of 100 nm from the emitting layer. We have studied the effect of each of these nano-structured gratings on enhancement of LDOS profile (LDOS is calculated at $\Delta = 50$ nm above the emitting layer) and evaluated the impact of the following factors on the results: I-the periodicity of the nano-gratings, II-the shape of nano-gratings, III-the thickness of the nano-gratings. Figure 1 shows the schematic of the geometries considered in this work.

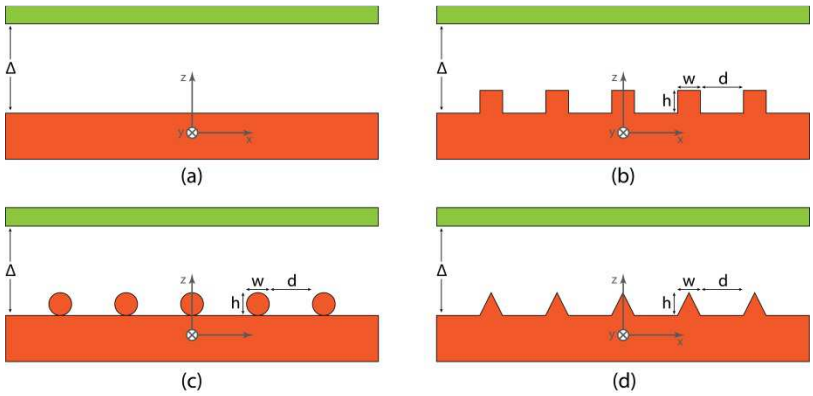

Figure 1: a) Perfectly flat parallel films separated by nano-gap. (emitting layer at the bottom, non-emitting layer on top). b) Rectangular nanoparticles placed on the emitting film separated by nano-gap from non-emitting film. c) Ellipsoidal nanoparticles placed on the emitting film separated by nano-gap from non-emitting film. d) Triangular nanoparticles placed on the emitting film separated by nano-gap from non-emitting film.

3. Results and Discussion

We have evaulated the impact of periodicity of elliptic nano-structred gratings placed on the emitting layer, on LDOS profile at frequency range of 1.5 rad/s-1.9 rad/s. Width and height of the gratings is shown in figure 1 with '*w*' and '*h*' respectively. The distance of nanoparticles is shown with '*d*' and NPs stands for Nanoparticles from hereon. We have compared the results of separate scenarios in which 2, 5, 10, 15, 20 and 25 SiC elliptic nano-gratings were placed in perfect contact with emitting layer. The size of ellipses was kept fixed and only the impact of periodicity of the gratings was observed. Each ellipse has a *w*=600 nm and *h*=20 nm. Here, *w* is chosen based on the fact that the thin layers are assumed to be very long in x-direction for these FDTD simulations. Hence, *w* has to be both small compared to the total length of the layers and yet not too small to make the simulation computationally too expensive. The distances between 2, 5, 10, 15, 20 and 25 nano-gratings were 14700, 3180, 1080, 480, 180, and 60 nm, respectively. We kept the *x* axis dimension and the width of CPML layers fixed across all simulations. Within this constraint, we could only fit up to 25 nanoparticles across. This provided adequate scope for a robust proof of concept. The results shows that enhancement factor of LDOS profile is directly proportional with the periodicity of nano-particles. In the case of 25 NPs each 60 nm apart from each other, 71% enhancement was observed when compared with the benchmark scenario in which no NPs were present at the surface of the emitting layer. We can observe that when $d < 0.005\lambda$ ($\lambda = 1059$ nm) we obtain maximum enhancement of LDOS. In the next step, we have compared the LDOS profile found for 10, the same size nano-gratings placed on emitting layer with different shapes. Results for rectangles, ellipses and triangles are compared with each other in Figure 3. It was observed that rectangles and ellipses show a similar impact on enhancement of LDOS when compared against triangles, with a slightly higher

enhancement observed for rectangles. Nano-gratings were set to have *w*=600 nm and *h*=20 nm and *d*=1080 nm ($d = 0.1\lambda$).

Finally, we tested different width sizes (600-1500 nm) for 10 elliptic nano-gratings with *h*=20 nm and *d*=1080 nm. The results were monitored to observe if the increase in the width of the elliptic nano-gratings has any impact on the LDOS value. The results showed a negligible change in LDOS profile. Figure 6 depicts the results found for this study.

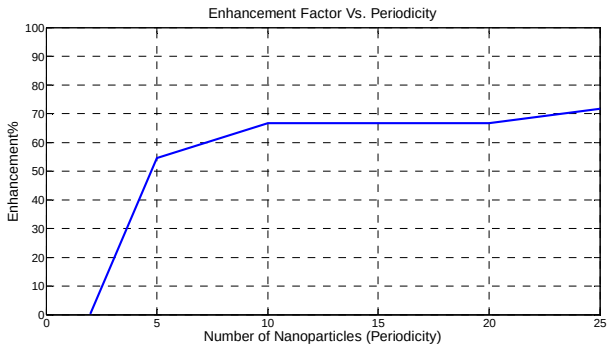

Figure 2: Enhacement Factor vs Periodicity for SiC elliptic case) vs nano-particles.

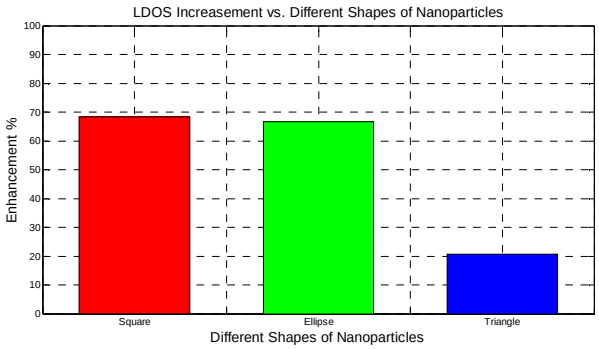

Figure 3: Enhacement of LDOS (over no-particle different shapes of nano-gratings.

We have also studied the effect of different shapes of nanoparticles in near-field heat flux. Figure 4 depicts the result found for this study. Rectangle nano-particles show the greatest impact on enhancement of near-filed heat flux when placed on emitting layer and compared against elliptic and triangle nanoparticles. In Figure 5 we have compared the results of near-field flux found at 300, 600 and 1000 K when 25 elliptic NPs were placed on top of emitting layer against the benchmark results in which there were no NPs present. The results are normalized to the peak value of the benchmark scenario. Enhancement of near-field flux at different temperatures due to the presence of the NPs can be clearly seen.

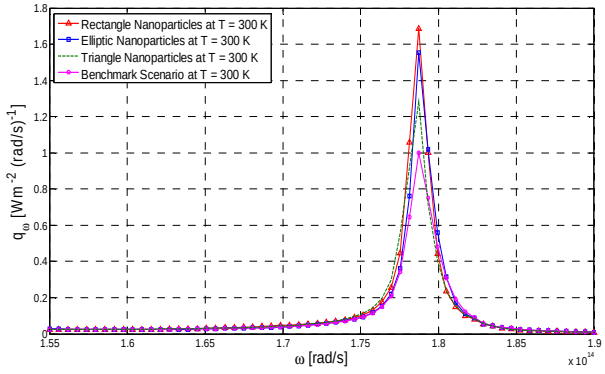

Figure. 4: Enhacement of heat flux at the presence of NPs and (over benchmark scenario) vs different shapes of nano-gratings.

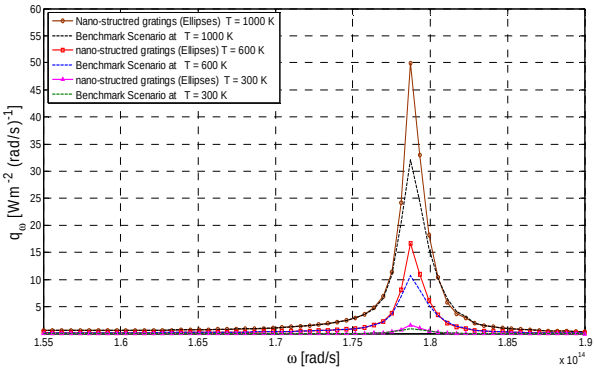

Figure 5: Near-field heat flux calculation at 300,600, 1000K at presence of elliptic nanoparticles vs the bechmarck scenario.

4. Concluding Remarks

Near-field thermal radiation has broad range of applications in areas including nano-thermophotovoltaics. Having a computational technique such as FDTD that can model complex electromagnetic geometries, in dispersive, anisotropic mediums where geometry complications may not allow analytical solutions can be promising for both current and future research. We have

developed a new FDTD method to model arbitrary shape nanoparticles and have evaluated their impact on LDOS profile. The results show an increase in the magnitude of LDOS with an increase in the periodicity of the nano-gratings, when the distance between the gratings is much smaller than the wavelength of interest. We evaluated the impact of arbitrary shape nano-gratings and observed that rectangles showed the greatest impact on enhancement of LDOS and heat flux value when compared against ellipses and triangles of the same sizes. Enhancement of near-field flux at different temperatures due to the presence of the elliptic NPs could be clearly seen when compared against the scenario in which no NPs were present. It was also observed that an increase in the width of elliptical SiC nano-particles did not make any distinguishable change in the LDOS value. While in this work we have focused on gratings of the same shape, future work would involve arbitrary combinations of nano-particle shapes.

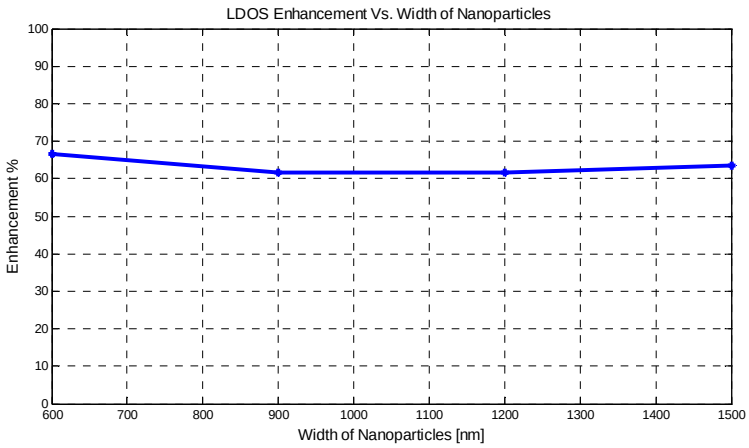

Figure 6: Enhacement of LDOS vs width of elliptic nanoparticles.

Acknowledgments

This project was partially funded by the FP-7-PEOPLE-IRG-2008 (Grant No.239382 NF-RAD) at Özyegin University, Istanbul, Turkey. AD is funded by CEEE at Özyegin University.

References

[1] A. Didari, M.P. Mengüç,"Analysis of Near-Field Radiation Transfer within Nano-Gaps Using FDTD Method", *J. Quant. Spectrosc. Radiat. Transf*, Vol.**146**, 214-226, 2014.

[2] M. Francoeur, M.P. Mengüç, and R. Vaillon, "Local Density of Electromagnetic Stateswithin a Nanometric Gap Formed Between Thin Films Supporting Surface Phonon Polaritons*", J. Appl. Phys*. vol.**107**, 034313–034318, 2010.

[3] E.A. Hawes, J.T. Hastings, C. Crofcheck, and M.P. Mengüç, "Spatially Selective Melting and Evaporation of Nanosized Gold Particles," *Optics Letters*, Vol.**33**, 1383-1385, 2008.

[4] G.M. Huda, E.M. Donev, M.P. Mengüç, J.T. Hastings, Effects of a Silicon Probe on Gold Nanoparticles on Glass under Evanescent Illumination, *Optics Express*, Vol. **19**, 12679-12687, 2011.

[5] V. Loke, and M.P. Mengüç, "Surface Waves and AFM Probe-Particle Near-Field Coupling: Discrete Dipole Approximation with Surface Interaction", *Journal of the Optical Society of America* A, Vol. **27** (10), 2293-2303, 2010.

[6] V. Loke, T.A. Nieminen, and M.P. Mengüç, DDA with Surface Interaction: Computational Toolbox for MATLAB, *J. Quant. Spectrosc. Radiat. Transf.* Vol. **112** (11), 1711-1725, 2011.

[7] A. Datas, D. Hirashima, K. Hanamura, FDTD simulation of near-field radiative heat transfer between thin films supporting surface phonon polaritons: Lessons learned, *J. Therm Sci Technol*. **8**, 91–105, 2013.

Near-field thermal radiation absorbed by a flat film in the vicinity of a semi-infinite emitter

Etienne BLANDRE[a*], P.-Olivier CHAPUIS[a], Mathieu FRANCOEUR[b] and Rodolphe VAILLON[a]

[a]*Université de Lyon, CNRS, INSA-Lyon, UCBL, CETHIL, UMR5008, F-69621, Villeurbanne, France*

[b]*Department of Mechanical Engineering, University of Utah, Salt Lake City, UT 84112, USA*

**corresponding author: etienne.blandre@insa-lyon.fr*

Keywords: Near-field thermal radiation, absorption depth, interferences, surface phonon-polaritons, resonance frequencies

It is now well established that thermal radiation is different from far-field Planck's radiation when distances are comparable to, or smaller than, Wien's wavelength (λ_W=10 µm at room temperature). Near-field heat transfer between a semi-infinite emitter and a non-emitting flat film of finite thickness is considered in this study. Amongst other works, near-field radiative heat transfer between thin films was already investigated (e.g. in [1,2]), showing that the film sizes can modify the spectral distribution of the radiative heat flux around the resonances. The case of the radiative heat flux between a semi-infinite and a coated metallic material was investigated in [3], where it was shown that the coupling of surface plasmons in the film can enhance the heat transfer between the two bodies. Here, a specific objective is to investigate the spatial distribution of the radiative heat flux absorbed in the film as a function of its thickness and the distance between the emitter and the film. For materials supporting surface phonon-polaritons, the resonance frequencies and their impact on the absorption of radiative heat flux in the film are examined in detail. An analysis of the conditions leading to interferences inside the film is performed in order to determine the impact on the absorbed flux, which also depends on possible interference effects in the gap.

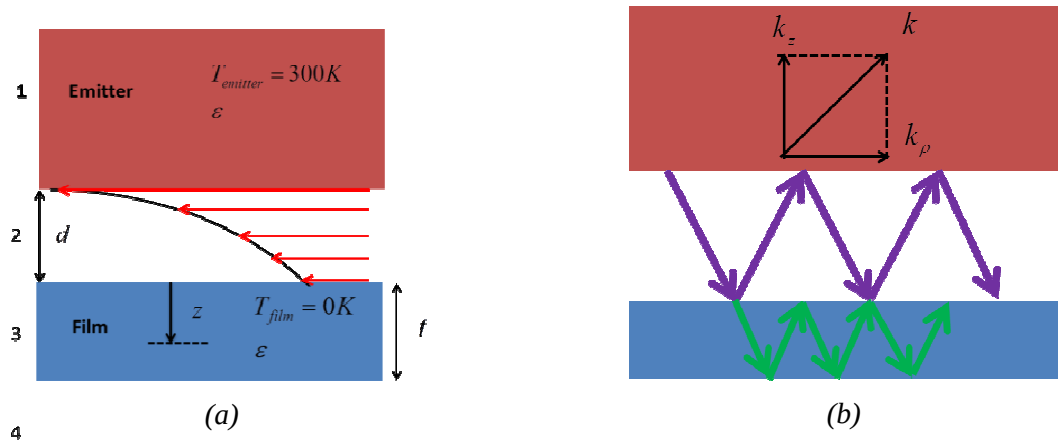

Figure 1: (a) Schematic representation of the considered configuration, which is known to involve radiative heat transfer due to evanescent waves. (b) The purple arrows represent the multi-reflections inside the vacuum gap, while the green ones represent the multi-reflections inside the film. k_z and k_ρ are the components of the wavevector respectively perpendicular and parallel to the interface.

The configuration under consideration is depicted in Figure 1(a): medium 1 is semi-infinite, while medium 3 has a finite thickness *t*. The two bodies are made of the same material and are separated by a vacuum gap of length *d* that can be smaller than the dominant wavelength of thermal radiation. By

using the fluctuational electrodynamics theory involving dyadic Green's functions, the propagative and evanescent components of the radiative heat flux at the entrance of the film (z=0) are respectively given by [2]:

$$q_\omega^{prop}(z=0) = \frac{\Theta(\omega, T_{emit})}{4\pi^2} \int_0^{\frac{\omega}{c}} k_\rho dk_\rho \sum_{\gamma=s,p} \frac{\left(\mathbf{1} - \left|\boldsymbol{r_{21}^\gamma}\right|^2\right)\left(\mathbf{1} - \left|\boldsymbol{R_3^\gamma}\right|^2\right)}{\left|\mathbf{1} - \boldsymbol{r_{21}^\gamma R_3^\gamma e^{2ik_{z_2}d}}\right|^2} \quad (1)$$

$$q_\omega^{evan}(z=0) = \frac{\Theta(\omega, T_{emit})}{\pi^2} \int_{\frac{\omega}{c}}^{\infty} k_\rho dk_\rho \boldsymbol{e^{-2Im(k_{z_2})d}} \sum_{\gamma=s,p} \frac{\boldsymbol{Im\left(r_{21}^\gamma\right) Im\left(R_3^\gamma\right)}}{\left|\mathbf{1} - \boldsymbol{r_{21}^\gamma R_3^\gamma e^{2ik_{z_2}d}}\right|^2} \quad (2)$$

where ω is the angular frequency, c is the speed of light in vacuum, $\Theta(\omega,T_{emit})$ is the mean energy of a Planck oscillator, r_{21}^γ is the Fresnel's reflection coefficient at the interface 21 where γ stands for the s or p-polarizations, and R_3^γ is the reflection coefficient of the film. To take into account all "directions", an integral is performed over the component of the wavevector which is parallel to the interface k_ρ, which runs also for values larger than ω/c (evanescent case). The bold terms are the transmission factors $T_e\left(k_\rho, \omega\right)$ [4,5]. To separate the contributions of the wave modes (propagative, evanescent) in the various parts of the system, the radiative heat flux is divided into three components:

- for $0 \le k_\rho < \frac{\omega}{c}$, the waves are propagative in the emitter, the vacuum gap and the film (fully-propagative modes),
- for $\frac{\omega}{c} \le k_\rho < \frac{n\omega}{c}$, where n is the real part of the complex refractive index of the material, the waves are propagative in the emitter, evanescent in the vacuum gap as a result of total internal reflection, and propagative in the film (frustrated or propagative–evanescent modes),
- for $\frac{\omega}{c} \le k_\rho < \infty$, the waves are evanescent in the emitter, the vacuum gap and the film (fully-evanescent or surface modes).

By depicting the variations of the transmission factor T_e in the (k_ρ,ω) plane, a spectral and directional analysis of the propagative, frustrated and purely-evanescent modes can be made, as a function of the film thickness t and the vacuum gap size d. This gives in particular the conditions for the existence of various resonances due to surface phonon-polaritons and for interferences in the vacuum gap and possibly in the film. Figure 2 shows that when the film is thin enough, the coupling of surface waves existing at the two interfaces of the film and the resonance of the surface wave at the interface of the semi-infinite emitter leads to the apparition of a third resonance frequency. Equations describing the behavior of those resonances are under consideration in our study.

When two bodies are separated by a distance that is comparable to or smaller than the dominant wavelength of thermal radiation (i.e. λ_W) the propagative modes of the thermally emitted waves can undergo interferences phenomena due to multiple reflections between the interfaces.

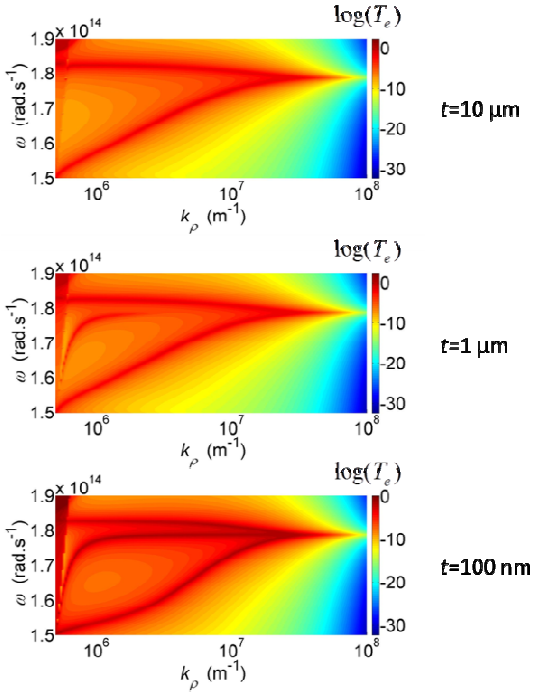

Figure 2: p-polarized component of the transmission factor T_e for SiC, as a function of k_ρ and ω, for various thicknesses t. The size of the vacuum gap is d=100 nm.

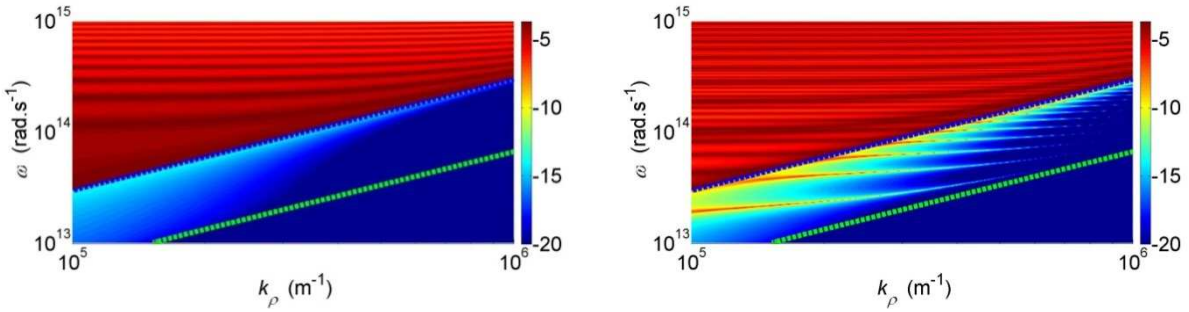

Figure 3: p-polarized component of the transmission factor T_e for a constant dielectric function $\varepsilon=20+i\,0.01$, as a function of k_ρ and ω. The size of the vacuum gap is d=10 µm, and the thickness of the film is t=100 nm for (a), and t=10 µm for (b). The equation of the blue line is $\omega = ck$, while the equation of the green line is $\omega = \frac{kc}{n}$, with n being the real part of the complex refractive index of the medium. The color map is in logarithmic scale.

Figure 3(a) shows that for d=10 µm, interferences appear for purely propagative modes ($k_\rho < \frac{\omega}{c}$) in the vacuum gap, leading to alternating minima and maxima. In Figure 3(b), as the film thickness t is comparable to the wavelength inside the film $\frac{\lambda_0}{n}$, interferences can also occur in the film. This is the case for the fully-propagative modes but interferences can also exist as well for the frustrated modes ($\frac{\omega}{c} \leq k_\rho < \frac{n\omega}{c}$), since they are propagative inside the film (see Figure 3(b)). The amplitude of the interferences associated to the frustrated modes is larger by several orders of magnitude than the amplitude of the interferences developing for the fully-propagative modes. This should lead to a strong modification of the spectrum of the thermal radiation.

We now divide the film into N control volumes in order to analyze the spatial distribution of the absorbed radiative power. Radiation absorbed in each control volume is given by the difference

between the radiative heat fluxes q at the boundaries of the control volume, which are computed by using a scattering matrix approach [6]. Figure 4 depicts the spatial distribution of radiation absorbed in the film q_{vol}=dq/dz. In panel (a), the resonance frequencies corresponding to the surface phonon-polaritons are clearly visible (around ω=1.8× 10^{14}rad.s^{-1}). As those modes have a large k_ρ, they have a low penetration depth, which explains why they decay quickly. When the depth z is larger than the penetration depth of the fully evanescent modes, the absorption is dominated by the frustrated modes, which have a larger penetration depth. Eventually, when the film is thin enough, the surface wave at the opposite side of the film can be excited (see Figure 4(b)), leading to an increase of absorption near that interface.

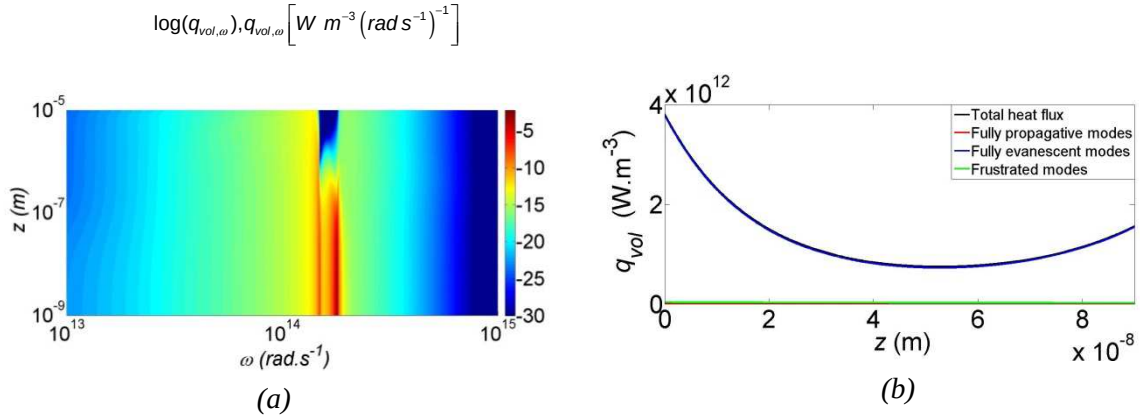

Figure 4: (a): Radiative power absorbed by the film as a function of the angular frequency ω and the depth inside the cell z for the case d=100 nm and t= 10 µm. (b): Total radiative power absorbed by the film as a function of the depth inside the film z, for the different modes for the case for d=100 nm and t= 100 nm.

As a conclusion, this study suggests that it is possible to tune the spectrum and the spatial distribution of the radiation absorbed by a film by varying the vacuum gap size d and the film thickness t [7]. This opens up new ways for controlling the location of absorption of near-field radiation within layered structures. Next work could also investigate the impact of surface imperfections, especially with regard to possible future experiments.

References

[1] P. Ben-Abdallah, K. Joulain, J. Drevillon, and G. Domingues, *J. Appl. Phys.* **106**, 044306, 2009.

[2] M. Francoeur, M.P. Mengüç, and R. Vaillon, *J. Phys. D: Appl. Phys.* **43**, 075501, 2010.

[3] S.-A. Biehs, *The European Phys. Journal B* **58**, 423-431, 2007.

[4] P. Ben Abdallah and K. Joulain, *Phys. Rev. B* **82**, 121419R, 2010.

[5] S.-A. Biehs, E. Rousseau, and J.-J. Greffet, *Phys. Rev. Lett.* **105**, 234301, 2010.

[6] M. Francoeur, M.P. Mengüç, and R. Vaillon, *J. Quant. Spectros. Radiat. Transfer* **110**, 2002-2018, 2009.

[7] E. Blandre, P.-O. Chapuis, M. Francoeur, and R. Vaillon, *arXiv*, 2014.

Thermal emission control with surface waves

Daniele COSTANTINI, Giovanni BRUCOLI, Henri BENISTY, François MARQUIER, Jean-Jacques GREFFET

Laboratoire C. Fabry, Institut d'Optique Graduate School, CNRS, 2 av Fresnel, 91127 Palaiseau, France

**corresponding author: jean-jacques.greffet@institutoptique.fr*

Keywords: thermal sources, coherent sources, metasurface, near-field thermal radiation.

1. Introduction

IR sources are required for spectroscopic applications and gas sensing for instance. Several IR lasers are available. Yet, there is no equivalent of a light emitting diode (LED) in the IR part of the spectrum. Hence, incandescent emitters such as globars or hot membranes are still the most common sources despite many drawbacks including a low efficiency, a low directivity and the impossibility of fast modulation. In this paper, we will introduce different strategies to overcome these limitations by taking advantage of surface waves.

2. Controlling the spectrum and the directivity

There have been several demonstrations on how to control the directivity and spectrum of thermal sources [1,2]. Owing to Kirchhoff's law, this amounts to control the directional and spectral absorptivity. Hence, one can take advantage of absorption due to resonant excitation of surface waves. In other words, designing a directional and spectrally selective emitter amounts to design an absorber. While several structures have been published demonstrating either directional or spectral control of the emission, controlling both simultaneously is more challenging. In this section, we will report recent progress along this line by using a periodic array of metal-insulator-metal square on a metal substrate. The key results are displayed in Figure 1 showing that it is possible to design a metasurface which is both monochromatic and directional.

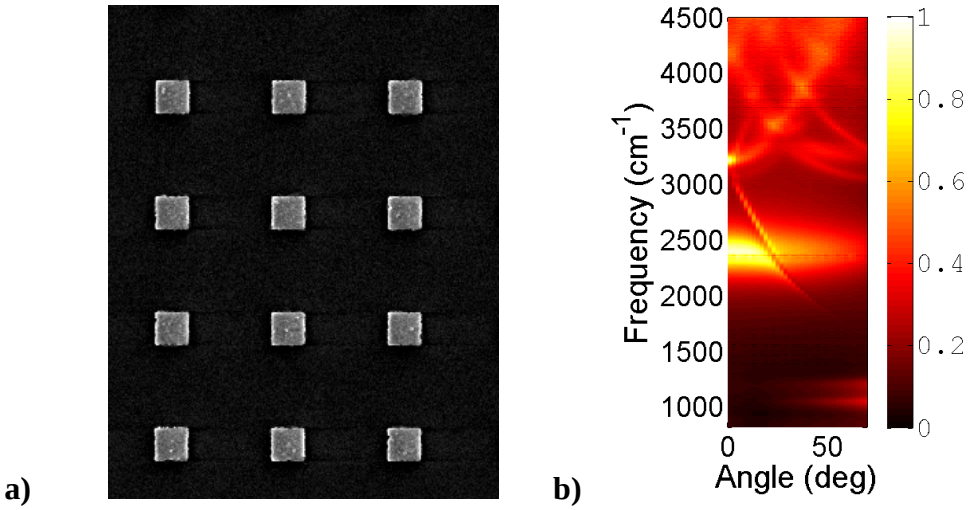

Figure 1: a) Metasurface made of a periodic array of patch metallic antennas, b) Measurement of the emissivity as a function of angle and frequency. Data are taken at 600°C.

3. Improving the efficiency

One of the major drawbacks of incandescent sources is their efficiency. A typical light bulb has a wall-plug efficiency of 3% in terms of useful radiation emitted in the visible. When using a globar for gas sensing, the spectral range of interest is very narrow thereby reducing the efficiency. Here, we report a hot membrane design allowing to improve significantly the efficiency for gas sensing applications [3]. We first discuss the different energy leakage mechanisms and show how to deal with them. Our design is based on a hot membrane encapsulated in vacuum to suppress convective losses. The membrane has a frequency selective coating in order to reduce unwanted radiative losses. Finally, we reduce significantly the conduction losses by heating only the central part of the membrane.

4. Introducing fast modulation for incandescent sources

As explained above, the key to a simple model of the control of radiation is the concept of emissivity. As the emitted flux is proportional to the product of emissivity and specific intensity of a black body, it is possible to modulate the flux by modulating the emissivity instead of modulating the temperature. In other words, the idea is to have a source that can oscillate between a "mirror" state and "blackbody" state depending on an applied voltage. Here, we will report the first proof of principle of this idea. The device uses the recently introduced concept of modulation based on the epsilon near zero (ENZ) mode [4]. The basic concept amounts to modulate the resonant absorption due to surface phonon polaritons. This is achieved by modulating the electrical density in a quantum well as discussed in [4]. The first electrical modulation of the emitted flux has been reported in ref. [5].

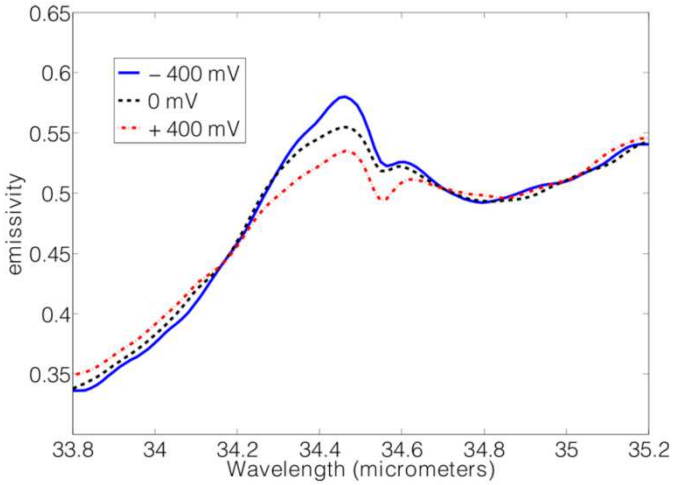

Figure 2: Proof of principle of the electrical modulation of emissivity using the ENZ effect.

References

[1] J-J. Greffet *et al. Nature* **416**, 61, 2002.

[2] C. Watts, X. Liu, W.J. Padilla, "Metamaterial Electromagnetic Wave Absorbers, *Advanced Optical Materials* **24**, p OP98, 2012.

[3] G. Brucoli *et al.*, "High efficiency quasimonochromatic IR emitter", *Appl.Phys.Lett.* **104**, 081101, 2014.

[4] S. Vassant *et al.*, "Epsilon-near-zero mode for active optoelectronic devices", *Phys.Rev.Lett.* **109**, 237401, 2012.

[5] S. Vassant *et al.*, "Electrical modulation of emissivity", *Appl.Phys.Lett.* **102**, 081125, 2013.

Session 3

Experimental heat conduction (1)

Thermal conductivity of porous silicon irradiated with swift heavy ions

Mouhannad MASSOUD[a,b,c*], P.-Olivier CHAPUIS[c], Bruno CANUT [a], Pascal NEWBY[a,b], Luc G. FRECHETTE [b] and Jean-Marie. BLUET[a]

[a]*Université de Lyon, Institut des Nanotechnologies de Lyon INL-UMR5270, CNRS, INSA de Lyon, F-69621 Villeurbanne, France*

[b]*Centre de Recherche en Nanofabrication et Nanocaractérisation (CNR2), Université de Sherbrooke, Sherbrooke, Québec, Canada*

[c]*Université de Lyon, Centre d'Energétique et de Thermique de Lyon CETHIL-UMR5008, CNRS, INSA de Lyon, F-69621 Villeurbanne, France*

**corresponding author: mouhannad.massoud@insa-lyon.fr*

Keywords: porous silicon films, swift heavy ion irradiation, thermal conductivity reduction.

Silicon (Si) is the main material of electronics and is also a material of choice in the majority of micro-electro-mechanical systems (MEMS) and sensors. It is well-known that its thermal conductivity is close to 150 $W.m^{-1}.K^{-1}$, which is quite large for non-metallic solids. In devices, it is often important to protect certain areas from heating and thermal insulators are required to do so. Among compatible materials, amorphous silicon dioxide of thermal conductivity usually close to 1.2 $W.m^{-1}.K^{-1}$ and silicon nitride can be used. Another choice is porous silicon (PSi). Obtained by electrochemical etching of single crystal silicon wafers (c-Si), PSi can possess an effective thermal conductivity measured to be 2 orders of magnitude lower than that of bulk c-Si [1, 2]. However, porosification has also a detrimental effect on the mechanical properties of PSi [3] and there is a limit to the increasing of porosity, so that there is also a limit to the reduction in thermal conductivity that can be achieved with such process. One additional option is to partially oxidize PSi, which can further reduce the effective thermal conductivity by a factor of two [4-5]. Note that increased oxidation causes swelling and stress in the PSi layer, which is a drawback for many devices [6-7]. In addition, oxygen incorporation reduces porosity, and it has been found that the thermal conductivity increases again beyond a given limit [4-5]. As a consequence of these drawbacks, there is still plenty of room for the development of alternative techniques which could lead to the smallest thermal conductivity of silicon-based materials. Since disorder is commonly associated to localized vibration modes and low thermal conductivity [8], amorphization of Si can provide an interesting way for this purpose. A reduction of two orders of magnitude with values ranging between 1 and 5 $W.m^{-1}.K^{-1}$ [9] has been evidenced.

Here, we propose to irradiate PSi with heavy ions in order to amorphize the silicon skeleton of the structure, therefore combining the advantages of porosification and amorphization. Previous works showed that irradiation with 4MeV $^{4}He^{+}$ ions can cause a densification of the porous layer [10] due to nuclear collision. In order to avoid this process, swift heavy ion irradiation is selected. This irradiation, in the electronic regime, causes the creation of a cylindrical damaged zone ("latent track") along the path of the ions [11-12]. Some of us have previously shown that irradiation with ^{238}U ions at energy of 110 MeV leads to amorphization and to a reduction of the thermal conductivity [13]. In the present study, we present results for various energies (29 and 91 MeV) and ion masses (^{238}U and ^{129}Xe) at different ion fluences, ranging from 10^{12} to 3 10^{13} cm^{-2}. The PSi porosity after chemical process and before irradiation is measured optically to be 56%.

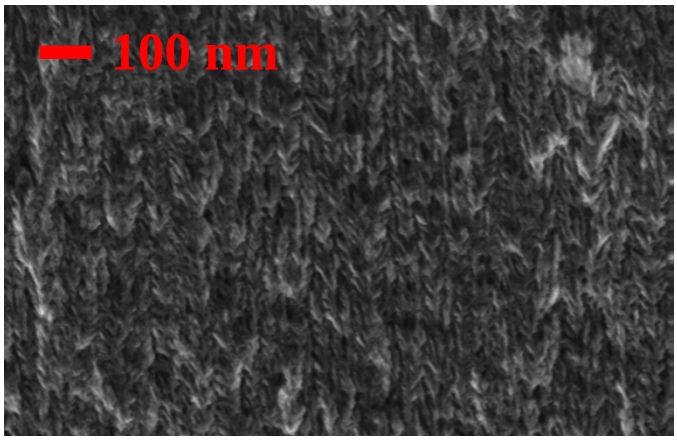

Figure 1: Algae-like structure of PSi after ion irradiation with a fluence of 3 10^{12} cm^{-2} at an energy of 29 MeV.

The structures of the samples are analyzed with scanning electron microscopy and various optical and spectroscopic means. The amorphous fraction of the irradiated porous silicon (IPSi) is determined by comparison of a sharp Raman peak associated to c-Si TO phonon mode and the extended bump associated to amorphous silicon, as presented in [13]. Effective thermal conductivities of the samples are deduced from two types of thermal measurements: (i) Raman thermometry, which builds on the analysis of the temperature-dependent shift of the Raman TO peak when increasing the illuminating power [13], and (ii) Scanning thermal microscopy (SThM) [14], which is based on the cooling of a heated AFM probe when set in contact with the sample.

Our results [14] show that increasing the irradiation fluence allows decreasing the thermal conductivity by a factor up to 4.4 in comparison to non-irradiated samples. The measurements also demonstrate that the effective thermal conductivity seems to depend linearly on the crystalline fraction of the materials, as shown in Figure 2. For the largest fluence and the largest energy, it appears that the thermal conductivity can be reduced to the level of silica, between 1 and 2 $W.m^{-1}.K^{-1}$. Since the fluences and energies have not been fully optimized until now, the results suggest that decreasing the thermal conductivity of a block of silicon to a value well below silica is possible.

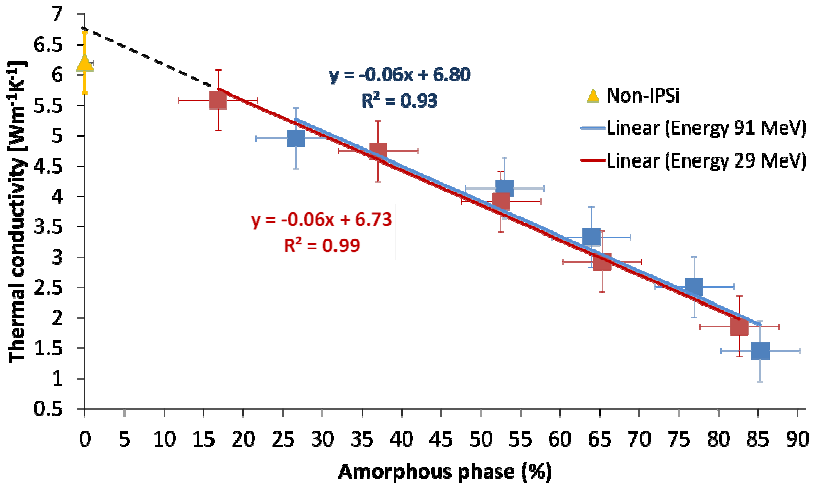

Figure 2: Thermal conductivities of the IPSi samples (Xe ions) as a function of their amorphous fraction.

Acknowledgements

We acknowledge the support of the joint international research unit UMI LN2 between CNRS and University of Sherbrooke, and of project BQR INSA MaNaTherm. Funding for this project was provided to M.M. by a CMIRA Explora Doc supporting grant from the Rhône-Alpes Région.

References

[1] G. Gesele, J. Linsmeier, V. Drach, J. Fricke, and R. Arens-Fischer, *J. Phys. D* **30**, 2911, 1997.

[2] V. Lysenko, S. Perichon, B. Remaki, and D. Barbier, *Sens. Actuators*, **A99**, 13, 2002.

[3] C. Populaire, B. Remaki, V. Lysenko, D. Barbier, H. Artmann and T. Pannek, *Appl. Phys. Lett*. **83**, 1370, 2003.

[4] S. Périchon, V. Lysenko, P. Roussel, B. Remaki, B. Champagnon, D. Barbier and P. Pinard, *Sens. Actuators*, **A 85**, 335, 2000.

[5] V. Lysenko, S. Perichon, B. Remaki, D. Barbier and B. Champagnon, *J. Appl. Phys*. **86**, 6841, 1999.

[6] K. Imai and H. Unno, *IEEE Trans. Electron Devices* **31**, 297, 1984.

[7] K. Barla, R. Herino and G. Bomchil, *J. Appl. Phys*. **59**, 439, 1986.

[8] D. G. Cahill, S. K. Watson and R. O. Pohl, *Phys. Rev. B* **46**, 6131, 1992.

[9] Y. He, D. Donadio and G. Galli, *Appl. Phys. Lett*. **98**, 144101, 2011.

[10] A. Simon, F. Paszti, A. Manuaba and A. Z. Kiss, *Nucl. Instrum. Methods Phys. Res. B* **158**, 658, 1999.

[11] W. Wesch, A. Kamarou and E. Wendler, *Nucl. Instrum. Methods Phys. Res. B* **225**, 111, 2004.

[12] N. Itoh, D. M. Duffy, S. Khakshouri and A. M. Stoneham, *J. Phys: Condens. Matter* **21**, 474205, 2009.

[13] P. J. Newby, B. Canut, J.M. Bluet, S. Gomès, M. Isaiev, R. Burbelo, K. Termentzidis, P. Chantrenne, L.G. Frechette and V. Lysenko, *J. Appl. Phys.* **114**, 014903, 2013.

[14] S. Gomes, P. Newby, B. Canut, K. Termentzidis, O. Marty, L. Frechette, P. Chantrenne, V. Aimez, J.M. Bluet and V. Lysenko, *Microelectronics Journal* **44**, 1029, 2013.

[14] M. Massoud, B. Canut, P. Newby, L.G. Fréchette, P.-O. Chapuis, and J.M. Bluet, *Nuclear Instr. Meth. Phys. Res. B*, in press (available online), 2014.

Coherent control of thermal conduction in two-dimensional phononic crystals

Nobuyuki ZEN, Tuomas A. PUURTINEN, Tero J. ISOTALO, Saumyadip CHAUDHURI and Ilari J. MAASILTA*

Nanoscience Center, Department of Physics, P. O. Box 35, FI40014 University of Jyväskylä, Finland

**corresponding author: maasilta@jyu.fi*

Keywords: thermal conduction, phonon heat transport, phononic crystal, ballistic transport

Controlling thermal transport has become more relevant in recent years, in light of the strong push to develop novel energy harvesting techniques based on thermoelectricity [1], the need to improve the heat dissipation out of semiconductor devices, and the push to increase the sensitivity of bolometric radiation detectors [2]. Traditionally, reduction of thermal conductivity is achieved by including impurities, nanoparticles, voids, etc., which increase the scattering of the relevant energy carrying quanta, electrons and phonons. As the phonon thermal transport component is present in all conducting and insulating materials, a lot of research has lately focused on lowering phonon thermal conductivity using nanoscale structuring of materials [3] to increase scattering. On the other hand, much less attention has been given to controlling phonon thermal conductance by engineering the phonon dispersion relations, in other words the phonon 'band structure'.

Dispersion relations determine both the group velocity and the density of states, and therefore directly influence thermal conduction. They are normally determined by the microscopic details of the atomic bonding of the material in question. However, many of the phonons involved in thermal conduction actually have wavelengths much larger than the atomic lattice constant [4]. Thus, if the material in question is structured at some longer length scale, the phonons with wavelengths around that length are predicted to undergo strong coherent Bragg scattering and interference. If this extra structuring is periodic, the devices are called phononic crystals [5] in analogy with periodic structures for electromagnetic wave engineering, photonic crystals. Due to this interference effect, the band structure of the long wavelength phonons is strongly modified so that changes in both the density of states and the group velocity, and thus in thermal conductance, are expected.

Here, we discuss this line of approach for controlling thermal conduction and present our recent experimental and computational studies of thermal conductance in two-dimensional phononic crystals (PnCs) at sub-Kelvin temperatures [6]. Figure 1 shows a scanning electron micrograph of a typical sample, which consist of periodic array of holes etched into a 0.5 µm thick silicon nitride membrane. We compared the results of two PnCs with different periodicities to an uncut membrane sample and observed a strong reduction of thermal conductance up to a factor of 30, with a concurrent change in the temperature dependence. This reduction and temperature dependence was in quantitative agreement, for both periodicities, with our numerical computation based on finite element method (FEM) simulations of the modified dispersion relations of the PnC devices. Note that the PnCs had the same amount of material removed and hence should have the same reduction in thermal conductivity, without any change in temperature dependence, if phonon interference were not present. As our calculation of the thermal conduction was performed in the fully ballistic limit, where no scattering at all is considered (this is expected in the sub-K range as all bulk scattering processes have been shown to freeze out), we have to draw the conclusion that coherent, interference-based phonon band structure

modification is behind the observations. In other words, there is clear evidence that phonon thermal conduction can be controlled by using the wave-properties of phonons, instead of just the particle (scattering) properties. This idea was also discussed theoretically recently in Ref. [7].

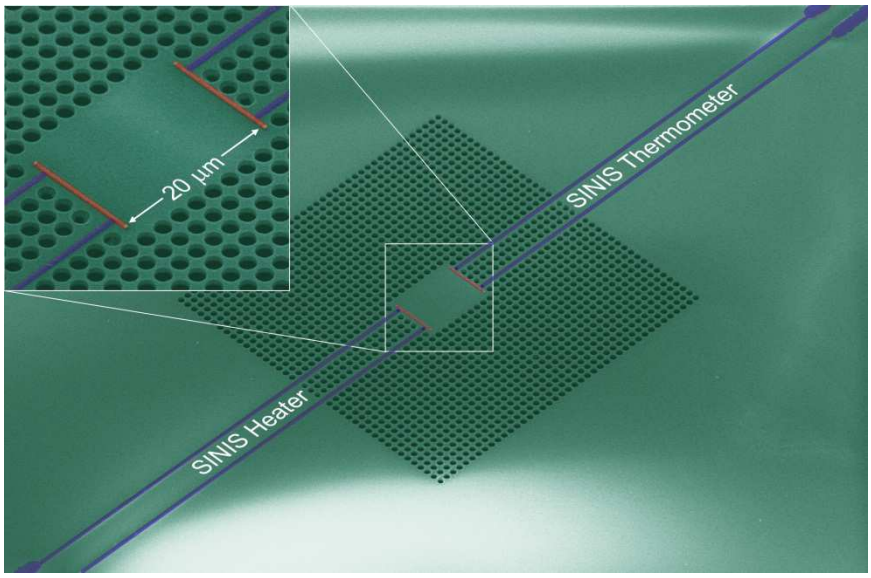

Figure 1: A scanning electron micrograph of a 2D phononic crystal sample fabricated from a SiN membrane. The heater and thermometer are normal metal-insulator-superconductor (NIS) tunnel junctions.

In future studies, we hope to answer several further questions related to coherent control of thermal conduction, one of them being as simples as: what are the optimal parameters of a particular lattice type (such as the square lattice) for minimization or maximization of thermal conductance? How will the situation change, if the holes are arranged in a random fashion (Bloch's theorem for band-structure not satisfied)? We already know that, for example, maximizing the band gap will not lead to the minimum thermal conductance.

References

[1] A. J. Minnich, M. S. Dresselhaus, Z. F. Ren, G. Chen, "Bulk nanostructured thermoelectric materials: current research and future prospects", *Energy Environ. Sci.* **2**, 466–479, 2009.

[2] Enss, Ch. Ed., *Cryogenic particle detection*, Springer, 2005.

[3] W. Kim, R. Wang, A. Majumdar, "Nanostructuring expands thermal limits", *Nanotoday* **2**, 40–47, 2007.

[4] I. J. Maasilta and A. Minnich , "Heat under the microscope", Phys. Today **67**, 285-290, 2014.

[5] Y. Pennec, J. O.Vasseur, B. Djafari-Rouhani, L. Dobrzynski, P. Deymier, "Two-dimensional phononic crystals: Examples and applications", *Surf. Sci. Rep.* **65**, 229–291, 2010.

[6] N. Zen, T. A. Puurtinen, T. J. Isotalo, S. Chaudhuri, I. J. Maasilta, "Engineering thermal conductance using a two-dimensional phononic crystal, *Nature Comm.* **5**, 3435, 2014.

[7] M. Maldovan, "Sound and heat revolutions in phononics", *Nature* **503**, 209-217, 2013.

Reduction of thermal conductivity in silicon thin film membranes by phononic engineering

Valeria LACATENA[a,b], M. HARAS[a,b], J.-F. ROBILLARD[b], S. MONFRAY[a], T. SKOTNICKI[a], E. DUBOIS[b]

[a]*STMicroelectronics 850, rue Jean Monnet, F-38926 Crolles, FRANCE*

[b]*IEMN UMR CNRS 8520, Institut d'Electronique, de Microélectronique et de Nanotechnologie, Avenue Poincaré, F-59652 Villeneuve d'Ascq, FRANCE*

**corresponding author: valeria.lacatena@isen.iemn.univ-lille1.fr*

Keywords: thermoelectricity, silicon, thermal conductivity, thin film, phononic crystal.

Abstract

Thermoelectric generation faces two major drawbacks: i) intrinsic efficiency limitation related to the optimization of antagonist and intricate transport properties, ii) scarcity, cost and harmfulness of state-of-the-art materials among which Sb, Te, Bi, Pb. Among promising materials, Si and Ge feature competitive Seebeck coefficient and electrical properties and compatibility with conventional CMOS fabrication processes. However, a significant thermal conductivity precludes the use of these materials in thermoelectric generators. Suspended membranes with phononic engineered structures or "thermocrystals" were recently proposed in order to hinder thermal transport in silicon. In this work, we present a fabrication methodology for such artificial materials and the procedure of integration onto micrometric thermal measurement platform is presented. The preliminary experimental results are supported by thermal conductivity measurements and molecular dynamic simulations by Green-Kubo methodology.

Introduction

The most commonly used thermoelectric materials are Bi_2Te_3 and Sb_2Te_3, but they present the drawback of being harmful/toxic, expensive and not CMOS compatible. For these reasons attention is rising toward materials such as Si, Ge or SiGe using nanostructuration methods to reduce their thermal conductivity [1]. To realize a CMOS compatible device the substrate chosen is silicon-on-insulator (SOI). Silicon is attractive for its high Seebeck coefficient (400 µV/K) [2] for highly doped p-Si and doping dependent electrical conductivity. However, its elevated thermal conductivity (148 W/m/K) makes it unsuitable to sustain the necessary heat gradients of a thermoelectric device. Nowadays, the interest in thermoelectric devices based on silicon as the active medium is increasing due to the innovative integration approaches to pattern phononic enclosures at very high resolution in nano-devices. Phononic crystals (PCs) are considered the elastic counterpart of photonic crystals [3]. The periodically modulated elasticity of these structures induces a shrinking of the Brillouin zone which in turn gives rise to additional phonon transport properties such as: i) Full or partial frequency band gaps preventing transport in given frequency ranges., ii) artificially induced anisotropic transport, iii) negative refraction, iv) reduction of the phonons group velocity. Considering the different order of magnitudes of the phonon mean free path (peaked distribution at 250 nm for Si at 300 K) and electron one (2-3 nm for Si at 300 K) it is possible to realize periodic nano-enclosures with tenths of nanometers dimensionality, permitting to decouple the phonon and electron transport to hinder the first one, without affecting the electrical conductivity. The phonons transport will be impeded by scattering

processes and interference effects due to such periodic nanostructuration of the silicon thin film. Recently it has been demonstrated [4][5][6] that it is possible to reduce the thermal conductivity by periodic patterning of the silicon layer with the aim of adding a phononic effect to the 10-fold reduction of the thermal conductivity due to the thin film contribution. The desired material has a low lattice thermal conductivity (2 W/m/K) and preserves the electron conductivity solving the well know "phonon glass – electron crystal" dilemma of thermoelectric materials optimization.

Phononic patterning and device nano-fabrication

The fabrication procedure counts several lithography steps to fully suspend the metrology platform. The substrate used is SOI with a silicon thickness of 72 nm. Firstly the nano-enclosures are defined by electron beam lithography and etched by RIE using "dots-on-the-fly" technique to speed up the writing process and reaching a high pattern resolution [7]. Once the holey film has been defined, it is possible to proceed with the cavities etching, the metallization of heater and sensor serpentines and the final BOX and Si-substrate etching. The final device is shown in figure 1(a). The membranes realized have dimension of 5-10 µm of width and 5-10-20-30 µm of length. A detail of the nano-inclusions with a pitch of 60 nm is shown in figure 1(b). The metrology platform is composed by a central fully suspended heater and two lateral partially suspended sensors. In such a way the heat produced by the voltage applied to the heater will flow through the nanostructured membranes and the resistance variation, temperature dependent, is measured at the sensor.

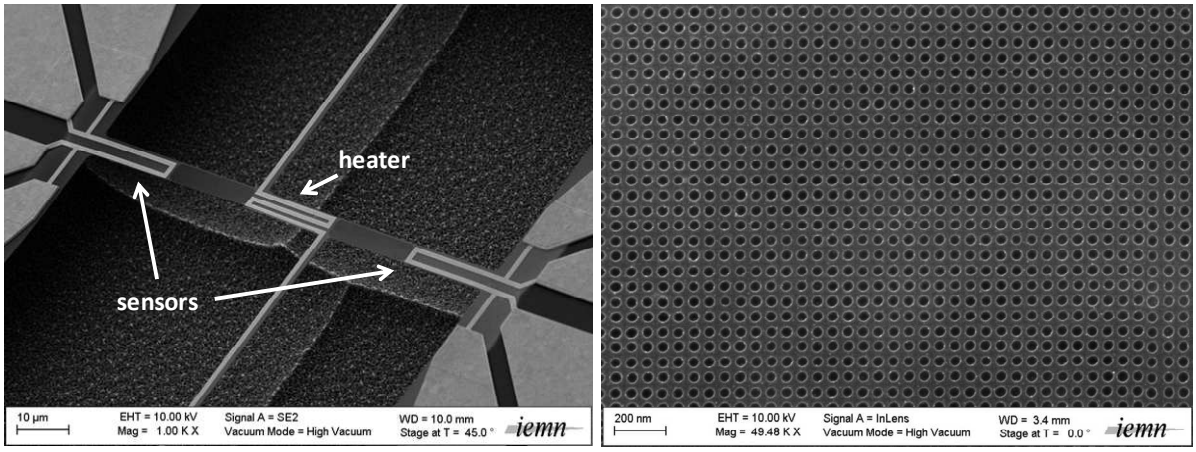

Figure 1 : (a) SEM image of the suspended membranes 20 µm x 5 µm with Pt heater and sensors, (b) SEM image details of the patterned holes on the suspended 60 nm thick membranes (pitch of 60 nm).

Preliminary thermal conductivity measurements have been performed to estimate the reduction of heat transport due to the thin film and the added effect due to the phononic structure. The measurements are conducted under vacuum (10^{-6} mTorr) to prevent convection mechanisms. Measurements show values that are more than one order of magnitude lower than ones obtained for bulk silicon, demonstrating the reduction of the heat transport due to surface patterning.

Molecular Dynamic simulations

The origins of the 100-fold reduction of thermal conductivity in nanophononic membranes is still a debated question. Indeed, while conductivity reduction in thin films is a well know phenomena that can be modeled, as an example, using the Fuchs-Sondheimer model, the further decrease of conductivity is sometimes attributed to various effects such as: i) increased silica/silicon interface area, ii) local disorder induced by the fabrication processes and finally iii) Bragg refraction of the phonons

on the artificial lattice. To go further, a molecular dynamics simulation scheme using Green-Kubo formalism is used. The Environment-Dependent Interatomic Potential has been chosen for its realistic depiction of silicon thermal properties. The simulation of bulk silicon are well reproducing the experimental results found by Glassbrenner *et al.* [8]. The same simulation scheme has been reproduced for demonstrating the reduction of thermal conductivity in thin film and in periodic cylindrical inclusion in bulky silicon. These simulations, despite known limitations, account for a significant decrease of thermal conductivity well below what is expected by porous media models.

Conclusions

A robust process has been established to realize decananometer scale, periodic patterning of SOI substrates and to integrate them onto suspended membranes for thermal conductivity metrology based on electro-thermal generation and sensing. Preliminary thermal conductivity measurements by suspended membranes 4-probes methodology have demonstrated the reduction of thermal conductivity in the nanostructured thin film membranes. Molecular dynamics aims to justify the relevance of the patterning methodology developed showing an efficient reduction of the thermal conductivity. Perspectives envision to extend these characterizations to the Seebeck coefficients, and electrical conductivity.

References

[1] M. Haras, V. Lacatena, S. Monfray, J.-F. Robillard, T. Skotnicki, and E. Dubois, “Unconventional Thin-Film Thermoelectric Converters: Structure, Simulation, and Comparative Study” , *J. Electron. Mater.*, vol. **43**(6), pp. 2109-2114, 2014.

[2] L. Weber and E. Gmelin, “Transport properties of silicon” , *Appl. Phys. Mater. Sci. Process.*, vol. **53**, no. 2, pp. 136–140, 1991.

[3] J.O. Vasseur, P.A. Deymier, G. Frantziskonis, G. Hong, B. Djafari-Rouhani, and L. Dobrzynski, “Experimental evidence for the existence of absolute acoustic band gaps in two-dimensional periodic composite media” , *J. Phys. Condens. Matter*, vol. **10**, no. 27, pp. 6051–6064.

[4] J.-K. Yu, S. Mitrovic, D. Tham, J. Varghese, and J.R. Heath, “Reduction of thermal conductivity in phononic nanomesh structures” , *Nat. Nanotechnol.*, vol. **5**, no. 10, pp. 718–721, Jul. 2010.

[5] S.J. Tang, H.-T. Wang, D. H. Lee, M. Fardy, Z. Huo, T. P. Russell, and P. Yang, “Holey Silicon as an Efficient Thermoelectric Material” , *Nano Lett*, vol. **10**, no. 10, pp. 4279–4283, 2010.

[6] P.E. Hopkins, C.M. Reinke, M.F. Su, R.H. Olsson, E.A. Shaner, Z.C. Leseman, J.R. Serrano, L.M. Phinney, and I. El-Kady, “Reduction in the Thermal Conductivity of Single Crystalline Silicon by Phononic Crystal Patterning” , *Nano Lett*, vol. **11**, no. 1, pp. 107–112, 2010.

[7] V. Lacatena, M. Haras, J.-F. Robillard, S. Monfray, T. Skotnicki and E. Dubois, “Phononic engineering of silicon using “dots on the fly” e-beam lithography and plasma etching”, *Microelectron. Eng.*, vol. **121**, pp. 131-134, 2014.

[8] C.J. Glassbrenner and G.A. Slack, “Thermal Conductivity of Silicon and Germanium from 3'K to the Melting Point”, *Phys Rev.*, vol. **134** (4A), 1964.

Joule heated micro- and nanowires: A versatile platform for high spatial and temporal resolution thermal investigations

Carlos M. QUINTERO[a*], Olena KRAIEVA[a,b,c], Edna M. HERNÁNDEZ[b], Franck CARCENAC[a], Denis LAGRANGE[a], Gábor MOLNÁR[b] and Christian BERGAUD[a]

[a]*LAAS, CNRS & Université de Toulouse (UPS, INSA, IAES), 7 Av de Colonel Roche, 31077 Toulouse, France*

[b]*LCC, CNRS & Université de Toulouse (UPS, INPT), 205 route de Narbonne, 31077 Toulouse, France*

[c]*Kyiv Polytechnic Institute, National Technical University of Ukraine, 37 Prospect Peremogy, Kiev 03056, Ukraine*

**corresponding author: cmquinte@laas.fr*

Keywords: Metallic wires, lithography, luminescence, transient heating, scanning probe microscopy.

The development of temperature sensors continues to attract much attention in various areas of science and technology. Not only has the need for development of new thermal nano-characterization techniques and use of novel nanomaterials dramatically increased, but also the demands for measuring and controlling temperature with nanoscale spatial resolution and high temporal-resolution have become a major concern for further developments.

Metallic nanowires have the potential for becoming submicrometer scale heating elements for temperature control (via the Joule effect, Figure 1). Due to their small thermal mass, micro- and nanowire based devices are particularly interesting with regards to their response times and also in terms of confinement of the induced temperature changes. The thermal characterization of these heating elements is a critical step; associated with appropriate electrical setups, luminescent probes and/or with scanning probe microscopy techniques, these devices allow for high spatial and temporal resolution investigation of thermal properties [1-5].

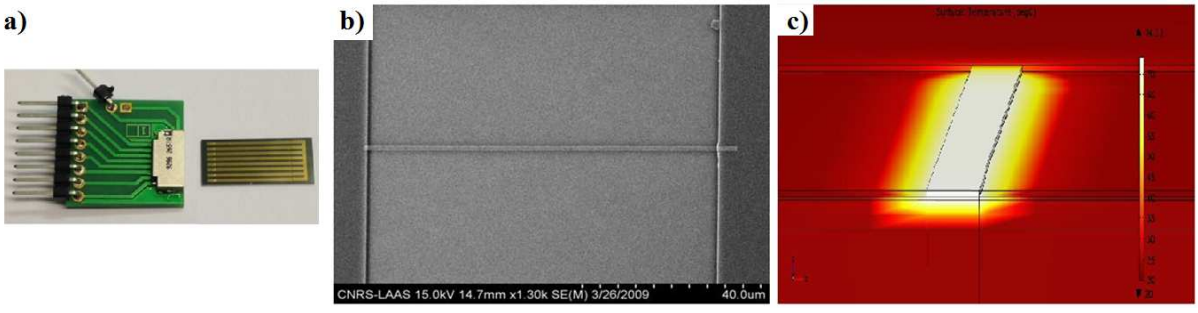

Figure 1: Metallic Au wires for localized heating purposes. a) Au micro/nano heaters embedded on a chip and its electrical connector, b) Scanning Electron Microscopy image of 50 nm x 1 µm x 80 µm wire and c) finite element simulation of the temperature distribution in this wire using COMSOL MULTIPHYSICS.

Methods

Micro- and nanowires were fabricated (thickness: 50 nm, length: 80 µm, width: 500 nm or 1 µm) and embedded on a chip by means of e-beam and photo lithography. The circuit was electrically isolated from the underlying silicon substrate by a 300 nm thick SiO_2 layer. When heated via the Joule effect using a current source, these wires are expected to provide fast, spatially localized temperature changes due to their small dimensions and low heat capacity. Steady-state and transient (current pulse) heating of the wires was characterized by both electrical (resistance) and optical (luminescence microscopy) techniques and the experimental results were completed by finite element simulations using COMSOL MULTIPHYSICS.

Results

Electrical characterization of the heaters in steady state was performed in two steps: first, the variation of the resistance of the wires as a function of temperature was observed; second, the change in resistance was also studied as a function of an applied electrical current. From these sets of data, it is possible to establish a relationship between an applied current and the mean variation in temperature induced along the wire (Figure 2a). The spatial distribution of these temperature changes was studied with fluorescence microscopy by depositing a thermo sensitive luminescent probe consisting on Rhodamine B [1] or spin crossover materials doped with Rhodamine 110[6]. The results were also compared to finite element simulations. These studies confirmed the flat and highly confined temperature variation expected in the vicinity of the heaters (Figure 2b).

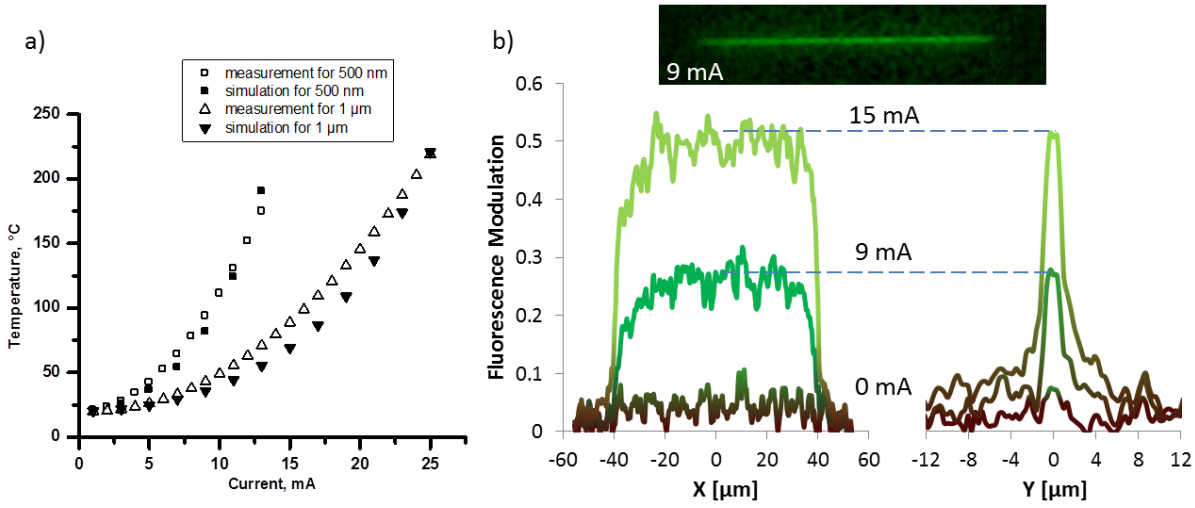

Figure 2: Electrical and optical steady-state characterization of Au heaters. a) Variation of the temperature as a function of the applied current for 500 nm and 1µm wide gold wires. b) Temperature profiles of an 80 µm x 1 µm wire inferred from fluorescence microscopy at different bias. A fluorescent spin crossover thin film was employed as a thermal probe.

The ideal experimental setup for characterizing the dynamics of the temperature jumps (T-jumps) induced by an applied step of electrical current in the micro/nano wires is one in which it is possible to correlate the integrated electrical response of the system to optical imaging measurements. To this end, a transient differential resistance setup coupled to a gated CCD camera (ICCD from Andor Technologies) was developed to perform pump-probe time-resolved luminescence spectroscopy while simultaneously measuring the electrical and optical responses caused by transient heating of the wires. Both observations revealed that after an electrical current step, these types of heaters reach a stationary

temperature within the microsecond range (Figure 3). As a result, use of these micro/nano wires as heat sources is promising for the development and optimization of cheap and simple high-speed temperature control on-chip strategies. Although the temporal responses of these heaters are not as fast as laser setups, it is suitable for characterizing a great number of molecular events in bio/chemistry.

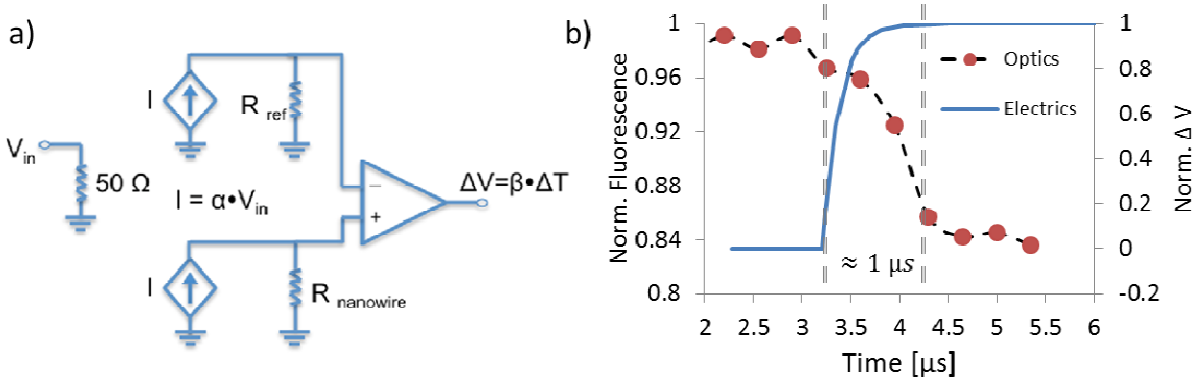

Figure 3 T-jump observations: a) Schematic of the differential amplifier setup for monitoring the thermal response to a current pulse applied to a heating element. The voltage obtained across a wire is compared to that of a reference resistance (negligible temperature dependence and equal to that of the wire at low currents). b) Electrical and optical transient heating response of a heater covered with a thin layer of Rhodamine B; as the temperature increases, revealing a decrease in fluorescence. In both cases, a stationary regime is reached after ca. 1μs.

Once it is characterized, this simple but very powerful platform of micro/nano heaters can be coupled to diverse setups. For example, we have employed these heaters together with an epifluorescence microscope to study the potential of spin coated fluorescent spin crossover thin films as surface temperature sensors with high spatial resolution. As the temperature rises, the variation of the optical properties resulting from the phase transition of the spin crossover nanomaterial will lead to an increase on the light emitted by the luminescent agent present in the film (Rhodamine 110) [7]. In this manner, we have been able to image the strong confinement of the temperature increase due to Joule heating in the vicinity of different heaters (Figure 2b).

In a different approach, we have also performed thermo-mechanical measurements with an atomic force microscope (AFM) and successfully imaged the variation of the Young's modulus during the thermally induced phase transition of the same spin crossover thin films (Figure 4) [5]. This hot wire scheme allowed us to induce the phase transition of the film in a small sample area inside the region under observation at will and in a controlled manner. In addition, using this configuration we also have an unchanged reference area of the sample just a few hundred nanometers away from the heater independent of the thermal perturbation generated by the wire. Moreover, contrary to the usual heating stages proposed by AFM manufacturers, our heaters do not induce any thermal drift of the sample. These three advantages bring a great simplification for the observation of thermally induced phenomena and the corresponding post-data analysis while working at high magnification conditions such as those of an AFM.

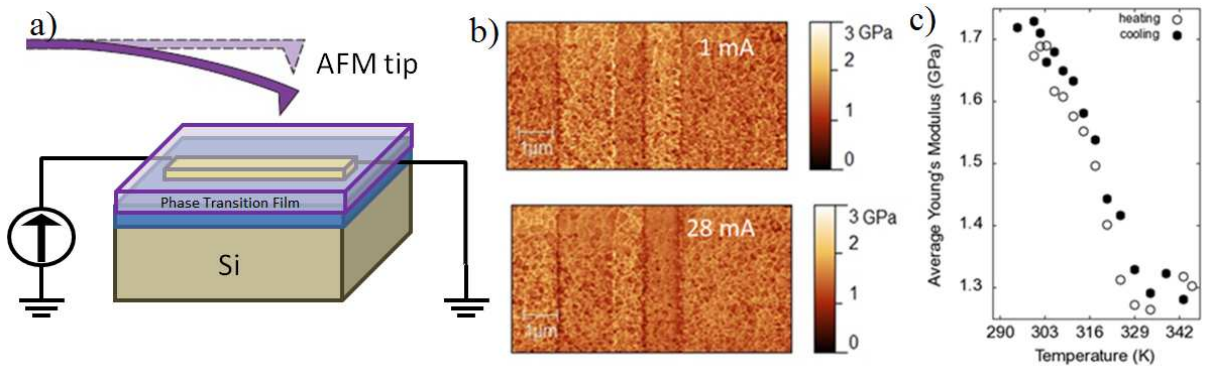

<u>Figure 4 Detection of a phase transition with AFM thermo-mechanical measurements:</u> a) Schematic of the setup employed to study the thermal phase transition in spin crossover thin films. b) Young's Modulus maps for I = 1 mA and 28 mA. c) Young's modulus dependence as a function of temperature in the region above the wires. An increase of current applied to the heaters leads to a very substantial decrease of the Young modulus in this region [5].

Conclusions

We have shown the versatility of Joule heated micro- and nanowires as a platform for high spatial and temporal resolution thermal investigations. This is supported by a series of diverse experimental and finite element simulation studies of the spatio-temporal thermal response of sub-micronic gold wires embedded on electrically insulated silicon substrates. Under this configuration, it is demonstrated that these heaters lead to fast (< µs) and spatially well localized (< µm) T-jump perturbations driven by an electrical current. The simplicity of this platform facilitates its integration to existing on-chip technologies for thermal excitation and temperature measurement purposes. To illustrate this flexibility, the platform has been coupled to an AFM to perform quantitative high spatial resolution thermo-mechanical measurements for phase transition thin films.

References

[1] P. Löw, B. Kim, N. Takama, C. Bergaud, "High-spatial-resolution surface temperature mapping using fluorescent thermometry", *Small*, **7**, 908, 2008.

[2] P. Bon, N. Belaid, D. Lagrange, C. Bergaud, H. Rigneault, S. Monneret, G. Baffou, "Three dimensional temperature imaging around a gold microwire", *Appl. Phys Lett.* **102**, 244103, 2013.

[3] L. Aigouy, E.Saidi, L. Lalouat, J. Labeguerie-Egea, M. Mortier, P. Löw, C. Bergaud, "Scanning thermal microscopy with Fluorescent Nanoprobes", *J. Appl. Phys*. **106**, 074301, 2009.

[4] E. Saïdi, B. Samson, L. Aigouy, S. Volz, P. Löw, C. Bergaud, M. Mortier, "Scanning thermal imaging by near-field fluorescence spectroscopy", *Nanotechnology*. **20**, 115703, 2009.

[5] E. M. Hernández, C. M. Quintero, O. Kraieva, C. Thibault, C. Bergaud, L. Salmon, G. Molnár, A. Bousseksou, "AFM imaging of molecular spin-state changes through quantitative thermo-mechanical measurements", *Adv. Mater*. 26, 2889, 2014.

[6] G. Molnar, I. A. Gural'skiy, L. Salmon, W. Nicolazzi, C, M. Quintero, A. Akou, K. Abdul-Kader, G. Félix, T. Mahfoud, C. Bergaud, C. Bartual, C. Thibault, C. Vieu, A. Bousseksou, "Bistable photonic nanostructures based on molecular spin crossover complexes", *in Proceedings of SPIE Photonics Europe - Photonic Crystal Materials and Devices X*, **8425**, 2012.

[7] C. M. Quintero, I. A. Gural'skiy, L. Salmon, G. Molnár, C. Bergaud, A. Bousseksou, "Soft lithographic patterning of spin crossover complexes. Part 1: Fluorescent detection of the spin transition in single nano-objects", *J. Mater. Chem*, **22**, 3745, 2012.

Session 4

Numerical heat transfer

Calculation of ballistic and Casimir-limit phonon thermal conduction in thin membranes

Tuomas PUURTINEN[a,*] and Ilari MAASILTA[a]

[a]*Nanoscience Center, Department of Physics, P. O. Box 35, University of Jyväskylä, FI-40014 Jyväskylä, Finland*

**corresponding author: tuomas.a.puurtinen@jyu.fi*

Keywords: phonon heat transport, 2D nanostructures, diffusive boundary scattering.

At room temperature, thermal conduction of dielectric nanostructures is characterized by structural properties of the material and phonon scattering mechanisms, such as phonon-phonon scattering and scattering from crystal defects or impurities [1]. However, at very low temperatures where the dominant phonon wavelength becomes large, these effects can become negligible. Phonon mean free path can then exceed the system dimensions leaving only specular scattering at the boundaries in effect. In that case we speak of ballistic thermal conduction.

Simplifying the system makes it easier to design structures with accurate thermal properties. For instance, in low temperature bolometric applications it is essential to the sensor sensitivity to reduce the thermal conductance of the supporting structure [2]. Suspended thin films and beams have been commonly applied there, but finding an optimal structural design in terms of strength and desired thermal properties is often a difficult problem.

In Ref. [3] we successfully used periodic hole patterning on suspended SiN membranes to alter phonon dispersion relations in order to reduce low temperature thermal conductivity. The measured data coincided with ballistic phonon model, providing proof that scattering processes did not play a role in the thermal transport. Surface roughness of the samples was measured to be 0.3 nm (RMS) which is orders of magnitude lower than the dominant phonon wavelength at 100 mK.

This leads us to another technique of engineering structures with reduced thermal conductivity. Surface of the structure can be roughened with features in the relevant phonon length scale to cause diffuse scattering in contrast to specular scattering. Purely diffusive scattering on the boundaries is called the Casimir limit, which was introduced for the case of one dimensional beams in Ref. [4]. We have previously generalized the diffusive boundary scattering model to two dimensional circular membranes and have performed numerical calculations for temperature profiles in membranes with diameter to thickness aspect ratios going up to 500 [5]. In this work, we compute the thermal properties of dielectric membranes using ballistic Lamb mode theory and radiative phonon theory in the 2D Casimir limit, and compare the two limits. We extend the earlier calculations to much higher aspect ratios, reaching a thickness below 100 nm for large membranes of diameter 500 µm. We also discuss the computational limits of the methods used.

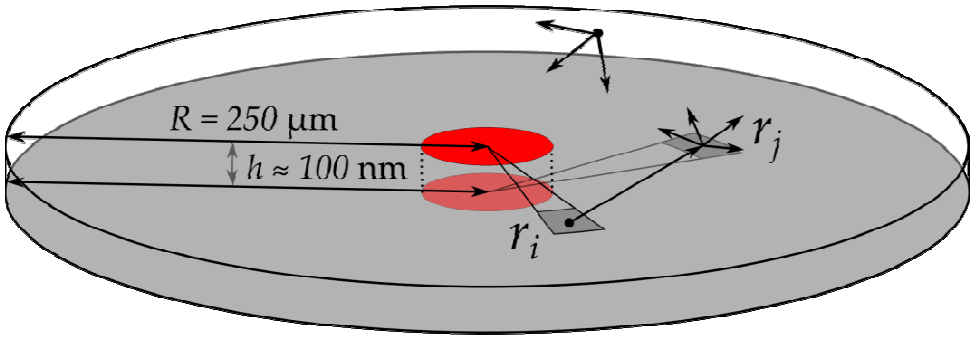

Figure 1: Illustration of the diffusive boundary scattering model for 2D membranes. Radiative balance is expected to exist between the surface elements r_i and r_j on the opposing membrane surfaces.

In the Casimir model, phonon emission from the surface element r_j (see Fig. 1) follows phonon blackbody radiation with phononic Stefan-Boltzmann constant σ, given by

$$\sigma = \frac{\pi^2 k_B^4}{120\hbar^3}\left(\frac{2}{c_t^2}+\frac{1}{c_l^2}\right)$$

where c_t and c_l are the transversal and longitudinal speed of sound. Radiative balance must exist in the steady state between the surface elements on the upper and lower boundary, which leads to equation

$$\frac{\sigma}{\pi}T_i^4\,\mathrm{d}r_i\sum_j \cos\vartheta_i \mathrm{d}\Omega_j = \frac{\sigma}{\pi}\sum_j T_j^4\cos\vartheta_j\,\mathrm{d}r_j\,\mathrm{d}\Omega_i + q\,\mathrm{d}r_i$$

where the left side corresponds to the total emitted power of element $\mathrm{d}r_i$ into surface elements $\mathrm{d}r_j$ and the right side is the total absorbed power at element $\mathrm{d}r_i$ from all other elements $\mathrm{d}r_j$ on the opposite membrane surface (see Fig. 1), in addition to a direct heater power load q. By transforming the sum to integration and by simplifying we derive [5] an integral equation for the temperature profile $Z = Z(r_1) = T^4(r_1)$

$$Z(r_1) = \int_0^R \mathrm{d}r_2\, G(r_1,r_2)\,Z(r_2) + Z(R)H(r_1) + C_\mathrm{P} f(r_1)$$

where kernel function $G(r_1,r_2)$ and coefficient function $H(r_1)$ are given by

$$G(r_1,r_2) = \frac{2d^2 r_2(r_1^2+r_2^2+d^2)}{[(r_1^2+r_2^2+d^2)^2-4r_1^2r_2^2]^{3/2}}, \qquad H(r_1) = \frac{1}{2}\left(\frac{r_1^2+d^2-R^2}{\sqrt{(r_1^2+R^2+d^2)^2-4r_1^2R^2}}+1\right).$$

Function $f(r_1)$ is the characteristic function of the power source (heater element) located at the center of the membrane upper and lower surfaces and C_P is the normalized external power input. Function $H = H(r_1)$ accounts for the bath temperature at the membrane outer edge. The equation for $Z(r_1)$ can be classified as a linear Fredholm equation of the second kind. We use the Nyström method for solving the equation, which uses the Gauss-Legendre quadrature for discretization [6]. LU decomposition is used for solving the resulting dense linear system. For Casimir model, the total emitted power $P_\mathrm{C}(T)$ of the heater at temperature T can be calculated by finding a heating power C_P so that $Z(0)^{1/4} = T$.

Our ballistic phonon model is based on elasticity theory. We approximate the membrane as an infinite isotropic domain of finite thickness. Given the elastic material constants, the allowed phonon modes can be solved analytically following the Rayleigh-Lamb theory [7]. The resulting dispersion relations

$\omega_j = \omega_j(\vec{k})$ for each phonon mode j then describe thermal behavior of the membrane by the emitted phonon power $P = P_{\mathrm{B}}(T)$

$$P_{\mathrm{B}}(T) = \frac{1}{2\pi^2} \sum_j \oint_\gamma d\gamma \int_K d\vec{k}\, \hbar\omega_j(\vec{k})\, n(\omega_j, T) \frac{\partial \omega_j(\vec{k})}{\partial \vec{k}} \cdot \vec{n}_\gamma \Theta\left(\frac{\partial \omega_j(\vec{k})}{\partial \vec{k}} \cdot \vec{n}_\gamma \right)$$

from the circular heater element γ with temperature T (see e.g. [3]). This quantity can be compared to $P_{\mathrm{C}}(T)$, from which a differential thermal conductance $G = \mathrm{d}P/\mathrm{d}T$ can also be calculated.

References

[1] R. Berman, *Thermal conduction in Solids*, Oxford University Press, Oxford, 1976.

[2] J. Wei, D. Olaya, B. S. Karasik, S. V. Pereverzev, A. V. Sergeev, and M. E. Gershenson, "Ultrasensitive hot-electron nanobolometers for terahertz astrophysics", *Nat. Nanotech.* **3**, 496-500, 2008.

[3] N. Zen, T. A. Puurtinen, T. J. Isotalo, S. Chaudhuri, and I. J. Maasilta, "Engineering thermal conductance using a two-dimensional phononic crystal", *Nature Communications* **5**, 3435, 2014.

[4] H. B. G. Casimir, "Note on the Conduction of Heat in Crystals", *Physica* **5**, 6, 495, 1938.

[5] I. J. Maasilta, "Two-dimensional phononic thermal conductance in thin membranes in the Casimir limit", *AIP Advances*, **1**, 041704, 2011.

[6] W. H. Press, B. P. Flannery, S. A. Teukolsky, and W. T. Vetterling, *Numerical Recipes*, 2nd edition, Cambridge University Press, Cambridge, 1992.

[7] K. F. Graff, *Wave Motion in Elastic Solid*, Dover Publications, New York, 1991.

Interfacial heat transport in liquids and nanobubble dynamics

Samy MERABIA[a*], Julien LOMBARD, Thierry BIBEN, Ali ALKURDI

[a]*Université de Lyon, CNRS, UCBL, ILM, UMR5306, F-69621, Villeurbanne, France*

**corresponding author: samy.merabia@univ-lyon1.fr*

Keywords: interfacial thermal resistance, nanoparticles, nanobubbles, liquids

Our understanding of heat transport in liquids is only partial. Standard textbooks generally mention the Green-Kubo formula for the thermal conductivity of fluids, which is widely used from a computational point of view, but which has a limited predictability for liquids. The main reason is partly ascribed to the lack of long-range order, which precludes the classical description in terms of phonons, i.e. collective propagative excitations. For the same reasons, our understanding of heat transport in the vicinity of solid/liquid interfaces is also partial. Thermal boundary resistance at liquid/solid interfaces has been probed experimentally [1] and from numerical simulations [2] during the years 2000. The common conclusion of this body of work is that the thermal resistance displayed by a liquid/solid interface takes values which are not different from a solid/solid interface.

Apart from the fundamental point of view understanding heat transport in liquids, and especially in the vicinity of solid/liquid interfaces may have important biomedical applications. With the advent of nanoplasmonics, metallic nanoparticles may be heated up by a laser pulse, and used as nano-heat sources creating very large temperature gradients in a liquid environment. In turn, such large temperature gradients may be used in hyperthermia, and to induce pressure waves propagating in the liquid phase. If the energy supplied by the laser is high enough, vaporization may be driven by the nanoparticles generating nanobubbles that may grow and expand in the liquid. These nanobubbles have been experimentally shown to be efficient in cancer cell therapy, as they concentrate large amounts of thermomechanical stresses that may be used to destruct diseased genetic material [3]. Despite their promising use, the fundamental description of the mechanisms at the origin of boiling under the extremely large temperature gradients is still missing. Under this situation, the thermal boundary resistance and the very large Laplace pressure created by the strong curvature of the interface, should compete to delay boiling. From the experimental point of view, our knowledge of nanobubble formation is still highly controversial: some studies conclude that nanobubble generation matches the crossing of the spinodal of the fluid in the vicinity of the nanoparticle [4], other studies report an energy threshold one order of magnitude higher, the difference being attributed to the huge Laplace pressure that should be overcome at the submicronic scale [3]. Theoretical modeling of the process at the origin of boiling around heated nanoparticles, is thus highly desired to understand the basics of liquid phase change under very large temperature gradients.

In this contribution, we study theoretically heat transport in liquids with an emphasis in nanobubble dynamics. The objective is twofold: first trying to understand which are the vibrational modes at the origin of the thermal boundary resistance between solid and liquid. Second, we aim at a theoretical description of energy transfer in the vicinity of strongly heated nanoparticles in water, in situations of local boiling.

First, we discuss a viscoelastic model to predict the value of the thermal boundary resistance at the interface between liquid water and solid. The model is a generalization of the acoustic model of Prasher, which accounts for the finite bonding strength between two materials [5]. We generalize this model through two aspects: first, we differentiate the longitudinal and transverse polarizations, and more importantly we account for the viscoelastic properties of the liquid at high frequencies (Thz). We unveil the important role of the high frequency viscoelastic properties of liquids. In particular, we show that acoustic models which do not account for the viscoelastic character of high frequency vibrations in liquids underpredict the thermal boundary conductance by one order of magnitude [6]. On the other hand, a viscoelastic generalization of the acoustic model may provide a good description of the experimental and simulation data available [6].

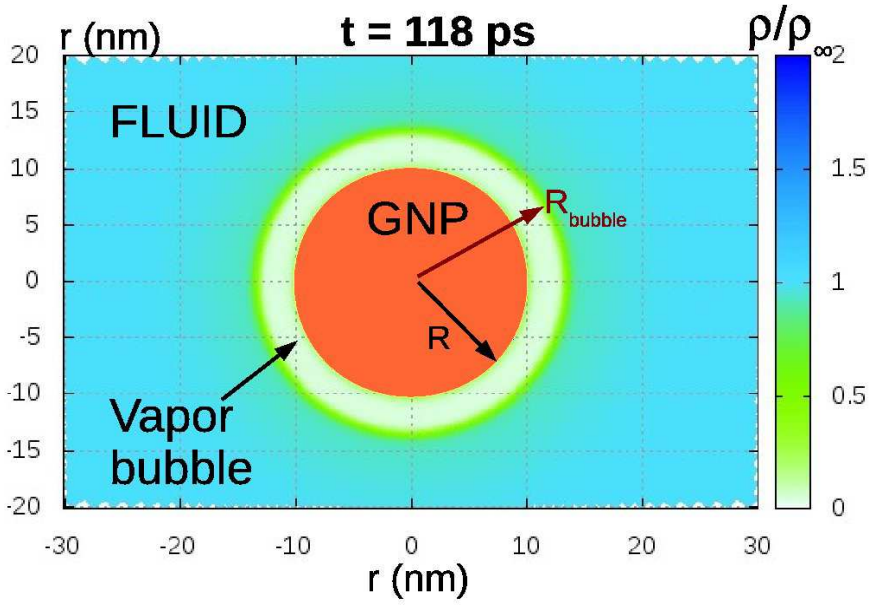

Figure 1: sketch of the system simulated: a hot gold nanoparticle surrounded by a vapor bubble expanding in liquid water.

Second, we will model nanobubble generation driven by heat transfer from heated gold nanoparticles in water [7]. Because the relevant length scales may be micronic, we model this situation using a mesoscopic model which accounts for the thermodynamics of liquid water, and the capillary effects through a free energy density functional coupled with hydrodynamic-like equations. We show that nanobubble generation corresponds to the crossing of the spinodal in the liquid at a distance 1-2 nm from the hot nanoparticle. Capillary effects are shown to have a minor effect in the value of the energy threshold for boiling. Comparison with experimental data conclude that nanoparticle melting should proceed before the onset of vaporization. This is explained by the separation of time scales: melting times being shorter than heating of the fluid which in turn is shorter than nanoparticle recrystallization. We unveil the critical role played by the thermal boundary resistance at the nanoparticle interface: close to the vaporization threshold the thermal boundary resistance significantly delays vaporization, thus allowing heat to be transferred to the fluid. offering optimal conditions for the energy conversion between the energy supplied by the laser and the mechanical work (pressure) necessary for the nanobubble growth [7]. Beyond the threshold the dynamics of the nanobubble is found to be asymmetrical, the growth being described by an adiabatic process while the collapse is consistent with an isothermal evolution of the vapor inside the bubble. This scenario is confirmed by a Rayleigh-Plesset analysis of the bubble dynamics showing that even though the bubble is generated under very large temperature gradients, a bulk-like analysis provides a good description of the simulation data. The same analysis allows to understand the competition between the different terms in the momentum

conservation equations, and conclude that the very large Laplace pressures due to the strong curvature of the bubble are indeed counterbalanced by viscous stresses. Because of these viscous stresses, the internal pressure inside the bubble quickly relaxes until thermal conduction has been allowed to set in and compete with compression forces to make the bubble collapse isothermal.

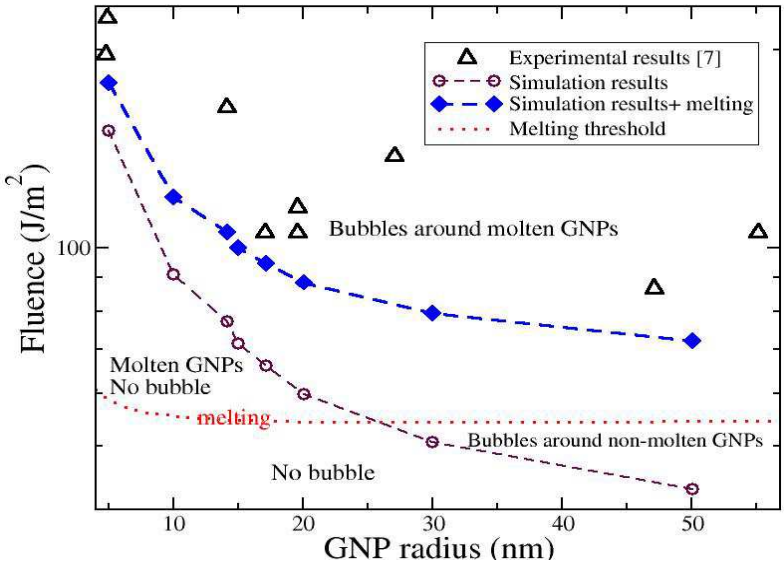

Figure 2: Minimal energy required to drive vaporization as a function of the nanoparticle radius. Dashed lines: simulation without and with particle melting; Open triangles: experimental data from [4].

We also highlight the major role played by the nature of the energy transport inside the bubble [8]. Energy transport inside the bubble no longer obeys Fourier's law, as the dimensions of the nanobubble becomes smaller than the mean free path of the gas molecules. Rather, heat is transported through ballistic transport of the molecules from the hot nanoparticle to the nanobubble/liquid interface, in a manner which is similar to a Knudsen layer. Depending on the duration of the laser pulse, ballistic transport inside the bubble may control the maximal volume of the nanobubble, a quantity of prime importance for biomedical applications. Simulations show that with a nanosecond pulse, ballistic heat transport inside the bubble may enhance the maximal volume of the bubble by a factor eight, as compared to the case of ultrashort pulse durations. We also discuss the relevance of ballistic heat transport in interpreting the experimental data regarding the maximum size of the bubbles.

Finally, we will compare the performance of silica-gold core shell nanoparticles in driving vaporization [9]. We conclude that core silica-gold shell nanoparticles display energy thresholds for vaporization almost one order of magnitude lower than the inverted configuration-gold core silica shell, and depending on the nanoparticle size, can be even more efficient in driving vaporization than bare gold nanoparticles.

References

[1] Z.B. Ge, D.G. Cahill and P.V. Braun, *Phys. Rev. Lett.*, **96** 186101, 2006.

[2] N. Shenogina, R. Godawat, P. Keblinski, S. Garde, *Phys. Rev. Lett.* **102**, 156101, 2009.

[3] E. Lukianova-Hleb, Y. Hu, L. Latterini, L. Tarpani, S. Lee, R.A. Drezek, J.H. Hafner, D.O. Lapotko, *ACS Nano* **4**, 21092123, 2010.

[4] A. Siems, S.A.L. Weber, J. Boneberg and A. Plech, *New J. Phys.* **13**, 043018, 2011.

[5] R. Prasher, *App. Phys. Lett.*, **94** 041905, 2009.

[6] S. Merabia, J. Lombard and A. Alkurdi, submitted (2014)

[7] J. Lombard, T. Biben, S. Merabia, *Phys. Rev. Lett.* **112**, 106701, 2014.

[8] J. Lombard, T. Biben, S. Merabia, in preparation (2014)

[9] J. Lombard, F. Detcheverry, S. Merabia, submitted (2014)

Thermal conductivity of modulated nanowires

Konstantinos TERMENTZIDIS* and David LACROIX

[a] *CNRS, Université de Lorraine, LEMTA, UMR7563, F-545006, Vandoeuvre les Nancy, France*

**corresponding author: konstantinos.termentzidis@univ-lorraine.fr*

Keywords: modulated nanowires, Si, SiC, Bi_2Te_3, molecular dynamics, thermal conductivity, phonon density of states.

Advances in nanofabrication technologies have made easier the elaboration of nanostructures and nanostructured materials. Their applications in molecular electronics, quantum computers, actuators, sensors, and molecular machines are rapidly spreading, electronics, photonics, biomedical, and energy harvesting devices [1]. Their novel functions involve unique mechanical, thermal, and electronic properties. Concerning thermoelectric devices, modulated nanowires exhibit better thermoelectric efficiency than pristine constant diameter nanowires and much better compared to bulk materials [2]. This is mainly due to the reduction of the thermal conductivity in nanostructured materials.

The parameters that reduce the thermal conductivity are: defects (impurities, doping, stoichiometry), geometric modulation (diameter modulation, kink nanowires), structural polytypism (fcc, hcp, stuck default interfaces), roughness of interfaces and free surfaces, amorphisation (core/shell nanowires). The main reasons for the reduction of the thermal transport are: spatial confinement of acoustic phonons, increase of the scattering processes between phonons and scattering centers (doping, rough interfaces, surfaces) or changes in the phonon group velocity and density of states (DOS).

In this communication, we shall show the effect on the thermal conductivity of a series of modulated nanowires, calculated with Molecular Dynamics:

- diameter and structure lattice modulation of SiC nanowires (figure-1),
- diameter and core/shell modulated Si and Ge nanowires (figure-2).

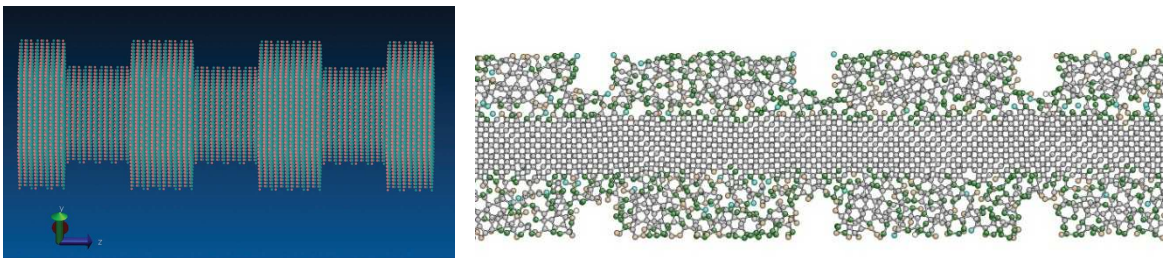

Figure 1: Left: diameter modulated SiC nanowires [3]. Right: cross-section of a diameter modulated crystalline core/ amorphous shell Si nanowires [4].

In all cases the thermal conductivity reduces considerably by a factor of 10 compared to the thermal conductivity of pristine constant diameter nanowires, or by three orders of magnitude compared to the thermal conductivity of their bulk materials. For the first case of SiC modulated nanowires, the reduction of the thermal conductivity is due to the additional free surfaces, the thermal interfacial resistance, the confinement of the phonon modes. For the case of Si or Ge core/shell nanowires, the above arguments are always valid and with the amorphous phases one can add extra scattering

mechanisms for phonons. Analyzing the vibrational density of states, we proved that the phonons feel the crystalline/amorphous interfaces effects much greater than they are. We modeled smooth interfaces [5], but as it can be seen in figure 2 [6], the density of states of the atoms in a distance of 0.5 nm away from the interface at the crystalline phase area is the same as the density of states of the bulk amorphous phase.

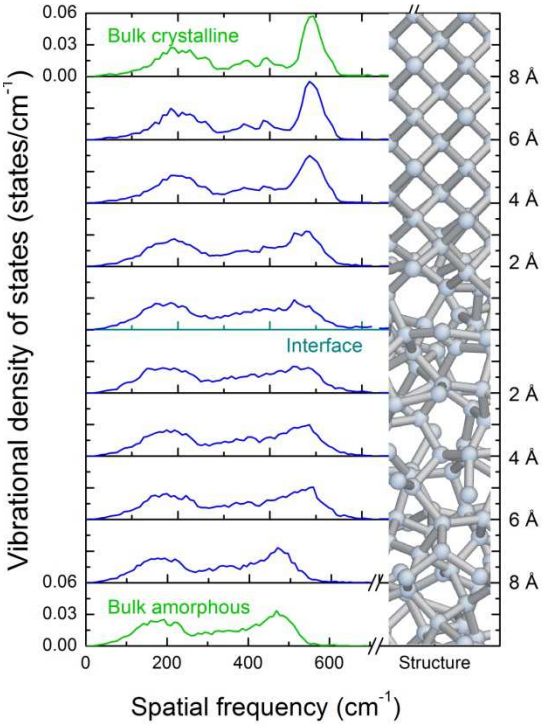

Figure 2: Vibrational density of states for groups of atoms close to the amorphous/crystalline interface.

References

[1] D Srivastava, M. A. Makeev, M. Menon and M. Osman, "Computational nanomechanics and thermal transport in nanotubes and nanowires", *J. Nanosci. Nanotechnol.* **8**, 3628, 2008.

[2] X. Zianni and P. Chantrenne, "Disorder-induced enhancement of the thermoelectric efficiency in diameter-modulated nanowires", *Microelectronic Engineering.* **112**, 235, 2013.

[3] K. Termentzidis *et al.*, "Disorder-induced enhancement of the thermoelectric efficiency in diameter-modulated nanowires", *Physical Review B*, **87**, 125410, 2013.

[4] E. Blandre, L. Chaput, S. Merabia, D. Lacroix and K. Termentzidis, "Important reduction of the thermal conductivity of modulated core/shell silicon nanowires", *in preparation*, 2014.

[5] A. France-Lanord, E. Blandre, S. Merabia,T. Albaret, D. Lacroix and K. Termentzidis, "Atomistic amorphous/crystalline interface modeling for superlattices and core/shell nanowires", *J. Physics, Condensed Matter*, **26,** 055011, 2014.

[6] A. France-Lanord, S. Merabia,T. Albaret, D. Lacroix and K. Termentzidis, "Thermal properties of amorphous/crystalline silicon superlattices ", *J. Physics, Condensed Matter*, **26,** 355801, 2014.

A comparative study of the anharmonicity of the transverse optical phonons in lead chalcogenides

Jawaher AL-OTAIBI* and G.P. SRIVASTAVA

School of Physics, University of Exeter, Exeter EX4 4QL, UK

**corresponding author: jma213@exeter.ac.uk*

Keywords: Anharmonicity, transverse optical phonons, heat transport, theory, Pb chalcogenides.

We have made a comparative theoretical study of the anharmonic relaxation rate of the low-lying transverse optical (TO) phonons in lead chalcogenides. We find that these phonons contribute in the range of 15%-20% towards the total lattice thermal conductivity of these materials.

Lead chalcogenides are important thermoelectric materials. These materials, PbTe, PbSe and PbS, are characterised by the presence of low-lying transverse optical (TO) phonons with speeds comparable to that of the transverse acoustic (TA) branches [1]. Therefore, when accounting for anharmonic interactions, the role of optical phonons (in particular the TO phonons) must be considered with the same degree of attention as the acoustic phonons.

In order to examine the anharmonic relaxation rate of the TO phonons we have applied an isotropic continuum model for the dispersion curves of acoustic as well as optical phonons, an isotropic continuum model for the cubic crystal potential, and first-order perturbation theory, by extending a previous work [2,3]. Expecting the three-phonon processes to adequately describe anharmonic interactions for acoustic as well as optical phonons, we modified the expressions in [2] for the relaxation rates for a phonon mode qs undergoing Normal (N) and Umklapp (U) three-phonon processes of class 1 type ($\vec{q}\,s+\vec{q}'\,s'\rightarrow\vec{q}''\,s''$) and class 2 type ($\vec{q}\,s\rightarrow\vec{q}'\,s'+\vec{q}''\,s''$).

In order to compute results we have used the material parameters available in the literature. The Grüneisen constant is taken as 0.8 for PbTe and PbSe and 1.6 for PbS. Although it is known that the Grüneisen constant is mode dependent, being much higher for TO than the other modes, we have considered a single mode average parameter. Figure 1 shows the room-temperature results for the anharmonic relaxation rate τ_{TO}^{-1} for TO phonons. The total optical phonons anharmonic relaxation rates in PbTe shows a quadratic frequency dependence at the low frequencies range. This result is also identified by Tian *et al*. [4]. In the long wavelength regime (small phonon wave vectors) we find that the TO relaxation rate is the highest for PbS. In the short wavelength regime (towards the Debye sphere) the relaxation rates for PbTe and PbS are similar, but the TO phonons are comparatively much longer lived in PbSe. In Fig. 2 we have presented the scattering rate of the TO phonons undergoing allowed three-phonon processes. The largest scattering rate for long wavelength TO phonons comes via the Normal (N) process TO+TA → TO (N) for PbS. The largest scattering rate of short wavelength TO phonons is contributed by the process TO + TA → LO (N) in PbTe.

We find, using the single-mode relaxation time theory developed for acoustic as well as optical phonons in [3], that for PbTe and PbSe the contribution of TO phonons is 20% of the total lattice conductivity at room temperature, while for PbS the percentage is about 15%, as shown in Fig. 3. The lattice thermal conductivity results we obtained for PbTe agree with the ab initio study performed by

Tian *et al*. [4], including the importance of the optical phonons in conducting heat in this material. In this work, we find that at high temperatures, the contribution of the TO phonons is comparable to that of the TA phonons for all the three materials. In addition, the TO branch contribution is the highest for PbTe and the lowest for PbS. This has been identified to result from the combined effect of anharmonic and impurity scatterings of TO phonons in these materials – the impurity scattering being the strongest for PbS, due to higher impurity concentration and broader TO frequency spectrum. At low temperatures, there is a significantly smaller conductivity contribution from the TO phonons, as these can be expected to be less occupied.

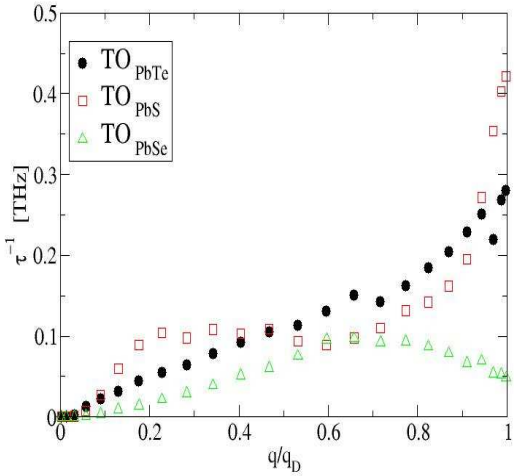

Figure 1: Anharmonic scattering rate of TO phonons at T= 300 K for PbTe, PbSe and PbS. Here q is phonon wavenumber and q_D is the Debye radius.

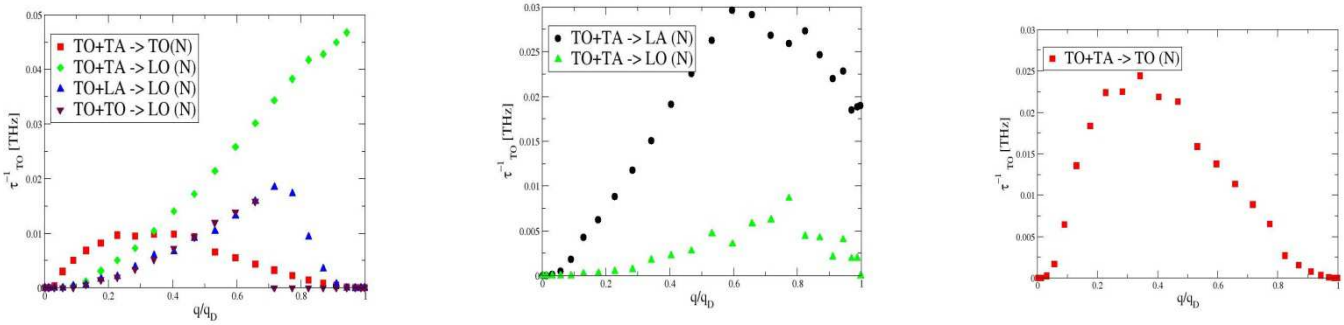

Figure 2: Frequency dependence of the important anharmonic scattering processes for TO phonons at room temperature: (a) PbTe, (b) PbSe and (c) PbS.

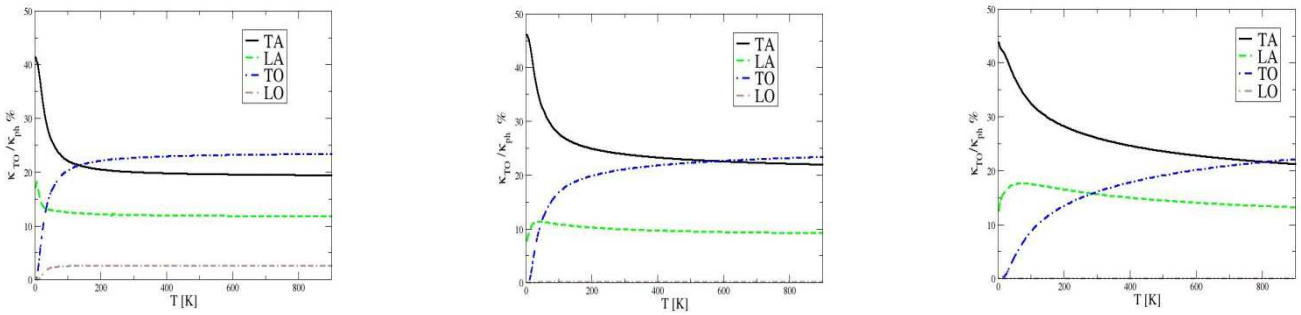

Figure 3: Percentage contribution of TO phonons towards the thermal conductivity in (a) PbTe, (b) PbSe and (c) PbS.

References

[1] B. Kress, Phonon Dispersion Relations in Insulators (Springer Series in Solid state Sciences, 1979).

[2] G. P. Srivastava, The Physics of Phonons (Taylor and Francis Group, 1990).

[3] J. Alotaibi and G. P. Srivastava, *J. Appl. Phys.* **116,** 043702, 2014.

[4] Z. Tian, J. Garg, K. Esfarjani, T. Shiga, J. Shiomi, and G. Chen, *Phys. Rev. B* **85**, 184303, 2012.

Session 5

Constrictions and wires

Phonon transport through constrictions in silicon nanowires

Valentin JEAN[a], Konstantinos TERMENTZIDIS[a], Sebastien FUMERON[a] and David LACROIX[a*]

[a]*Université de Lorraine, LEMTA, CNRS, UMR7563, F-54506, Vandœuvre les Nancy , France*

**corresponding author: david.lacroix@univ-lorraine.fr*

Keywords: phonon heat transport, constriction, nanowires, Monte Carlo simulation

Heat transport in nanostructures has become a well-established research domain that addresses several applicative fields like microelectronics, energy efficiency, innovative materials, biophysics, etc. Besides, it is now commonly accepted that heat transport properties in low dimensional materials are no longer the ones of the bulk state and they depend among other parameters on the geometry at the microscopic scale. For example, nano-devices like superlattices, thin films, nanotubes and nanowires exhibit outstanding phononic and electronic properties that can be used for a plethora of applications. So far, the tailoring of these properties by nanostructuration techniques is a quite new subject. In this study, we focus on nano-constriction effect on the thermal transport properties of individual silicon nanowires. The purpose of our work is to appraise the thermal conductance *G* in these constrictions and to predict the variations of the overall thermal conductivity *k* in silicon nanowires. We will demonstrate that the shape of the constriction as well as its magnitude can significantly alter the latter thermal properties through the modification of the phonon mean free path (MFP) in the considered nanostructures [1,2]. All the thermal properties are derived from the resolution of the Boltzmann transport equation for phonons in the framework of the relaxation time approximation by Monte Carlo simulations.

A constriction within a nanostructure, as well as point contacts between two materials (for example AFM tip – sample) can be modeled by a more or less steep variation of the diameter of a cylindrical structure. As an example, Figure 1 depicts two different types of these constrictions.

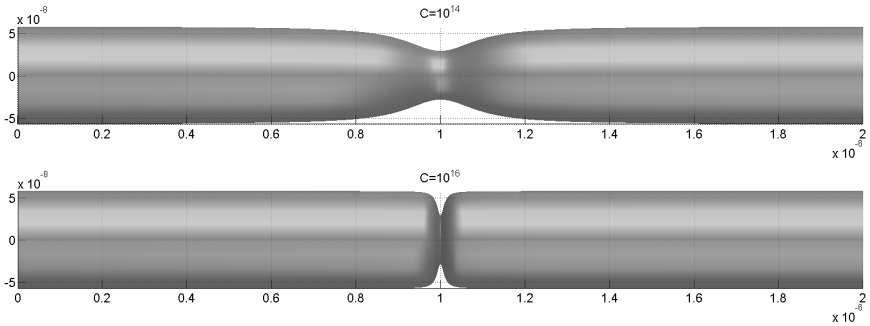

Figure 1: Modeling of smooth to steep constrictions in a nanowire, d_{max}=115nm, d_{min}=57.5nm, Lz = 2µm

The above constrictions were obtained assuming that the nanowire diameter follows the law given by:

$$d(z) = d_{max}\left[1 - \frac{(1-R_d)}{1+C(z-z_0)^2}\right] \;;\; \text{with } C \geq 10^{14}\ \text{m}^{-2} \text{ and } z_0 \geq 1\,\mu m \qquad (1)$$

Where d_{max} is the nanowire maximum diameter, R_d the diameter ratio $R_d = d_{min}/d_{max}$, z_0 the constriction localization along the *z* axis and *C* a constant that rules the stiffness of the constriction (typically in the range of 10^{14} to 10^{17} m^{-2}).

For these constricted nanowires a Monte Carlo simulation tool has been built in order to accurately depict the 3 phonon scattering processes as well as those related to boundary variations. It shall be noted that even if the global nanostructure MFP is reduced by constrictions and nanowire boundaries, 3-phonon processes need to be considered because their average MFP is in the same range as the geometric one. Furthermore, they are necessary to ensure restoration of the thermal equilibrium. In this framework, the model lies on a previously developed tool for Cartesian geometries [3] and includes recent improvements for phonon sampling [4] that allows better energy conservation and thus more accurate results. An illustration of what can be derived from such calculations is plotted in Figure 2 where heat fluxes, temperatures profiles and overall thermal conductivities (TC) of two different constricted nanowires (smooth and steep) are given and compared to a nanowire without constriction.

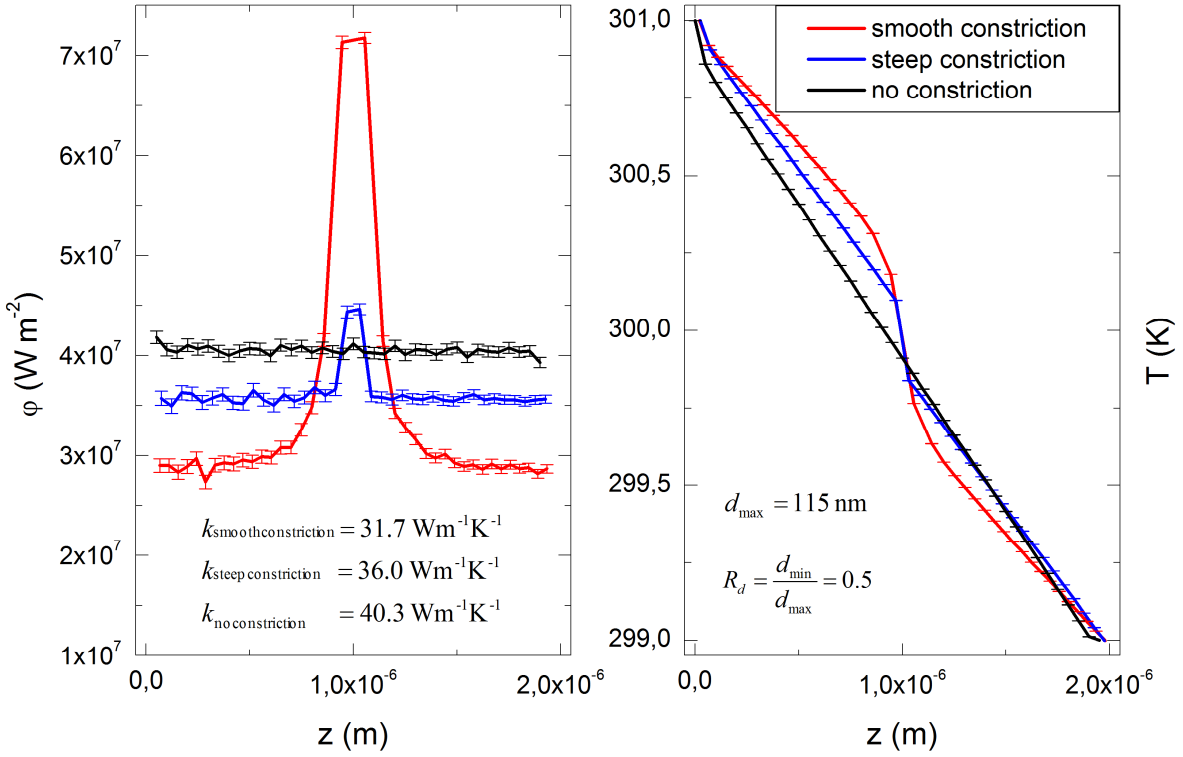

Figure 2: Heat fluxes (left) and temperature profiles (right) of smooth (red - $C=10^{14}m^{-2}$), steep (blue - $C=10^{16}m^{-2}$) constricted nanowire and of a nanowire without constriction (black) ; d_{max}=115nm, d_{min}=57.5nm, Lz =2µm

The comparison of these simulation data obviously pointed out the fact that the constriction shape notably modifies the nanowire thermal conductivity by the introduction of a new resistive process. In the case of a steep constriction, the TC is reduced when compared to the unconstricted nanowire because of the supplementary internal thermal resistance. This effect is even enhanced for smooth constriction. An explanation could be proposed considering the geometric MFP variations for steep and smooth constrictions. In the latter case, it is smaller because the nanowire diameter reduction is less localized and occurs on the larger portion of the nanowire length. Therefore, considering the kinetic theory model, MFP lowering induces TC lowering also. Besides, one can see that heat flux density φ, calculated along the nanowire axis z, increases in the vicinity of the constriction. In the present calculation, 40 cells have been considered. This is enough to have a reasonable description of the smooth constriction but it is a little bit unsatisfaying to address accurately the case of a steep (and narrow) constriction. For our calculations in order to ensure the stability of the Monte Carlo simulation, in a given configuration, each cell has the same volume. Thus, an accurate evaluation of

the maximum heat flux density requires more cells. In Figure 3, φ is plotted for the same constriction geometry with 40 and 180 cells. It can be observed that both plots are superimposed, but the maximum value in constriction neck increases for a finer spatial discretization. Yet, calculations of the heat flux Φ (namely φ × cross-section) within the structures leads to nearly a constant and equal value for the two meshes. This is confirmed by the extracted TC that are also very similar in both cases.

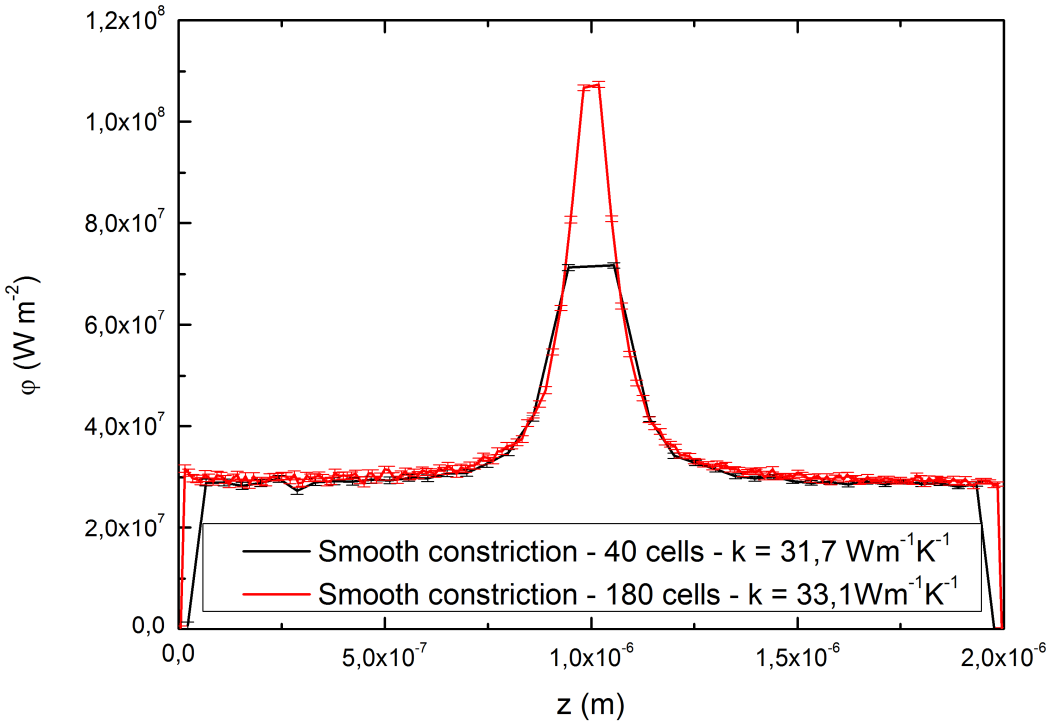

Figure 3: Heat fluxes and thermal conductivity of a smooth constricted nanowire for two spatial discretization (black - 40 cells) (red – 180 cells) ; d_{max}=115nm, d_{min}=57.5nm, Lz =2μm, C=$10^{14}m^{-2}$.

More details about the involved mechanisms and results for a broad range of constrictions will be given during the presentation of this study.

References

[1] R. Prasher, "Predicting the thermal resistance of nanosized constrictions", *Nano Letters*, **5** (11), 2155-2159, 2005.

[2] H. Fangohr, D. S. Chernyshenko, M. Franchin, T. Fischbacher and G. Meier, "Joule heating in nanowires", *Phys. Rev. B* **84**, 054437, 2011.

[3] D. Lacroix, K. Joulain, and D. Lemonnier, "Monte carlo transient phonon transport in silicon and germanium at nanoscales", *Phys. Rev. B* **72**, 064305, 2005.

[4] J.-P. M. Péraud and N. G. Hadjiconstantinou, "Efficient simulation of multidimensional phonon transport using energy-based variance-reduced monte carlo formulations", *Phys. Rev. B* **84**, 205331, 2011.

Heat transfer in modulated nanowires with variable thickness

Xanthippi ZIANNI

Dept. of Aircraft Technology, Technological Educational Institution of Sterea Ellada, 34400 Psachna, Greece

Dept. of Microelectronics, INN, NCSR 'Demokritos', 153 10 Athens, Greece

**corresponding author: xzianni@teihal.gr; xzianni@gmail.com*

Keywords: thermal conductivity, nanowires, transmission coefficient, transmissivity, nanoscale thermal energy conversion, thermoelectric efficiency

Low thermal conductivity is needed for limiting the parasitic heat flow and increase the efficiency of the thermal to electrical energy conversion. Nanowires have been proposed as efficient thermoelectric materials because their thermal conductivity decreases significantly when their width decreases. Very thin wires are, however, not easy to fabricate and their electrical conductivity is poor. As an alternative, it has been proposed to use diameter-modulated nanowires [1]. A schematic representation of a nanowire with variable thickness is shown in Figure 1. Current state of the art of the fabrication technology allows for the realization of modulated nanowires with control on the modulation morphology. For instance, an entirely bottom-up method has been developed to modulate nanowire shape along the growth axis with sub-10 nm spatial resolution [2].

In modulated nanowires, the transport properties of electrons and phonons are modified. In the case of electrons this can be attributed to the modified energy states [1,3]. For phonons, the modified thermal conductivity has been studied in two transport regimes: (i) in the ballistic regime where phonons are treated as waves, and (ii) in the diffusive transport regime where phonons are treated as particles. Here, we discuss the thermal conductvity of nanowires with variable thickness in the two regimes.

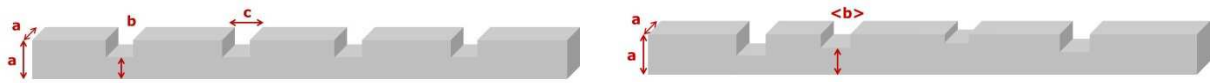

Figure 1: Schematics of modulated nanowires with variable thickness

In the ballistic transport regime, the phonon mean free path is big compared with the characteristic dimensions of the nanosctructure and scattering effects can be neglected. This is valid at low temperatures. Phonons behave like waves and the thermal conductivity is determined by the transmission probability of the phonon modes

$$\kappa = \frac{\hbar^2}{k_B T^2} \sum_m \frac{1}{2\pi} \int_{\omega_m}^{\infty} T_m(\omega) \frac{\omega^2 e^{\hbar\omega/k_B T}}{\left(e^{\hbar\omega/k_B T} - 1\right)^2} d\omega \qquad (1)$$

where ω_m is the cut-off frequency of the mth mode and $T_m(\omega)$ is the transmission coefficient for each phonon mode and phonon frequency ω. The integration is over the frequency of the modes m propagating in the structure.

In perfect nanowires, phonons occupy one-dimensional subbands and the transmission coefficient has a staircase structure (Figure 2). In modulated nanowires, the transmission coefficient of the phonon modes deviate from the stair-case structure [4]. All phonon modes have now a lower transmission probability as it can be seen in Figure 2. This explains the reduced thermal conductivities shown in Figure 3, with respect to the universal value $\kappa_o = \pi^2 k_B^2 / 3h$. The transmission coefficient depends on the modulation profile, as it is shown in Figure 2 for 1 and 5 width modulation segments. It has been found that the thermal conductance shows a corresponding dependence upon the modulation profile (Figure 3). It is thereby indicated that in this regime, the thermal conductivity can be controlled by engineering the transmission coefficient of the modulated nanowire through designing of the modulation geometry.

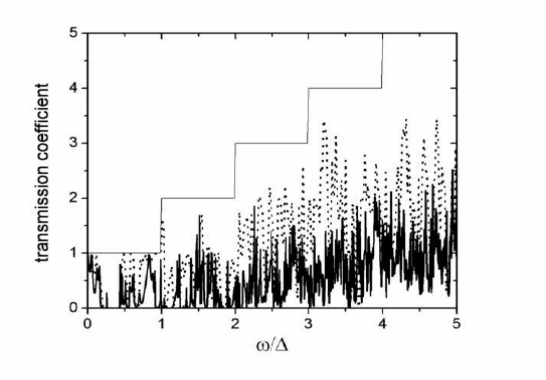

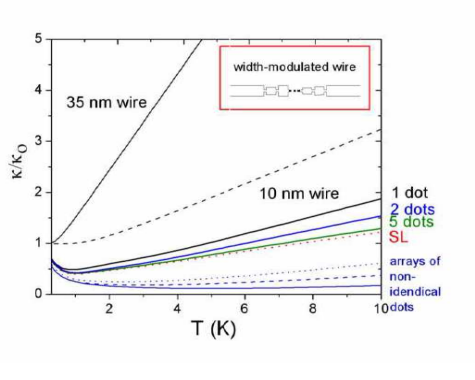

Figure 2: The transmission coefficient versus the reduced phonon frequency for a straight wire (upper solid curve), for a wire modulated by 1 segment (dotted curve) and by 5 segment (lower solid curve).

Figure 3 : The reduced thermal conductance versus temperature for straight nanowires and for wires modulated by arrays of identical dots and by arrays of non-identical dots.

In thicker nanowires, the phonon energy subband spectrum is denser and eventually turns to a continuum for thick nanowires. Moreover, the phonon mean free path is smaller than the nanowire characteristic dimensions and scattering dominates the phonon transport. Phonons can be treated like particles and the thermal conductivity κ can be calculated semiclassically using the relaxation time approximation:

$$\kappa = \sum_k \sum_p C(k,p) v^2(k,p) \tau(k,p) \cos^2(\theta) \qquad (2)$$

where k is the phonon wavevector, p is the polarization, v is the group velocity determined by the dispersion curves: $v(k,p)=d\omega(k,p)/dk$, ω is the phonon frequency, $\tau(k,p)$ is the phonon relaxation time due to scattering, θ is the angle between the wavevector and the direction of the wire, and $C(k,p)$ is the specific heat per unit volume.

We have studied the phonon thermal conductivity of modulated nanowires within the kinetic theory [5]. Boundary scattering was included using a geometrical mean free path. In addition, the modification of the phonon transmissivity in modulated nanowires was taken into account. A very significant decrease of the thermal conductivity with increasing nanowire width modulation (Figure 4)

was found. The decrease was found to be more significant in thicker nanowires. This behavior has been confirmed by systematic phonon Monte Carlo simulations on the thermal conductivity of width-modulated nanowires [6]. Our simulations indicated that width-modulated nanowires that are relatively thick and operate in the boundary scattering regime could be used to tune the thermal conductivity. It has been indicated the possibility for heat flow control by designing the width-modulation without strict limitations for the modulation profile. This is enabled by the identified scaling behavior: the reduction of the thermal conductivity scales with the transmissivity that is entirely determined by the modulation geometry irrespectively of the material choice (Figure 5).

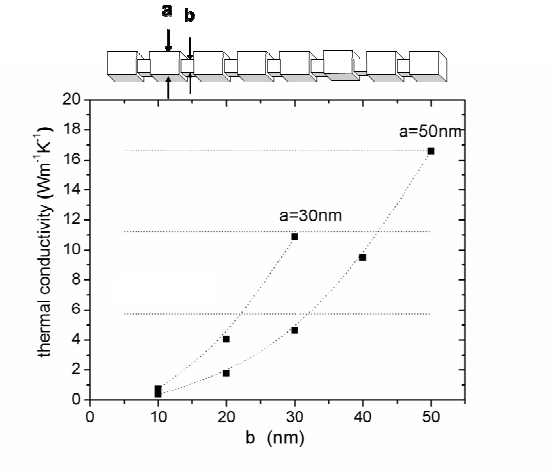

Figure 4: Thermal conductivity of Si modulated Si nanowires with wide parts width a = 30 nm and 50 nm versus the width of the narrow parts, at T = 300 K. The horizontal lines are for nanowires with constant width of 50 nm, 30 nm, and 10 nm.

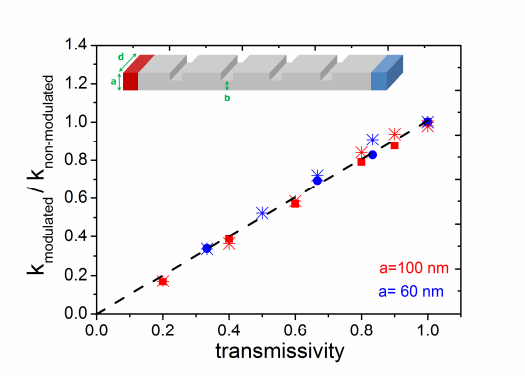

Figure 5: The ratio of the thermal conductivity of the periodically modulated nanowire over the thermal conductivity of the non-modulated nanowire versus the transmissivity for two modulated Si nanowires with a = d, and a = 100 nm (red squares) and a=60 nm (blue dots) versus the constriction width b.

We have performed Monte Carlo simulations for Si nanowires. The numerical technique can be applied to several materials where the phonon contribution dominates the thermal conductivity. The obtained scaling behavior of the thermal conductivity with the modulation geometry should also hold for these materials. Our work indicates that a wide range of materials can be suitable for efficient nanoscale heat management by designing the nanostructure width modulation.

Acknowledgment

Funding by the European Social Fund (ESF)-European Unions and National Resources within the framework of the Grant of Excellence “ARISTEIA” is acknowledged.

References

[1] X. Zianni, “Diameter-modulated nanowires as candidates for high thermoelectric energy conversion efficiency”, *Applied Physics Letters* **97** 233106, 2010.

[2] J.D. Christensen, C.W. Pinion, E.M. Grumstrup, J.M. Papanikolas, J.F. Cahoon, “Synthetically encoding 10 nm morphology in Silicon nanowires”, *Nano Letters* **13** 6281, 2013.

[3] X. Zianni, 'Band structure engineering in geometry-modulated nanostructures for thermoelectric efficiency enhancement', *Journal of Electronic Materials* DOI : 10.1007/s11664-014-3125-2, 2014.

[4] X. Zianni, **'**The effect of the modulation shape in the ballistic thermal conductance of modulated nanowires', *Journal of Solid State Chemistry* **193** 53, 2012.

[5] X. Zianni, P. Chantrenne, 'Thermal conductivity of diameter-modulated nanowires within a frequency-dependent model for the phonon boundary scattering', *Journal of Electronic Materials* **42** 1509, 2013.

[6] X. Zianni, V. Jean, K. Termentzidis and D. Lacroix, unpublished.

Phonon transport in silicon nanowires using a full-band Monte Carlo approach

Jérôme LARROQUE[a*], Jérôme SAINT-MARTIN[a] and Philippe DOLLFUS[a]

[a]*Institut d'Electronique Fondamentale, UMR CNRS 8622, Université Paris-Sud, Orsay, France*

**corresponding author: jerome.larroque@u-psud.fr*

Keywords: computational sciences, phonon heat transport, Monte Carlo algorithm, nanowires.

A Monte Carlo (MC) method to simulate phonon transport in silicon or germanium nanowires is presented. With an MC algorithm, phonon trajectories are described individually and it is possible to simulate out-of-equilibrium systems and transient regimes. The specificity of our simulator is to take into account the anisotropy of the phonon dispersion.

The phonon dispersion is obtained from 3D spline interpolation of a numerical calculation. The reciprocal space is cut in cubes. In each cube, the angular frequency depends on the 3 components of the wave vector $\vec{q}$ according to the equation (1). In each cube, the eight coefficients ω_0, v_{0x}, v_{0y}, v_{0z}, a_{0x}, a_{0y}, a_{0z} and b_0 are calculated to satisfy the continuity criterion at the eight vertices.

$$\omega(\vec{q}) = \omega_0 + v_{0x}q_x + v_{0y}q_y + v_{0z}q_z + a_{0x}q_yq_z + a_{0y}q_xq_z + a_{0z}q_xq_y + b_0q_xq_yq_z \quad (1)$$

The values of angular frequency on each knot are estimated within a semi-empirical method, the Adiabatic Bond Charge Model (ABCM) [1]. This method uses only four adjustable parameters and it allows obtaining an error lower than 2% with respect to experimental data in silicon from [2].

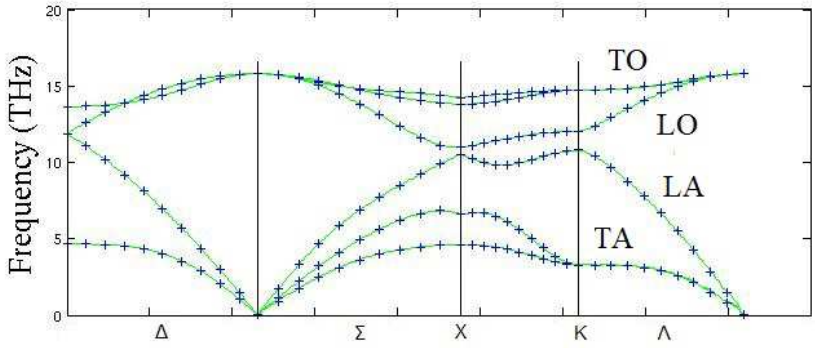

Figure 1: Phonon dispersion in silicon. The solid lines represent the 3D linear spline interpolation. The crosses represent the values obtained with the ABCM [1].

In this work, one eighth of the Brillouin zone (for $q_x > 0$, $q_y > 0$ and $q_z > 0$) is divided in 16×16×16 cubes. The figure 1 shows the dispersion obtained with the spline interpolation on the knots of the cubes compared with the values obtained with the ABCM. The advantages of this kind of interpolation are the continuity of the dispersion and its ease of use. The current MC algorithm does not simulate optical modes because their low group velocity makes their contribution to the thermal transport negligible.

The figure 2 presents the cross-sections of the three acoustic modes used in the MC algorithm. It should be noted that the wave vector q_x and the group velocity $\vec{v} = \vec{\nabla}_q \omega$ are not usually collinear. This fact is not taken into account in the common isotropic approximation of the dispersion [3-4].

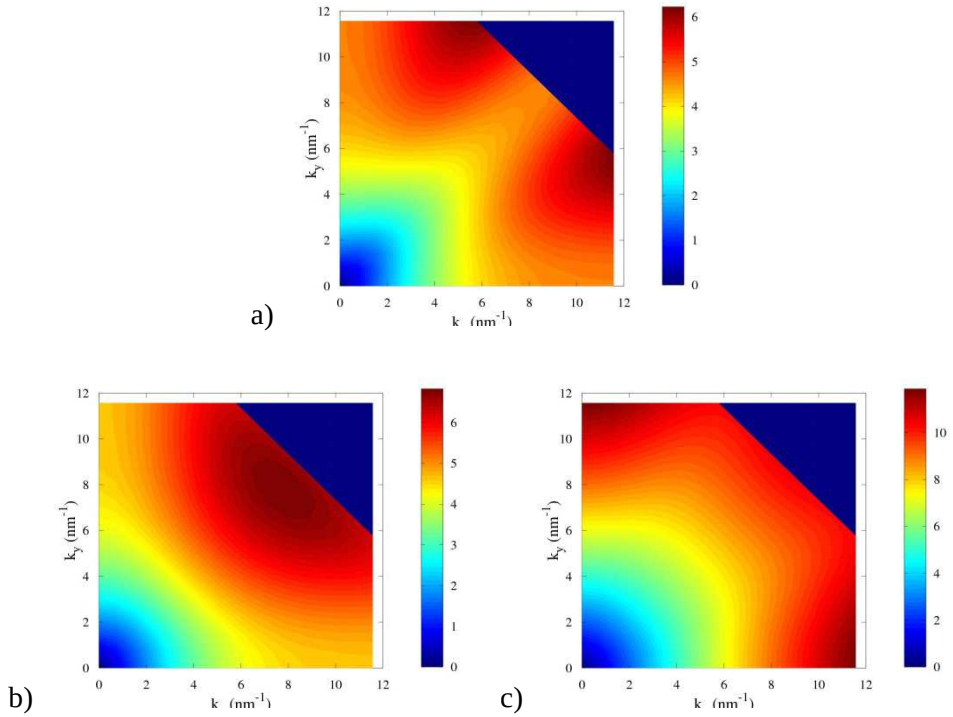

<u>Figure 2:</u> Cross-section of phonon dispersion for q_z=0. The color bar is the frequency in THz. a) first transverse acoustic mode, b) second transverse acoustic mode and c) longitudinal acoustic mode.

In our MC algorithm, the Brillouin zone is cut in 64×64×64 cubes. The initial distribution of phonons in the cubes is the Bose-Einstein distribution. The phonons are randomly chosen to obtain this distribution. Then the phonons move one by one, time step after time step as described in the figure 3.

The scattering processes are computed within the relaxation time approximation proposed in [3]. The free flight duration is randomly chosen within an exponential distribution. The expression of relaxation time is given in [4]. When an interaction occurs the phonon disappears and a new phonon is randomly chosen according to the distribution of eq. (2), where T is the temperature, τ is the relaxation time, f_{BE} is the Bose-Einstein distribution and n is the cube index. This modified distribution is needed to balance creation and destruction mechanisms.

$$F_r(n,T) = \frac{\sum_{i=1}^{n} f_{BE}(i,T) \times \tau^{-1}(i,T)}{\sum_{i=1}^{N} f_{BE}(i,T) \times \tau^{-1}(i,T)} \qquad (2)$$

The spectrum of phonons after the initialization step is plotted in figure 3. It reproduces well the theoretical spectrum obtained by multiplying the ABCM Density Of State (DOS) and the Bose-Einstein distribution.

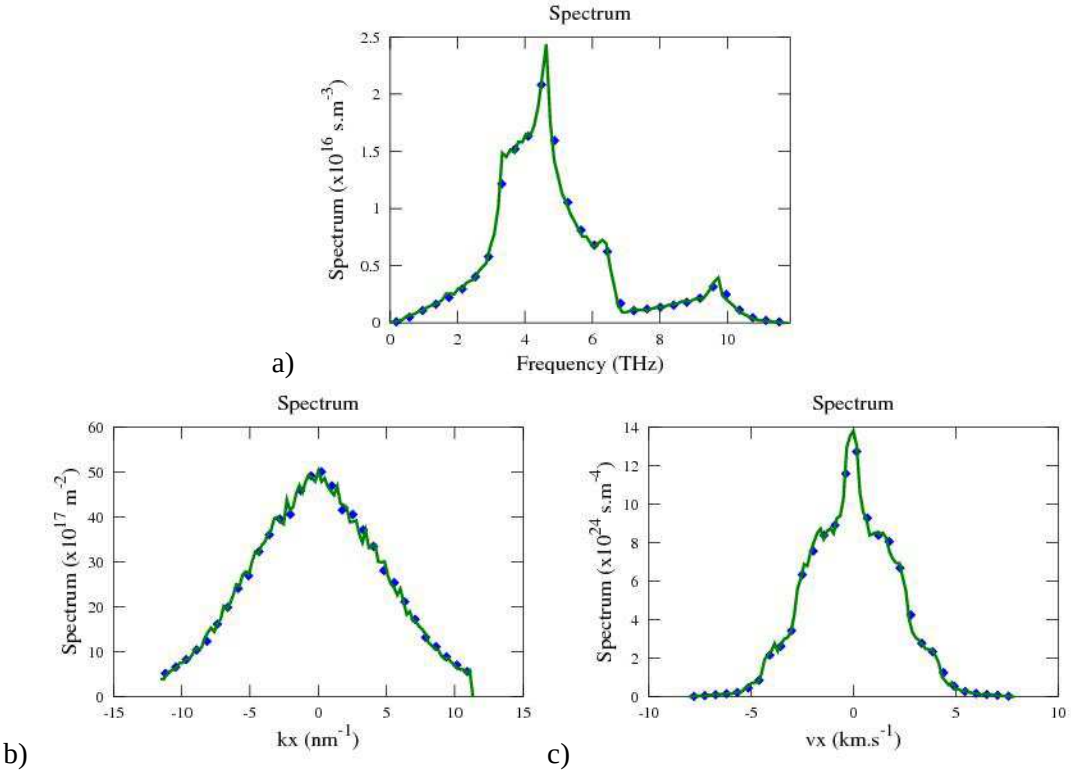

Figure 3: Phonon distributions at 300K. a) frequency distribution, b) wave vector distribution and c)velocity distribution along the transport direction. Blue diamonds are the product of DOS and Bose-Einstein distribution. Green solid line is the distribution of simulated phonons in the MC algorithm.

The figure 4 shows the spectrum for an out-of-equilibrium device. All phonons which go to the right come directly from the hot source (400K) but some of them have a wave vector with a negative contribution along the transport direction. It is because the frequency decreases along q_x in a part of the Brillouin zone as shown in the figure 2. This phenomenon does not appear with the common isotropic approximation of the dispersion.

The full band MC algorithm is able to simulate equilibrium and out-of-equilibrium regimes. A possible evolution is to add non-specular surface and heterogeneous interface.

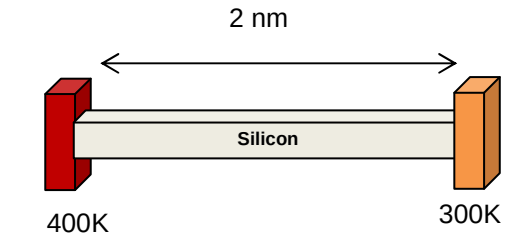

a)

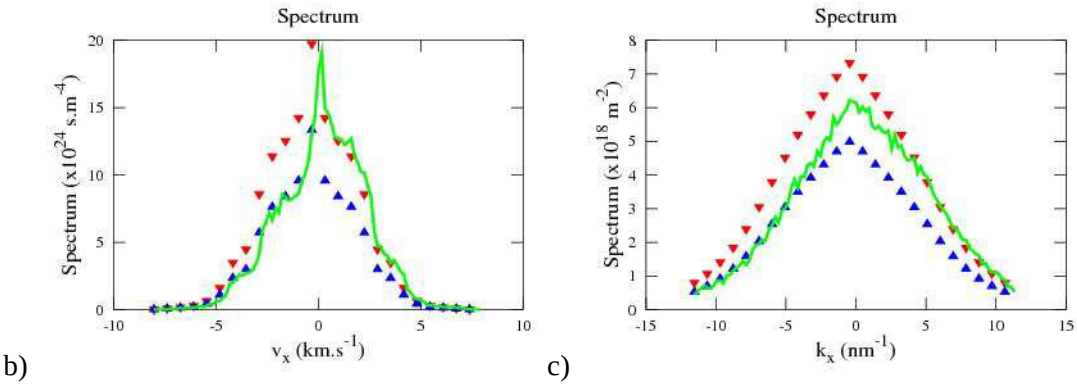

b) c)

Figure 4: a) Schema of the device. b) Velocity and c) wave vector spectra of phonons in the central cell of the device (green solid line). Equilibrium distributions at 400K (red downward-pointing triangle) and 300K (blue upward-pointing triangle).

Acknowledgment

This work is supported by the Agence Nationale de la recherche (ANR) through the project JCJC NOE.

References

[1] W. Weber, "Adiabatic bond charge model for the phonons in diamond, Si, Ge and α-Sn", *Phys. Rev. B* **15**, 4789, 1977.

[2] J. Kulda, D. Strauch, P. Pavone, Y. Ishii, "Inelastic-neutron-scattering study of phonon eigenvectors and frequencies in Si", *Phys. Rev. B* **50**, 13347, 1994.

[3] D. Lacroix, K. Joulain, D. Lemonnier, "Monte Carlo transient phonon transport in silicon and germanium at nanoscales", *Phys. Rev. B* **72**, 064305, 2005.

[4] G. Holland, "Analysis of lattice thermal conductivity", *Phys. Rev.* **132**, 2461, 1963.

Session 6

Surface modes

Ultrafast plasmon heat transfer around subwavelength structures

Olga LOZAN[a], Mathias PERRIN[a], Buntha EA-KIM[b], Jean-Michel RAMPNOUX[a], Stefan DILHAIRE[a] and Philippe LALANNE[c],

[a]*Laboratoire Onde et Matière d'Aquitaine, CNRS-Université de Bordeaux, 33400 Talence, France*

[b]*Laboratoire Charles Fabry, CNRS-IOGS-Université Paris XI, Institut d'Optique, 91120 Palaiseau, France.*

[c]*Laboratoire Photonique, Numérique et Nanosciences, CNRS-IOGS-Université de Bordeaux, Institut d'Optique d'Aquitaine, 33400 Talence, France.*

**corresponding author: olga.lozan@u-bordeaux.fr*

Keywords: Thermoreflectance measurement, plasmon heat transfer, subwavelength apertures, plasmonic devices.

Semiconductor electronics and dielectric photonics have reached their critical limits in terms of device dimensions and operating speed. The further evolution in this direction is possible through *plasmonics*, which offers the opportunity to combine the size of nanoelectronics and the speed of photonics.The key properties of plasmons are that they exhibit an unparallel ability to concentrate light in volumes under diffraction limit (localized surface plasmons) and that they can carry light along the metal surface for comparatively vast distances (surface plasmon polaritons or SPP).

We apply femtosecond thermoreflectance [1] to image indirectly SPP, by detecting the heat dissipated by plasmons while they propagate. This represents a *far-field*, *noninvasive* way to detect the temperature increase due to energy deposited by the SPPs in the metal. Combined with the femtosecond temporal resolution of the experimental set-up, we study also the dynamics of SPPs. Contrary to all the other techniques, which have access to the field component of plasmons in the dielectric, the particularity of our technique is that we image the profile of the absorbed plasmon energy *in the metal.*

This technique allowed us to reveal an anomalous light absorption profile around the canonical diffractive single slit. Transmission and scattering by subwavelength apertures in metal films are fundamental phenomena of wave physics and are important in modern sciences and techniques [2]. However, little is presently known about the heat dissipated by the electromagnetic field in the metal surface around the aperture. Actually, we show that, as it propagates away from the slit, this field heats the metal and *paradoxically* the heat dissipated at the surface remains constant over a broad spatial scale of several tens of wavelengths.

For the experiment we consider a subwavelength slit, etched through a multilayered gold film deposited on a glass substrate. The slit is illuminated from the rear glass/gold interface by a first laser beam (Fig1.a). A fraction of the incident energy is funneled through the slit. At the front aperture, light is either diffracted in the far field or is launched on the metal surface and is dissipated as heat at the air-gold interface. A second laser pulse probes the air-gold interface and records the reflectance variations ΔR at a fixed delay of ≈ 500 fs. Figure 1.b shows the thermal profile of the front interface for TM and TE polarizations. We observe that, at intermediate distances from the slit, surprisingly, the

absorption exhibits a remarkable feature in the form of a *plateau*. This *plateau* displays a nearly constant absorption over a large spatial interval (15 μm≈ 18 λ). The observed *plateau* depends on the complex heat transport that takes place in the metal during the experimental time-window (500fs). We carried out numerical simulation, using a fully-vectorial aperiodic-Fourier-modal method [3]. Consistently with the experimental observation, the profile of the absorbed power density A(x) displays a plateau that is almost constant over a 10-μm spatial interval (Fig.1.c).

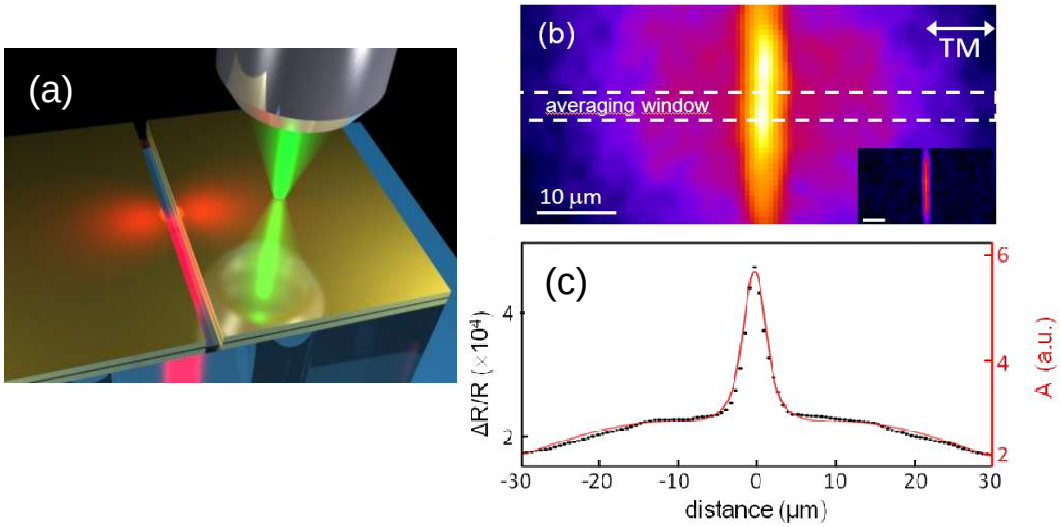

Figure1: (a) Sketch of the pump-probe slit-experiment. ***(b)****Thermoreflectance images obtained for TM polarization (the inset is obtained for TE).* ***(c)*** *Data (black dots) are obtained by averaging 40 line scans from (b) The solid red curve represents the calculated absorption profile A(x).*

In order to gain physical insight into this anomalous behavior we adopt the dual-wave picture in [4] by assuming that the field scattered by the slit is composed of SPPs and quasi-cylindrical waves. Based on this, we have developed an analytical model which well predicts all the salient features of the absorption profile. According to the model, the "anomalous" absorption profile is understood as resulting from a beating of a SPP and a quasi-cylindrical wave. The phenomenon is general since the *same* absorption plateau occurs for a variety of topologies, irrespective of whether the aperture shape corresponds to one-dimensional line (slit) or point-like (hole) sources.

To conclude, application of thermoreflectance technique allowed us to reveal an anomalous light absorption profile around *the canonical single slit*. In the plateau region, the power actually dissipated can be much weaker than the power lost by the plasmon launched at the surface alone. This property opens interesting perspectives for optimizing the performance of metallic devices for energy harnessing in complex plasmonic systems that combine surface plasmons and localized plasmonic resonances. More details concerning this work in [5].

References

[1] S. Dilhaire, G. Pernot, G. Calbris, J. M. Rampnoux, and S. Grauby, "Heterodyne Picosecond Thermoreflectance Applied to Nanoscale Thermal Metrology", *J. Appl. Phys*.,**110**, 2011.

[2] C. Genet and T. W. Ebbesen, "Light in tiny holes," *Nature* (London) **445,** 39-46, 2007.

[3] E. Silberstein, P. Lalanne, J.-P. Hugonin, and Q. Cao.,"Use of grating theories in integrated optics", *J. Opt. Soc. Am. A.* **18**, 2865-75, 2001.

[4] P. Lalanne, J. P. Hugonin, H. T. Liu, B. Wang,"A microscopic view of the electromagnetic properties of sub-λ metallic surfaces", *Surf. Science Report* **64**, 453–459, 2009.

[5] O. Lozan, M. Perrin, B. Ea-Kim, J.M. Rampnoux, S. Dilhaire, P. Lalanne, "Anomalous light absorption around subwavelength apertures in metal films", *Phys. Rev. Lett.* **112**, 193903, 2014.

Large penetration depth in hyperbolic metamaterials

Slawa LANG[a], Maria TSCHIKIN[b], Svend-Age BIEHS[b*], Philippe BEN-ABDALLAH[c], Alexander PETROV[a] and Manfred EICH[a]

[a]*Institute of Optical and Electronic Materials, Hamburg University of Technology, 21073 Hamburg, Germany*

[b]*Institut für Physik, Carl von Ossietzky Universität, D-26111 Oldenburg, Germany*

[c]*Laboratoire Charles Fabry, UMR 8501, Institut d'Optique, CNRS, Université Paris-Sud 11, 2, Avenue Augustin Fresnel, 91127 Palaiseau Cedex, France*

**corresponding author: biehs@theorie.physik.uni-oldenburg.de*

Keywords: nanoscale heat transfer, multilayer and nanowire hyperbolic metamaterials penetration depth.

We investigate the penetration depth of thermal near-field heat flux in different kinds of hyperbolic metamaterials. First we begin with a study of near-field heat radiation between two semi-infinite bulk GaN materials, two hyperbolic multilayer GaN/Ge bilayer structures (mHMM), and two nanowire hyperbolic metamaterials with GaN nanowires immersed into a Ge host (wHMM) as shown in Fig. 1 using effective medium theory and the known expressions for near-field heat transfer for anisotropic materials [1]. We show that in the distance regime where the near-field heat flux is dominated by the hyperbolic modes [2,3,4,5], the penetration depth within the hyperbolic metamaterials can be orders of magnitude larger than in the GaN bulk materials (see Fig. 2) where the penetration depth is ultrasmall due to the surface-mode dominated heat flux [6,7]. This finding might be useful in near-field applications such as near-field thermophotovoltaics [8,9,10], for instance.

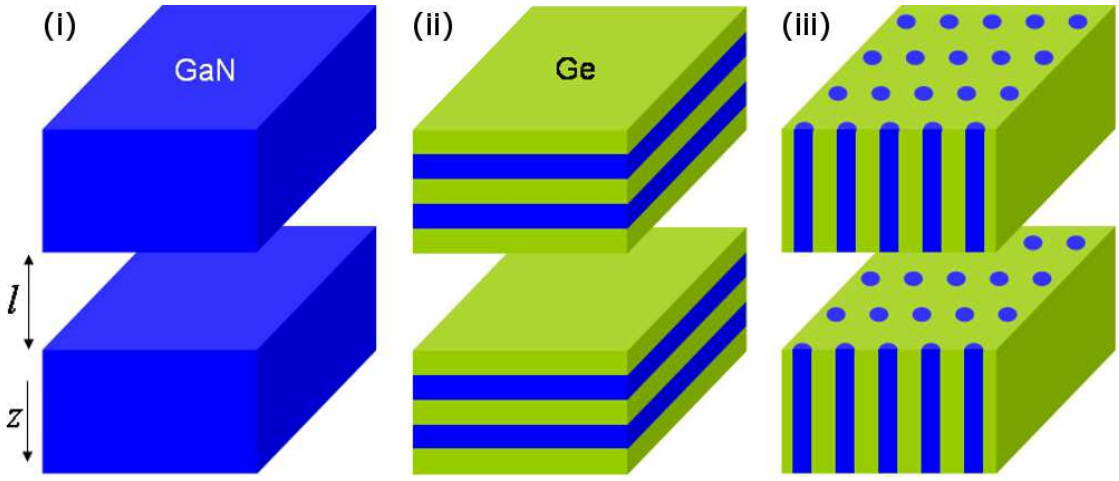

Figure 1: Systems to be analyzed. Two identical half spaces of (i) bulk GaN, of (ii) GaN/Ge layer HMMs and of (iii) GaN/Ge wire HMMs separated by a vacuum gap. The HMMs are modeled as effective media. The GaN filling factor of the layer HMM is 50 %, the one of the wire HMM is 30 %.

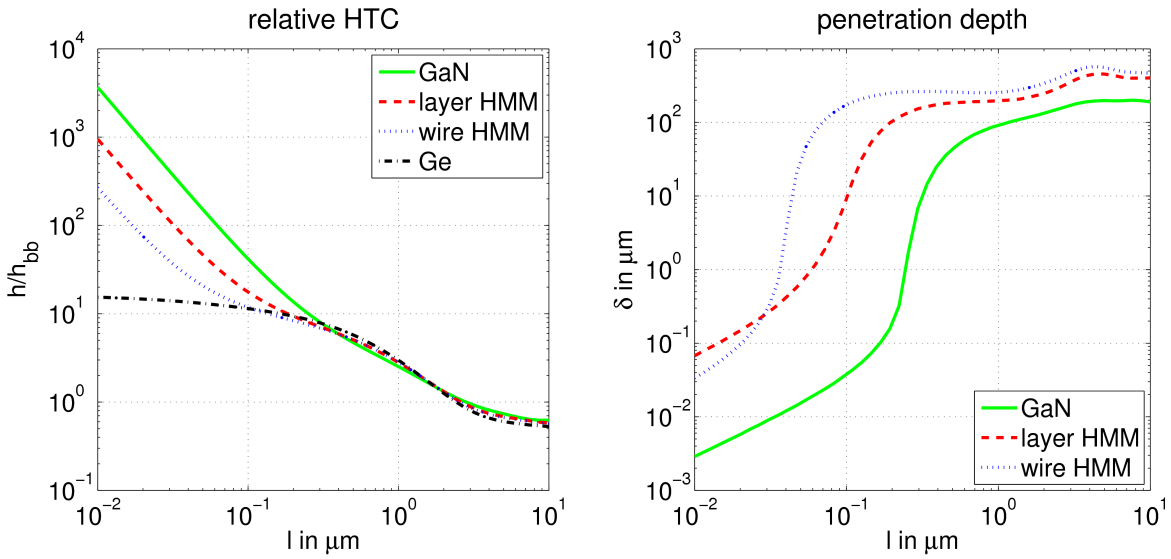

Figure 2: Resulting heat flux (left) and penetration depth (right) for the different systems using effective medium theory.

In addition, we study the mHMM structures in more detail within an exact approach based on the Green's function formalism, S-matrix theory, and Rytov's fluctuational electrodynamics [11]. We show that the effective medium theory tends to underestimate the penetration depth and to overestimate the near-field heat flux. Furthermore, we study the dependence of the heat flux and the penetration depth on the design parameters, i.e. the volume filling fraction, the period of the multilayers and the distance between the mHMMs using a Bloch wave approach. Some of our results can be seen in Fig. 3 where we compare effective and exact results of the heat transfer coefficient and the penetration depth for a GaN/Ge mHMM such as in Fig. 1 (ii). More detailed discussions and results including the spectral heat transfer coefficient and the spectral penetration depth can be found in Refs. [7,12]

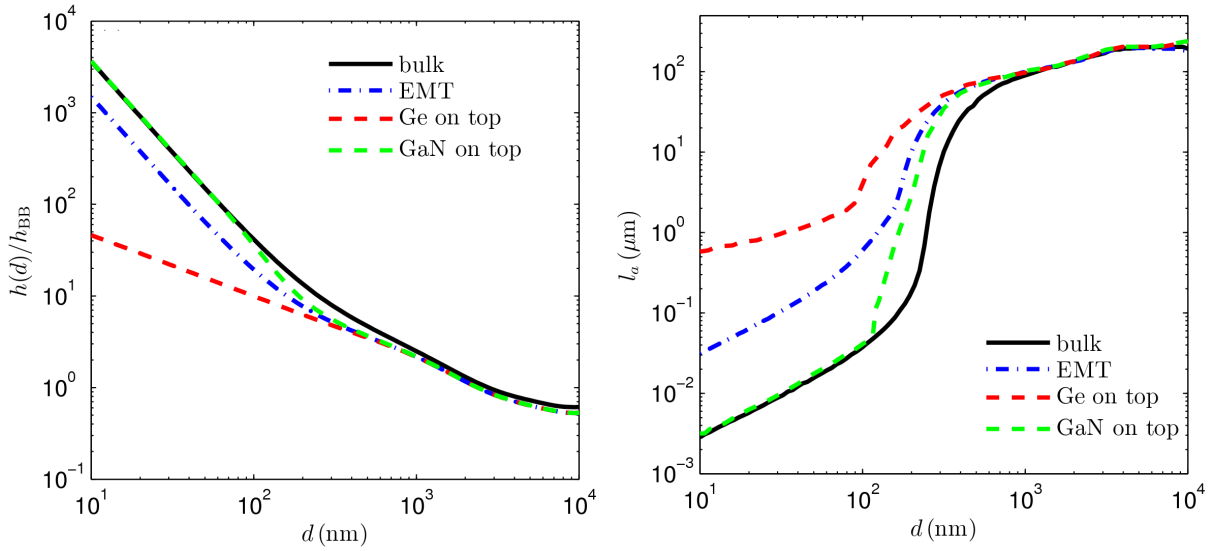

Figure 3: Resulting heat flux (left) and penetration depth (right) for a GaN/Ge mHMM with a period of 100nm and a filling factor of 0.5. Obviously the effective results tend to overestimate the heat flux and they tend to underestimate the phenetration depth.

References

[1] S.-A. Biehs, F. S. S. Rosa, P. Ben-Abdallah, K. Joulain, and J.-J. Greffet, "Nanoscale heat flux between nanoporous materials", *Opt. Expr*. **19**, A1088-A1103, 2011.

[2] S.-A. Biehs, M. Tschikin, and P. Ben-Abdallah, "Hyperbolic Metamaterials as an Analog of a Blackbody in the Near Field", *Phys. Rev. Lett*. **109**, 104301, 2012.

[3] Y. Guo, C. L. Cortes, S. Molesky, and Z. Jacob, "Broadband super-Planckian thermal emission from hyperbolic metamaterials", *Appl. Phys. Lett*. **101**, 131106, 2012.

[4] I. S. Nefedov and C. R. Simovski, "Giant radiation heat transfer through micron gaps", *Phys. Rev.* B **84**, 195459, 2011.

[5] S.-A. Biehs, M. Tschikin, R. Messina, and P. Ben-Abdallah, "Super-Planckian Near-Field Thermal Emission with Phonon-Polaritonic Hyperbolic Metamaterials", *Appl. Phys. Lett.* **102**, 131106, 2013.

[6] S. Basu and Z.M. Zhang, "Ultrasmall penetration depth in nanoscale thermal radiation", *Appl. Phys. Lett*. **95**, 133104, 2009.

[7] S. Lang, M. Tschikin, S.-A. Biehs, A. Yu. Petrov, and M. Eich, "Large penetration depth of near-field heat flux in hyperbolic media", *Appl. Phys. Lett*. **104**, 121903, 2014.

[8] R. S. DiMatteo, P. Greiff, S. L. Finberg, K. A. Young-Waithe, H. K. Choy, M. M. Masaki, and C. G. Fonstad, "Enhanced photogeneration of carriers in a semiconductor via coupling across a nonisothermal nanoscale vacuum gap", *Appl. Phys. Lett*. **79**, 1894, 2001.

[9] A. Narayanaswamy and G. Chen, "Surface modes for near field thermophotovoltaics", *Appl. Phys. Lett.* **82**, 3544, 2003.

[10] C. Simovski, S. Maslovski, I. Nefedov, and S. Tretyakov, "Optimization of radiative heat transfer in hyperbolic metamaterials for thermophotovoltaic applications", *Opt. Expr*. **21**, 14988, 2013.

[11] M. Francoeur, P. Menguc, R. Vaillon, "Solution of near-field thermal radiation in one-dimensional layered media using dyadic Green's functions and the scattering matrix method", *J. Quant. Spect. Rad. Transf*. **110**, 2002, 2009.

[12] M. Tschikin, S.-A. Biehs, P. Ben-Abdallah, S. Lang, A. Yu. Petrov, and M. Eich, "Transport of radiative heat flux by hyperbolic metamaterials',' *arXiv*: 1403.2664, 2014.

Fresnel-like formulas for the reflection and transmission of surface phonon-polaritons at a dielectric interface

Jose ORDONEZ-MIRANDA[a], Laurent TRANCHANT[a], Thomas ANTONI[a,b] and Sebastian VOLZ[a*]

[a]*Laboratoire d'Energétique Moléculaire et Macroscopique, Combustion, UPR CNRS 288, Ecole Centrale Paris, Grande Voie des Vignes, 92295 Chatenay Malabry, France.*

[b]*Ecole Centrale Paris, Laboratoire de Photonique Quantique et Moléculaire, UMR CNRS 8537, Ecole Normale Supérieure de Cachan, Grande Voie des Vignes, F-92295 Châtenay-Malabry cedex, France.*

**corresponding author: jose.ordonez@ecp.fr*

Keywords: Surface phonon-polaritons, Reflection and transmission, Polariton and radiation energy, Thermal energy guiding.

The blossoming of nanotechnology involving the miniaturization of devices with enhanced rates of operation requires a profound understanding and optimization of their thermal performance. This is particularly critical in nanomaterials, due to the sizeable reduction of their thermal conductivity as their size is scaled down. The surface phonon-polaritons (SPPs) are surface electromagnetic waves generated by the fluctuation of the electrical dipoles of polar media (Fig. 1(a)), and they have shown wide potential to enhance the energy transport through these materials [1-6]. SPP energy is determined by material permittivities and hence it can be modified by material discontinuities, however their effect on the heat transport is not well understood to date, especially in absorbing nanomaterials.

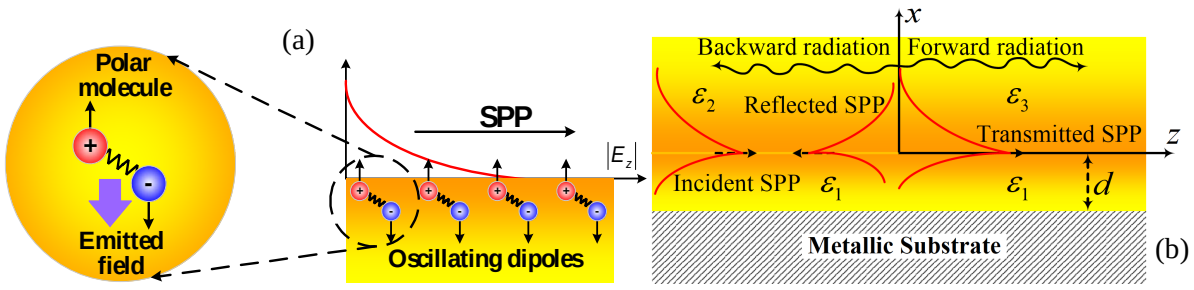

Figure 1: (a) Generation of SPPs by the fluctuation of electrical dipoles. (b) SPP and radiation modes generated by an incident SPP at a dielectric interface. The metallic substrate of the polar film of thickness d is used to diminish the radiation modes and enhance the SPP energy transport.

In this work, the reflection and transmission coefficients of a surface phonon polariton propagating along the surface of a thin film of SiO2 and crossing the interface of two dielectric media are analytically determined (Fig. 1(b)). Based on the expansion of the electrical and magnetic fields in terms of normal modes, explicit expressions for the reflectivity and transmissivity of the radiation fields generated at the dielectric interface are also obtained. The symmetrical Fresnel-like formulas in Eqs. (1a) and (1b) hold for nanofilms and their simplicity represents one of their greater advantage with respect to previous numerical results reported for the analogous problem dealing with surface plasmon-polaritons [7,8]. For the dielectric interfaces of air/BaF2 and air/Al2O3, it is shown that: i) The polariton reflectivity (transmissivity) decreases (increases) as the film thickness increases (Fig. 2(a)), while its radiation equivalent follows the opposite behavior. ii) The SPP and radiation

transmissivities are significantly more sensitive than their corresponding reflectivities to the changes on the permittivity mismatch of the dielectric interface. For a 143 nm-thick film, the polariton transmissivity (reflectivity) changes by 13.2% (1.9%), when this mismatch varies by 50%. iii) The reflectivity and transmissivity of the radiation fields are smaller than their polariton counterparts, which together account for around 82% of the total energy. The proposed formalism fulfils the principle of conservation of energy with an uncertainty of less than 2%, for describing the reflection and transmission of both the polariton and radiation fields generated at a dielectric interface, as shown in Fig. 2.

$$r = \frac{\sqrt{\varepsilon_3} - \sqrt{\varepsilon_2}}{\sqrt{\varepsilon_3} + \sqrt{\varepsilon_2}}, \tag{1a}$$

$$\tau = 4\frac{\sqrt[4]{\varepsilon_2\varepsilon_3}}{\sqrt{\varepsilon_3} + \sqrt{\varepsilon_2}} \frac{\sqrt{\varepsilon_2\varepsilon_3(\varepsilon_2 - \varepsilon_1)(\varepsilon_3 - \varepsilon_1)}}{\varepsilon_2(\varepsilon_2 - \varepsilon_1) + \varepsilon_3(\varepsilon_3 - \varepsilon_1)}. \tag{1b}$$

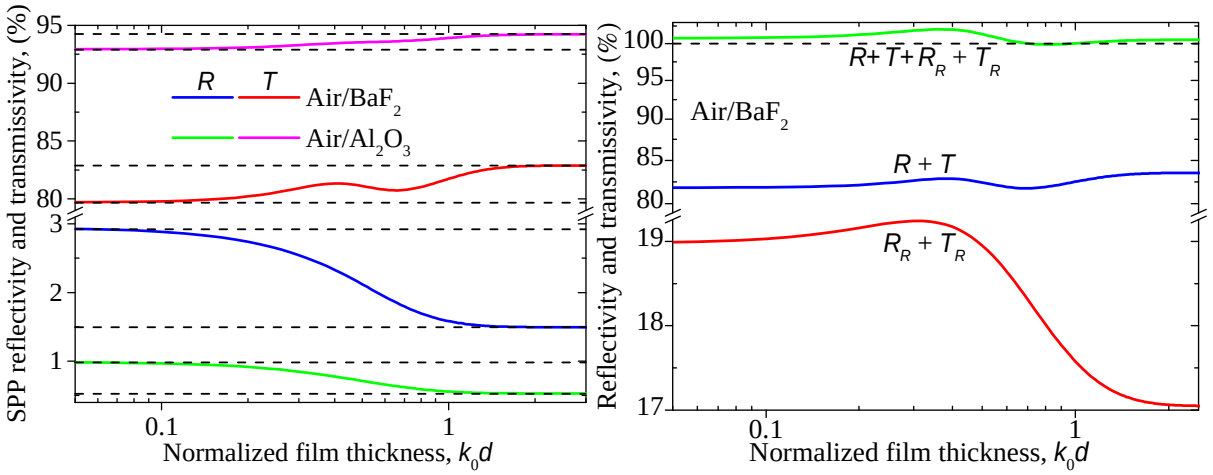

Figure 2: Film thickness dependence of the (a) reflectivity and transmissivity of a SPP propagating along the surface of a SiO2 film and crossing a dielectric interface of Air/BaF2 and Air/Al2O3, and (b) Reflectivity+transmissivity involved in the SPP and radiation fields.

References

[1] J. Ordonez-Miranda, L. Tranchant, T. Tokunaga, B. Kim, B. Palpant, Y. Chalopin, T. Antoni, S. Volz, "Anomalous thermal conductivity by surface phonon-polaritons of polar nano thin films due to their asymmetric surrounding media", *J. Appl. Phys.* **113**, 084311, 2013.

[2] J. Ordonez-Miranda, L. Tranchant, B. Kim, Y. Chalopin, T. Antoni, S. Volz, "Effects of anisotropy and size of polar nano thin films on their thermal conductivity due to surface phonon-polaritons ", Appl. Phys. Express. **7**, 035201, 2014.

[3] J. Ordonez-Miranda, L. Tranchant, Y. Chalopin, T. Antoni, S. Volz, "Thermal conductivity of nano-layered systems due to surface phonon-polaritons ", *J. Appl. Phys.* **115**, 054311, 2014.

[4] J. Ordonez-Miranda, L. Tranchant, T. Tokunaga, B. Kim, B. Palpant, Y. Chalopin, T. Antoni, S. Volz, "Anomalous thermal conductivity by surface phonon-polaritons of polar nano thin films due to their asymmetric surrounding media", *J. Appl. Phys.* **113**, 084311, 2013.

[5] J. Ordonez-Miranda, L. Tranchant, B. Kim, Y. Chalopin, T. Antoni, S. Volz, "Quantized Thermal Conductance of Nanowires at Room Temperature Due to Zenneck Surface-Phonon Polaritons ", *Phys. Rev. Lett.* **112**, 055901, 2014.

[6] D. Z. A. Chen, A. Narayanaswamy, G. Chen, "Surface phonon-polariton mediated thermal conductivity enhancement of amorphous thin films", *Phys. Rev.* B **72**, 155435, 2005.

[7] R. F. Oulton, D. F. P. Pile, Y. Liu, X. Zhang, "Scattering of surface plasmon polaritons at abrupt surface interfaces: Implications for nanoscale cavities", *Phys. Rev.* B **76**, 035408, 2007.

[8] T. Vary, P. Markos, “Propagation of surface plasmons through planar interface”, *SPIE* **7353**, 73530K, 2009.

Session 7

Experimental heat conduction (2)

In-situ calibration of thermal sensors to measure absolute heat fluxes at the nano-scale

Konstantin KLOPPSTECH, Nils KÖNNE and Achim KITTEL*

Carl von Ossietzky Universität Oldenburg, AG EPKOS, Carl-von-Ossietzky-Strasse 9-11, 26129 Oldenburg, Germany

**corresponding author: Kittel@uni-oldenburg.de*

Keywords: near-field thermal radiation, nano-scale, sensor calibration, measurement of absolute heat fluxes.

Experimental analysis of near field mediated heat transfer under well-controlled conditions has shown the predicted increase of heat flow for distances between two bodies smaller than the thermal wavelength, which is about 10µm at room temperature. It has even been shown that these near field mediated heat fluxes exceed the far field limit [1-2]. These and other outstanding results are enabling a much deeper understanding of the near field coupling between two bodies inspiring theoretical work on this topic [3-10]. But when it comes to distances in the nanometer regime there is a lack of distinct experimental data. Published experimental approaches [6,9,10] cannot probe this regime appropriately. Our experimental approach with the Near-field scanning thermal microscope (NSThM) [5] can resolve sub nanometer distances between the probe and a surface. It utilizes a probe that functions as an ordinary scanning tunneling microscopy (STM) probe which is enhanced with a sub-micron thermocouple. Allowing to record a topographic scan, with sub-nanometer resolution and a mapping of heat fluxes with a lateral resolution of about 6 nm [11], simultaneously. Furthermore the thermal coupling can be probed as a function of probe-surface distance with a sensitivity of about 25 nW in the sub-nanometer regime. This experiment is done in highly controlled environment, namely the setup is held in ultra-high vacuum (UHV). A scheme of our probe is depicted in Fig. 1.

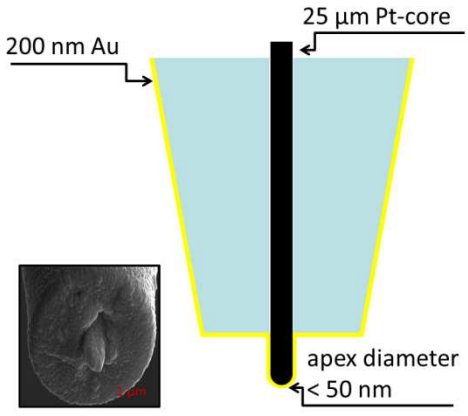

Figure 1: Illustration and SEM image of the Near-field scanning thermal microscope probe. The probe consits of a 25 µm platinum wire, encased with glass and evaporation coated with about 200nm of gold. The protruding part of the Au coated Pt-wire has a diameter of less than 50 nm. This configuration allows standard STM techniques and measurements of heat fluxes.

Experimental details can be found in [5]. Our setup allows a profound analysis of the behavior of the near field coupling at sub-nanometer distances [4] as the distance between probe and sample is due to the use of STM techniques well defined. This method has led to outstanding results, for example we have recently shown that a monolayer of NaCl deposited on an Au(111)-surface enhances the near

field coupling by about a factor of two at distances of 4 nm [11]. By this our experimental data influences theoretical work and gives a completely new insight in the behavior of the thermal near field. To provide experimental results that are comparable with theoretical predictions prior experimental and theoretical analysis of our NSThM-probe [4, 5] have been done, to be able to measure absolute heat fluxes. These approaches are quiet sophisticated.

Firstly, we present here a new easy to apply in-situ method of characterizing our NSThM-probes. After characterizing our NSThM-probe in that way we are able to measure absolute heat fluxes with high accuracy. Therefore, we adopt the in [12] presented method of utilizing an AC heated 1µm thin metal wire as a metrological controllable and accessible heat reservoir. This wire is held in UHV, so that convection effects can be neglected. Furthermore the wire is heated in such a small manner that radiative heat losses do not occur. Because of the huge aspect ratio 6000/1 of the wire (6 mm in length) the situation can be described by the 1D heat flux equation in good approximation. In a first baseline measurement the thermal resistance of the wire is determined, by heating the wire with small AC currents and calculating the wire´s temperature rise from the change in its electrical resistivity. In a second step the wire is approached by our NSThM-tip, which is brought in tunneling distance to the wire. At these distances the probe couples thermally to the wire via the near-field and represents an additional heat sink in the center of the wire changing its local temperature. Repeating the first measurement with this configuration will lead to a change in the wire´s temperature distribution as a specific amount of heat will flow from the wire into the NSThM-tip. This is depicted in Fig. 2. From this change in averaged temperature of the wire one can calculate via Fourier´s law the amount of heat that flows from the wire to the NSThM-probe. A measurement of the thermo voltage delivered by the sensor gives the opportunity to determine the relation between heat flux and thermo voltage, i.e. a calibration curve of the NSThM-sensor. Here we show that a first order linear approximation for calculation of heat fluxes from the wire in the NSThM-probe, which is based upon the Fourier´s law, is indeed correct. From this linear dependency between thermo power and heat flux we determine the slope for our Gold coated NSThM-probes to be 2.4 µV/µW. By means of this factor we are able to determine the absolute value of the heat flux at any given position of and distance to the sample surface. This characterization takes place right before the actual measurement and is done under the same conditions as the actual measurement of heat fluxes from a sample to our probe, particularly the interaction region is exactly the same as later during the actual measurements. As we analyze this experimental system for characterization with Gaussian error calculation we optimized the method of characterization with respect to precision. This enables us to probe near field mediated heat fluxes by means of absolute values with overall relative uncertainties of about 10%. Furthermore we investigated the long time stability of the tunneling gap between the NSThM-probe and the heated wire in detail. This proofs that a stable gap is possible, which seems to be quiet surprising because of the low mechanical stability of the heated wire. A stable tunneling gap leads to a very stable thermal coupling as the characteristic coupling scales of the near field are much larger than the ones of a stable tunneling current [11]. Such a stable coupling allows us not only to calculate the thermal resistivity of the thermal coupling but the thermal resistivity of our NSThM-probe. We were able to confirm our former results published in [5].

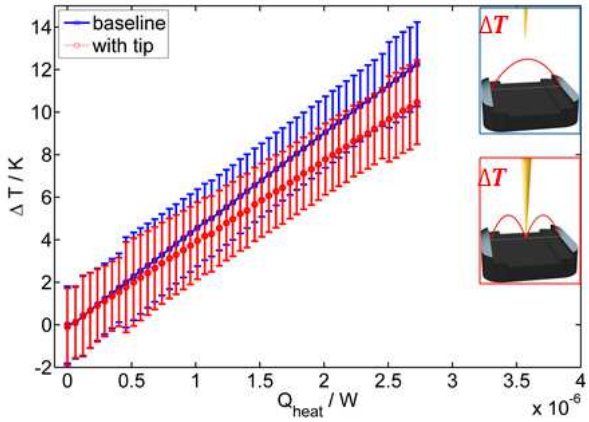

Figure 2: Mean temperature rise of heated platinum wire for various heating powers. From the slope the thermal resistance of the wire can be calculated. The baseline measurement without the tip in contact has a larger slope, meaning a lager effective thermal resistance, than the wire with the tip approached. From this change in slopes the amount of heat leaving the wire can be calculated. This heat flux generates a thermo-power signal which is measured simultaneously. The two insets show schemes of the temperature increase along the wire with respect to the surrounding caused by the heating current with and without the presence of the NSThM tip.

Second we present recent experimental data for near field mediated heat fluxes by means of absolute values and show a detailed analysis with theoretical expectations calculated with the proximity force approximation-for distances up to 5 nm.

Summarizing we utilize standard STM techniques, to approach samples with our NSThM-probe. With our NSThM we achieve both topography and lateral resolved heat fluxes. But even a distance depended analysis of thermal coupling can be performed. Because a very stable thermal coupling is achieved it is possible to characterize the behavior of the near field for various distances up to 5 nm. We are able to resolve heat fluxes down to 25 nW with a lateral spatial resolution of about 6 nm. This enables us with the above described characterization to measure absolute heat fluxes in the sub-nanometer regime. Our Au coated NSThM-probes generate 2.4 µV thermo power at a heat flux of 1 µW. This factor of sensitivity has a relative uncertainty of about 10% meaning that we can determine precise heat fluxes. Because we utilize an enhanced STM technique we are able to study various metal surfaces decorated with different materials. As presented in [11] monoatomic layer islands of NaCl on an Au(111) surface have a significant influence on the near field mediated coupling. We will focus on this topic for a better understanding of the influence of surface layers on the near-field mediated coupling with our characterized sensors. As we are able to measure exact heat fluxes comparison with theoretical statements are possible. This evokes a whole new theme, namely the possibility to tune the near field on small scales and demands new theoretical approaches for exact calculations. Only a complete understanding of the mechanisms will allow a complete and detailed understanding of the behavior of near-field radiation at nano-scale.

References

[1] L. Hu, A. Narayanaswamy, X. Chen, and G. Chen, *Appl. Phys. Lett*. **92**, 133106, 2008.

[2] A. Narayanaswamy, S. Shen, and G. Chen, *Phys. Rev.* B **78**, 115303, 2008.

[3] A. Kittel, U. F. Wischnath, J. Welker, O. Huth, F. Rüting, and S.-A. Biehs , *Appl. Phys. Lett*. **93**, 193109, 2008.

Quantitative thermal conductivity measurement by scanning thermal microscopy with nanofabricated thermal probes - methodology and modeling

Jerzy BODZENTA[a*], Mihai CHIRTOC[b] and Justyna JUSZCZYK[a]

[a]*Institute of Physics - Centre for Science and Education, Krzywoustego 2, 44-100 Gliwice, Poland*

[b]*Multiscale Thermophysics Lab. GRESPI-CATHERM, Université de Reims Champagne Ardenne URCA, Moulin de la Housse BP 1039, 51687 Reims, France*

**corresponding author: jerzy.bodzenta@polsl.pl*

Keywords: scanning thermal microscopy, nanofabricated thermal probes, quantitative thermal measurement, heat transfer modeling.

This work is intended as a contribution towards assessing the SThM method as a metrological tool for calibrated local thermal conductivity measurements. Development of the scanning thermal microscopy (SThM), since its invention in 1986 by Williams and Wickramasinghe, has led to work out measuring methods for quantitative thermal measurement making use of SThM equipment. Nowadays thermal probes (TP) for SThM provide spatial resolution better than 100 nm. However all these methods face the problem with relatively low dynamic range of measured signal. A few orders of magnitude change in the thermal conductivity k of the sample causes no more than 20-30% change in the measured signal. Additionally, the thermal conductivity of a sample is typically read from a calibration curve obtained with reference samples. To achieve reasonable accuracy of measurement signals for investigated and reference samples have to be determined with low uncertainties.

When the probe is driven by ac current of frequency ω, the signal contains ω and 3ω components. With Wollaston wire TPs, detection of the 3ω component is preferred because of its higher sensitivity to k. As these probes are relatively massive they have low resonant frequency and their bending caused by thermal stresses does not disturb the measurement. In the case of nanofabricated TPs this effect seriously impedes experiments and can lead to probe damage. To avoid thermoelastic vibration, the measuring technique in which the probe is driven by a sum of dc and (low) ac currents was proposed [1]. In this case, the signal additionally contains a dc component and a 2ω component. All theoretically predicted components are shown in Fig. 1.

It was shown that the sensitivity of the ω component amplitude to k is three times higher than the one of dc component (for $\omega\tau << 1$).

In practice the determination of k can be based on measurement of the static ($R_s = U/I$) and dynamic ($R_d = \mathrm{d}U/\mathrm{d}I$) resistances of the TP at $\omega\tau << 1$, using the dc and the ω components, respectively. Moreover, the $R_d - R_s$ difference is proportional to the thermal resistance to heat transfer between the probe and the sample R_{th}, which in turn is directly related to k. Normalization of this quantity for the TP in air minimizes the influence of environmental factors (e.g. instability of room temperature).

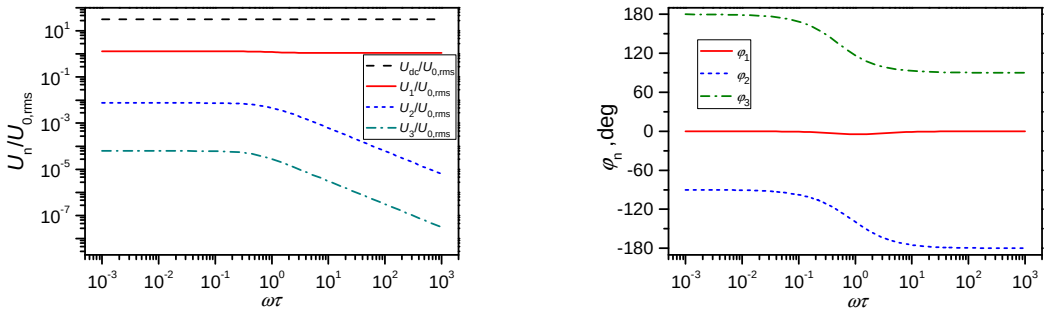

Figure 1: The dc component and amplitude and phases of ac components of the signal of resistive TP driven by the sum of dc and ac currents. The ratio of dc current to the amplitude of ac current was 20.

This technique was used for determination of the thermal conductivity of thin layers of BaTiO3 [2] and iron phthalocyanine [3]. The idea of thermal measurement with the thermal probe driven by the sum of dc and ac components can be also useful in thermal imaging. It utilizes advantages of lock-in detection and, what is important in the case of scanning microscopy, requires shorter time constant compared with the 3ω detection [1]. This technique was used in investigation of multilayered photonic structures [4].

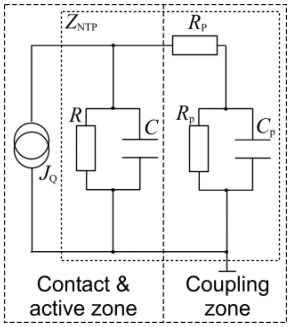

Figure 2: Two-cell quadrupole model of the probe-sample system

For nanofabricated TPs, the known model based on the lumped approximation of suspended wire (LASW) containing a single time constant should be treated as the simplest approximation. That is why a more complex model of the probe-sample system is proposed. It is based on consideration of the heat exchange channels between electrically heated probe, a sample and its surroundings, in transient and harmonic regimes [5]. Three zones in the probe-sample system are distinguished and modeled by using electrical analogies of heat flow through a chain of quadrupoles built from thermal resistances and thermal capacitances. The first zone is an active zone which embraces the vicinity of the probe sample contact. Its characteristic dimension is of the order of 1 μm. The second one is an active zone (~10 μm), where heat sources are localized. The last one is a coupling zone (~100 μm), connecting the active zone with the probe base. In the simplest case the system can be modeled by the two-cell quadrupole chain shown in Fig.2. The thermal transfer function of this circuit in the frequency domain is

$$Z_{\mathrm{NTP}} \approx \frac{1}{\dfrac{1+j2\omega\tau}{R} + \dfrac{1}{R_\mathrm{p} + \dfrac{1}{\dfrac{1+j2\omega\tau_1}{R_\mathrm{p}}}}}, \qquad (1)$$

where $\tau = RC$, and $\tau_1 = R_pC_p$. Consequently, the system has two characteristic times describing dynamic processes in the active and coupling zones.

In Fig 3 results of fitting experimental data with curves calculated from the LASW and with the two-cell quadrupole chain model are shown. One may conclude that the LASW does not properly describe the system. In the second case an agreement between experimental data and the model is satisfactory. Better agreement can be achieved by increasing the number of cells in the chain model.

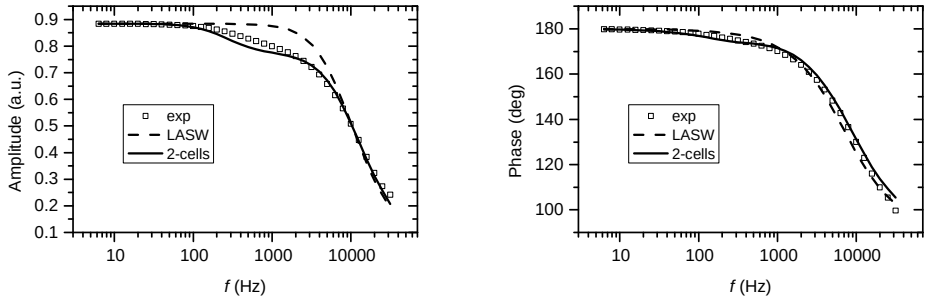

Figure 3: Amplitude and phase dependencies on the frequency of the 3ω signal component measured for the nanofabricated TP together with fitted theoretical curves calculated from the LASW (dotted lines) and two-cell quadrupole model (solid lines)

The validity of the model is examined by comparing computed values of discrete RC elements with results of finite element simulations and with experimental data. The performance in dc regime can be simply obtained in the limit of zero frequency. One concludes that the low NTP sensitivity to sample thermal conductivity is due, much like in dc regime, to significant heat by-pass by conduction through the cantilever, and to the presence of probe-sample contact resistance in series with the sample.

The model can be also useful for analysis of experiments carried out with other TPs with localized heat sources.

References

[1] J. Bodzenta, J. Juszczyk, M. Chirtoc, "Quantitative thermal microscopy (SThM) based on determination of thermal probe dynamic resistance", *Rev. Sci. Instrum.* **84**, 093702, 2013.

[2] A. Kaźmierczak-Bałata, M. Krzywiecki, J. Juszczyk, P. Firek, J. Szmidt, J. Bodzenta, "Application of scanning microscopy to study correlation between thermal properties and morphology of $BaTiO_3$ thin films", *Thin Solid Films* **545**, 217-221, 2013.

[3] M. Krzywiecki, L. Grządziel, J. Juszczyk, A. Kaźmierczak-Bałata, A. Erbe, J. Bodzenta, "Correlation between morphology and local thermal properties of iron (II) phthalocyanine thin layers", *J. Phys. D* **47**, 335304, 2014.

[4] J. Juszczyk, M. Krzywiecki, R. Kruszka, J. Bodzenta, "Application of scanning thermal microscopy for investigation of thermal boundaries in multilayered photonic structures", *Ultramicroscopy* **135**, 95-98, 2013.

[5] J. Bodzenta, M. Chirtoc, J. Juszczyk, "Reduced thermal quadrupole heat transport modeling in harmonic and transient regime scanning thermal microscopy (SThM) using nanofabricated thermal probes", *J. Appl. Phys.* (accepted).

Strain based thermal conductivity tuning on nanoscale polycrystalline AlN thin-films

J. JARAMILLO-FERNANDEZ[a*], W. KASSEM[b], V. REMONDIERE[a], U. SOUPREMANIEN[a], E. OLLIER[a] and S. VOLZ[b]

[a]*Laboratoire de Récupération des Micro-Energies LITEN/DTNM/SERE, CEA, 38000 Grenoble, France*

[b]*Laboratoire d'Energétique Moléculaire et Macroscopique, CNRS, Ecole Centrale Paris, 92295 Châtenay-Malabry, France*

**corresponding author: juliana.jaramillo@cea.fr*

Keywords: thermal conductivity tuning, strain-thermal transport coupling, solid-solid interfaces, structural non-homogeneity, amorphous-crystalline structures, 3-omega method.

Heat transport and thermal conductivity control at small scales has attracted increasing interest in recent years due to its importance in a wide range of applications, such as phonon engineering, thermoelectric generators, energy devices and thermal management in micro and nanoelectronics. Considering the strong size effects in nano-structured thin films, where crystallite sizes are comparable to the heat carrier mean free path, external application of stress/strain should provide a mechanism to tune the thermal conductivity of materials. Recently, Li *et al.*[1] demonstrated theoretically that applying strain/stress affects the thermal conductivity of nanostructures. However, there are limited experimental results [2,3] that show stress/strain effects on the thermal conductivity of thin films.

In the current work, we aimed at investigating the influence of an applied macroscopic strain on phonon transport properties of nano-structured aluminum nitride (AlN) polycrystalline thin films. First, in order to understand scattering mechanisms at the interface between film and substrate, grain boundaries and oxygen related defects, AlN monolayer and multilayer samples were prepared by varying the film thickness from 270 nm up to 1500 nm. For multilayer preparation, deposition process was interrupted and vacuum was broken periodically to grow multiple AlN layers, one on top of the other, intentionally introducing oxygen-related defects at the AlN/AlN interfaces. Fig. 1 illustrates monolayer and multilayer AlN samples.

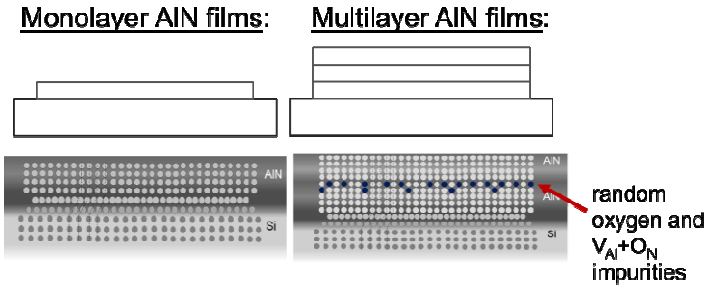

Figure 1: Monolayer and multilayer configurations. For monolayers, a periodical interruption of deposition process breaking the vacuum was performed to create interfaces with oxygen-related defects or impurities.

We explored the effect of atomic structure, crystallite sizes and out-of plane disorientation of grains on the phonon thermal transport properties of non-strained AlN sputtered thin films. Texture, crystallite size, microstructure and interfacial structure of the films were characterized by X-ray diffraction, scanning and transmission electron microscopy. 3 omega measurements were carried out to correlate

structural features with thermal conductivity. Moreover, theoretical calculations based on the Boltzmann transport equation were performed for grained materials and then compared to experimental values of thermal conductivity (Fig.2(a)). The study of thermal properties of non-strained AlN polycristalline was done to further understand the phonon thermal transport properties in complex-structured polycrystalline thin films.

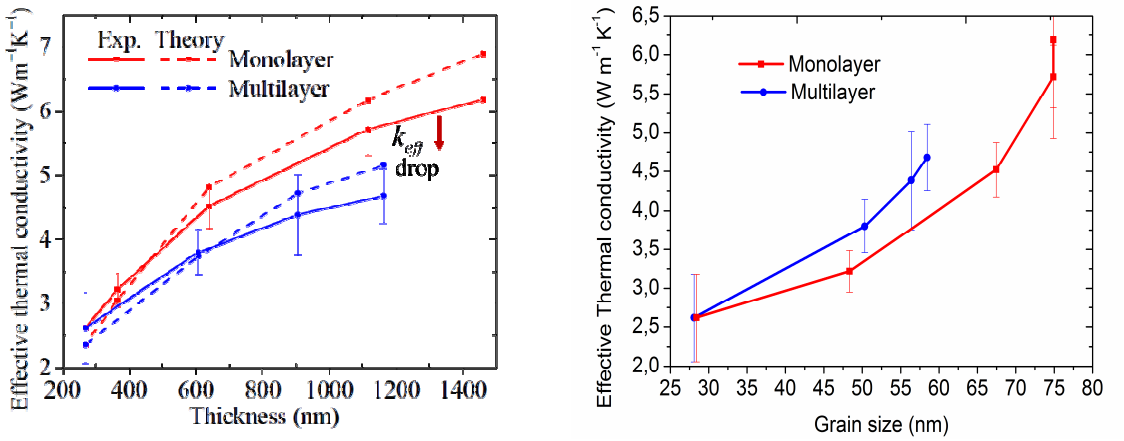

(a) (b)

Figure 2: (a) Comparison between experimental and theoretical values of the k_{eff} of grained monolayers and multilayers as a function of their thickness and (b) k_{eff} as a function of grain size.

Our theoretical calculations based on the Boltzmann transport equation for grained materials are in good agreement with the experimental values. The results in Fig. 2 show that thermal-conductivity increases with thickness and grain size in both monolayer and multilayer configurations and that a clear dependence on the microstructure and growing conditions exists. The overall drop in thermal conductivity for multilayer films indicates that oxygen-related defects at the AlN/AlN interfaces are created by the interruption of the deposition process thereby increasing the interface scattering of phonons. The thermal boundary resistance (TBR) between AlN films and the silicon substrate was found to depend on the near-interface planar microstructure and defects of the AlN.

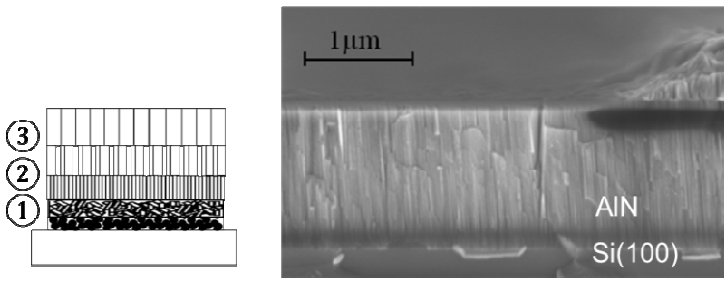

(a) (b)

Figure 3: (a) Schematic of the grain structure of the AlN films on Si (100) in the cross-plane, according to [4-6], (b) SEM images of monolayer AlN films on Si (100).

The theoretical results evidenced that the thickness dependence of thermal conductivity arises from the evolution of grain structure through the cross-plane of the films. Stress release, growth mechanisms and crystal lattice mismatch between AlN and Si causes this structural non-homogeneity of the AlN films[4]. Grain structure in the cross-plane is showed in Fig. 3(a). The film can be decomposed into three domains: (3) the columnar region of the film where the grain size is large with a preferential crystalline orientation, (1) the amorphous region near the Si substrate that has a disordered structure within a limited thickness, and (2) the microcrystalline transition region between the bulk and

amorphous that features different grain sizes and crystalline orientations. In our case, the so-called effective thermal conductivity and the thermal boundary resistance (TBR) include overall resistive contributions of the amorphous and transition regions. SEM analysis confirms that crystallization and microstructure change with thickness thereby modifying phonon transport properties Fig.3(b). Additionally we found that the interruption of the deposition process creates oxygen-related defects at the interface between AlN layers, degrading the phonon transport.

In the second part of this work, thermal conductivity measurements under external applied strain were performed coupling the 3-ω method to a 4 points bending system (Fig.4).

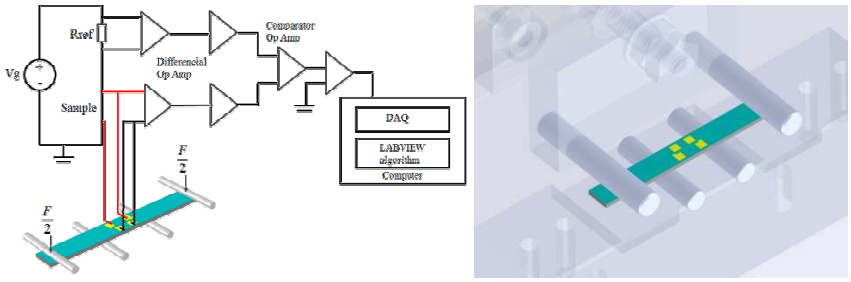

Figure 4: 3 omega method coupled to a 4 points bending system.

In order to investigate how microstructure and out-of plane crystal disorientation influence strain-thermal properties coupling, we measured the thermal conductivity of highly and poorly textured AlN monolayers as a function of external applied stress. Additionally, we did the same measurements on AlN/AlN multilayers to determine the influence of oxygen related defects on thermal transport properties. Samples with close values of thermal conductivity at zero applied stress were used (Table 1) for the sake of comparison. Crystallinity, thickness and the out-of-plane crystal orientation, described by the decrease of the full width half maximum of the rocking curve, are given in Table 1.

Sample	Crystallinity	k_{eff} non strained, ($W.m^{-1}.K^{-1}$)	Thickness (nm)	FWHM RC (°)
Monolayer	Highly textured	4,975	640	2,93
Multilayer	Highly textured	5,369	905	3,20
Monolayer	Poorly textured	4,994	850	8,5

Table1: Effective thermal conductivity of poorly and highly c-axis oriented monolayer and multilayer AlN films as a function of mechanical strain.

The results in Fig. 5 show a strong effect of external applied stress on thermal-conductivity for poorly textured films. Thermal conductivity modulation from 4,99 down to 2,91 $Wm^{-1}K^{-1}$ is achieved under 164,2 MPa. By contrast, in highly textured layers, thermal conductivity was found to be almost independent of stress, except for a possibly not significant 35% decrease in a narrow stress range around 80 MPa for multilayers. In order to explain the observed influence of strain on thermal conductivity, we calculated the interface thermal resistance of the 3 samples (Table 2).

Sample	TBR ($m^2.K\ GW^{-1}$)
Highly textured monolayer	62,736
Highly textured multilayer	62,736
Poorly textured monolayer	104,20

Table 2: Interface thermal resistance of poorly and highly c-axis oriented monolayer and multilayer AlN films.

We found that poorly textured samples have higher interfacial thermal resistance, which means higher interfacial disorder.

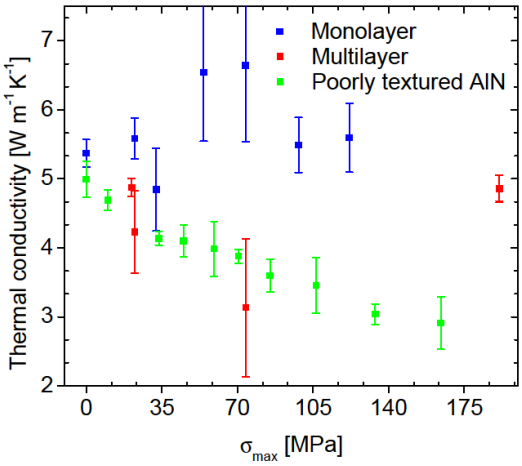

Figure 5: Effective thermal conductivity of poorly and highly c-axis oriented monolayer and multilayer AlN films as a function of applied macroscopic stress.

We propose that higher interfacial disorder produce strong phonon scattering and localization of high frequency vibrations, thus amplifying the strain-thermal conductivity coupling. However, in spite of the of the highly dislocated AlN layer grown at the Si/AlN interface of all samples and the oxygen-related defects at AlN/AlN interface for the multilayer configuration, non-localized vibrational modes in highly-textured AlN films lead to non-observable strain–thermal conductivity coupling.

We are currently extending our work with experimental characterizations of the interface and grain boundaries atomic structure by transmission electron microscopy and in situ X-ray measurements using the BM32 Laue micro-diffraction setup from the European Synchrotron Research Facility (ESRF) coupled to a four points bending system for monitoring strain-induced structural deformations and variations of deviatoric lattice parameters during flexion. Future research in understanding the mechanisms of phonon scattering at grain boundaries and interfacial structure is crucial to describe theoretically the underlying physics driving thermal conductivity tuning observed in nanoscale polycrystalline AlN thin films.

References

[1] X. Li, K. Maute, M.L. Dunn, and R.Yang, “Strain effects on the thermal conductivity of nanostructures” *Phys. Rev. B* **81**, 245318, 2010.

[2] H.-F. Lee, S. Kumar, M.A. Haque, “Role of mechanical strain on thermal conductivity of nanoscale aluminum films”, *Acta Materialia* **58**, 20, 2010.

[3] M. T. Alam, M. P. Manoharan., M. A. Haque, C. Muratore, and A.Voevodin, *J. Micromech. Microeng*. **22** 045001, 2012.

[4] J.P. Kar, G. Bose, S. Tuli, A. Dangwal, and S. Mukherjee, “Growth of AlN Films and Its Process Development for the Fabrication of Acoustic Devices and Micromachined Structures” *J. Mater. Eng.* Perform **18**, 2009.

[5] J. H. Song, J. L. Huang, J. C. Sung, S. C. Wang, H. H. Lu, and D. F. Lii, “Interfacial Microstructure Evolution of (B, Al)N Films Grown on Diamond Substrates” *Thin Solid Films* 519 **13**, 2011.

[6] G. Radtke, M. Couillard, G. A. Botton, D. Zhu, and C. J. Humphreys, Structure and chemistry of the Si(111)/AlN interface, *Appl.Phys.Lett.* **100**, 011910, 2012.

Session 8

Phonon simulations

High temperature increase of the thermal conductivity of zirconium carbide explained by atomistic simulations

Jean-Paul CROCOMBETTE

CEA Saclay, DEN/DMN/Service de Recherches de Métallurgie Physique F-91191, France

jpcrocombette@cea.frr

Keywords: electron heat transport, phonon heat transport, Lorenz number, molecular dynamics, density functional theory, Kubo-Greenwood formula

Most practical applications of zirconium carbide involve heat generation at high temperature. Combined with very high melting temperature its rather good thermal conductivity is an essential feature for these applications. The thermal conductivity (κ) of ZrC is also interesting from the fundamental point of view as it exhibits a very uncommon variation with temperature: from room temperature up to melting, the thermal conductivity rises continuously (see [1] and references therein). Complete understanding of this increase is still lacking and has been the subject of controversy for decades. This behaviour is indeed puzzling, as for metallic systems (such as ZrC) κ should be constant at high temperatures. Moreover the exact repartition of electronic and phononic heat conduction mechanisms is still unknown. Two qualitative arguments have been proposed to explain this anomalous increase of the conductivity with temperature. First ZrC is a semi-metallic compound, in the sense that it exhibits a pseudo-gap in its electronic density of states close to the Fermi level. Then the Lorenz number (ratio of thermal conductivity to the product of electrical conductivity and temperature) should not be constant but rather increasing with temperature. Second zirconium carbide being almost always understoichiometric in carbon, it contains many carbon vacancies. These vacancies should induce an electrical resistivity which is supposed to be constant with temperature. This additional electrical resistivity induces an increase of the thermal conductivity.

We revisit this puzzle with numerical simulations at the atomic scale. We calculate both electronic and phononic contributions to the conductivity and deal with the effect of non-stoichiometry by considering various amounts of carbon vacancies spanning compositions from purely ZrC to $ZrC_{0.9}$. We obtain values for electrical and thermal conductivities in very good agreement with experiments. Phononic contribution to heat transport is found to be much smaller than electronic heat transport at high temperature. The increase of thermal conductivity with temperature is quantitatively reproduced. We are finally able to discuss the origin of the increase of thermal conductivity. We find that the common explanations are partially valid but a major additional source of increase of the thermal conductivity is brought to light, namely the increase of density of states at the Fermi level with increasing temperature.

Vibrational thermal conductivity is calculated through empirical potential molecular dynamics. We use the potential by Li *et al.* especially designed for ZrC [2]. Technically we calculate the thermal conductivity with the homogeneous nonequilibrium MD formalism [3] in which a fictitious external force is added to the atomic interactions and induces a heat current in the simulation box without a temperature gradient. This heat flux is then, to first order, proportional to the thermal conductivity.

Non-stoichiometry is described by the random introduction of 1%, 3% and 9% of carbon vacancies in the 8000 atom simulation box.

As far as electronic thermal conductivity is concerned, we consider the scattering of electrons by phonons and point defects. The Onsager coefficients (L_{ij}) relating thermal and electrical conductivity to temperature and electrical potential gradients can be evaluated in the framework of Kubo–Greenwood theory. In practice it involves calculating with an electronic structure code, in the present work Abinit [4,5], the L_{ij} coefficients on a simulation box for various atomic positions to obtain an average value. To obtain such positions, we use constant temperature MD simulations with the same empirical potential as for the calculation of the vibrational part of the thermal conductivity. The electronic calculation is performed in the generalized gradient approximation of the density functional theory (DFT). As in the former calculations various amounts of carbon vacancies are introduced to account for carbon understoichiometry.

Eventually the total thermal conductivity is calculated as the sum of its phonon and electronic parts. We restricted our calculations to temperatures rather higher than the Debye temperature (649 K). Doing so, we can safely disregard any vibrational quantum effect.

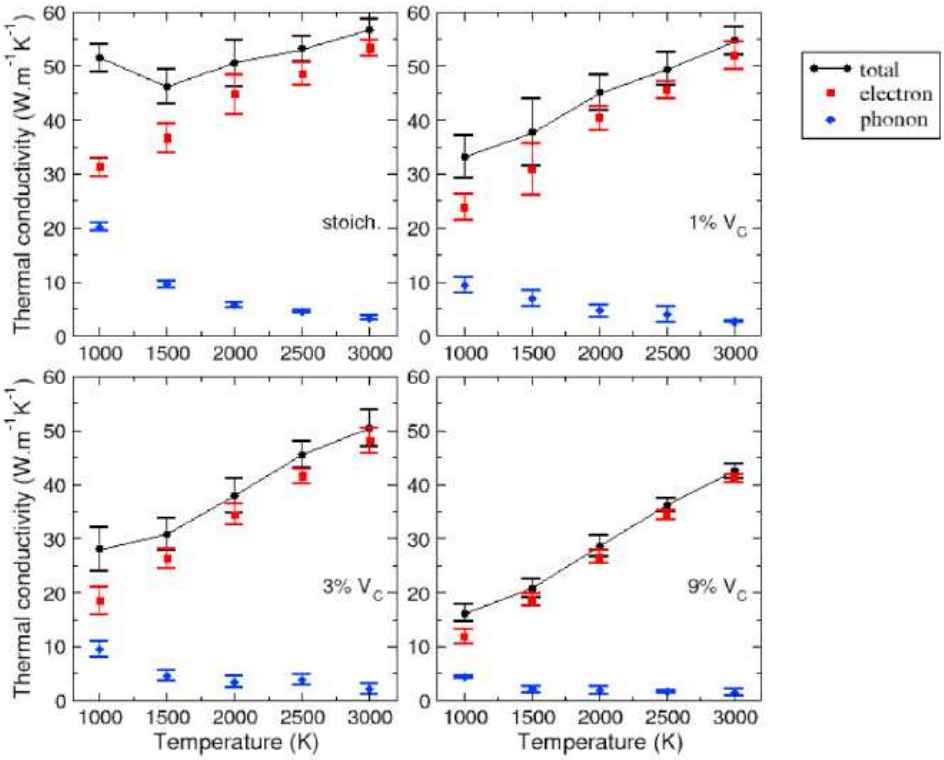

Figure 1: Thermal conductivity of ZrC as a function of temperature for various numbers of carbon vacancies (from ZrC to $ZrC_{0.91}$). Total, phonon and electron contributions are indicated.

The results obtained for the thermal conductivity are summarized in figure 1 which shows, for each composition, the variation of phonon, electronic and total thermal conductivity with temperature. The total thermal conductivity does exhibit an increase with temperature. This is true even for the perfectly stoichiometric material. Second, the phonic contribution regularly decreases with temperature for all compositions and the rise of total conductivity relies entirely on the electronic part which is vastly dominant at temperatures higher than 1500 K. One can observe that phonon transport falls very rapidly

with the introduction of vacancies. In contrast electron transport seems much less affected, particularly at high temperature. This makes the rise of thermal conductivity more and more pronounced with increasing deviation from stoichiometry.

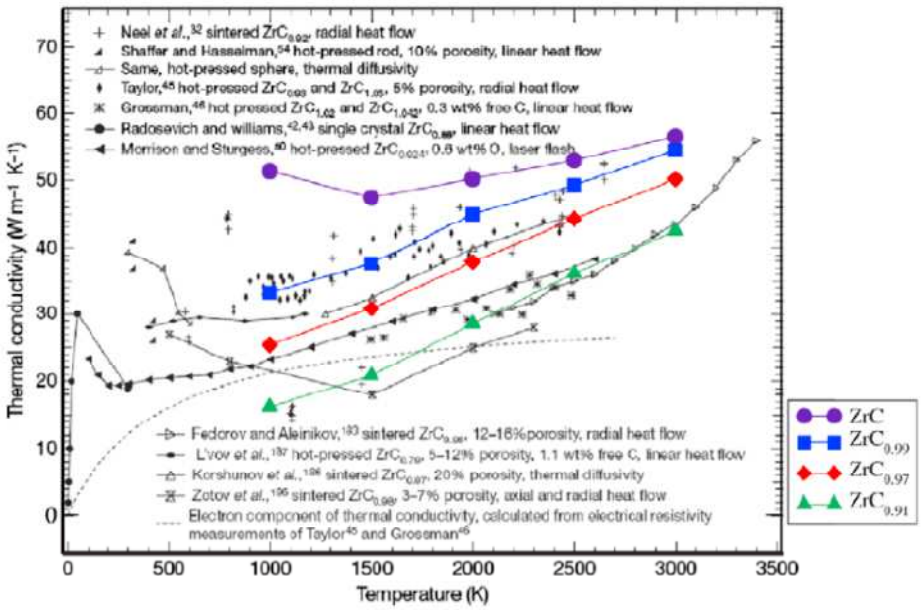

Figure 2: Total thermal conductivity of ZrC as a function of temperature. The calculated values for various stoichiometries are superimposed on a figure of experimental values gathered by Jackson et al. [1]

Our results are graphically compared with experiments in figure 2. One can first note the rather large spread of the experimental values. This spread is due to the variations of the state of the material in terms of composition, porosity and microstructure. Nevertheless, our results prove to be quite close to the experimental values. They are on the higher side of the experiments. This quite probably comes from the fact that some sources of thermal resistance are not dealt with in our calculations. Indeed the thermal conductivity of real materials can be reduced by, e.g. polycrystallinity, presence of impurities or dislocations, or existence of porosity. All in all the agreement of our results with experiments is good enough to allow the discussion of the origin of the increase of the conductivity with temperature.

First, an increase of Lorenz number with temperature due to the pseudo-gap in the electronic density of states at the Fermi level is indeed observed. However this increase amounts at most to 40% of the increase of conductivity even for the stoichiometric material.

Second, the introduction of vacancies does create a thermal and electrical resistance which in turn translates into a rise in thermal conductivity at high temperature. However this resistance is not constant with temperature as it is commonly supposed but rather decreases with temperature.

Eventually, we found an additional phenomenon responsible for the rise of κ: the increase of the density of states (DOS) close to the Fermi level. Electronic conductivity is naturally proportional to the amount of electrons available to conduct heat or charge. This amount is proportional to the DOS at the Fermi level. DOSs are usually implicitly thought to be almost constant with temperature. At the opposite we found an unexpected important increase of the DOS at the Fermi level with temperature. This increase directly increases the electrical and thermal conductivity. Moreover, for a given

temperature, the introduction of vacancies also induces a rise of the DOS at the Fermi level. This effect is therefore important for both the stoichiometric and understoichiometric compounds.

In summary, the mysterious increase of thermal conductivity with temperature in this material has been reproduced and explained. We found that the phonon thermal conductivity is negligible at high temperatures. For the electronic part, three phenomena are responsible for its rise with temperature. The first two were already identified: the semi-metallic shape of the DOS and the additional electrical resistivity induced by carbon vacancies. The last phenomenon, namely the rise of the DOS close to the Fermi level with either temperature or the concentration of vacancies, was not mentioned before. We believe the mechanisms highlighted for ZrC to be valid for other transition metal carbides which also exhibit an increase of conductivity with temperature (e.g. TiC, HfC). This study has recently been published [6]. We plan to check on other metals exhibiting a pseudo gap if the same increase of DOS is also observed and its relation with thermal conductivity evolution.

References

[1] H.F. Jackson and W.E. Lee, "Properties and characteristics of ZrC" in Comprehensive Nuclear Materials, ed. R J M Konings, T R Allen, R E Stoller and S Yamanaka, Elsevier, 2012.

[2] J. Li, D. Liao, S. Yip, Najafabadi R and Ecker L," Force-based many-body interatomic potential for ZrC ", J. *Appl. Phys.* **93**, 9072, 2003.

[3] D. Evans and G. Morriss, "*Statistical Mechanics of Nonequilibrium Liquids"*, Academic, 1990.

[4] X. Gonze *et al*., "ABINIT: First-principles approach to material and nanosystem properties", *Comput. Phys. Commun.* **180**, 2582, 2009.

[5] S. Mazevet, M. Torrent, V. Recoules and F. Jollet, "Calculations of the transport properties within the PAW formalism", *High Energy Density Phys.* **6**, 84, 2010.

[6] J.-P. Crocombette, "Origins of the high temperature increase of the thermal conductivity of transition metal carbides from atomistic simulations", *J. Phys.: Condens. Matter* **25**, 505501, 2013.

Phonon interference and thermal conductance reduction in atomic-scale metamaterials

Haoxue HAN[a*], Yuriy A. KOSEVICH[a,b] and Sebastian VOLZ[a]

[a]*CNRS, UPR 288 Laboratoire d'Énergetique Moléculaire et Macroscopique, Combustion (EM2C), Ecole Centrale Paris, Grande Voie des Vignes, 92295 Châtenay-Malabry, France*

[b]*Semenov Institute of Chemical Physics, Russian Academy of Sciences, Kosygin Street 4, 119991 Moscow, Russia*

**corresponding author: haoxue.han@ecp.fr*

Keywords: Phonon interference, thermal conductance, atomic-scale metamaterials, molecular dynamics.

Context and Objective

Two-photon interference can result in a total cancellation of the photon output because of the coalescence of the two single photons. This interference effect occurs because two possible photon paths interfere destructively, which produces the famous Hong-Ou-Mandel (HOM) dip in the detection probability of the output photons. Similar destructive interference effect which results in a total reflection can be realized in a phonon system [1]. Constant endeavor has been devoted to the precisely control of heat conduction. Recent efforts concentrated on reducing the thermal conductivity κ via nanostructured materials with superlattices and embedded nanoparticles. Most works attributed the reduction in κ to the increased phonon scattering rate and thus the decreased mean free path (MFP), which are particle descriptions. However, the role of destructive phonon-wave interferences is not well understood in the tailoring of thermal transport in a wave picture.

Here, we introduce and model a realistic 3D atomic-scale phononic metamaterial that allows for manipulating the flow of thermal energy [2]. Phonon reflection is generated by exploiting two-path phonon interference on internal interfaces with embedded defects. The 2D planar defects force phonons to propagate through two paths: through unperturbed (matrix) and perturbed (defect) interatomic bonds. The resulting phonon interference yields transmission antiresonances (zero-transmission resonances) in the phonons spectrum that can be controlled by the masses, force constants and 2D concentration of the defect atoms.

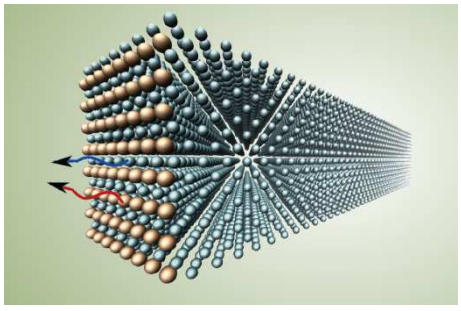

Figure 1: A phononic metamaterial with a FCC lattice containing a defect plane in which an impurity-atom array is embedded. The red and blue curve refer to the phonon path through the impurity atom bonds and through the host atom bonds, respectively.

Model and Methodologies

An atomic presentation of the 3D phononic metamaterial with a face-centered cubic (FCC) lattice including a 2D array of heavy defect atoms is depicted in Fig. (1). When the defects do not fill entirely the defect plane, phonons have two paths to cross such an atom array whereas the phonon path through the host atoms is blocked when the defect layer is constituted by a uniform impurity-atom array, 100% packed with impurity atoms. Two types of atomic metamaterials were studied using realistic interatomic potentials: a FCC lattice of Argon (Ar) where the defects are heavy isotopes and a diamond lattice of Si with Germanium (Ge) atoms as the defects. The interactions between Ar atoms are described by the Lennard-Jones potential. The covalent Si:Si/Ge:Ge/Si:Ge interactions are modeled by the Stillinger-Weber (SW) potential. To probe the phonon transmission, MD-based phonon wave packet (WP) method was used to provide the per-phonon-mode energy transmission coefficient. The spatial width l (coherence length) of the WP is taken much larger than the wavelength λ_c of the WP central frequency, corresponding to the plane-wave approximation.

Results and Discussion

The transmission coefficient $\alpha(\omega)$ of the WP with $l = 20\lambda_c$, retrieved from MD simulations of an Ar metamaterial is presented in Fig. (2). The incident phonons undergo a total reflection on the defect layer at the antiresonance frequency ω_R. Phonon transmission spectra displays an interference antiresonance profile since the two phonon paths interfere destructively at ω_R, analogous to the two-photon interference which results in the HOM dip. A total transmission at ω_T follows the interference antiresonance, which is reminiscent of the Fano resonances. For a uniform defect-atom array, the zero-transmission antiresonance profile will be totally suppressed and replaced by a monotonous decay of transmission with frequency. In the later case, only the phonon path through the defect atoms is accessible.

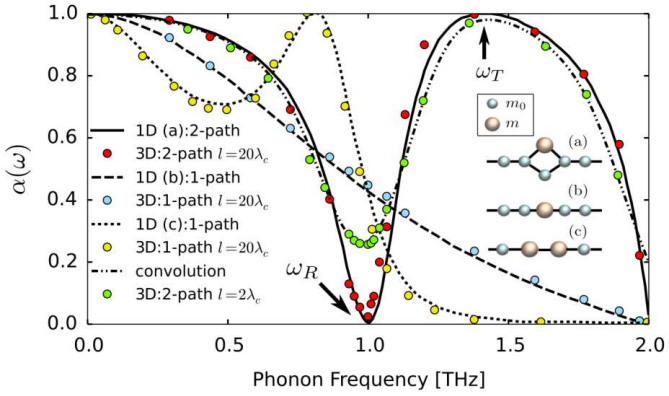

Figure 2: Spectra of phonon energy transmission coefficient predicted by equivalent quasi-1D model (solid and dashed lines) and by MD simulations (symbols) of a 3D Ar metamaterial with planar defect containing heavy impurities, with mass $m = 3m_0$. Dashed-dotted line is the convolution of $\alpha(\omega)$ in Eq. (1) with a Gaussian WP with $l = 2\lambda_c$. Red, blue and yellow symbols represent transmission of WP with $l = 20\lambda_c$ through the two paths, one path with a single and two successive layers of defect atoms, respectively; green symbols represent transmission of WP with $l = 2\lambda_c$ through two paths. (Inset) Three possible quasi-1D lattice models describing phonon propagation through the lattice region containing the local defect.

To further understand the phonon antiresonances caused by the interference between two phonon channels, we use an equivalent model of monatomic quasi-1D lattice of coupled harmonic oscillators [3], depicted in the inset in Fig. (2). In model (a), phonons propagate through two paths: through the host atom bonds, and through those of the impurity atoms, whereas in model (b) and (c), only the second channel remains open. The model (a) gives the energy transmission coefficient for plane wave:

$$\alpha(\omega)=\frac{(\omega^2-\omega_R^2)^2(\omega_{\max}^2-\omega^2)}{(\omega^2-\omega_R^2)^2(\omega_{\max}^2-\omega^2)+C\omega^2(\omega^2-\omega_T^2)^2}, \tag{1}$$

where $\omega_{R,T}$ are the frequencies of the reflection and transmission resonances, $\omega_{\max}$ is the maximal phonon frequency for a given polarization, $\omega_R<\omega_T<\omega_{\max}$. C is a real positive coefficient given by the atomic masses, force constants. The ω_R frequency exists only in the presence of an additional channel which is open for wave propagation through the bypath around the defect atom, see inset (a) in Fig. (2). As follows from Eq. (1) and Fig. (2), $\alpha(\omega_R)=\alpha(\omega_{\max})=0$ and $\alpha(\omega_T)=\alpha(0)=1$. In the transmission of a narrow WP with $l=2\lambda_c$, given by the convolution of $\alpha(\omega)$ for plane wave from Eq. (1) with a Gaussian WP with $l=2\lambda_c$, the interference effect is weakened by more frequency components when the plane-wave approximation ($l\gg\lambda_c$) is broken and the transmission at ω_R is not zero any more, i.e. $\alpha(\omega_R)>0$, which is the case also in the two-photon interference. As depicted in Fig. (2), an excellent agreement in transmission coefficients is demonstrated between the equivalent quasi-1D model provided by Eq. (1) and the MD simulations of the 3D atomic-scale phononic metamaterial with the use of realistic interatomic potential.

We calculate the interfacial thermal conductance G by following the Landauer-like formalism:

$$G=\int\sum_{\nu}\hbar\omega(\mathbf{k},\nu)v_{g,z}(\mathbf{k},\nu)\alpha\frac{\partial}{\partial T}n_{\mathrm{BE}}(\omega,T)\frac{\mathrm{d}\mathbf{k}}{(2\pi)^3},$$

where $\hbar$ is the reduced Planck constant, $v_{g,z}$ the phonon group velocity in the cross-plane direction, $n_{\mathrm{BE}}(\omega,T)=[\exp(\hbar\omega/k_BT)-1]^{-1}$ is the Bose-Einstein distribution of phonons at temperature T, k_B is the Boltzmann constant. The integral is carried out over the Brillouin zone and the sum is over the phonon branches.

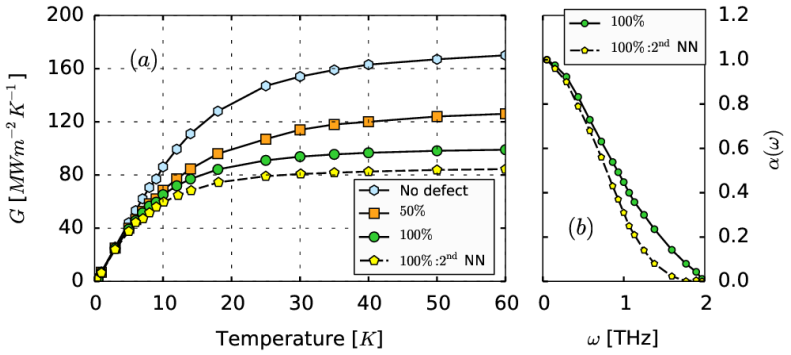

Figure 3: (a) The temperature-dependent interfacial thermal conductance across a defect plane 50%-filled with periodic array of impurities (rectangles) and across a uniform defect plane with (pentagons) and without (circles) the second phonon path induced by non-nearest-neighbor bonds, in comparison with that of a atomic plane without defects (hexagons). (b) $\alpha(\omega)$ for a uniform defect plane with (pentagons) and without (circles) the second phonon path.

By embedding defect atoms in a monolayer, we manage to reduce the thermal conductance by 30% in respect to the case of no defects, as shown in Fig. (3a). This destructive-interference induced effect can be used to explain the remarkable decrease of κ of SiGe alloy with very small amount of Ge, with respect to pristine Si. G is further reduced by considering the second nearest-neighbor bonds C_2 between the host atoms on the two sides of the uniform defect layer in addition to the nearest neighbor bond C_1 linking the host and adjacent defect atoms. This reduction comes from the suppression of phonon transmission at high frequencies, shown in Fig. (3b), which is due to the opening of the second phonon path through the non-nearest-neighbor bonds C_2 interfering destructively with the first path through the nearest-neighbor bonds C_1. The emergence of the second phonon path substantially reduces G by 16% despite the weakness of the corresponding bonds: $C_2 = 0.08C_1$ in the Ar lattice. This demonstrates another advantage of the application of the two-path destructive phonon interference for controlling the heat conduction: more heat flux is blocked by the opening of the additional phonon paths.

Conclusions and Perspectives

In conclusion, we provide comprehensive modeling of atomic-scale phononic metamaterial for the control of heat conduction by exploiting two-path phonon interference antiresonances. Thermal phonons crossing a defect array undergo strong destructive interference, pointing out similarities of the phononic phenomena with their photonic counterparts. Such patterned atomic planes can be considered as high-finesse atomic-scale phononic mirrors. And, at last, we would emphasize that strong optical reflection observed in stereometamaterials can also be interpreted as photon interference antiresonances in optically transparent plane, embedded with periodic plasmonic nanostructures. Our results show that the patterning of the defect-atom arrays can lead to a new departure in thermal energy management, offering potential applications in thermal filters, thermal diodes and thermal cloaking.

References

[1] Yu. A. Kosevich, “Capillary phenomena and macroscopic dynamics of complex two-dimensional defects in crystals”, *Prog. Surf. Sci*. **55**, 1, 1997.

[2] H. Han, L. G. Potyomina, A. A. Darinskii, S. Volz, and Yu A. Kosevich, "Phonon interference and thermal conductance reduction in atomic-scale metamaterials", *Phys. Rev. B* **89**, 180301(R), 2014.

[3] Yu. A. Kosevich, “Multichannel propagation and scattering of phonons and photons in low-dimension nanostructures”, *Physics-Uspekhi*, **51**, 848, 2008.

Session 9

Energy conversion

Increasing thermoelectric efficiency: dynamical models unveil microscopic mechanisms

Giuliano BENENTI[a,b*] and Giulio CASATI[a,b]

[a]*Center for Nonlinear and Complex Systems, Università degli Studi dell'Insubria, Como, Italy*

[b]*INFN, Sezione di Milano, Italy*

**corresponding author: giuliano.benenti@uninsubria.it*

Keywords: coupled charge and energy flows, fundamental aspects of heat to work conversion

The understanding of coupled charge and heat transport in complex systems is a fundamental problem, also of practical interest in connection with the challenging task of developing high-performance thermoelectric heat engines and refrigerators, the low efficiency of existing thermoelectric devices being the factor which limits their use. To investigate this problem, we follow a new approach which starts from first principles i.e. from the fundamental microscopic dynamical mechanisms which determine the phenomenological laws of heat and particle transport. In this connection, as it is well known, the enormous achievements in nonlinear dynamical systems and the new tools developed have led to a much better understanding of the statistical behavior of dynamical systems. For example, the question of the derivation of the phenomenological Fourier law of heat conduction from the dynamical equations of motion has been studied in great detail. Theoretical work in this direction even led to the possibility to control the heat current and devise heat diodes, transistors, and thermal logic gates. We are confident that this theoretical approach, combined with the present sophisticated numerical techniques, may lead to substantial progress on the way of improving thermoelectric efficiency. An additional motivation in favor of this approach is that thermoelectric technology, at small sizes (e.g. at micro or nano-scale), is expected to be more efficient than traditional conversion systems. Indeed the efficiency of mechanical engines decrease very rapidly at low power level. The recent progress in engineering nanostructured materials opens now new possibilities. The study of dynamical complexity of these structures may lead to the design of new strategies for developing materials with high thermoelectric efficiency.

We compute the basic transport coefficients (isothermal charge conductivity, heat conductivity, thermopower, and Peltier coefficient) starting from the microscopic equations of motion of stylized models, including billiard models and single-level quantum dots. The transport coefficients are computed by means of nonequilibrium simulations (stochastic reservoirs) and of the Green-Kubo formula in classical models, while the (multi-terminal) Landauer-Büttiker approach is used for non-interacting quantum systems.

We show that for systems with a single relevant constant of motion, notably momentum conservation, the thermoelectric efficiency reaches the Carnot efficiency in the thermodynamic limit [1]. Such general result is illustrated by means of numerical simulations in the case of a diatomic chain of hard-point elastically colliding particles [1] as well as for a two-dimensional gas of interacting particles [2].

For systems with broken time-reversal symmetry, we show [3] that the maximum efficiency and the efficiency at maximum power are both determined by two parameters: a generalized figure of merit and an asymmetry parameter, given by the ratio of the thermopowers obtained for opposite directions of the magnetic field [3-5]. In contrast to the time-symmetric case, the figure of merit is bounded from

above; nevertheless the Carnot efficiency can be reached at lower and lower values of the figure of merit and far from the so-called strong coupling condition as the asymmetry parameter increases. Moreover, the Curzon-Ahlborn limit for efficiency at maximum power can be overcome within linear response, as we have shown numerically in a few examples (Aharonov-Bohm interferometer formed with three non-interacting quantum dots, transmission windows model) [6]. Finally, always within linear response, it is not forbidden by the laws of thermodynamics to have Carnot efficiency and nonzero power simultaneously [3].

We also discuss the efficiency of a thermal engine working in linear response regime in a multi-terminal configuration [7]. We provide a general definition of local and non-local transport coefficients (electrical and thermal conductances, and thermoelectric powers). Within the Onsager formalism and in the three-terminal case, we derive analytical expressions for the efficiency at maximum power, which can be written in terms of generalized figures of merit. Also, using two examples (single and double dot), we investigate numerically how a third terminal could improve the performance of a quantum system, and under which conditions non-local thermoelectric effects can be observed.

While our approach has been so far limited to the linear response steady-state regime, we can foresee his extension to nonlinear transport as well as to time-dependent drivings, i.e. to microscopic thermal machines performing cycles. Moreover, the above discussed mechanisms could be tested by means of molecular dynamics or other kind of simulations of more realistic models. We know that symmetry breaking together with nonlinearity are at the key ingredients for thermal diodes and transistors and we are confident that relevant results can be obtained on the same basis also with regard to the problem of improving thermoelectric efficiency.

References

[1] G. Benenti, G. Casati, W. Jiao, “Conservation laws and thermodynamic efficiencies”, *Phys. Rev. Lett.* **110**, 070604, 2013.

[2] G. Benenti, G. Casati, C. Mejia-Monasterio, “Thermoelectric efficiency in momentum-conserving systems”, *New J. Phys.* **16**, 015014, 2014.

[3] G. Benenti, K. Saito, G. Casati, “Thermodynamic bounds on efficiency for systems with broken time-reversal symmetry”, *Phys. Rev. Lett.* **106**, 230602, 2011.

[4] K. Saito, G. Benenti, G. Casati, T. Prosen, “Thermopower with broken time-reversal symmetry”, *Phys. Rev. B* **84**, 201306(R), 2011.

[5] M. Horvat, T. Prosen, G. Benenti, G. Casati, “Railway switch transport model”, *Phys. Rev. E* **86**, 052102, 2012.

[6] V. Balachandran, G. Benenti, G. Casati, “Efficiency of three-terminal thermoelectric transport under broken time-reversal symmetry”, *Phys. Rev. B* **87**, 165419, 2013.

[7] F. Mazza, R. Bosisio, G. Benenti, V. Giovannetti, R. Fazio, F. Taddei, “Thermoelectric efficiency of three-terminal quantum thermal machines”, preprint.arXiv:1404.0924, *New J. Phys.* (in press).

Near-field thermodynamics and nanoscale energy harvesting

Ivan LATELLA[a], Agustín PÉREZ-MADRID[a], Luciano C. LAPAS[b] and J. Miguel RUBI[a]*

[a]*Departament de Física Fonamental, Facultat de Física, Universitat de Barcelona, Martí i Franquès 1, 08028 Barcelona, Spain*

[b]*Universidade Federal da Integração Latino-Americana, Caixa Postal 2067, 85867-970 Foz do Iguaçu, Brazil*

**corresponding author: mrubi@ub.edu*

Keywords: near-field thermal radiation, maximum work flux, energy-harvesting nanodevices.

The amount of energy exchanged between bodies separated by a submicron distance is notably higher than that for bodies separated by macroscopic lengths [1-3]. The tunneling of evanescent electromagnetic waves is responsible for this enhancement, an effect that can rise only when the bodies are close to each other. Due to the contribution of evanescent modes, the local density of states is modified near an interface separating two media. This implies that also the thermodynamic functions will depend on this contribution and will show a very different behavior from the corresponding one in the far field case [4]. Furthermore, at the interface of polar materials, the coupling of phononic excitations with the electromagnetic fields results in the so-called surface phonon-polaritons. When two planar sources supporting surface phonon-polaritons are placed at a distance smaller than the thermal wavelength, the resonance of these modes is responsible for the considerable increase of the emitted radiation. These surface waves can be thermally excited at the nanoscale due to their existence in the infrared [5,6].

In addition, using the fluctuation-dissipation theorem, the correlations of electromagnetic fields can be computed, whence the average Poynting vector is obtained [5]. The Poynting vector gives the radiated energy flux $\dot{U}(T)$, and from this quantity the entropy flux $\dot{S}(T)$ can be computed, where T is the temperature of the radiating body. Both energy and entropy fluxes depend on the spectral flux of modes $\varphi(\omega)$ which contains the information about optical properties of the materials. Here, we show that the maximum work that can be obtained from the thermal radiation emitted between two planar sources in the near-field regime is much larger than the one corresponding to the blackbody limit [7]. This quantity and an upper bound for the efficiency of the process are computed from a thermostatistic formulation in the near-field regime. Both maximum work flux and efficiency depend on the optical properties of the materials, and the explicit dependence on the frequency of the surface phonon-polariton has been obtained. In Figure 1, we show the maximum work flux and the upper bound for the efficiency as a function of the temperature of the hot source T_{h} for two materials, hexagonal boron nitride (hBN) and silicon carbide (SiC), and for two different environmental temperatures T_{e}. Once the energy and entropy fluxes are known, the maximum work flux is given by $\dot{\mathcal{W}} = T_{\mathrm{e}}\Delta\dot{S} - \Delta\dot{U}$, where $\Delta\dot{S} = \dot{S}(T_{\mathrm{e}}) - \dot{S}(T_{\mathrm{h}})$ and $\Delta\dot{U} = \dot{U}(T_{\mathrm{e}}) - \dot{U}(c)$, and an upper bound for the efficiency can by computed as $\bar{\eta} = \dot{\mathcal{W}}/\dot{U}(T_{\mathrm{h}})$. The maximum work flux is also called the ideal work flux since it is obtained for a process with no entropy production.

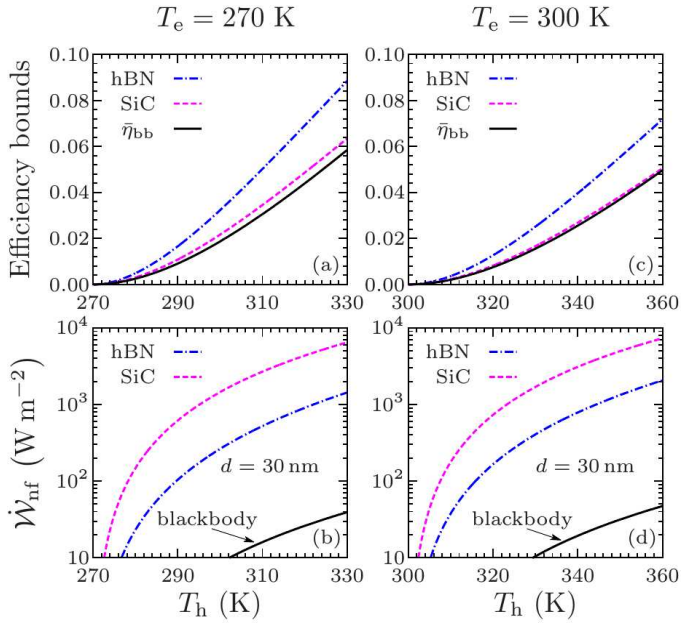

Figure 1: Efficiency bound and ideal work flux as a function of the temperature of the hot source for two different environmental temperatures (taken from Ref. [7]). The materials are modeled by using the Lorentz model for the dielectric constants.

Energy converters can be used with the purpose of capturing thermal energy from their surroundings and transform it into usable work. Here we consider this energy harvesting process in an ideal situation. We consider a semi-infinite medium acting as a thermal energy source at a temperature higher than the environment temperature. This medium could be a certain component of a device which, as a consequence of an independent task, is kept at a working temperature T_h. A second semi-infinite medium is placed near the first one, with a vacuum gap separating the (planar) surfaces of the two media. The second medium is assumed to be in thermal equilibrium with the environment at temperature T_e. Due to the difference of temperatures, a certain amount of work can be extracted from the thermal radiation. This function is assigned to the converter, which can be assumed to be coupled to the medium at temperature T_e. The specific mechanism utilized by the converter to transform the radiation will determine the entropy production and, therefore, the efficiency of the process. If this mechanism is not particularized, bounds for the efficiency and work flux can be obtained by considering an ideal process. In particular, we focus on the case where the difference of temperature between the hot medium and the environment is relatively small. Small temperature differences are the physically relevant situation for energy harvesters at the nanoscale, where near-field thermal radiation is the dominant contribution.

The energy flux can be written as $\dot{U}(T) = \int_0^\infty \mathrm{d}\omega\, \hbar\omega\, n(\omega, T)\, \varphi(\omega)$, where $\hbar$ is the reduced Plank constant, and $n(\omega, T)$ is the average number of photons in a single mode of frequency ω. Introducing the reflection coefficients of the vacuum-material interface $R_\alpha(\kappa, \omega)$ for the polarizations $\alpha = \mathrm{p}, \mathrm{s}$, the spectral flux of modes for two identical half-spaces separated by a vacuum gap of width d is defined by

$$\varphi(\omega) = \sum_{\alpha=\mathrm{p,s}} \left\{ \int_0^{\omega/c} \frac{\mathrm{d}\kappa\, \kappa}{4\pi^2} \frac{[1 - |R_\alpha(\kappa,\omega)|^2]^2}{|1 - e^{2i\gamma d} R_\alpha^2(\kappa,\omega)|^2} + \int_{\omega/c}^\infty \frac{\mathrm{d}\kappa\, \kappa}{\pi^2} \frac{e^{-2|\gamma| d}\, \mathrm{Im}^2[R_\alpha(\kappa,\omega)]}{|1 - e^{-2|\gamma| d} R_\alpha^2(\kappa,\omega)|^2} \right\}, \tag{1}$$

where c is the speed of light in vacuum, and κ is the component of the wave vector parallel to the surfaces satisfying $\gamma = \sqrt{(\omega/c)^2 - \kappa^2}$. Furthermore, the entropy flux associated to the radiation can

be obtained by considering the thermodynamic relation $T^{-1} = d\dot{S}/d\dot{U}$ and, therefore, be written as $\dot{S}(T) = \int_0^\infty \mathrm{d}\omega\, k_B\, m(\omega,T)\, \varphi(\omega)$, where k_B is the Boltzmann constant and we have introduced $m(\omega,T) = [1+n(\omega,T)]\ln[1+n(\omega,T)] - n(\omega,T)\ln n(\omega,T)$. For polar materials supporting surface phonon-polaritons, the main contribution to the spectral flux of modes in the near-field regime is due to p-polarized evanescent waves (the second term in curly brackets in (1) with $\alpha = \mathrm{p}$). As a consequence, the spectral flux of modes in this regime becomes [7,8]

$$\varphi_{\mathrm{nf}}(\omega) = g_d(\omega)\delta(\omega-\omega_0), \qquad g_d(\omega) = \frac{\mathrm{Re}\left[\mathrm{Li}_2\left(R_{\mathrm{p}}(\omega)\right)\right]}{4\pi d^2 f'(\omega)}, \tag{2}$$

where δ is a Dirac-delta distribution, ω_0 is the frequency of the surface phonon-polariton, $\mathrm{Li}_2(z)$ is the dilogarithm function, and $f(\omega) = \mathrm{Im}\left[R_{\mathrm{p}}(\omega)^2\right]/\mathrm{Im}^2\left[R_{\mathrm{p}}(\omega)\right]$ so that $f'(\omega) = df(\omega)/d\omega$. Thus, using (2), the considered thermodynamic quantities show an explicit dependence on the resonance frequency ω_0.

The formulation of the thermodynamics in the near-field regime sheds light on thermal radiation energy conversion exploiting optical properties of the emitters. In particular, our analysis highlights how these properties influence the performance of an energy-harvesting process. This analysis can be further elaborated by taking into account a concrete converter and, according to the specific conversion mechanism, including the corresponding entropy production. This will provide a better bound for the efficiency, as happens with blackbody radiation.

References

[1] E. Rousseau, A. Siria, G. Jourdan, S. Volz, F. Comin, J. Chevrier, and J.-J. Greffet, "Radiative heat transfer at the nanoscale", *Nature Photon.* **3**, 514, 2009.

[2] S. Shen, A. Narayanaswamy, and G. Chen, "Surface Phonon Polaritons Mediated Energy Transfer between Nanoscale Gaps", *Nano Lett.* **9**, 2909, 2009.

[3] A. Pérez-Madrid, L. C. Lapas, and J. M. Rubi, "Heat Exchange between Two Interacting Nanoparticles beyond the Fluctuation-Dissipation Regime", *Phys. Rev. Lett.* **103**, 048301, 2009.

[4] I. Dorofeyev, "Thermodynamic functions of fluctuating electromagnetic fields within a heterogeneous system", *Phys. Scr.* **84**, 055003, 2011.

[5] K. Joulain, J.-P. Mulet, F. Marquier, R. Carminati, and J.-J. Greffet, "Surface electromagnetic waves thermally excited: Radiative heat transfer, coherence properties and Casimir forces revisited in the near field", *Surf. Sci. Rep.* **57**, 59, 2005.

[6] A. I. Volokitin and B. N. J. Persson, "Near-field radiative heat transfer and noncontact friction", *Rev. Mod. Phys.* **79**, 1291, 2007.

[7] I. Latella, A. Pérez-Madrid, L. C. Lapas, and J. M. Rubi, "Near-field thermodynamics: Useful work, efficiency, and energy harvesting", *J. Appl. Phys.* **115**, 124307, 2014.

[8] E. Rousseau, M. Laroche, and J.-J. Greffet, "Asymptotic expressions describing radiative heat transfer between polar materials from the far-field regime to the nanoscale regime", *J. Appl. Phys.* **111**, 014311, 2012.

Detailed analysis of heat generation in silicon solar cells

Romain COUDERC[a,b,*], Mustapha LEMITI[b] and Mohamed AMARA[a]

[a]*Université de Lyon, CNRS, INSA-Lyon, UCBL, CETHIL, UMR5008, F-69621, Villeurbanne, France*

[b]*Université de Lyon, CNRS, INSA-Lyon, UCBL, INL, UMR5270, F-69621, Villeurbanne, France*

**corresponding author: romain.couderc@insa-lyon.fr*

Keywords: heat generation, joule, superposition, silicon solar cell.

Introduction

In recent year the researches devoted to increase electrical conversion efficiency have led to the limit of 25% [1] at standard conditions i.e., AM1.5 spectrum and cell temperature at 25°C. However, the performances during their use are lower. This degradation caused by the temperature is generally described mathematically with a linear expression of the efficiency given by $\eta=\eta_{st}(1-\beta(T-T_{st}))$, where η_{st} is its value at cell's temperature equal of 25°C. A review of β coefficient is summarized by Skoplaki *et al*.[2].

The general approaches available in literature to predict thermal behavior of PV cell, consist to use empirical correlations which link cell's temperature to its environmental conditions (ambient temperature, solar irradiation, etc.) [2]. Other methods are based a resolution of energy balance equation, i.e., the incident solar irradiation absorbed within the PV panel is balanced between the electrical and the thermal energy. A good review of this approach is given by Jones *et al*. [3]. On the other hand, there are a few theoretical studies about coupling heat transfer and carriers transport in semiconductor devices [4]–[7]. Only Vaillon *et al*. studied silicon solar cells in particular. However, its thermal model based on [6] did not included heats sources generated by thermoelectric and Joule effects outlined by Lindefelt and Watchutka.
The purpose of the present paper is to propose an insight into heat generation in silicon solar cells. The paper starts with the description of the physical problem. Then, a detailed analysis of heating and cooling mechanisms within the photovoltaic cell under short-circuit conditions are discussed. And finally, the variation of the temperature of a solar cell as a function of the applied bias is presented.

Simulation parameters

To study the thermal and electrical behavior in a solar cell, a set of parameters related to the cell characteristics are listed in Table I and a scheme of the studied n^+p junction solar cell is shown in Fig. 1.

The results are obtained under AM1.5G illumination. The surroundings areas are modeled as a black body at 25°C exchanging radiative energy with the solar cell. The ambient temperature is set to 25°C, and a convective thermal transfer is considered via a symmetrical convection coefficient *h* at the boundaries of the cell.

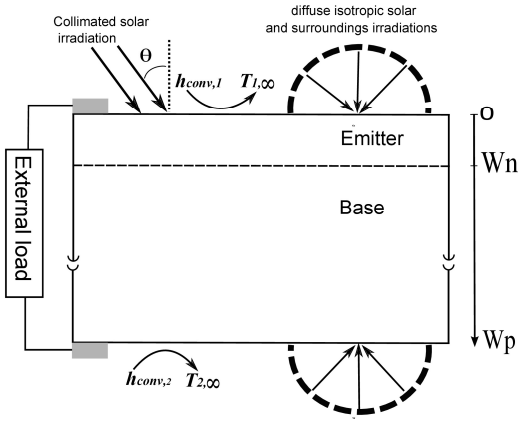

Figure 1: One dimension model of a n^+p solar cell

Base doping (p-type, uniform)	10^{15} cm^{-3}
Emitter doping (n-type,	10^{19} cm^{-3}
Junction depth	300 nm
Wafer thickness	250 µm
Front surface recombination	1000 cm.s^{-1}
Rear surface recombination	10000 cm.s^{-1}
No front antireflection coating	
Si/Air back interface	

Table 1: Parameters of the simulated solar cell

The different values used for the symmetrical convection coefficients are: h=2 W.m^{-2}.K^{-1} (very low natural convection, no wind), h=5 W.m^{-2}.K^{-1} (natural convection, weak wind), h=10 W.m^{-2}.K^{-1} (strong natural convection, strong wind) and h=100 W.m^{-2}.K^{-1} (forced convection, cooling system). The simulations are performed thanks to the coupled solution of the radiative transfer problem, the continuity equations and the thermal transfer equation. The operating temperature of the cell depends on the illumination, the radiative and convective thermal transfers and the efficiency of the cell.

Discussion about non-isothermal conditions

The thermal sources and the thermal boundaries conditions determine the operating temperature of the cell. Among the thermal sources of a solar cell, the Thomson and the Joule effect [4] are of particular interest regarding that they had been ignored until this paper for the analysis of the heat generation in a solar cell. For the sake of brevity, we only focus on these effects at J_{sc} in this abstract.

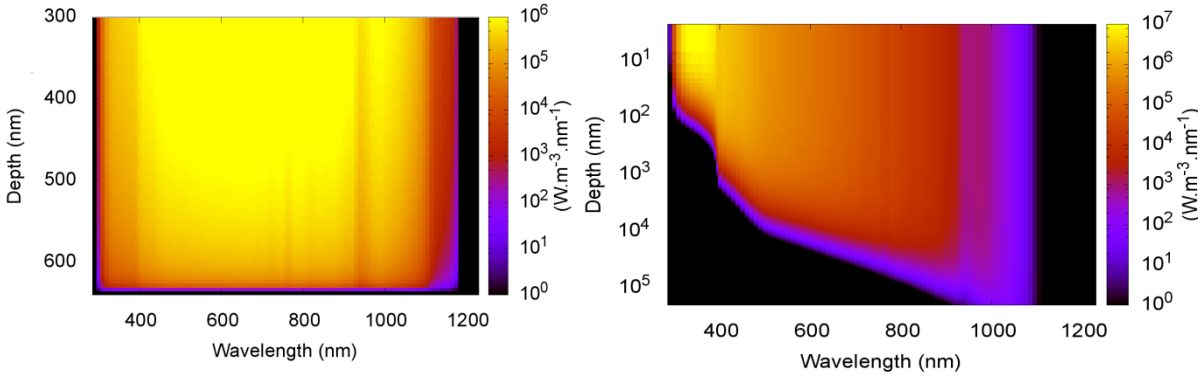

(a) (b)

Figure 2: Spatial and spectral map of heat generation from Joule effect (a) and thermalization (b) of the charge carriers

Fig.2 portrays the local spectral heat generation within the depletion region due to the Joule effect at J_{sc} The rest of the cell is assumed to be quasi-neutral, i.e., E=0. Furthermore, only heat generation within the base part of the depletion area is shown because the doping characteristics of the cell leads to a very thin charge zone in the emitter, i.e. X_N= 0.3nm and X_P=341 nm (see Fig.1). Basically, within the SCR zone, the maximum value of electric field occurs at metallurgical junction (top of Fig.2a) and vanishes at its boundaries. The current flow is uniform through the cell. These two facts lead to a decrease of heat generation in-depth of the depletion zone. As for the low value of the Joule heat

source for the wavelength in between 300 and 400 nm and in between 1100 and 1200 nm, this is readily explained by the low value of irradiation in these spectral ranges. Fig.2b shows the heat generation from the thermalization of the charge carriers at J_{sc}.

The Thomson effect reflects the balance between the generation and the recombination of carriers for each position in the cell. In regions where the recombinations exceed the generation rate, the Thomson effect generates heat whereas where the generation is higher than the recombination, it carries out of the cell heat. These behaviors are shown in Fig.3.

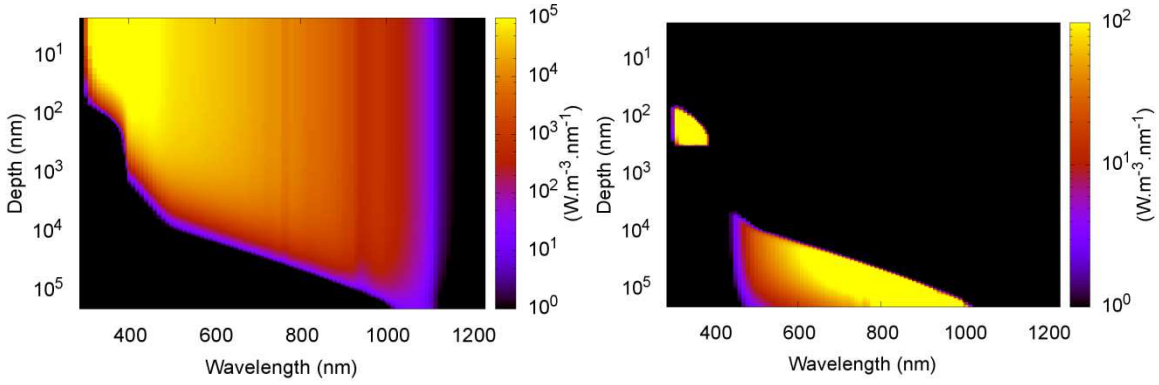

(a) (b)

Figure 3: Spatial and spectral maps of Thomson effect: (a) Heat source, (b) Heat sink

In the usual analysis, in application of the principle of superposition, the temperature is determined at J_{sc} and then considered constant for all polarizations although NRR and Joule heat sources vary with voltage. These variations change the thermal equilibrium of the solar cell and consequently the operating temperature. Fig.4a represents the different thermal sources and sinks at short-circuit J_{sc}, maximum power point M_{pp} and open-circuit V_{oc} conditions.

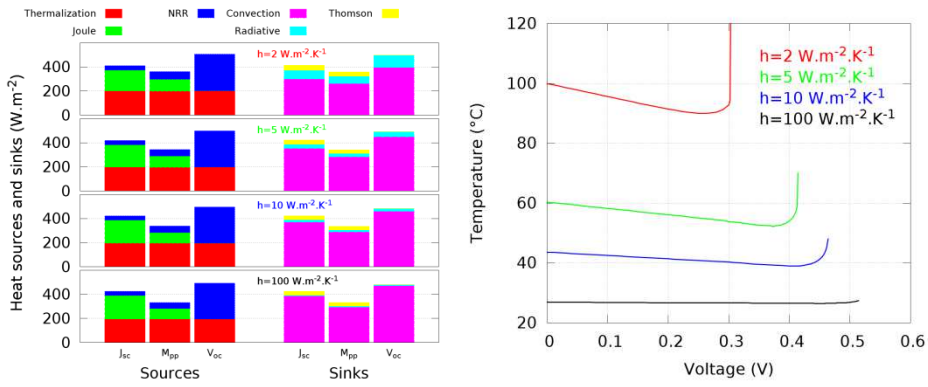

(a) (b)

Figure 4: Heat sources and sinks of the solar cell at J_{sc}, M_{pp} and V_{oc} conditions on the left (a) and temperature of the solar cell as a function of applied voltage for h = 2, 5, 10 and 100 W.m^{-2}.K^{-1} on the right (b)

Three sources are considered: thermalization of the carriers, the Joule effect and the NRR heat source. The sources are very similar for a given voltage for any *h* because the sources are quite independent of the convective conditions. Thermalization is almost constant with the applied voltage and *h*.

At J_{sc}, the Joule and the thermalization sources are equally important whereas the NRR source is small compared to the two others. The Joule heat source is important at J_{sc} because the photocurrent losses energy during the crossing of the potential barrier of the cell via phonon emission whereas at V_{oc}, no current flows in the solar cell thus the Joule heat source is null. On the contrary, the NRR thermal

source is low at J_{sc} and increases with the voltage to reach a maximum at V_{oc}. The diode is blocked at J_{sc}, so the recombinations are low, but approaching V_{oc}, the potential barrier of the junction decreases, increasing the amount of recombination to reach the total amount of photogenerated charges.
Convection is the main heat sink for any h and any voltage, and the higher h, the lower the temperature at any polarization. The two other sinks, Thomson and radiative, are weak in comparison with convection, although they affect the temperature. Fig.4b depicts the variation of the temperature as a function of the applied voltage resulting from the equilibrium between heat sources and sinks. The greater the value of h, the weaker the radiative sink because the temperature of the cell is lower hence the cell emits less than with low h. Convection has little impact on the Thomson sink, which falls from its maximum value at J_{sc} where recombinations are low, to zero at V_{oc} where recombinations and generation are equal.

For large h, the temperature is rather invariant with respect to the bias of the cell. The greater the value of h, the lower the temperature at any polarization. It is worth noting that the lowest temperature is reached close to M_{pp} which is consistent with the fact that when the electrical output is maximal, the thermal losses that heat the cell are close to the minimum. This is important because the more efficient a solar cell is, the lower the operating temperature will become. One can also note that the temperature attains a maximum at V_{oc} in accordance with the fact that all the absorbed energy is transformed into heat at $V_{oc.}$

Conclusion

A coupled solution of the multiphysics problem taking place in a solar cell is used to analysis the heat generation in a solar cell. The detailed analysis shows that the consideration of the variation of the temperature of a solar cell with the applied bias is not negligible when h is low. Therefore, we recommend that the nominal operating cell temperature be determined at M_{pp} instead of V_{oc} as defined in the ASTM standard and to take into account the temperature at M_{pp} in the optimization of solar cells.

References

[1] M. A. Green, K. Emery, Y. Hishikawa, W. Warta, and E. D. Dunlop, “Solar cell efficiency tables (version 43)”, *Prog. Photovoltaics Res. Appl.*, vol. **22**, no. 1, pp. 1–9, 2014.

[2] E. Skoplaki and J. a. Palyvos, “On the temperature dependence of photovoltaic module electrical performance: A review of efficiency/power correlations”, *Sol. Energy*, vol. **83**, no. 5, pp. 614–624, 2009.

[3] A. D. Jones and C. P. Underwood, “A thermal model for photovoltaic systems”, *Solar Energy*, vol. **70**, no. 4, pp. 349–359, 2001.

[4] U. Lindefelt, “Heat generation in semiconductor devices”, *J. Appl. Phys.*, vol. **75**, no. 2, p. 942, 1994.

[5] G. K. Watchutka, “Rigorous Thermodynamic Treatment of Heat Generation and Conduction in Semiconductor Device Modeling”, *IEEE Trans. Comput. aided Des.*, vol. **9**, no. 11, pp. 1141–1149, 1990.

[6] M. Dramicanin, Z. Ristovski, P. Nikolic, D. Vasiljevic, and D. Todorovic, “Photoacoustic investigation of transport in semiconductors: Theoretical and experimental study of a Ge single crystal”, *Phys. Rev. B*, vol. **51**, no. 20, pp. 14226–14232, 1995.

[7] R. Vaillon, L. Robin, C. Muresan, and C. Menezo, “Modeling of coupled spectral radiation , thermal and carrier transport in a silicon photovoltaic cell”, *Int. J. Heat Mass Transf.*, vol. **49**, pp. 4454–4468, 2006.

Low concentration solar-thermophotovoltaic system using high-temperature photonics

Makoto SHIMIZU[a*], Asaka KOHIYAMA[a], Fumitada IGUCHI[a] and Hiroo YUGAMI[a]

[a]*Graduate School of Engineering, Tohoku University, Aoba6-6-01 Aramaki Aoba-ku, Sendai, Japan*

**corresponding author: m_shimizu@energy.mech.tohoku.ac.jp*

Keywords: Thermophotovoltaic, Thermal radiation, Solar selective absorber, Selective emitter, Multi-layer coating,

Solar thermophotovoltaic generation systems (STPV) are a type of a photovoltaic generation system. In this system, the solar absorber, heated by the irradiated solar energy, causes the emitter to heat up and radiate thermal energy; the thermal radiation from emitters is then converted into electricity at a photovoltaic (PV) cell as shown in Fig. 1. Some advantages over conventional PV generation systems can be seen in STPV system. For instance, it is possible to control the thermal radiation spectrum of the emitter to optimize electron excitation in the inherent sensitive region. By such spectral matching in a single-junction PV cell, a PV conversion efficiency comparable to that of a triple-junction PV cell system can be obtained. Furthermore, in this system, the power generation density is very high, and unlike a multi-junction cell, the generation efficiency is not sensitive to seasonal solar spectrum fluctuations.

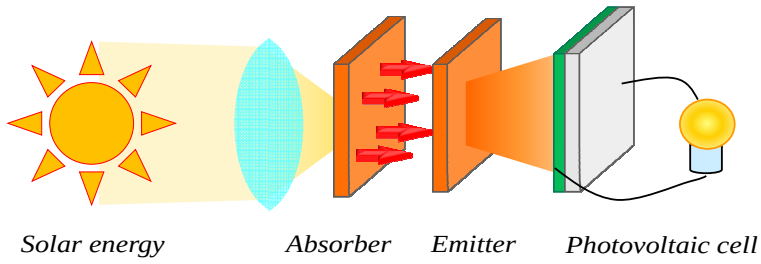

Figure 1: Schematic illustration of solar-TPV system.

In recent years, the study of solar-TPV systems has attracted attention. In 2014, an MIT group reported 3% net efficiency of a solar-TPV system. This system uses an InGaAs cell that has a 0.55 eV bandgap and an operating temperature of 1285 K [1]. System efficiencies of STPVs [1-4] have gradually increased through technological improvements, but remain low. The low system efficiency is mainly a result of excessive heat loss from the high-temperature absorber/emitter. Therefore, suppressing energy losses is necessary to obtain a high efficiency system.

To obtain high system efficiency on STPVs, two main losses should be reduced. One is the energy losses at absorber such as reflection and infrared radiation losses and the other is at emitter such as spectrum mismatch with spectral response of TPV cells. Therefore, we can improve the energy efficiency by controlling thermal radiation spectrum, which we call “High-temperature photonics”, on both absorber and emitter. In this study, we develop a high-efficiency STPV using a monolithic planar spectrally selective absorber/emitter. Power generation tests in the fabricated equipment were conducted using a GaSb TPV cell under a concentration ratio of solar irradiance of several hundreds using a solar simulator.

In STPV, solar irradiance is converted into useful thermal radiation at the emitter. Therefore, in these kinds of systems, regarded as photon-photon conversion systems, spectral matching with PV cells in order to attain high operating temperatures with low input power is critical for obtaining high efficiency. With this in mind, we considered the planar absorber/emitter as being appropriate for a STPV. Owing to the small surface area, the input power required for a planar type absorber/emitter can be reduced to one third of volumetric cavity type absorber/emitter for the same temperature. However, the optical losses of the planer type absorber/emitter cannot be ignored. Therefore, for efficient photon-photon conversion in STPVs using a planar absorber/emitter, it is important to control thermal radiation spectrum from both absorber and emitter surfaces.

The monolithic planer absorber/emitter, which has absorber and emitter on the front and back sides of a single planer metal substrate, is fabricated. For the absorber/emitter, the spectrally selective properties are obtained by fabricating a multi-layered coating that consists of thin film tungsten (W) layer sandwiched between yttria stabilized zirconia (YSZ) layers as depicted in the inset of Fig. 2 (a). Spectrally selective absorption, regarded as emission, could be a product of destructive interference. Therefore, the enhanced wavelength range can be controlled by thickness of the coatings as shown in Fig. 2 (a). Optimum properties calculated from measured reflectance of the absorber and the emitter are shown in Fig. 2 (b). The optical properties are well consistent with simulated results.

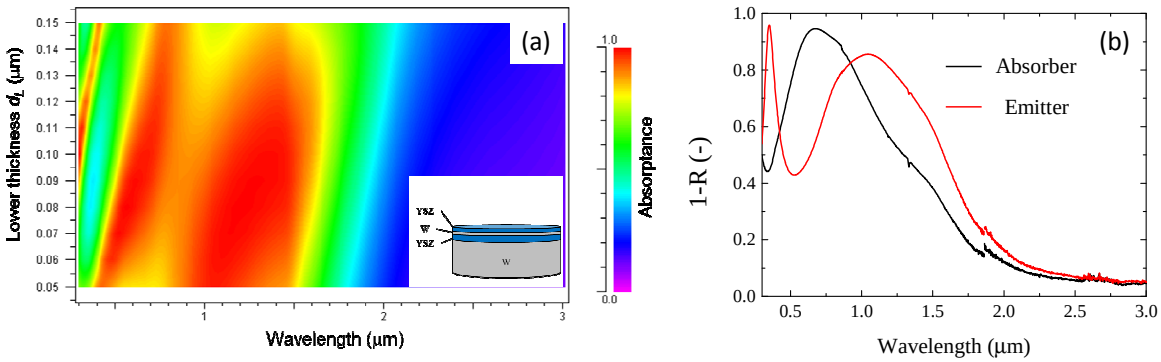

Figure 2: (a) Contour of absorptance spectra for various thickness of lower YSZ layer. (b) Absorptance spectra calculated from measured reflectance of fabricated absorber and emitter.

The solar-TPV system was designed and fabricated to conduct a power generation test. In this system, a solar simulator was used as a light source to conduct the experiment under stable conditions. The energy density of the light can be adjusted from 8 to 100 W/cm^2. The incident light reaches the absorber through ϕ9 mm pinhole. The absorber is fabricated on ϕ9 mm area at center of ϕ15 mm substrate. A silicon dioxide filter is attached to the emitter with a small gap that blocks infrared radiation. Gap between a GaSb TPV cell (10 × 15 mm) and the emitter is 30 mm and the cell is mounted on the stainless steel water jacket to prevent degradation of TPV cell performance. The test was conducted under a high-vacuum condition (1.0×10^{-5} Pa). Reached temperature as a function of input power is shown in Fig. 3. The required power to obtain working temperature can be drastically reduced from our previous study using blackbody cavity type absorber/emitter [2]. As shown in Fig. 3, over 1500 K, which is sufficient to perform power generation by GaSb TPV cell, is obtained by incident power less than 1000 sun.

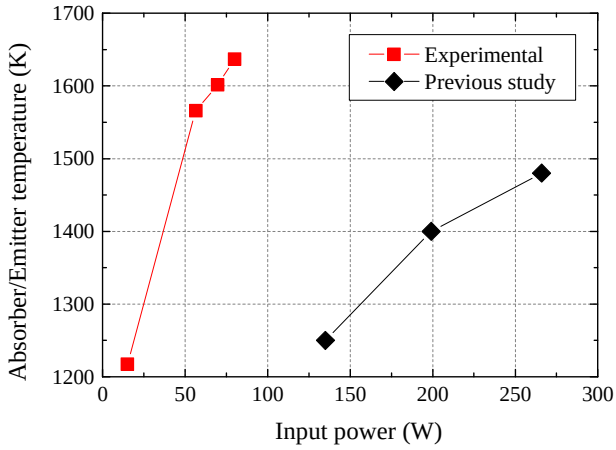

Figure 3: Temperature of absorber/emitter as a function of input power comparing with previous STPV system [2].

From the test, the system efficiency η_{system} is calculated from the following formula,

$$\eta_{system} = \frac{P_{\max}}{E_{solar}} \times F_{emitter-cell} \tag{1}$$

where E_{solar} is incident light power from the solar simulator, P_{max} is the maximum output power from the cell, and $F_{emitter\text{-}cell}$ is view factor between the emitter and the cell. Therefore, η_{system} indicates the efficiency when thermal radiation from the emitter is fully reached to the cell, i.e. view factor is assumed to be 1. The highest η_{system} of 8% is obtained at 1640 K. The maximum PV conversion efficiency of 23% was also achieved at 1640 K. Though the incident power density is almost similar to 1 sun, due to small $F_{emitter\text{-}cell}$ (≈ 0.01), the achieved efficiency exceeded 20%, which is defined as the Shockley–Quisser limit [5] for a GaSb bandgap energy of 0.67 eV.

In this paper, we describe STPV system using a high-temperature photonics. For solar absorber/emitters, reaching very high temperatures with low input solar power is essential for high efficiency. We designed the STPV system using the monolithic planer spectrally selective absorber/emitter based on multi-layer coating, in order to experimentally evaluate the system efficiency. Temperature of the absorber emitter is reached at over 1500 K by input power lower than 1000 sun. This energy density can be easily obtained by Fresnel type concentrator. A PV conversion efficiency of 23% exceeded the Shockley–Quisser limit is achieved due to the spectral matching. High system efficiency of 8% comparing with the previous studies is also indicated taking into consideration a view factor. It is expected that these results have a great contribution to practical realization of STPV systems.

References

[1] A. Lenert, D. M. Bierman, Y. Nam, W. R. Chan, I. Celanovic, M. Soljacic, and E. N. Wang, ″A nanophotonic solar thermophotovoltaic device″, *Nature nanotechnology*, **9**, 126, 2014.

[2] H. Sai, H. Yugami, K. Nakamura, N. Nakagawa, H. Ohtsubo, and S. Maruyama, ″Selective emission of $Al_2O_3/Er_3Al_5O_{12}$ eutectic composite for thermophotovoltaic generation of electricity″, *Japanese Journal of Applied Physics Part 1-Regular Papers Brief Communications & Review Papers***, 39**, 1957, 2000.

[3] A. S. Vlasov, V. P. Khvostikov, O. A. Khvostikova, P. Y. Gazaryan, S. V. Sorokina, and V. M. Andreev, ″TPV systems with solar powered tungsten emitters″, *AIP Conference Proceedings*, **890**, 327, 2007.

[4] A. Datas and C. Algora, ″Development and experimental evaluation of a complete solar thermophotovoltaic system″, *Progress in Photovoltaics*, **21**(5), 1025, 2013.

[5] W. Shockley and H. J. Queisser, ″Detailed Balance Limit of Efficiency of p-n Junction Solar Cells″, *Journal of Applied Physics*, **32**(3), 510, 1961.

Session 10

Subwavelength radiation (2)

Thermal radiation between two plates: regime map and analytical expressions for the net radiative heat flux from far to near field

Jeff MAYO[a], Yoichiro TSURIMAKI[b,c], P.-Olivier CHAPUIS[b], Junnosuke OKAJIMA[c], Atsuki KOMIYA[c], Shigenao MARUYAMA[c], Arvind NARAYANASWAMY[a*] and Rodolphe VAILLON[b*]

[a]*Department of Mechanical Engineering, Columbia University, NY 10027, New York, USA*

[b]*Université de Lyon, CNRS, INSA-Lyon, UCBL, CETHIL, UMR5008, F-69621, Villeurbanne, France*

[c]*Institute of Fluid Science, Tohoku University, 980-8577, Sendai, Japan*

**corresponding authors: arvind.narayanaswamy@columbia.edu, rodolphe.vaillon@insa-lyon.fr*

Keywords: micro and nanoscale thermal radiation, thermal insulation, interferences, far-field/transition/near-field regimes.

It is now well understood that the net radiative heat flux exchanged by two bodies at different temperatures depends on the distance between the bodies [1]. At large distances, the usual laws of incoherent thermal radiation (use of the specific intensity, Stefan-Boltzmann and Wien's law,…) hold. This is the *far-field regime*. At distances smaller than the characteristic wavelength for thermal radiation, usually estimated as being the Wien's wavelength of thermal radiation (10 µm at room temperature), the contribution of evanescent waves appears. When the distance becomes very small, the heat flux due to the evanescent waves is dominant and can exceed the far-field radiative heat flux by several orders of magnitude. This is the *near-field regime* for thermal radiation.

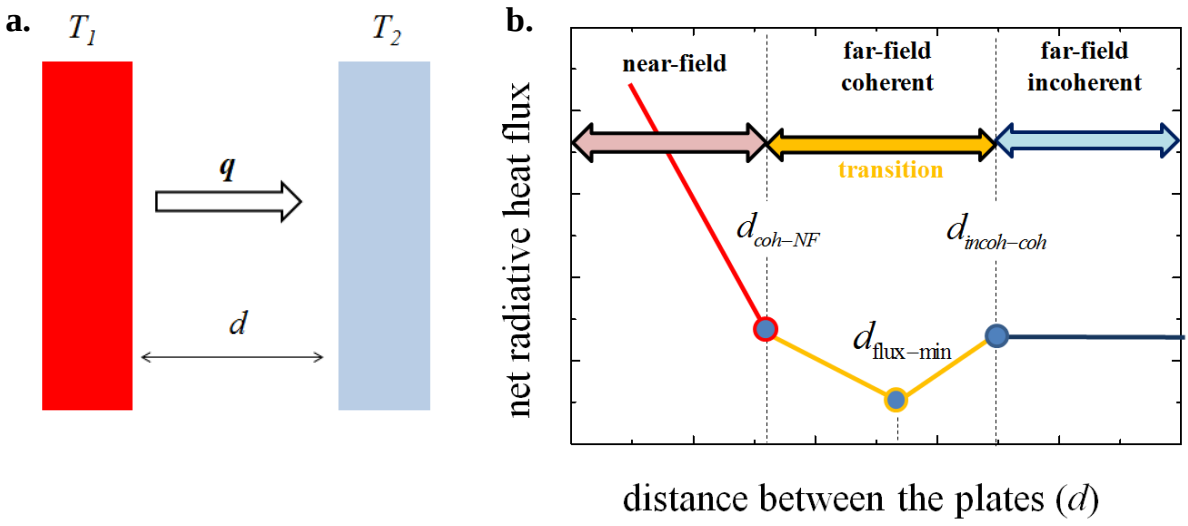

Figure 1: a. Two parallel plates at different temperatures T_1 and T_2 exchanging heat through thermal radiation. b. far-field to near-field regimes for thermal radiation between the two plates.

The *transition zone* between the near-field and the classical macroscopic thermal radiation is the focus of the present study. It is often estimated that the broadband spectrum of thermal radiation does not allow observing sharp interference features. For a monochromatic radiation, interference of multiply-reflected waves in the vacuum gap between the plates can lead to a decrease of the net radiative heat

flux, unless the evanescent wave contribution overrides it. The present work shows that a decrease of the net radiative heat flux in comparison to the far-field value is possible even in the case of broadband thermal radiation. This is a consequence of the existence of a far-field coherent regime, which had been overlooked in past studies. We provide the characteristic distances defining (i) the transition between the far-field incoherent regime and the far-field coherent regime $d_{incoh\text{-}coh}$ and (ii) the transition between the far-field coherent regime and the near-field regime $d_{coh\text{-NF}}$. In addition, we provide the distance at which the net radiative heat flux is minimum $d_{\text{flux-min}}$ for the case of metals and an analytical expression of the flux value. All the characteristic distances are given by equalities $T.d = f(\varepsilon)$, where the function f depends on universal constants k_B, c, $\hbar$ and on the optical properties of the involved materials.

To do so, we first compute the net radiative heat transfer flux exchanged by two semi-infinite parallel plates as a function of the distance between the plates for various dielectric and metallic materials using the expression proposed by Polder and Van Hove [2]. Spectral and directional analyses of the transmission term in the formulation of the propagative component of the flux allow emphasizing the conditions of existence of constructive interferences and of reduction of the exchanged radiative heat flux [3,4]. The temperature and distance dependence of the radiative heat transfer coefficient is investigated. For aluminium, Figure 2.a shows that the location where the flux starts to decrease ($T.d_{incoh\text{-}coh}$) and the location of the minimum ($T.d_{\text{flux-min}}$) are superimposed for all temperatures [3,4]. For silicon carbide (Figure 2.b), there is not necessarily a unique minimum and a wavy behaviour can be observed for the propagative contribution to the radiative heat transfer coefficient.

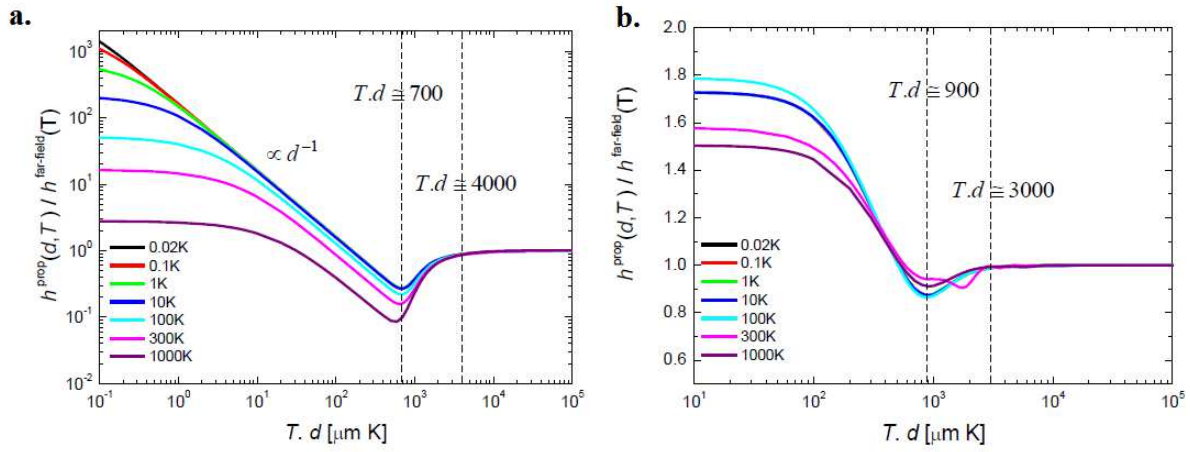

Figure 2: a. Far-field (propagating wave) conductance h=lim q/δT for a metal (Al). b. Far-field thermal conductance h for a resonant dielectric (SiC)

Then, we derive analytically approximate equations defining the far-field regime and the regions of decreasing or increasing fluxes in the transition regime. We also find analytically the distance at which a minimum is observed (see [5] for metallic materials). As a result, laws defining boundaries between incoherent far-field, coherent far-field – when it exists – and near-field regimes of thermal radiation between plates made of the same material are proposed.

Finally, experimental conditions that would allow the observation of a decrease of the net radiative heat flux exchanged by two parallel plates made of bulk metals, and ways of enhancing the amplitude of this decrease are discussed. Future analyses will investigate the impact on the aforementioned observations of surface roughness and temperature dependence of the permittivities.

References

[1] M.F. Modest, *Radiative heat transfer*, third edition, Academic Press, New York, 2013.

[2] D. Polder, M. Van Hove, "Theory of radiative heat transfer between closely spaced bodies", *Physical Review B* **4**, 3303-3314, 1971.

[3] Y. Tsurimaki, P.-O. Chapuis, R. Vaillon, J. Okajima, A. Komiya, S. Maruyama, "Radiative heat transfer between two semi-infinite parallel plates in the far-to-near field transition regime", *in: Proceedings of the 2nd international Workshop on Micro and Nano Thermal Radiation*, Shanghai, China, June 7-9, 2014.

[4] Y. Tsurimaki, P.-O. Chapuis, R. Vaillon, J. Okajima, A. Komiya, S. Maruyama, "Reducing thermal radiation between parallel plates in the far-to-near field transition regime", *in: Proceedings of the 15th International Heat Transfer Conference*, Kyoto, Japan, Aug. 10-15, 2014.

[5] J. Mayo and A. Narawanaswamy, "Minimum radiative transfer between two metallic planar surfaces", *in: Proceedings of the 11th AIAA/ASME Joint Thermophysics and Heat Transfer Conference*, Atlanta, USA, June 16-20, 2014.

Heat transfer between anisotropic nanoparticles: enhancement and switching

Roberta INCARDONE[a,b], Thorsten EMIG[c] and Matthias KRÜGER[a,b]

[a]*Max-Planck-Institut für intelligente Systeme – Heisenbergstr. 3, D-70569 Stuttgart, Germany*

[b]*Institut für Theoretische Physik IV, Universität Stuttgart – Pfaffenwaldring 57, D-70569 Stuttgart, Germany*

[c]*Laboratoire de Physique Théoriqueet Modèles Statistiques, CNRS UMR 8626- Bât. 100, Université Paris-Sud, 91405 Orsay cedex, France*

**corresponding author: incardo@is.mpg.de*

Keywords: theoretical science, tunability of the heat transfer, transfer switch, radiative heat transport.

We theoretically study heat transfer between two anisotropic nanoparticles in vacuum, using scattering theory [1]. We derive closed expressions for nanoparticles, whose scattering properties are well described by their anisotropic dipole polarizabilities. The heat transfer between anisotropic nanoparticles allows for a large freedom of tunability. For a typical dielectric material, the transfer between anisotropic particles (i.e. spheroids) can be 30-40 times as large as for two isotropic objects (i.e. spheres) of equal volumes. Such increase with anisotropy is also found for the heat emission of an isolated small spheroid. Furthermore, we observe a strong dependence of transfer on the relative orientation (factors up to 10^3 or 10^4 by a simple twist of one of the objects), yielding the interpretation as a heat transfer switch.

Considering a typical material for the two interacting objects, SiC, we express the dielectric constant $(\varepsilon(\omega))$ as follows [2]

$$\varepsilon(\omega) = \varepsilon_\infty \frac{\omega^2 - {\omega_{LO}}^2 + i\omega\gamma}{\omega^2 - {\omega_{TO}}^2 + i\omega\gamma} \quad . \tag{1}$$

Here $\varepsilon_\infty = 6.7$, and ω_{LO}, ω_{TO} and γ take values 0.12, 0.098 and 5.88 x 10^{-4}, all in eV, see Fig.1.

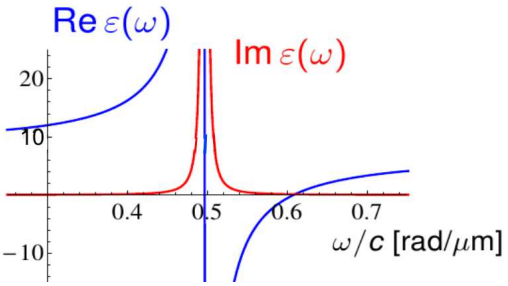

Figure 1: Representation of the imaginary and real part of the dielectric constant for SiC.

SiC supports surface resonances, so called surface phonon polaritons, and is hence a good candidate for radiative near-field heat transfer [3,4]. Figure 1 shows the transfer as a function of the eccentricity.

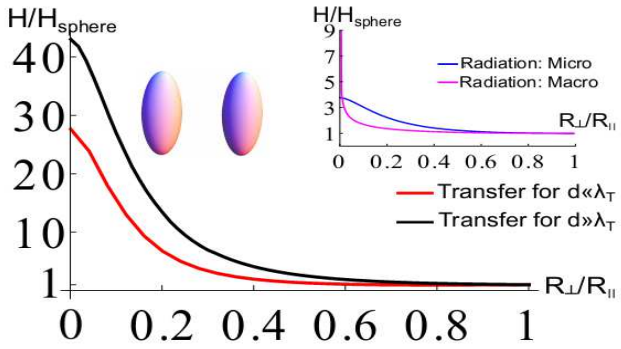

Figure 2: Heat transfer between two identical parallel spheroids with $T_1 = 300\ K$ and $T_2 = 0\ K$, of fixed volumes as a function of $R_\perp/R_\parallel$ (radii that characterize them) in the limit of small (red curve) and large (black curve) distance. Inset: Dashed blue and magenta lines represent the heat radiantion of an isolated microspheroid and a macroscopic spheroid (computed by Stefan-Boltzmann law), respectively. All curves in the figure are normalized by the value for spheres with volumes equal to the spheroid volumes. Note that in all the curves, the particles are considered small enough such that their radiation is proportional to their volumes.

The inset of Fig. 2 shows the transfer as a function of relative angle β, displaying a pronounced dependence. Main graph represents the quality, defined as the ratio between maximal and minimal value in the inset, as a function of the eccentricity.

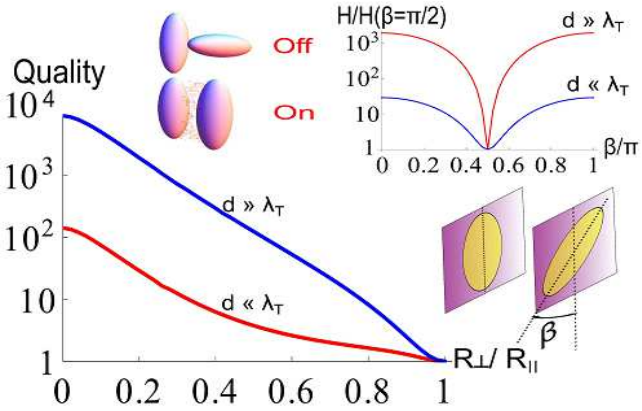

Figure 3: Heat transfer between two identical spheroids, as a function of angle β (see inset). Main graph gives the quality of the transfer switch as a function of $R_\perp/R_\parallel$. In the shown limits for d (distance between the center of the center of the objects), the transfer assumes simple power laws, such that the given ratios are d-independent.

References

[1] R. Incardone, T. Emig, M. Krüger, *Europhys. Lett.*, **106**, 41001, 2014.

[2] W.G. Spitzer, D. Kleinmann and D. Walsh, *Phys. Rev.*, **113**, 127, 1959.

[3] J.-P. Mulet, K. Joulain, R. Carminati and J.-J. Greffet, *Appl. Phys. Lett.* **78**, 2931, 2001.

[4] A.V. Shchegrov, K. Joulain, R. Carminati and J.-J. Greffet, *Phys. Rev. Lett.* **85**, 1548, 2000.

Far field diffraction of thermal Surface Phonon-Polaritons at the tip of micrometric glass tubes

Laurent TRANCHANT[a*], Jose ORDONEZ-MIRANDA[a], Thomas ANTONI[a,b] and Sebastian VOLZ[a]

[a]*Laboratoire d'Energétique Moléculaire et Macroscopique, Combustion, UPR CNRS 288, Ecole Centrale Paris, Grande Voie des Vignes, 92295 Chatenay Malabry, France.*

[b]*Ecole Centrale Paris, Laboratoire de Photonique Quantique et Moléculaire, UMR CNRS 8537, Ecole Normale Supérieure de Cachan, Grande Voie des Vignes, F-92295 Châtenay-Malabry cedex, France.*

**corresponding author: laurent.tranchant@ecp.fr*

Keywords: Surface Phonon-Polariton, near-field thermal radiation, heat waveguide, microstructure.

One of the main issues of the study of heat transfer at nanoscales is the drastic decrease of the phonon thermal conductivity of nanodevices, nevertheless this kind of devices has consequently a very high surface-to-volume ratio, which enables to use surface effects to enhance the nanoscale thermal transport. One of the surface energy carriers is the surface phonon-polariton (SPP), which is an evanescent electromagnetic wave propagating along the interface of polar-dielectric materials. These surface waves can offset the reduction of phonon thermal conductivity if we enhance their propagation [1,2].

In this work, we investigate the propagation of SPP along nanometric-micrometric glass tubes, aimed at showing that the coupling of these surface waves increases their propagation length and therefore it enhances the global thermal conductivity of the device [2]. We intend to prove experimentally this effect, by measuring the diffraction of SPP at the tip of micrometric glass tubes. Moreover, the effect of the tip geometry (walls thickness, outer/inner radius) on the enhancement of heat propagation is analyzed. We proposed an original experiment, which enables us to measure thermally excited SPP from near field to far field, in a similar way to the detection of SPP diffracted through surface gratings [3,4]. In addition, the diffraction of SPP is localized thanks the use of an infrared (IR) Microscope.

The experimental setup is composed of a Fourier Transform InfraRed (FTIR) spectrometer coupled with an IR microscope. The radiation is collected through a Cassegrain objective between an angle of 23° and 46° (figure 1). A copper coating is deposited on the basis of the glass tube to allow for heating the tube by focusing a green laser on it. Temperatures close to 600°C at the focus point can be reached through this method. SPPs are thermally excited at the focal point and propagate then along the tube to be finally diffracted at the tip. This is the reason why we decided to measure the radiation coming from the tip set in three positions: horizontal, vertical, and tilted at 35°. SPP diffraction is expected to be measured for the tilted configuration. Indeed in this position the tip axis is in the direction of the detection cone of the Cassegrain objective, which is not the case for the horizontal and vertical ones. Moreover the angular width of the SPP emission in the far field is estimated to be lower than 20° which is also the angular width of the detection cone. This diffraction behaviour is similar to the one due to a grating [3,4] except that in our case all the frequencies are diffracted in the same direction: along the axis of the tube (see FDTD simulations in figure 2).

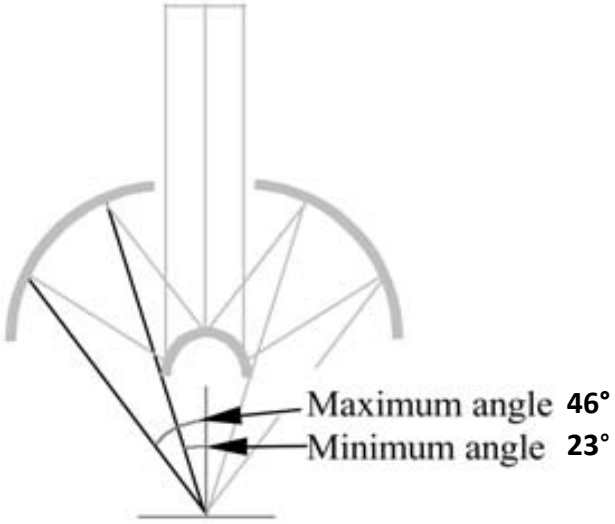

Figure 1: Schematic of the Cassegrain objective used to detect the thermal emission of the tube (figure provided by Thermo Fisher Scientific).

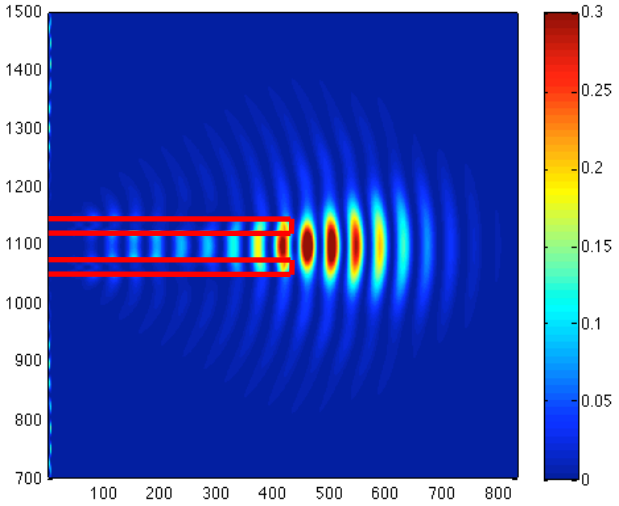

Figure 2: FDTD simulation of the normalized electric field of SPP being diffracted at the tip of a glass tube with 3 microns thick wall. The outer diameter of the tip is 12 microns. The units are arbitrary.

The emission spectra are shown in figure 3. The amplitudes of the signals collected for each tilt were very different, which led us to arbitrarily normalize the spectra to establish a qualitative comparison. The peak due to SPP is expected around 1200 cm^{-1} [2] and we did observe it for a tilt of 35 degrees and for the horizontal setup. The relatively small peak for the first configuration could indicate the presence of SPP. The peak was not expected for the horizontal setup, its presence could be due to noise or the anisotropy of the glass tube emission determined by its geometry. Further studies need to be implemented to clarify the direction dependence of the tube emission. Based on our current calibration process, these results pave the way for detecting SPP thermally excited in the far field even though the non linearity problems of the MCT detector are not yet been completely solved. More quantitative results linking the heating of the laser and the energy radiated by SPP will be possible with appropriate reference signals not yet available today.

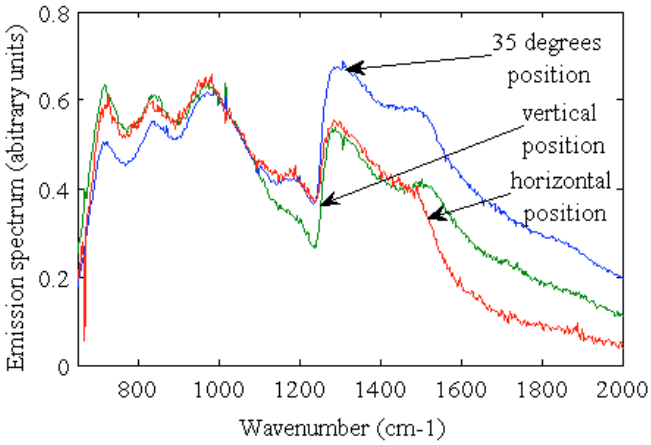

Figure 3: Normalized emission spectra of the glass tube for three different tilts. A small peak appearing at 1200 cm^{-1} could be due to SPP.

References

[1] D.-Z. A. Chen, A. Narayanaswamy and G. Chen, "Surface phonon-polariton mediated thermal conductivity enhancement of amorphous thin films", *Phys Rev* B, **72**, 155435, 2005.

[2] J. Ordonez-Miranda *et al*., "Anomalous thermal conductivity by surface phonon-polaritons of polar nano thin films due to their asymmetric surrounding media", *J. of App. Phys.* **113**, 084311, 2013.

[3] J. Le Gall, M. Olivier, and J.-J. Greffet., "Experimental and Theoretical Study of Reflection and Coherent Thermal Emission by a SiC Grating supporting a Surface Phonon Polariton", *Phys Rev B* **55**, 10105, 1997.

[4] F. Marquier *et al*., "Coherent spontaneous emission of light by thermal sources", *Phys Rev B* **69**, 155412, 2004.

Radiative thermal memory

Viacheslav KUBYTSKYI[a], Svend-Age BIEHS[b] and Philippe BEN-ABDALLAH[a*]

[a]*Laboratoire Charles Fabry, UMR 8501, Institut d'Optique, CNRS, Université Paris-Sud 11, 2, Avenue Augustin Fresnel, 91127 Palaiseau Cedex, France*

[b]*Institut für Physik, Carl von Ossietzky Universität, D-26111 Oldenburg, Germany*

**corresponding author: pba@institutoptique.fr*

Keywords: Radiative heat transfer, energy storage, bistability, phase change

Nowadays, the control of electric currents in solids is the cornerstone of modern electronics devices which have revolutionized our daily life. Astonishing, the same control for heat flows exchanged between bodies out of thermal equilibrium is not at all so frequent. In 2006 Baowen Li *et al.* [1] have proposed a thermal analog of field-effect transistor by replacing both the electric potentials and the electric currents in the electronic circuits by thermostats and heat fluxes carried by phonons through solid segments. Few years later, several prototypes of phononic thermal logic gates [2] as well as thermal memories [3, 4] have been fabricated and characterized. More recently photonic analogs of these devices have been proposed [5-10] to overcome the problem of the operating speed limitation of phononic systems. He we pursue these developments by discussing the concept of radiative thermal memory we have recently introduced [11].

The system we consider in this study is sketched in Fig.1-a. It consists in two simple membranes of silica and vanadium dioxide, a metal-insulator phase transition material [12-13], separated by a vacuum gap and surrounded on the right and on the left by two thermal baths at two different temperatures. These membranes interact together radiatively on one side through the intracavity fields and on the other side with the fields emitted by the thermal baths.

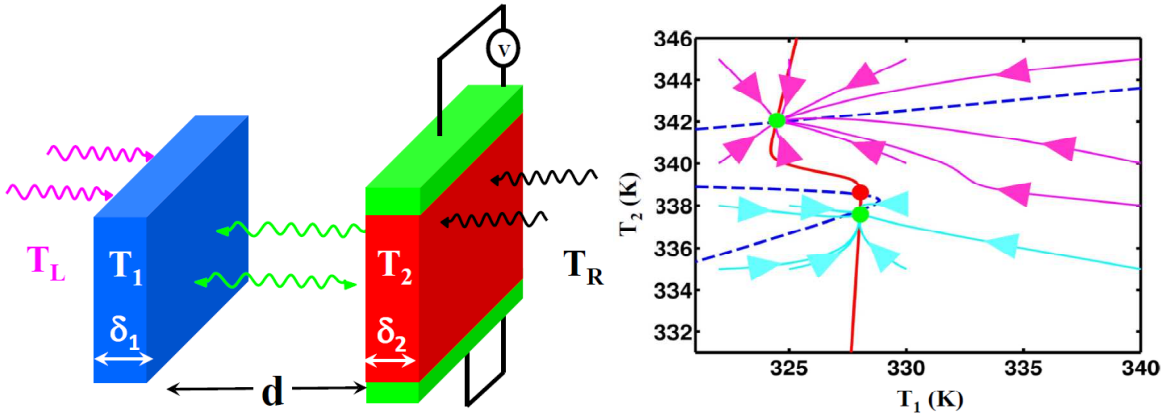

Figure 1: (a) A two membranes SiO2/VO2 system surrounded by two thermal baths at different temperatures TL and TR. The temperature T2 of the VO2 membrane can be tuned (either increased or reduced) using Joule heating with a voltage difference applied through a couple of electrodes or using Peltier elements. (b) Example of Trajectories of membranes temperature (pink and turquois lines) for different initial conditions with δ1 = δ2 =1 μm. The blue dashed and red solid lines represent the local equilibrium conditions for each membrane (i.e Φ1 = 0 and Φ2 = 0). The green and red points denote the stable and unstable equilibrium states, respectively. The temperature of thermal reservoirs are TL = 320K and TR = 358K and the separation distance is d=200 μm.

On the VO2 membrane a volumetric power can be either added or extracted through electrodes (by joule effect) or Peltier elements. By calculating the radiative heat flux through all planes parallel to exchange surfaces using a many body generalization [14-15] of the Polder and van Hove theory [16], the temperature fields in both membranes can be calculated at any time. In Fig. 1-b we show the time evolution of the membrane temperatures without external excitation for different initial temperatures by assuming each membrane as isothermal.

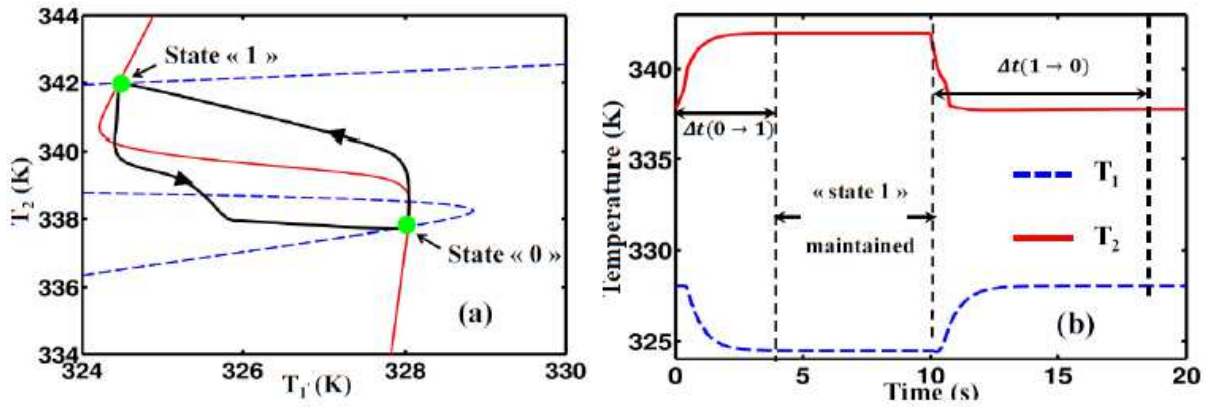

Figure 2: (a) Hysteresis of the VO2 membrane temperature during a transition between the thermal states "0" and "1" inside a two membrane SiO2/VO2 system with $\delta 1 = \delta 2 = 1$ μm (those thicknesses have been chosen to generate several equilibrium states). The volumetric powers supplied and extracted from the VO2 layer during a time interval $\Delta t1 = 0.4$ s and $\Delta t2 = 1.5$ s are $Q2 = 10^{-2}$ W.mm^{-3} and $Q2 = -2.5 \times 10^{-2}$ W.mm^{-3}, respectively. The writing time of state "1" ("0") from the state "0" ("1") is $\Delta t(0 \rightarrow 1) = 4$ s ($\Delta t(1 \rightarrow 0) = 8$ s). (b) Time evolution T1(t) and T2(t) of SiO2 and VO2 membrane temperatures. The thermal states "0" and "1" can be maintained for arbitrary long time provided that the thermostats (TL = 320K and TR = 358K) remain switched on like in a volatile memory.

This evolution is represented by the pink and turquois curved lines in the (T_1, T_2) plane. They converge toward two points which correspond to the global thermal equilibrium states highlighting so the bistable behavior of system. These two states can be viewed as two binary states "🗀" and "🗁". This bistable thermal behavior results from the phase transition of the VO2 membrane around its critical temperature (T_c=340K) which gives to this layer two radically different optical behaviors.

The thermal bistability can be exploited to build a thermal memory able to switch the system from one thermal state to the other. We illustrate this in Fig.2. We illustrate the operating modes of such a memory when a thermal power is either added in or extracted from the VO2 membrane. We see in Fig. 2-a that the temperatures in the system follow a hysteresis curve when the former transits from one state to the other one showing so the symmetry breaking in the system temporal evolution. In Fig. 2-b we see that the writing time is of the order of the second. Obviously this time could be drastically reduced using more important thermal powers.

References

[1] B. Li, L. Wang and G. Casati, Negative differential thermal resistance and thermal transistor, *Appl. Phys. Lett.* **88**, 143501, 2006.

[2] L. Wang, B. Li, Thermal Logic Gates: Computation with Phonons, *Phys. Rev. Lett.* **99**, 177208, 2007.

[3] L. Wang and B. Li, Thermal Memory: A Storage of Phononic Information, *Phys. Rev. Lett.* **101**, 267203, 2008.

[4] N. Li, J. Ren, L. Wang G. Zhang, P. Hänggi, and B. Li, Phononics: manipulating heat flow with electronic analogs and beyond, *Rev. Mod. Phys*. **84**, 1045, 2012.

[5] C. R. Otey, W. T. Lau, and S. Fan, Thermal rectification through vacuum, *Phys. Rev. Lett*. **104**, 154301, 2010.

[6] P. Ben-Abdallah and S.-A. Biehs, Phase-change radiative thermal diode, *Appl. Phys. Lett.* **103**, 191907, 2013.

[7] P. Ben-Abdallah and S.-A. Biehs, Near-field thermal transistor, *Phys.Rev. Lett*. **112**, 044301, 2014.

[8] L. Zhu, C. R. Otey and S. Fan, Negative differential conductance through vacuum, *Appl. Phys. Lett*. **100,** 044104, 2012.

[9] E. Nefzaoui, K. Joulain, J. Drevillon and Y. Ezzahri, Radiative thermal rectification using superconducting materials, *Appl. Phys. Lett*. **104** , 103905, 2014.

[10] E. Nefzaoui, J. Drevillon, Y. Ezzahri and K Joulain, Simple far-field radiative thermal rectifier using Fabry–Perot cavities based infrared selective emitters, *Applied Optics*, **53**, 16, 3479-3485, 2014.

[11] V. Kubytskyi, S.-A. Biehs and P. Ben-Abdallah, Radiative bistability and thermal memory, *Phys. Rev. Lett.*, **113**, 074301, 2014.

[12] A. S. Barker, H. W. Verleur, and H. J. Guggenheim, Infrared Optical Properties of Vanadium Dioxide Above and Below the Transition Temperature, *Phys. Rev. Lett*. **17**, 1286, 1966.

[13] P. van Zwol, K. Joulain, P. Ben-Abdallah, and J. Chevrier, Phonon polaritons enhance near-field thermal transfer across the phase transition of VO2, *Phys. Rev. B(R),* **84**, 161413, 2011.

[14] R. Messina, M. Antezza, and P. Ben-Abdallah, Three-body amplification of photon heat tunneling, *Phys. Rev. Lett*. **109**, 244302, 2012.

[15] R. Messina and M. Antezza, Scattering-matrix approach to Casimir-Lifshitz force and heat transfer out of thermal equilibrium between arbitrary bodies, *Phys. Rev. A* **84**, 042102, 2011.

[16] D. Polder and M. Van Hove, Theory of Radiative Heat Transfer between Closely Spaced Bodies, *Phys. Rev. B* **4**, 3303, 1971.

[17] Handbook of Optical Constants of Solids, edited by E. Palik (Academic Press, New York, 1998).

Super Planckian thermal emission of subwavelength disks

Karl JOULAIN[a*], Younès EZZAHRI[a] and Jérémie DREVILLON[a]

[a]*Institut Pprime, CNRS-Université de Poitiers-ENSMA, UPR3346, 2, Rue Pierre Brousse, F-86073, Poitiers, France*

**corresponding author: karl.joulain@univ-poitiers.fr*

Keywords: near-field thermal radiation, thermal emission, nanostructured materials

We calculate by means of fluctuationnal electrodynamics and coherence theory, thermal emission of a circular aperture filled by a vacuum or a material at temperature *T*. We show that thermal emission is very different whether the aperture size is large or small compared to the thermal wavelength. Aperture with a size much larger than thermal wavelength emits radiation with a well-known emissivity simply related to the material Fresnel reflection coefficients. Subwavelength apertures behave completely differently: thermal emission is strongly decreased for wavelength larger than the aperture size. A simple expression of the emissivity is obtained. In the case of subwalengths aperture separating the vacuum at temperature *T* from the outside, it is shown that the emissivity tends to 0 when the aperture size goes to 0. Moreover, subwavelength apertures have a typical radiation variation law in T^6 compare to the usual T^4 law given by the Planck law. When the disk is constituted of a material, it is still found that thermal radiation can hardly exit from the material. However, if the material support surface waves or exhibit resonances, thermally excited evanescent resonant modes are scattered by the aperture. Thermal emission is enhanced so that it occurs at one particularly frequency and is larger than the usual thermal emission predicted by the Planck theory. An expression of the emissivity is here also derived showing that this new enhanced emissivity is strongly related to the near-field radiation close to the material. We think this behavior could open the way to very useful applications such as very narrowband passive source.

We now consider thermal emission of a circular aperture with radius r_0 surrounded by a perfect reflector. Our goal is to calculate the thermal energy emitted by such a system and susceptible to be detected by an optical device. Fluctuational electrodynamics allows to calculate the electromagnetic field above a planar emitter. More precisely the electromagnetic field spatial correlation above a plane semi-infinite interface has been known for more than a decade [1]. The question addressed here is to see what is happening when near-field thermal electromagnetic field is confined to a certain subsurface and what is the consequence on the field radiated at large distance. Since the seminal work of Walther [2], it has been shown that coherence properties can be related to radiometric quantities such as the specific intensity. This last quantity is actually the Wigner transform of the electromagnetic field **E** the electric field and **H** the magnetic field), performed over the emitter aperture

$$L_\omega(r,u)=\frac{k_0^2}{32\pi^2}c\cos\theta\int_{aperture}\left\langle\varepsilon_0 E(r+r'/2)E^*(r-r'/2)+\mu_0 H(r+r'/2)H^*(r-r'/2)\right\rangle e^{-ik_0 u_\perp r'}d^2r' \qquad (1)$$

where θ is the angle between the normal to the surface and direction **u** considered. $u_\perp$ is the unit vector direction component perpendicular to the normal i.e. parallel to the interface, **r** is the point where the specific intensity is calculated and ω is the angular frequency at which the calculation is

performed. The flux emitted by the aperture is calculated by an integration of the specific intensity over the aperture

$$\phi_\omega = \int \cos\theta L_\omega(r,u)T(r)d^2r\,d\Omega \quad (2)$$

where $T(r)$ is the transmission function of the system so that $T(r)=1$ if $\mathbf{r}$ is in the domain where the material emits and 0 in the opposite case. Fluctuationnal electrodynamics field spatial correlation function calculation above a planar interface can be found in the literature [1,4]. From these calculations, emission of an aperture can be expressed in the form $\phi_\omega = H_\omega^0(T)S\varepsilon_{eff}$ where S is the aperture surface, $H_\omega^0(T)$ is the blackbody emittance and ε_{eff} the effective emissivity where

$$\varepsilon_{eff} = \int_0^{2k_0r_0} W_T(u,k_0r_0)du \left\{ \begin{array}{l} \int_0^1 \frac{\kappa d\kappa}{\sqrt{1-\kappa^2}}(2-|r^s|^2-|r^p|^2)J_0(\kappa u) \\ +\int_1^\infty \frac{4\kappa^3 d\kappa}{\sqrt{\kappa^2-1}}\left[\Im(r^s)+\Im(r^p)\right]e^{-2\sqrt{\kappa^2-1}k_0z}J_0(\kappa u) \end{array} \right\} F(u) \quad (3)$$

where $F(u)=\left[\sin u - u\cos(u)\right]/u^3$, J_0 is the Bessel function of order 0 and $W_T(r,r_0)=\frac{2}{\pi}\left\{\cos^{-1}(r/2r_0)-r/2r_0\sqrt{1-(r/2r_0)^2}\right\}$ [3]. Equation (3) has actually to be evaluated in the limit where the distance to the interface z tends to 0. $r^{s,p}$ are the Fresnel reflection coefficient in s and p polarization. This expression is the sum of a contribution of propagative waves for which the normalized parallel wave vector κ is between 0 and 1 and of a contribution of evanescent waves for which the normalized parallel wave vector is larger than one.

Let us now examine the simple situation of an aperture filled with vacuum. In that case, reflection coefficients are equal to 0 and

$$\varepsilon_{eff} = \int_0^{2k_0r_0} 2\sin u \frac{\sin u - u\cos u}{u^3} W_T(u,k_0r_0)du \quad (4)$$

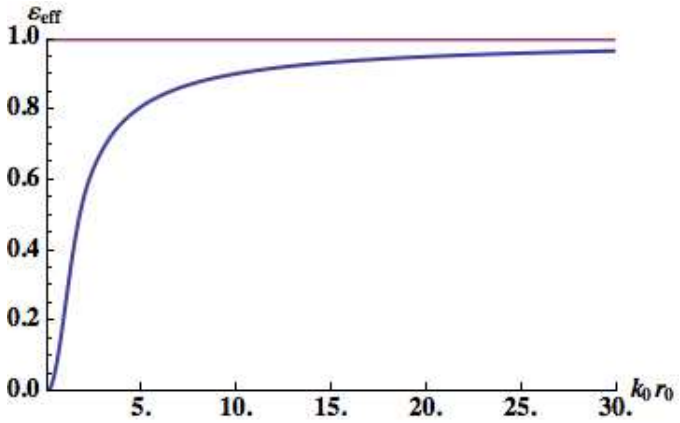

Figure 1: Effective emissivity of an aperture with k_0r_0.

which variations are plotted versus k_0r_0.We observe that emissivity tends to unity when the wavelength is much larger than the aperture and to zero when the aperture reaches a subwavelength size.

Integration over frequency can also be performed. It is shown that total emission follows a T^4 law for large apertures and T^6 law for small one. Transition between the two regimes is shown in Figure 2 in the thick blue curve which converges to the two regimes shown in the dashed curves.

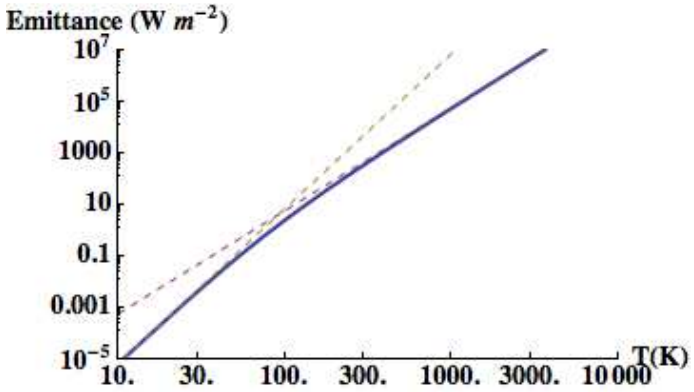

Figure 2: Total emission of an aperture of 10µm radius versus temperature (Thick blue). At low temperature, emission follows a T^6 law whereas it is a T^4 law at high temperature (dashed curves).

We now go the case of disks of materials surrounded by a perfect reflector. First of all, one notes that both propagating and evanescent waves contribute to thermal emission. As it is the case for vacuum propagative waves, contribution is reduced for subwavelength disks due to the fact that they can hardly escape from the apertures. Evanescent wave contribution is very similar to what can be obtained when one calculate the density of energy above a planar interface. Close to an interface, there is an increase of the local density of electromagnetic states due to the presence of electrostatic modes. Moreover, this increasing can be even more important when the material support surface waves.

We plot in Figure 3, the emission spectrum of a nanodisk of amorphous silica (SiO2) for different size of disks. For a large disk radius (here 100 microns), thermal emission is limited to the one of a semi-infinite plane of SiO2. Around 8 and 20-micron wavelength, emission is very low due to the fact that SiO2 is a very reflecting material in this spectral range. When the aperture size approaches the typical thermal wavelength, emission is increasing. We see that the disk emits much more than would emit an ideal blackbody. If thermal emission is normalized to the one of a blackbody which shape is a disk, one finds that this body emits with an emissivity greater than one. The more the hole is small, the more the disk emits compare to its size. What is happening actually is due to the fact that the additional evanescent modes due to the presence of surface waves are scattered by the aperture. Therefore, in addition to the usual propagative modes that can escape the system, additional evanescent modes are coupled to the far-field by the aperture. The more the aperture is small, the more high spatial frequency modes can be scattered and radiated and the more classical heat radiation will be surpassed.

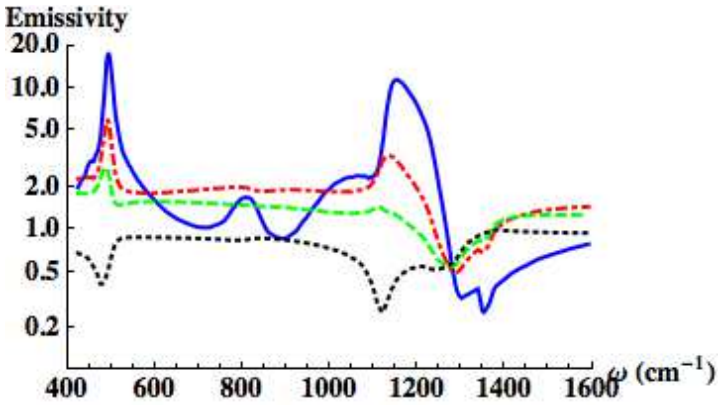

Figure 3: Emissivity spectrum of SiO2 disks for different radii: . Thick blue : 1 micron. Dot-dashed red : 4 microns. Dashed green : 10 microns. Dotted black : 100 microns.

We have shown that thermal emission of a material is greatly affected by its size. Propagative waves with wavelength larger than the emitter size can hardly exit from the material so that this contribution is lowered. An evanescent wave contribution exists when the material is emissive especially if the material support surface waves. In that case, the finite emitter size scatters evanescent waves so that thermal emission is enhanced especially at the resonant waves frequency. It has been shown that the emissivity defined as the emitted flux divided by the emittance multiplied by the surface emitter can exceed 1. Applications such as narrow band emitter could be designed with this method.

References

[1] C. Henkel, K. Joulain, R. Carminati and J.-J. Greffet, "Spatial Coherence of Thermal Near-Fields", *Optics Commun.* **186**, 57-67, 2000.

[2] A. Walther, "Radiometry and Coherence", *J. Opt. Soc. Am.* **63**, 1622-1623, 1973.

[3] B. Steinle and H.P. Baltes, "Radiant intensity and apatial coherence for finite planar sources", *J. Opt. Soc. Am.*, **67**, 241-247, 1977.

[4] C. Henkel and K. Joulain, "Electromagnetic field correlations near a surface with a nonlocal optical response", *Appl. Phys. B*, **84**, 61-68, 2006.

Session 11

Phonons and vibrations

Experimental investigation of single molecule thermal conductance

Nils KÖNNE, Konstantin KLOPPSTECH and Achim KITTEL

Carl-von-Ossietzky Universität Oldenburg, Institut für Physik, EHF, Epkos, Carl-von-Ossietzky-str 9-11, 26129 Oldenburg, Germany

**corresponding author: kittel@uni-oldenburg.de*

Keywords: thermal conduction, single molecule, near-field scanning thermal microscope

The characterization of a single molecule is a topic of high interest, with a lot of progress in terms of experimentally probing the electronic nature of several different individual molecules [1,2]. Despite this fact, the investigation of the thermal conduction stagnates, mainly due to the experimental difficulties concerning the needed resolution in the range of 10 – 100 pW/K as calculated by Segal *et al*. [3] in case of octanedithiol. This experimental challenge is by now circumvented by probing not the thermal conductance of a single molecule but the thermal conductivity integrated over a defined molecular film area, from which a single molecule thermal conductance of 6-50 pW/K can be determined by means of the area per molecule [4,5]. Our ansatz for directly measuring the thermal conductance of a single molecule is to use our self-build Near Field Scanning Thermal Microscopy (NSThM) consisting of a commercial variable-temperature scanning tunneling microscope (VT-STM) with a thermocouple at the apex of the NSThM tip. By means of calibrated sensors and applying a temperature difference between the tip and the sample we are able to observe simultaneously the resulting absolute heat flux and tunneling current in UHV environment (Figure 1).

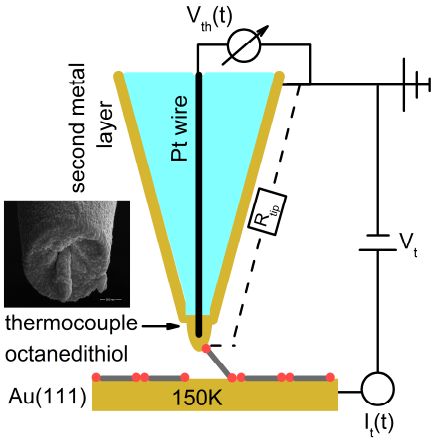

Figure 1: Schematic representation of the NSThM-setup used for the thermal conductance measurements on single octanedithiol molecule.

To contact a single molecule we use the so called *I(t)*-method introduced by W. Haiss [2]. Therefore, a Au(111) substrate is covered with a low density monolayer of octanedithiol. After transferring our sample into the ultra high vacuum system (UHV) of the NSThM the sample is cooled down to about 150 K while the tip stays at room temperature. Thereafter, NSThM-tip is brought into close proximity of the molecules keeping the control loop of the STM opened. By recording the tunneling current *I(t)* as a function of time, the spontaneous formation of a substrate-molecule-tip bridge results in distinct step like current changes in the time trace with a quantized step height per molecule of 1nS, revealing the amount of molecules involved in the bridge. These signatures in the *I(t)*-signal are correlated with

the simultaneous recorded time trace of the thermo voltage to determine the thermal conductance of a single molecule.

The NSThM-tip used for our experiments consists of a Platinum-Chromium-thermocouple for which the calibration reveals a sensitivity of 14 µV/µW. This leads together with a 600 nV noise amplitude of the thermo voltage and a tip-sample temperature difference of 150 K to a thermal conductance resolution of about 300 pW/K. We have measured hundreds of time traces with multiple of the distinct current step height of 1 nS but not a single signature in corresponding thermo voltage signal could be observed. Representative time traces of both signals are shown in Fig. 2. The step height of 3 nS in the electrical conductance (black) corresponds to the switching of three octanedithiol molecules at once. The signal to noise ratio for the corresponding thermal conductance (grey) is below one, leading to an experimental determined upper limit of 100 pW/K for a single octanedithiol molecule.

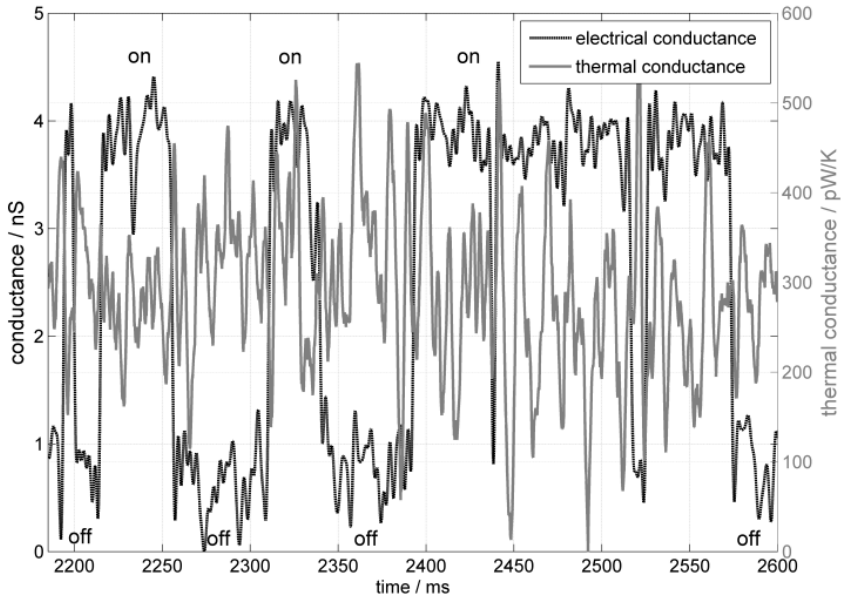

Figure 2: The step-like current changes in the electrical conductance (black) result from the switching of three octanedithiol molecules. At the same time the heat flux is recorded. In the time trace of the heat flux no signature of switching can be observed. By means of the resolution of out sensor one can deduce that each molecule must contributes less than 100pW/K to the thermal conductance (grey).

We are currently working on the improvement of our heat flux resolution by reducing the noise further to finally measure the single molecule thermal conductance. This is done by an improved experimental setup and by a more sophisticated data analysis method.

References

[1] X. Xiao, B. Xu and N.J. Tao, "Measurement of Single Molecule Conductance: Benzenedithiol and Benzenedimethanethiol", *Nano Letters*, **4**, 267-271 (2004).

[2] W. Haiss *et al*, "Measurement of single molecule conductivity using the spontaneous formation of molecular wires", *Phys. Chem. Chem. Phys.* **6**, 4330-4337 (2004).

[3] D. Segal, A. Nitzan and P. Hänggi, "Thermal conductance through molecular wires", *J. Chem. Phys*, **119**, 6840 (2003).

[4] R. Y. Wang, R. A. Segalman, A. Majumdar, "Room temperature thermal conductance of alkanedithiol self-assembled monolayers", *Appl. Phys. Lett.* **89**, 173113 (2006).

[5] Z. Wang *et al*., "Ultrafast Flash Thermal Conductance of Molecular Chains", *Science*, **317**, 787-790 (2007).

Modification of Akhieser mechanism in Si nanoresonators

Emigdio CHÁVEZ-ÁNGEL[a, b*], Ramon A. ZARATE[c], Daniel NAVARRO-URRIOS[d], Jordi GOMIS-BRESCO[a], Francesc ALZINA[a] and Clivia .M. SOTOMAYOR TORRES[a, e]

[a]*Catalan Institute of Nanoscience and Nanotechnology (ICN2), Campus UAB 08193 Bellaterra (Barcelona), Spain*

[b]*Dept. of Physics, Universitat Autònoma de Barcelona, Campus UAB, 08193 Bellaterra (Barcelona), Spain*

[c]*Dpto de Física, Universidad Católica del Norte, UCN, Av. Angamos 0610, Antofagasta, Chile*

[d]*NEST, Istituto Nanoscienze – CNR and Scuola Normale Superiore, Piazza San Silvestro 12, Pisa, I-56127*

[e]*Catalan Institution for Research and Advanced Studies (ICREA) 08010 Barcelona, Spain.*

**corresponding author: emigdio.chavez@icn.cat*

Keywords: Akhieser model, Thermal conductivity, nanomembranes, mechanical resonators, *Q*-factor

Abstract. We consider Si nanoresonator with mechanical mode frequencies in the GHz range. In these a reformulated Akhieser model is validated, which takes into account the reduction of the thermal conductivity due to the impact of boundary scattering on the thermal phonons lifetime and accounts for the observed shortening of the mechanical mode lifetime. From this model the thermal conductivity can be extracted from the measured lifetime of mechanical modes in the high-frequency regime, thereby showing that the *Q*-factor can be used as an indication of the thermal conductivity and/or diffusivity of a mechanical resonator.

Introduction

Advances in nanofabrication processes have enabled the progression from the micro-to nano-electromechanical systems (MEMS and NEMS). The vast scope of their applications ranges from semiconductor based technology to fundamental science [1]. In particular, MEMS- and NEMS-based oscillators have been exploited as extremely sensitive mass [2], force [3], charge [4] and spin [5] detectors.

As consequence of this miniaturization trend, the operation frequency of mechanical resonators is entering into the GHz regime [6]–[13]. Therefore, the total energy dissipation will be limited mainly by intrinsic damping mechanism arising from phonon-phonon interaction. This introduces a fundamental limit in the performance of the resonators, which is usually expressed by the *"Q·f"* product of the quality factor, *Q*, and the operating frequency, *f*. As phonon-phonon interaction processes depend on materials properties, it is important to consider the changes arising from decreasing feature size. In this context, the reduction of the thermal conductivity observed in nanoscale materials will affect the lifetime of the thermal phonons and, consequently, the intrinsic phonon-phonon interaction processes will be modified.

In the present work, we report the impact of modified thermal properties of a mechanical resonator on the intrinsic Akhieser damping mechanism. The intrinsic mechanical mode absorption is calculated

using the Akhieser damping model [14] modified to take into account the size effect on the thermal conductivity due to thermal phonons scattering at the boundaries. Furthermore, we show that from lifetime measurements it is possible to extract the thermal conductivity. This opens the prospect of using the *Q*-factor as a measure of the thermal conductivity and or diffusivity of the resonator. As an example, we calculate the thermal conductivity of a 1D optomechanical crystal [12], [13].

Results

The energy dissipation of the nanoresonators is divided into intrinsic and extrinsic components. While the first is related to the anharmonic decay, i.e., phonon-phonon scattering processes, the latter is due to scattering from fabrication defects, air damping and rough surfaces and interfaces. The intrinsic acoustic phonon attenuation arises from phonon-phonon interactions described as Akhieser damping processes [14], expressed as [14]–[16] :

$$\tau_{AK}^{-1}(\omega_i) = \frac{C_V T}{\rho v_s^2} \frac{\omega_s^2 \tau_{TH}}{(1+\omega_s^2 \tau_{TH}^2)} \gamma^2 \tag{1}$$

where C_V is the volumetric heat capacity, T the temperature, ρ the mass density, v_s the group velocity of the mode s and $\bar{\gamma}$ is an average of the Grüneisen parameter taken over the entire spectrum of the thermal phonons. In general, the lifetime of the thermal phonons, τ_{TH}, can be expressed as:

$$\tau_{TH} \approx \frac{3\kappa}{C_V \bar{v}^2} \tag{2}$$

where κ is the thermal conductivity of the system and v the sound velocity. In this context, it is well known that thermal conductivity of thin layers and membranes, κ_{film}, decreases appreciably compared to their bulk counterpart, κ_{bulk}. This reduction is mainly associated with decreasing phonon mean free path and, concomitantly, with the phonon lifetime due to diffuse phonon scattering at the boundaries [17]–[20]. As a consequence, the lifetime of thermal phonons will depend on the system size and the intrinsic phonon relaxation rate in the Akhieser regime can then be rewritten as:

$$\begin{aligned} \tau_{AK}^{-1} &= 3T \frac{C_V}{\rho} \left(\frac{\bar{v}}{v_s} \right)^2 \frac{\omega_s^2 (\kappa_{film} / C_V)}{(\bar{v}^4 + (3\omega_s \kappa_{film} / C_V)^2)} \bar{\gamma}^2 \\ &= 3TC_P \left(\frac{\bar{v}}{v_s} \right)^2 \frac{\alpha \omega_s^2}{(\bar{v}^4 + (3\alpha\omega_s)^2)} \bar{\gamma}^2 \end{aligned} \tag{3}$$

where $\alpha = \kappa_{film}/C_V$ is the thermal diffusivity and C_P the specific heat capacity.

In simple systems the reduction function of the system is well known being typically the Fuchs reduction function. However, in many instances the shape of the nano/micro oscillators can be quite complex and the reduction function and/or the experimental values of the thermal conductivity are unknown. Taking this into consideration, we propose the possibility to extrapolate the thermal conductivity from the experimental values of phonon lifetime or *Q* factor of the nano/micro oscillators. By assuming that the phonon attenuation/damping of the system is dominated by pure Akhieser mechanism, it is possible to estimate the thermal conductivity/diffusivity by fitting the phonon lifetime or *Q*-factor with the equation (3) for different values of the thermal conductivity. As an example, we calculate the thermal conductivity of a 1D optomechanical crystal [12]. The

complexity of this structure, shown in the inset to figure 1, makes the calculation of the reduction function virtually unfeasible. Figure shows the experimental and theoretical quality factor as a function of the phonon frequency. The experimental data were taken from reference [12]. The thermal conductivity was extracted from the best fit to the experimental quality factor. The obtained value, $\kappa_{beam} = 56.2\ \mathrm{WK^{-1}m^{-1}}$, is in good agreement with a similar structure reported by Marconnet *et al*. [21].

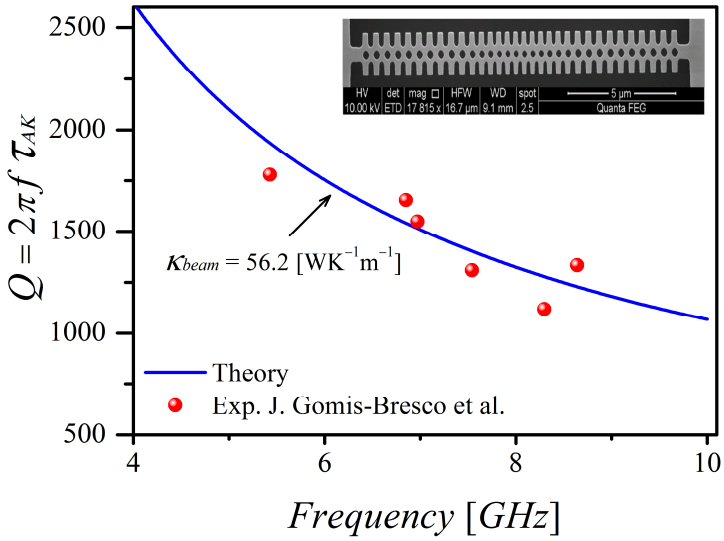

Figure 1: Experimental and theoretical quality factor of different phonons mode in a nano-oscillator. The experimental data (red dots) were measured in the structure reported in reference[12]. Theoretical curve is shown in blue solid line.

The dependence of the lifetime with the thermal conductivity has a direct impact on the upper limit of the nano-resonators *Q*-factor which, depending on the frequency regime, could enhance or degrade the resonator performance. In addition, we suggest the possibility to extract thermal conductivity values from lifetime measurements, which opens the possibility to use the *Q*-factor as indicative of the thermal conductivity/diffusivity of nano-resonators.

Acknowledgements

The authors acknowledge the financial support from the FP7 project MERGING (grant nr. 309150), as well as the Spanish MINECO projects nanoTHERM (grant nr. CSD2010-0044) and TAPHOR (MAT2012-31392). E.C.A. gratefully acknowledges a Becas Chile 2010 CONICYT fellowship from the Chilean government.

References

[1] D. J. Young, C. A. Zorman, and M. Mehregany, "MEMS/NEMS Devices and Applications," in Springer Handbook of Nanotechnology, B. Bhushan, Ed. Berlin, Heidelberg: Springer Berlin Heidelberg, 2004, pp. 225–252.

[2] Y. T. Yang, C. Callegari, X. L. Feng, K. L. Ekinci, and M. L. Roukes, "Zeptogram-scale nanomechanical mass sensing", *Nano Lett.*, **6**, 583, 2006.

[3] H. J. Mamin and D. Rugar, "Sub-attonewton force detection at millikelvin temperatures", *Appl. Phys. Lett.*, **79**, 3358, 2001.

[4] A. N. Cleland and M. L. Roukes, "A nanometre-scale mechanical electrometer", *Nature*, **392**, 160, 1998.

[5] D. Rugar, R. Budakian, H. J. Mamin, and B. W. Chui, "Single spin detection by magnetic resonance force microscopy", *Nature*, **430**, 329, 2004.

[6] V. Cimalla, J. Pezoldt, and O. Ambacher, "Group III nitride and SiC based MEMS and NEMS: materials properties, technology and applications", *J. Phys. D. Appl. Phys.*, **40**, 6386, 2007.

[7] J. Weber, M. Link, R. Primig, D. Pitzer, W. Wersing, and M. Schreiter, "Investigation of the scaling rules determining the performance of film bulk acoustic resonators operating as mass sensors", *IEEE Trans. Ultrason. Ferroelectr. Freq. Control*, **54**, 405, 2007.

[8] J. Chan, T. P. M. Alegre, A. H. Safavi-Naeini, J. T. Hill, A. Krause, S. Gröblacher, M. Aspelmeyer, and O. Painter, "Laser cooling of a nanomechanical oscillator into its quantum ground state", *Nature*, **478**, 89, 2011.

[9] L. Ding, C. Baker, P. Senellart, A. Lemaitre, S. Ducci, G. Leo, and I. Favero, "Wavelength-sized GaAs optomechanical resonators with gigahertz frequency", *Appl. Phys. Lett.*, **98**, 113108, 2011.

[10] X. Sun, X. Zhang, M. Poot, C. Xiong, and H. X. Tang, "A superhigh-frequency optoelectromechanical system based on a slotted photonic crystal cavity", *Appl. Phys. Lett.*, **101**, 221116, 2012.

[11] A. H. Safavi-Naeini, J. T. Hill, S. Meenehan, J. Chan, S. Groeblacher, and O. Painter, "Two-Dimensional Phononic-Photonic Band Gap Optomechanical Crystal Cavity", *Phys. Rev. Lett.*, **112**, 153603, 2014.

[12] J. Gomis-Bresco, D. Navarro-Urrios, M. Oudich, S. El-Jallal, A. Griol, D. Puerto, E. Chavez, Y. Pennec, B. Djafari-Rouhani, F. Alzina, A. Martínez, and C. M. Sotomayor Torres, "A one-dimensional optomechanical crystal with a complete phononic band gap", *Nat. Comms.*, **5**, 4452, 2014.

[13] D. Navarro-Urrios, N. E. Capuj, J. Gomis-Bresco, F. Alzina, A. Griol, A. Martinez, and C.M. Sotomayor Torres, "Synchronization of an optomechanical oscillator and thermal/free-carrier self-pulsing using optical comb forces," *arXiv:*1403.6043, 2014.

[14] A. Akhieser, "On the Absorption of Sound in Solids", *J. Phys. USSR*, **1**, 277, 1939.

[15] B. C. Daly, K. Kang, Y. Wang, and D. G. Cahill, "Picosecond ultrasonic measurements of attenuation of longitudinal acoustic phonons in silicon", *Phys. Rev. B*, **80**, 174112, 2009.

[16] H. J. Maris, "6 - Interaction of Sound Waves with Thermal Phonons in Dielectric Crystals," in Physical Acoustics: Principles and methods, vol. 8, W. P. Mason and R. N. Thurston, Eds. Academic Press, 1971, pp. 279–345.

[17] P. Hyldgaard and G. D. Mahan, "Phonon Knudsen flow in GaAs/AlAs superlattices", in Thermal conductivity 23, pp. 172–182, 1996.

[18] M. Asheghi, Y. K. Leung, S. S. Wong, and K. E. Goodson, "Phonon-boundary scattering in thin silicon layers", *Appl. Phys. Lett.*, **71**, 1798, 1997.

[19] W. Liu and M. Asheghi, "Phonon–boundary scattering in ultrathin single-crystal silicon layers", *Appl. Phys. Lett.*, **84**, 3819, 2004.

[20] G. H. Tang, Y. Zhao, G. X. Zhai, and C. Bi, "Phonon boundary scattering effect on thermal conductivity of thin films", *J. Appl. Phys.*, **110**, 046102, 2011.

[21] A. M. Marconnet, T. Kodama, M. Asheghi, and K. E. Goodson, "Phonon Conduction in Periodically Porous Silicon Nanobridges," *Nanoscale Microscale Thermophys. Eng.*, **16**, 199, 2012.

The low thermal conductivity of clathrates: a phononic filter effect

Stéphane PAILHES[a], Valentina M. GIORDANO[a,d], Holger EUCHNER[b,c], Régis DEBORD[a] and Marc DE BOISSIEU[d]

[a]*Institut Lumiere Matiere, UMR5306 Universite Lyon 1-CNRS, Universite de Lyon 69622 Villeurbanne cedex, France*

[b]*Institut fur Theoret. und Angwandte Physik, Universitat Stuttgart, D-70550 Stuttgart, Germany*

[c]*Institute of Materials Science and Technology, Vienna University of Technology, A-1040 Vienna, Austria*

[d]*SIMAP, UJF, CNRS, INP Grenoble, F-38402 St Martin d'Heres, France*

Keywords: phonons, heat transport, thermal conductivity, clathrates, inelastic scattering, complex metallic alloys

One of the most challenging tasks for our society consists in facing the energy crisis by developing new energy sources which are environment friendly and economically affordable. Although many different ways have been explored, some are still far from realizing their full potential due to several limiting factors in their development and large scale applicability. Among these there is the thermoelectricity, *i.e.* the conversion of wasted heat into electrical current. It is obviously an extremely interesting and potentially useful way of producing energy as there are many sources of wasted heat in the day-to-day life. Moreover, thermoelectrical devices present several advantages with respect to other energy conversion technologies such as simplicity, compactness, absence of pollution-emission greenhouse gas emissions, lack of mechanical noise and inconvenience, lack of surfaces exposed to degradation of natural and/or human, weather-independent, reliability, long life, etc. Despite these promising bases, the low efficiency and high cost of the current commercial devices has hindered the spreading of this technology.

In order to change this status, research in thermoelectricity needs to go beyond the already existing thermoelectric materials and look for novel materials with properties allowing for dramatically decreasing the cost of the device and improving the energy conversion efficiency. The challenge is to realize the Phonon Glass Electric Crystal ideal: a material conducting well the electricity but not the heat.

An efficient and economic way to reduce the thermal conductivity of bulk materials, without degrading their electronic properties, is to profit of the nanostructuration or of the complex crystalline structure to reduce the phonons lifetime and then their efficiency in heat propagation. In this latter case a very convenient way is to take advantage of inelastic resonant scattering between heat-carrying acoustic and non-propagative phonons, arising from isolated impurities with internal oscillator degrees of freedom. In cage compounds like skutterudites or clathrates, the network of guest atoms was formerly regarded as an assembly of isolated harmonic oscillators (Einstein oscillators), characterized by a discrete frequencies spectrum [1]. The host-guest interaction leads then to resonant scattering phenomena between acoustic phonons of the host lattice and non-propagative guest phonons within narrow frequencies ranges centered at the Einstein frequencies. At a macroscopic level and, in the framework of the relaxation-time approximation of the Boltzmann equation, such resonant scattering lead to additional resonant relaxation times [2] currently used to fit data of thermal conductivity measurements [3]. In opposition to this picture of a freely rattling guest atom in a host cage, recent

neutrons studies demonstrated that the guest atoms are coherently coupled with the host-lattice dynamics [4,5]. In this circumstance, the mechanism of energy dissipation through local resonators as described above cannot be strictly applied and the effect of the host-guest interaction of the heat transport is still not understood.

In this talk, I will briefly introduce both neutrons and X-ray inelastic scattering techniques which probe simultaneously the momentum and the energy of phonons. I will in particular point out the difficulties in evaluating the intrinsic energy width, i.e. phonon lifetime, and the dynamical structure factor of a phonon mode from the measurement. I will then show experimental results on a clathrate, focusing on the mechanisms leading to a low thermal conductivity in such systems. [5,6].

References

[1] M. Christensen *et al*., *Dalton Trans*., **39**, 978, 2010.
[2] R. O. Pohl, *Phys. Rev. Lett*. **8**, 481, 1962; M. V. Klein, *Phys. Rev*. **186**, 839, 1969.
[3] J. Yang *et al*., *Phys. Rev. B* **67**, 165207, 2003 ; J. M. Cohn, *Phys. Rev. Lett*. **82**, 779, 1999.
[4] M. M. Koza *et al*., *Nature* 7, **805**, 2008.
[5] H. Euchner *et al*., *Phys. Rev. B* **86**, 224303, 2012.
[6] S. Pailhes *et al*., *Phys. Rev. Lett*. (accepted, 2014)

Acoustic frequency combs as a tool for measuring adhesion in a thin two-layer system

Martin GROSSMANN[a*], Matthias KLINGELE[a], Patricia SCHEEL[a], Oliver RISTOW[a], Mike HETTICH[a], Chuan HE[a], Reimar WAITZ[a], Martin SCHUBERT[a], Axel BRUCHHAUSEN[b], Vitalyi GUSEV[c], Elke SCHEER[a] and Thomas DEKORSY[a]

[a]*University of Konstanz, Phys. Dept., 78464 Konstanz, Germany*

[b]*Instituto Balseiro & Centro Atómico Bariloche (CNEA) and CONICET, Argentina*

[c]*IMMM, UMR-CNRS 6283, Université du Maine, Av. O. Messiaen, 72085 Le Mans, France*

**corresponding author: martin.grossmann@uni-konstanz.de*

Keywords: coherent acoustic phonons, frequency comb, femtosecond pump-probe spectroscopy, phonon interface scattering, phonon transport.

The influence of interfaces on phonon scattering is currently of great interest in the context of phonon lifetimes and heat transport. Wherever two materials with different properties are in contact with each other, the interface between them plays an important role. Also the adhesion between two different materials is dominated by the interface structure and the roughness is a critical parameter.

In this study the influence of different adhesion strengths between a thin Al film and a Si membrane on the phonon spectrum is investigated. By modeling the adhesion through a spring between the two layers we are able to simulate the features in the spectra induced by the dilatational mode oscillation of the Al film. Due to the small thickness of the Si membrane the generated phonon pulse passes through the interface between the two layers up to thirteen times, which is favorable to study the effect of the interface. This is a novel non-invasive approach for measuring adhesion between two layers.

The coherent acoustic phonons were generated and detected by optical pump-probe spectroscopy, whereby the technique used is asynchronous optical sampling (ASOPS) [1]. ASOPS utilizes two coupled femtosecond Ti:sapphire oscillators with a repetition rate of 800 MHz. An actively stabilized fixed offset in the repetition rates changes the time delay between the two laser pulses increasingly, allowing measuring a time window of 1.25 ns in 0.2 ms. All investigated samples have the same layer structure with varying thicknesses. The samples consist of a thin Al film on top of a single crystalline Si membrane. The membranes are obtained from a commercially available Si-on-insulator wafer, which is wet-etched from the backside with potassium hydroxide using a silicon-nitride etch mask, resulting in ~340 nm thick Si membranes. On top of the membranes, 10-20 nm thick Al films are evaporated or sputtered, leading to a different adhesion strength.

Previously we showed the results for a Al/Si membrane with strong adhesion [1]. We generated broadband acoustic frequency combs in the 100 GHz frequency range over nearly an octave using Al/Si membranes. 9 to 45 well separated modes could be excited, given by the harmonics of the fundamental mode. A frequency shift of the higher harmonics due to the different mechanical properties of the two layers was observed with great precision. By comparing the individual reflected pulses it was possible to obtain the lifetimes for an Al/Si layer system over the whole frequency range.

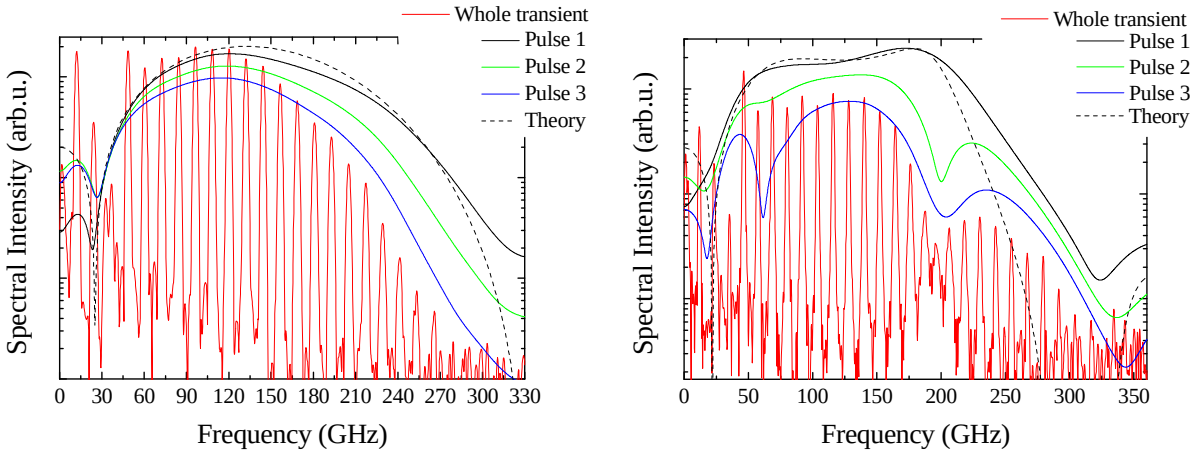

Figure 1: Time transient spectra of an Al/Si-system. The whole spectrum and the spectra of individual pulses are shown. Additionally the theoretically predicted spectrum is displayed a) for a system with strong adhesion, b) for a system with weak adhesion.

In figure 1 the Fourier spectra of a well adhered film (a)) and a poorly adhered film (b) are shown. The spectra consist of the spectrum of the whole time transient and the first three individual pulses visible in the time transient. Additionally the theoretical spectrum of the first pulse, calculated with the strain profile generated by a thermoelastic excitation and deformation potential, is shown, including reverberation at the Al/Si-interface.

In general one can see that the spectrum of the first pulse becomes damped after one and two round trips. Thereby one is able to extract the lifetimes of the different frequencies. Additionally due to the cavity-like structure of the two-layer system the whole spectrum resembles an optical frequency comb, where only the cavity-allowed frequencies are visible. For the individual first pulses, in comparison with the weakly adhered sample a plateau is visible in the spectrum instead of a parabolic behavior. Modeling the interface by assuming a spring between the two layers, we are able to derive an analytical term for the spectrum of the first pulse, only depending on the material parameters and a variable spring constant. As one can see in figure 1, the features are described quite clearly. However, the main effect of the weak adhesion reveals itself after the next passing of the interface. An additional dip at ~200 GHz appears, corresponding to the acoustic eigenfrequency of the Al film. The eigenmode oscillation affects strongly both the damping and the phase of this frequency regime in the spectrum.

In future works the adhesion evaluated here will have to be compared to other measurement techniques. Also the influence on the heat conduction due to weak adhesion instead of the damping of distinctive frequencies has to be investigated.

This work was supported by the DFG (SFB 767).

References

[1] A. Bartels, R. Cerna, C. Kistner, A. Thoma, F. Hudert, C. Janke, T. Dekorsy, "Ultrafast time-domain spectroscopy based on high-speed asynchronous optical sampling", *Rev. Sci. Instrum.*, **78**, 035107, 2007.

[2] M. Grossmann, M. Klingele, P. Scheel, O. Ristow, M. Hettich, C. He, R. Waitz, M. Schubert, A. Bruchhausen, V. Gusev, E. Scheer, T. Dekorsy, "Femtosecond spectroscopy of acoustic frequency combs in the 100-GHz frequency range in Al/Si membranes", *Phys. Rev. B*, **88**, 205202, 2013.

Acoustic phonon dispersion in ultra-thin Si membranes under static stress field

Bartlomiej GRACZYKOWSKI[1*], Jordi GOMIS-BRESCO[1], Francesc ALZINA[1], Juan S. REPARAZ[1], Andrey SHCHEPETOV[2], Mika PRUNNILA[2], Jouni AHOPELTO[2] and Clivia M. SOTOMAYOR TORRES[,3]

[1] *ICN2-Institut Catala de Nanociencia i Nanotecnologia, Campus UAB, E-08193 Bellaterra (Barcelona), Spain*

[2] *VTT Technical Research Centre of Finland, PO Box 1000, FI-02044 VTT, Espoo, Finland*

[3] *ICREA-Institucio Catalana de Recerca i Estudis Avançats, E-08010 Barcelona, Spain*

**corresponding author: bartlomiej.graczykowski@icn.cat*

Keywords: acoustic phonons, Si membranes, Brillouin light scattering, stress field

Stress-induced changes in the dispersion relations of GHz acoustic phonons propagating in 27 nm thick single crystalline Si membranes were investigated experimentally and theoretically. The static tensile stress acting on the Si membranes of up to 0.3 GPa was achieved using an additional strain compensating silicon nitride frame [1]. Thermally activated hypersonic phonons were measured by means of Brillouin light scattering spectroscopy [2,3]. The theory of Lamb wave propagation was developed for anisotropic materials subjected to an external static stress field using the elastic continuum approximation [3,4]. In addition, we showed how Brillouin spectroscopy provides a contactless and nondestructive tool for the stress measurements in the nm-scale systems.
Figure 1 shows the experimental dispersion curve compared to the theoretical calculations for the static stress $\sigma = \sigma_{11} = \sigma_{22} = 0.304$ GPa .

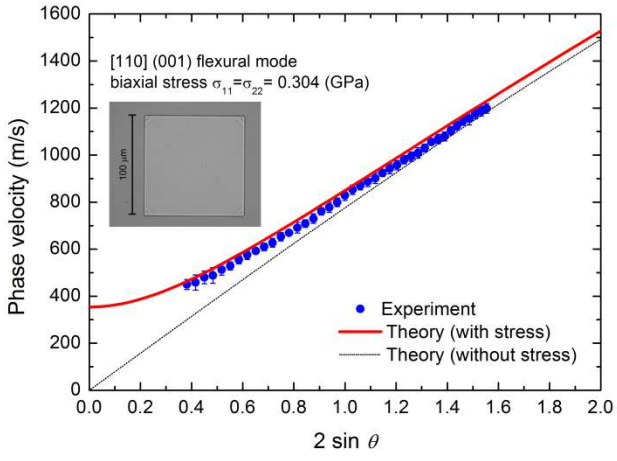

Figure 1: Comparison between experiment and theory of the A0 mode dispersion relation of the 27 nm thick Si membrane under the applied load σ = 0.304 GPa.

The thermal properties of the samples were studied in a contactless manner by means of two-laser Raman thermometry [5]. These studies have impact on micro- and nano-electromechanical systems (MEMS and NEMS) development as well as deep implications in thermal conductivity engineering.

References

[1] A. Shchepetov, M. Prunnila, F. Alzina, L. Schneider, J. Cuffe, H. Jiang, E. I. Kauppinen, C. M. Sotomayor Torres and J. Ahopelto, *Applied Physics Letters* **102**, 192108, 2013.

[2] J. Cuffe, E. Chavez-Angel, A. Shchepetov, P.-O. Chapuis, E. H. El Boudouti, F. Alzina, T. Kehoe, J. Gomis-Bresco, D. Dudek, Y. Pennec, B. Djafari-Rouhani, M. Prunnila, J. Ahopelto, and C.M. Sotomayor Torres, *Nano Letters* **12**, 3569, 2012.

[3] B. Graczykowski, J. Gomis-Bresco, F. Alzina, J.S. Reparaz, A. Shchepetov, M. Prunnila, J. Ahopelto and C.M. Sotomayor Torres, *New Journal of Physics* **16**, 073024, 2014.

[4] Y.H. Pao, W. Sachse, and H. Fukuoka, Physical Acoustics, edited by W.P. Mason and R.N. Thurston, Vol. **17** (Academic Press, New York, 1984) pp. 61-143.

[5] J.S. Reparaz, E. Chavez-Angel, M.R. Wagner, B. Graczykowski, J. Gomis-Bresco, F. Alzina and C.M. Sotomayor Torres, *Rev. Sci. Instrum.* **85**, 034901, 2014.

Nanoscale and Microscale Heat Transfer IV

Poster contributions

Poster session 1

Radiative thermal rectification using superconducting materials

Jérémie DREVILLON[a*], Elyes NEFZAOUI[b], Younes EZZAHRI[a] and Karl JOULAIN[a]

[a]*Institut Pprime, Université de Poitiers-CNRS-ENSMA, 2, Rue Pierre Brousse, Bâtiment B25, TSA 41105, 86073 Poitiers Cedex 9, France*
[b]*Université de Lyon, CNRS, INSA-Lyon, UCBL, CETHIL, UMR5008, F-69621, Villeurbanne, France*

**corresponding author: jeremie.drevillon@univ-poitiers.fr*

Keywords: radiative heat transfer, radiative thermal rectification.

Thermal rectification can be defined as an asymmetry in the heat flux when the temperature difference between two interacting thermal reservoirs is reversed. We present a far-field radiative thermal rectifier based on high-temperature superconducting materials with a rectification ratio up to 80%. This value is among the highest reported in literature. We examine the heat exchange between a superconductor ($Tl_2Ba_2CaCu_2O_8$) and a black body. Presented results might be useful for energy conversion devices, efficient cryogenic radiative insulators engineering, and thermal logical circuits' development.

For a system in an initial state characterized by a given thermal gradient, the rectification ratio can be defined by

$$R = \frac{q_{FB} - q_{RB}}{max(q_{FB}, q_{RB})}$$

where q_{FB} is the heat flux in the initial state (Forward Bias, FB) and q_{RB} is the heat flux when the thermal gradient is reversed (Reverse Bias, RB). A nonzero rectification means that a reversal of the thermal gradient induces, in addition to the reversal of the heat flux direction, a variation of its magnitude. The realization of a device exhibiting such an uncommon behavior, a thermal rectifier, for instance, can be very useful for thermal insulation applications. It would also pave the way for the development of thermal circuits in the manner non-linear electronic devices marked the genesis of modern electronics [1]. Indeed, as in electronics, thermal logical circuits need a thermal diode, which can be defined as an ideal rectifier, i.e., a one-way heat transmitter. Consequently, an increasing interest has been given to thermal rectifiers during the past decade. First works focused on heat conduction devices and led to rectification models based on non-linear lattices [2-5], graphene nano-ribbons [6,7] and several other interesting mechanisms [8,9]. Some authors went beyond the thermal rectification issue and proposed theoretical models of thermal logical gates [10] and a thermal transistor [11]. During the last 4 years, a few authors tackled the question of radiation-based thermal rectification. A theoretical study and an experimental suggestion of a radiative thermal rectifier based on non-linear solid-state quantum circuits operating at very low temperatures (a few mK) were first presented [12]. A rectification ratio up to 10% was predicted. Later on, two theoretical schemes of radiative thermal rectification based on near-field thermal radiation control were proposed [13,14]. A rectification ratio up to 30% (according to the present paper rectification definition and using the references data) was theoretically predicted for temperature differences ranging between 100K and 300K. Comparable rectification ratios have also been reached, for the same temperature differences, by a Fabry-Pérot cavity based far-field radiative thermal rectifier we recently presented [15]. We reported a maximal rectification ratio of 19%. We shall note here that the interacting bodies in all

these early radiative rectifiers are discrete modes resonators: bulk materials supporting surface resonances, surface phonon-polaritons or surface plasmon-polaritons for instance, nanostructured materials with cavity modes or nonlinear quantum resonators. Rectification is therefore achieved by controlling the coupling between the two bodies modes. Switching from a state where the two thermal reservoirs modes are strongly coupled, FB, to a state of weak coupling, RB, leads to a decrease in the exchanged radiative heat flux (RHF), thus to a thermal rectification.

More recently, the idea of broadband radiative thermal rectification (BRTR) emerged with the use of a phase change material (PCM), VO_2, for instance [16-18]; Heat flux contrasts up to 80% and 90% have been experimentally proven in the far-field and the near-field respectively. We emphasize here that these contrasts are only observed around VO_2 metal-insulator transition temperature (67°C), which strongly restricts their potential practical scope. Using these contrasts to design a VO2–based thermal rectifier was then proposed [19-20] and rectification ratios up to 70% and 90% for small and large temperature differences were reported, respectively. Consequently PCM seems to be good candidate for efficient thermal rectification.

Superconducting materials are a subset of PCM and we propose here a far field radiative thermal rectifier based on high temperature superconductors. We choose these materials for two reasons. First, when they are switched from the normal to the superconducting state, their reflectance significantly increases to almost 1 in the far infrared, while the mid-infrared spectrum remains almost unchanged [22]. The second reason is that a black body at $T \approx 100$ K emits almost 90% of its intensity in the spectral range above 20 μm, i.e, in the far infrared. This is exactly the spectral domain where these materials show large TOP (thermo-optical properties) which makes them good candidates for radiation based thermal rectifiers. We investigate here the radiative heat transfer between a black body and the supercondconductor $Tl_2Ba_2CaCu_2O_8$(Tc=125 K).

A rectification ratio of almost 80% can be reached with the proposed implementation for small temperature differences around T_c=125K. The proposed device is composed of two opaque thermal baths 1 and 2 held at temperatures T_1 and T_2 , respectively, and exchanging heat through thermal radiation.

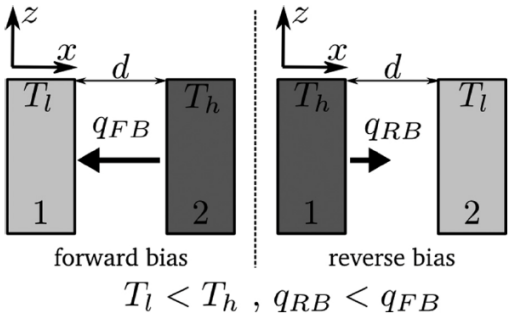

Figure 1: Two parallel planar bodies separated by a vacuum gap of thickness d. In FB configuration $T_1=T_l$ and $T_2= T_h$. In RB, $T_1=T_h$ and $T_2=T_l$.

Figure 1 shows a schematic of the proposed device, which is composed of two parallel planar bodies 1 and 2 separated by a gap of thickness d and characterized by their optical properties, their emissivities for instance, and temperatures (ε_1 (T_1), T_1) and (ε_2 (T_2), T_2), respectively. In FB, $T_1=T_l$ and $T_2=T_h$. Subscripts l and h stand for low and high temperatures, respectively. The two bodies temperatures are swapped in RB. The two bodies are assumed to be in vacuum. Consequently, q is a RHF density. Their emissivities and reflectivities (ε and ρ, respectively) are completely governed by their dielectric

functions and geometries. In the case of opaque bodies, energy conservation and Kirchhoff's laws combination lead to the following relation between the monochromatic emissivity and reflectivity at a given temperature:

$$\varepsilon(T,\lambda) = 1 - \rho(T,\lambda)$$

We also assume here that the two bodies are Lambertian sources, i.e., with isotropic radiative properties. Consequently, ε and ρ are direction independent. The gap width d is assumed to be much larger than the dominant thermal radiation wavelength. The net RHF density exchanged by the two media reduces then to the far-field contribution. Indeed, the near-field contribution becomes significant when the distance separating the interacting bodies is of the order or lower than the characteristic wavelength of thermal radiation since it is due to evanescent waves. On the other hand, the far-field contribution, due to propagative waves and described by Planck's law, is distance independent for the considered configuration. The net RHF density can then be written as follows [22]

$$q(T_1,T_2) = \pi \int_{\lambda=0}^{\infty} [I^0(\lambda,T_1) - I^0(\lambda,T_2)]\tau(\lambda,T_1,T_2)d\lambda,$$

where

$$I^0(\lambda,T) = \frac{2hc^2}{\lambda^5}\frac{1}{e^{hc/\lambda k_B T} - 1}$$

is the black body specific intensity of radiation at a temperature T and

$$\tau(\lambda,T_1,T_2) = \frac{[1-\rho_1(\lambda,T_1)][1-\rho_2(\lambda,T_2)]}{1-\rho_1(\lambda,T_1)\rho_2(\lambda,T_2)}$$

is the monochromatic RHF density transmission coefficient between 1 and 2.

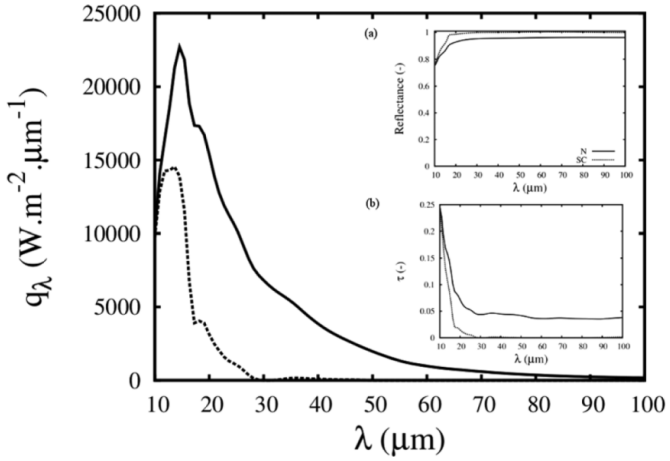

Figure 2:. Exchanged spectral radiative heat flux density in FB (solid line) and RB (dashed line). Insets: (a) Experimental data of Tl2Ba2CaCu2O8 reflectance in the normal (solid line) and superconducting (dashed lines). (b) Spectral transmission coefficient in FB (solid line) and RB (dashed line) using the reflectance data shown in inset (a).

First, consider the case where T_l =77 K (liquid nitrogen boiling point) and T_h = 140 K. Body 1 is a black body so that $\varepsilon(\lambda,T)=1$. Body 2 is made of $Tl_2Ba_2CaCu_2O_8$ (T_c=125 K). Figure 2 depicts the resulting exchanged radiative heat flux spectral density in forward and reverse bias, respectively. A rectification ratio R=0.7 is obtained. The behavior of the rectification ratio as a function of the temperature difference between the two bodies is shown in Figure 3. The low temperature is maintained at T_l =77K and T_h is given by $T_h=T_l + \Delta T$ with ΔT ranging between 1 and 65 K. No rectification is observed for $T_h<T_c$. The rectification ratio reaches its maximum $R_{s,max}$=0.79, when Th is slightly larger than T_c then slowly decreases. This value is of the order of the maximal experimentally observed contrasts in far-field radiative heat transfer with phase change materials. Since our calculations are based on experimental reflectance data, we also represent in Figure 3 the uncertainty range of the rectification ratio (dashed lines) corresponding to a 10% uncertainty on used reflectance

data. This shows a relative uncertainty on the maximal rectification ratio ranging over [-10%, +5%]. The inset of Figure 3 illustrates the exchanged RHF density in FB (solid line) and RB (dashed line). Both fluxes increase over the whole range as ΔT increases. When $T_h<T_c$, $q_{FB}=q_{RB}$, since the optical properties of both the black body and the superconducting material do not vary between T_l and Th. This leads to zero rectification. When T_h slightly surpasses T_c, the superconducting material becomes less reflecting in FB, i.e., when $T_2=T_h$, which explains the sharp increase of the exchanged RHF density. Indeed, at $T_2 \geq T_c$, in addition to the flux increase due to ΔT rise, FB RHF density is strongly enhanced due to the non-linearity of the superconducting material TOP. Such materials with a strongly variable thermal conductance can find promising applications in insulation engineering.

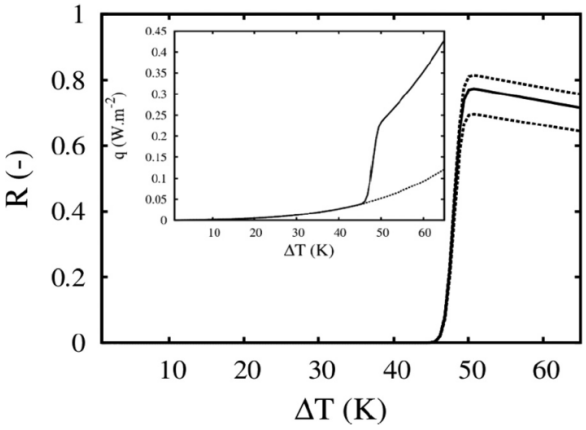

Figure 3: Rectification ratio as a function of the temperature difference with 10% uncertainty on the superconducting material reflectance experimental data (dashed lines). Inset: exchanged radiative heat flux density in FB (solid line) and RB (dashed line) as a function of the temperature difference.

References

[1] L. Wang and B. Li, *Phys. World* **21**, 27, 2008.

[2] M. Terraneo, M. Peyrard, and G. Casati, *Phys. Rev. Lett*. **88**, 094302, 2002.

[3] B. Li, L. Wang, and G. Casati, *Phys. Rev. Lett*. **93**, 184301, 2004.

[4] B. Li, J. Lan, and L. Wang, *Phys. Rev. Lett*. **95**, 104302, 2005.

[5] B. Hu, L. Yang, and Y. Zhang, *Phys. Rev. Lett*. **97**, 124302, 2006.

[6] J. Hu, X. Ruan, and Y. P. Chen, *Nano Lett*. **9**, 2730, 2009.

[7] N. Yang, G. Zhang, and B. Li, *Appl. Phys. Lett*. **95**, 033107, 2009.

[8] D. Segal, *Phys. Rev. Lett*. **100**, 105901, 2008.

[9] N. Yang, N. Li, L. Wang, and B. Li, *Phys. Rev. B* **76**, 020301, 2007.

[10] L. Wang and B. Li, *Phys. Rev. Lett*. **99**, 177208, 2007.

[11] W. C. Lo, L. Wang, and B. Li, *J. Phys. Soc. Jpn*. **77**, 054402, 2008.

[12] T. Ruokola, T. Ojanen, and A.-P. Jauho, *Phys. Rev. B* **79**, 144306, 2009.

[13] C. R. Otey, W. T. Lau, and S. Fan, *Phys. Rev. Lett*. **104**, 154301, 2010.

[14] S. Basu and M. Francoeur, *Appl. Phys. Lett.* **98**, 113106, 2011.

[15] E. Nefzaoui, J. Drevillon, Y. Ezzahri, and K. Joulain, *Applied Optics*, **53**, 3479, 2014.

[16] P. J. van Zwol, K. Joulain, P. Ben Abdallah, J. J. Greffet, and J. Chevrier, *Phys. Rev. B* **83**, 201404, 2011.

[17] P. J. van Zwol, K. Joulain, P. Ben-Abdallah, and J. Chevrier, *Phys. Rev. B* **84**, 161413, 2011.

[18] P. J. van Zwol, L. Ranno, and J. Chevrier, *Phys. Rev. Lett.* **108**, 234301, 2012.

[19] J. Huang, Q. Li, Z. Zheng, and Y. Xuan, *Int. J. Heat Mass* Transfer **67**, 575, 2013.

[20] P. Ben-Abdallah and S.-A. Biehs, *Appl. Phys. Lett*. **103**, 191907, 2013.

[21] D. B. Tanner and T. Timusk, "Optical properties of high-temperature superconductors," in Physical Properties of High Temperature Superconductors III (World Scientific, 1992).

[22] M. F. Modest, Radiative Heat Transfer (McGraw-Hill, 1993).

Analysis of thermal conductance of ballistic point contacts using Boltzmann Transport Equation

T. T. Trang NGHIEM[a*], Jérôme SAINT-MARTIN[b] and Philippe DOLLFUS[b]

[a]*Université de Lyon, CNRS, INSA-Lyon, UCBL, CETHIL, UMR5008, F-69621, Villeurbanne, France*

[b]*Université de Paris Sud, CNRS, IEF, F91405 Orsay cedex, France*

**corresponding author: tthutrang.nghiem@gmail.com*

Keywords: phonon Boltzmann transport equation, nano-pillar contact, GaAs, phonon occupation, thermal conductivity.

1. Introduction

In the context of semiconductor device miniaturization, thermal management at the nanometer scale is a critical issue. From a theoretical point of view, the modeling of thermal transport in devices of size comparable to the phonon mean free path, typically about 100 nm in usual semiconductors, must be able to include not only ballistic but also quasi-ballistic effects as some scattering events can still occur at this intermediate scale.

Recently, in 2012, Bartsch and co-workers [1] demonstrated the fabrication of air-gap heterostructures based on ultra short GaAs pillars with a diameter of 100 nm (Fig. 1a). Two different pillar lengths (between GaAs substrate and the capping layer) of 4 nm and 6 nm have been fabricated. The thermal conductance measured in these structures was reduced by several orders of magnitude compared to that of bulk GaAs. In their theoretical interpretation of the results, the authors assumed the pillar to be perfect ballistic point contacts and the phonon current through the pillars was considered as fully ballistic, i.e. not influenced by any scattering mechanism.

In this work, by numerically solving the Boltzmann Transport Equation (BTE) with an accurate phonon dispersion, we investigate the influence of scattering mechanisms on phonon transport in such GaAs pillars. We show that at room temperature, some scattering events occur even in 4 nm-long pillars and have a significant influence on the thermal conductance at high temperature.

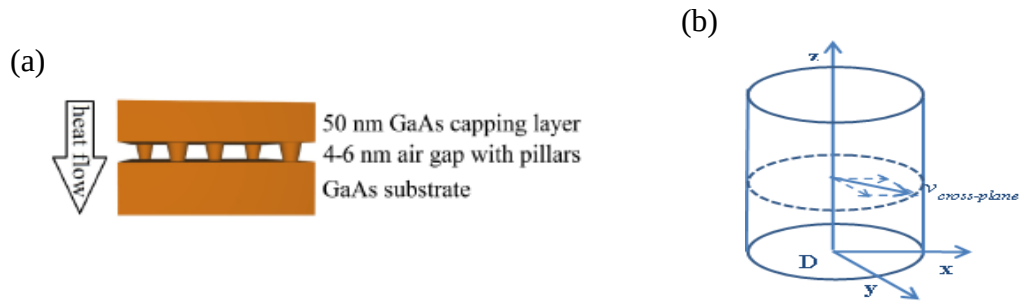

Figure 1: (a) Scheme of experimental structure from Ref. [1]. (b) Schematized view of studied pillar structure and coordinates.

2. Model

To investigate the thermal conductance of nanometer-long pillars, one longitudinal acoustic mode (LA) and two transverse acoustic phonon modes (TA) were considered. For each mode, the BTE was

used to model the phonon behavior in the crystal lattice. The common relaxation time approximation (RTA) was used to model the complex scattering term. In the absence of external forces, the steady-state 1D BTE for phonons (along *z*-direction) can be written as

$$v_{gz,s} \cdot \frac{\partial N_s(z,\vec{q})}{\partial z} = -\frac{N_s(z,\vec{q}) - N_{s,Tscattering}(z,\vec{q})}{\tau_s}, \quad (1)$$

where N_S is the phonon distribution function, *s* is the phonon mode, τ_s is the relaxation time of phonon mode *s* and $T_{scattering}$ the temperature at which the equilibrium distribution $N_{S,Tscattering}$ is calculated (according to the Bose-Einstein statistics). This scattering temperature is provided by the solution of the heat Fourier equation.

A sine approximation is used to model the acoustic phonon dispersion in GaAs. This function was experimentally calibrated for bulk GaAs in Ref. [2] and written as

$$\omega_s(q) = \omega_s^{\max} \cdot \sin\left(\frac{qa}{4}\right), \quad (2)$$

where *a* is the lattice constant and ω_s^{max} is the maximum phonon frequency. The values of ω_s^{max} are taken from ref. [3]. As in Ref. [1], the optical phonon modes are neglected. This is a reasonable approximation since these phonons have low group velocity and high activation energy [4] and hence do not strongly contribute to the thermal flux.

Based on the Holland's model [5], our scattering parameters for Normal (N) and Umklapp (U) phonon-phonon scattering rates have been adjusted to fit the thermal conductivity in bulk GaAs. All scattering mechanisms and corresponding parameters are reported in Table 1. The resulting thermal conductivity in bulk GaAs material matches very well the experimental data in the range 2-300K [6].

Scattering type			
phonon-phonon	TA – Normal $\tau_{TA}^{-1} = B_{TN}\omega T^4$, with $B_{TN} = 1.98\times10^{-11}\ K^{-4}$	TA – Umklapp $\tau_{TA}^{-1} = B_{TU}\omega^2 / \sinh(\hbar\omega/k_B T)$, with $B_{TU} = 0$ (if $\omega < \omega_{cut}$), $B_{TU} = 4.58\times10^{-18}\ s$ (if $\omega > \omega_{cut}$)	LA $\tau_{NU}^{-1} = B_L\omega^2 T^3$, with $B_L = 6.8\times10^{-24}\ sK^{-3}$
phonon-impurity	$\tau_I^{-1} = A\omega^4$, with $A = 1.25\times10^{-44}\ s^{-3}$		
phonon- boundary	$\tau_b^{-1} = v_{g,s}/LF$, with $L = 0.51\times10^{-2}\ m$, and $F = 0.68$		

Table 1: Relaxation times for the phonon scattering mechanisms used in this work. k_B *is the Boltzmann constant,* $v_{g,s}$ *is the group velocity of mode* s, F *is an average form factor,* q *is the phonon wave vector,* Δ *is the roughness parameter,* θ_B *is the incident angle of particle to the surface. The frequency* $\omega_{cut} = \omega(q_{\max}/2)$ *corresponds to the frequency at which the Umklapp scattering processes for TA phonons become possible.*

Besides, in the nanopillar schematized in Fig. 1, the cross-plane phonon-boundary scattering mechanism is also considered. The corresponding relaxation rate is given by

$$\tau_b = \frac{D_{pillar}}{v_{cross-plane}} \quad (3)$$

In Ref [1], the pillar diameter D_{pillar} was experimentally estimated to be 100 nm. The in-plane group velocity $v_{cross\text{-}plane}$ is defined as $v_{cross-plane} = \sqrt{v_{gx}^2 + v_{gy}^2}$. Finally, the total relaxation time (including phonon-phonon, phonon-impurity and phonon-cross-plane boundary scatterings) is computed by applying the Matthiessen's rule. The authors have developed a similar model for phonon transport in Si to study self-heating effects in short-channel transistors [7].

3. Results and discussion

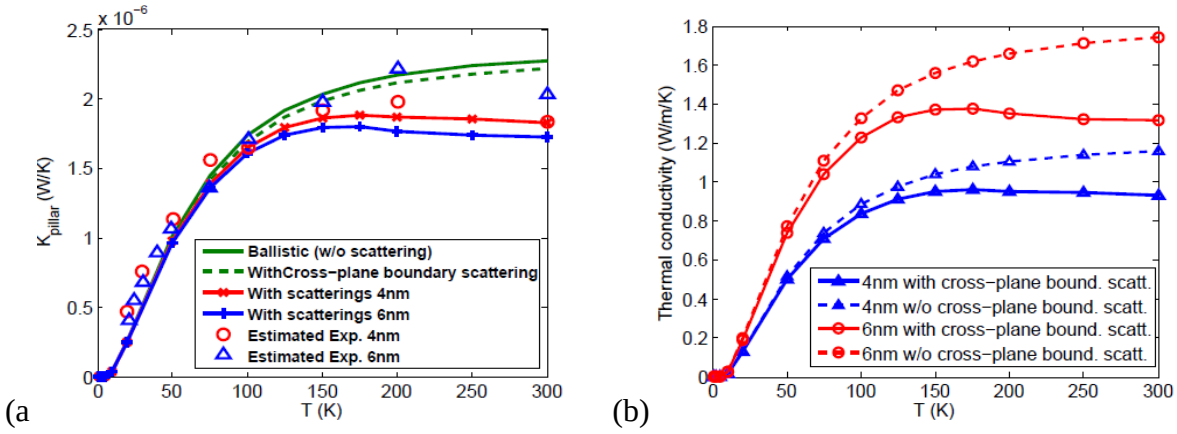

Figure 2: (a) Evolution of the thermal conductance as a function of temperature in single pillar: pure ballistic pillar (solid green line), only with cross-plane boundary scattering mechanism (dashed green line), with all scattering mechanism in 4 nm (red line with cross) and 6 nm (blue line with add symbol) long pillars. Estimated experimental data for 4 nm (red circles) and 6 nm (blue triangles) long pillars from [1]. (b) Evolution of the thermal conductivities in 4nm- (blue triangles) and 6nm-(red circles) long pillars with (continuous lines) and without (dashed lines) the cross-plane boundary scattering.

In Fig. 2a, the thermal conductivity is plotted for 4 nm- and 6 nm-long nanopillars in the case of pure ballistic pillar, in which only the cross-plane boundary scattering mechanism is considered, and pillar with a complete set of scattering mechanisms. As expected, the pure ballistic case gives the highest value of conductivity. For both 4 nm and 6 nm-long pillars, with complete set of scattering mechanisms (phonon-phonon, phonon-impurity and phonon-boundary), the conductance is lower than that of ballistic cases for temperature higher than 100 K. This difference suggestss that the scattering mechanisms limit the heat transfer even in such short nano-pillars. This phenomenon is less pronounced in the 4 nm-long pillar than in the 6 nm-long ones but it is still significant. The corresponding thermal conductivities are shown in Fig. 2b. It should be mentioned that, due to the nanostructuring, these conductivities, in the range 1-2 $Wm^{-1}K^{-1}$, are more than one order of magnitude lower than the bulk GaAs conductivity that is equal to 46 $Wm^{-1}K^{-1}$.

To illustrate the quasi-ballistic nature of phonon transport, the spatial evolutions of the phonon distributions along a 6 nm-long-pillar are shown in Fig. 3. For an applied temperature gradient of 20 K, both the LA and TA distributions are presented in the case of three different average temperatures: 50, 100 and 300 K. If the transport was perfectly ballistic everywhere in the device, the distributions of phonons with a negative wave vector (left side) would have been exactly the same form as that injected at the cold side (blue line). Similarly, the positive part of the distribution should be that injected at the hot contact T_h. However, in Fig. 3 we can see that, at all studied temperatures, the evolution of the distributions between the hot and cold contacts is not fully abrupt, in particular for phonons with small wave vector q_z. This means that although the ballistic regime is clearly dominant even at room temperature, some scattering events occur and have an impact. Indeed, as we can see on

Fig 2a, only the onset of scattering can explain the decrease of thermal conductance observed experimentally at high temperature.

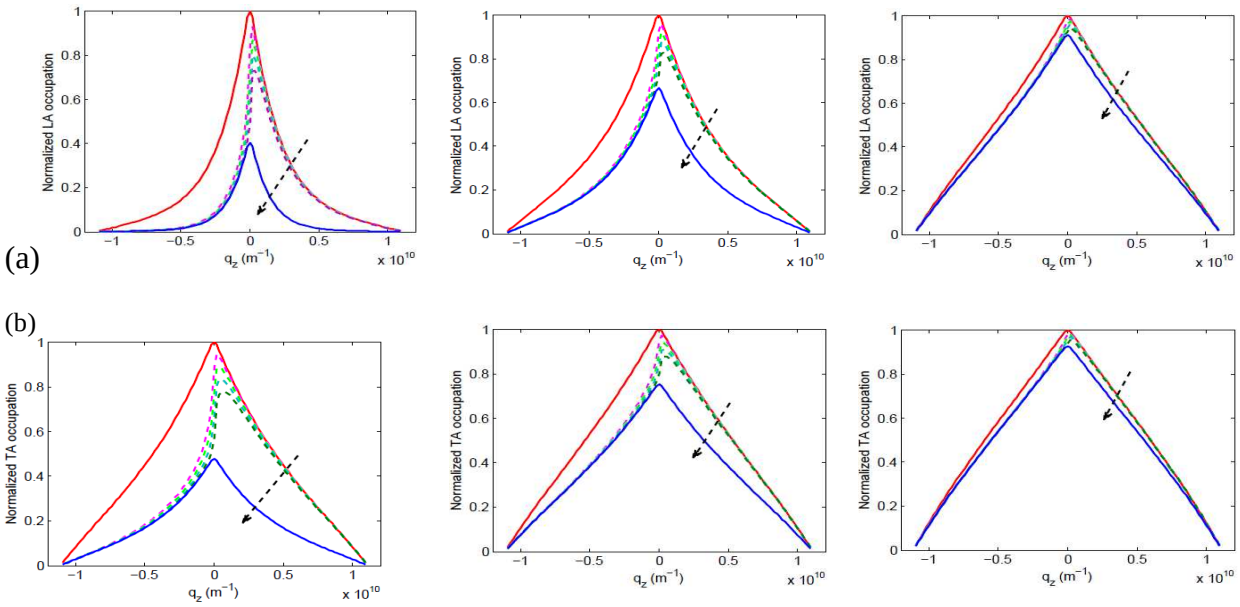

Fig. 3. Spatial evolution of the phonon distribution in the 6 nm long pillar with T_h and T_c = [60 K, 40 K], [110 K, 90 K] and [310 K, 290 K], from left to right, respectively. The normalization is done with respect to the phonon occupation at the hot temperature T_h. (a) LA phonons. (b) TA phonons. The arrow gives the hot to cold direction.

4. Conclusion

In this work, the steady state BTE has been solved considering a sine dispersion. This modeling approach is able to satisfactorily reproduce the evolution of the experimental thermal conductance of 4 nm and 6 nm-long-nanopillars as a function of temperature. Our work suggests that at temperature higher than 100K even sub-10 nm-long pillars do not reach the full ballistic regime, which manifests in the decrease of thermal conductance when the temperature increases.

References

[1] Th. Bartsch, M. Schmidt, Ch. Heyn, W. Hansen, “Thermal conductance of ballistic point contacts”, *Phys. Rev. Let.* **108**, 075901, 2012.

[2] D. Strauch, B. Dorner, “Phonon dispersion in GaAs”, *J. Phys.: Condens. Matter* **2**, 1457, 1990.

[3] J. S. Blakemore, “Semiconducting and other major properties of gallium arsenide”, *J. Appl. Phys.* **53**, R123, 1982.

[4] G. Chen, “Thermal conductivity and ballistic phonon transport in the cross-plane direction of superlattices”, *Phys. Rev. B* **57**, 14958, 1998.

[5] M. G. Holland, “Analysis of lattice thermal conductivity”, *Phys. Rev.* **132**, 2461, 1963.

[6] M. G. Holland, “Phonon scattering in semiconductors from thermal conductivity studies”, *Phys. Rev.* **134**, A471, 1964.

[7] T. T. Trang Nghiêm, J. Saint-Martin, P. Dollfus, “New insights into self-heating in Double-Gate Transistors by solving Boltzmann transport equations”, *J. Appl. Phys.* **116**, 074514, 2014.

Focusing of surface phonon-polaritons along conical and wedge polar structures

Sergei GLUCHKO[a,b*], Jose ORDONEZ-MIRANDA[a], Laurent TRANCHANT[a], Thomas ANTONI[a,b] and Sebastian VOLZ[a]

[a]*Laboratoire d'Energétique Moléculaire et Macroscopique, Combustion, UPR CNRS 288, Ecole Centrale Paris, Grande Voie des Vignes, 92295 Chatenay Malabry, France*

[b]*Ecole Centrale Paris, Laboratoire de Photonique Quantique et Moléculaire, CNRS UMR 8537, Ecole Normale Supérieure de Cachan, Grande Voie des Vignes, F-92295 Châtenay-Malabry cedex, France*

**corresponding author: sergei.gluchko@ecp.fr*

Keywords: Surface phonon-polaritons, Thermal energy focusing, Polariton energy guiding.

Modern microelectronics technology requires developing more efficient ways of heat extraction and device cooling at the tens-nanometer scale. The thermal conductivity of materials decreases as their characteristic sizes are scaled down, while the influence of the surface effects increases with the growth of surface-to-volume fraction. This is why the surface phonon-polaritons (SPPs), which are evanescent electromagnetic waves propagating along polar-dielectric interfaces and generated by the fluctuation of the electrical dipoles of polar media (Fig. 1(a)), are expected to lead to a significant enhance of the thermal conductivity of these materials [1-6]. Focusing of SPPs could be an efficient way of heat extraction in nanodevices [7], but this effect is not well explored yet.

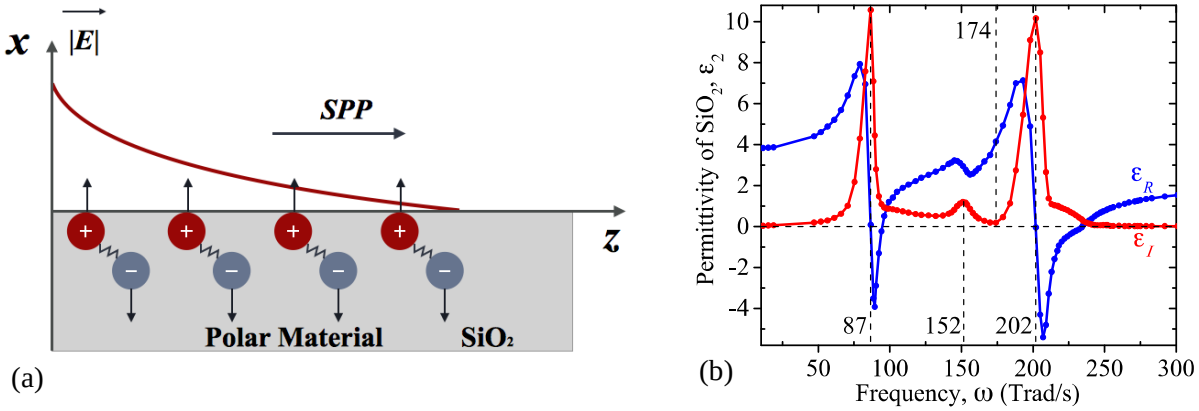

Figure 1: (a) Generation of SPPs due to the fluctuation of electrical dipoles. (b) Real (ε_R) and imaginary (ε_I) parts of the permittivity of SiO_2 as a function of frequency.

In the present work, the focusing of SPP energy along conical and wedge structures of SiO_2 surrounding by air is analyzed based on the analytical solution of Maxwell's equations. In the conical structure, the SPPs are propagating along the SiO_2-air interface toward the point-like tip, where the SPP energy is focused (Fig. 2(a)), while in the wedge this focusing is along its linear edge (Fig. 2(b)). The dispersion relations for the cone and the wedge are given in Eqs. (1a) and (1b), where $\varepsilon_1(\omega)$ is SiO_2 permittivity as a function of frequency ω, ε_2 is a permittivity of the surrounding medium (air), $I_n(\alpha\lambda)$, is modified Bessel functions of first kind and of order *n*; $P_\lambda^{(1)}(X)$ is associated Legendre function of first order; $X=\cos(\alpha)$; α is the aperture angle of each structure.

$$X\left(\frac{\varepsilon_1(\omega)}{\varepsilon_2}-1\right)+\frac{\varepsilon_1(\omega)}{\varepsilon_2}\frac{P_{\lambda+1}^{(1)}(-X)}{P_{\lambda}^{(1)}(-X)}+\frac{P_{\lambda+1}^{(1)}(X)}{P_{\lambda}^{(1)}(X)}=0, \tag{1a}$$

$$\varepsilon_1(\omega)\tanh(\eta\alpha)=-\varepsilon_2\tanh(\eta(\pi-\alpha)). \tag{1b}$$

The solutions of these dispersion relations for the propagation parameters λ and η are complex, due to the fact that SiO_2 is an absorbing material with a complex and frequency-dependent permittivity, as shown in Fig. 1(b). The real part of propagation parameter η is associated with the attenuation of the electro-magnetic field; while its imaginary part is related to the propagation of the electro-magnetic wave along the SiO_2–air interface. The solution of the dispersion relation for the wedge structure and its effect on the electrical and magnetic fields of SPPs is performed (Fig. 3). The existence of SPPs is

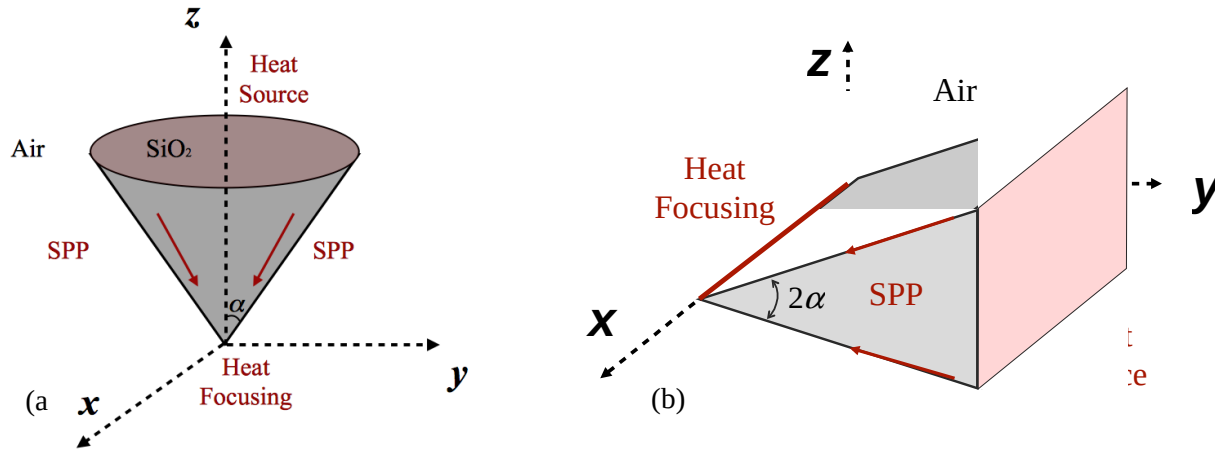

Figure 2: Schematics of the (a) conical and (b) wedge structures of SiO_2 surrounded by air. The red arrow indicates propagation of SPPs from the heat source to the cone tip and wedge edge.

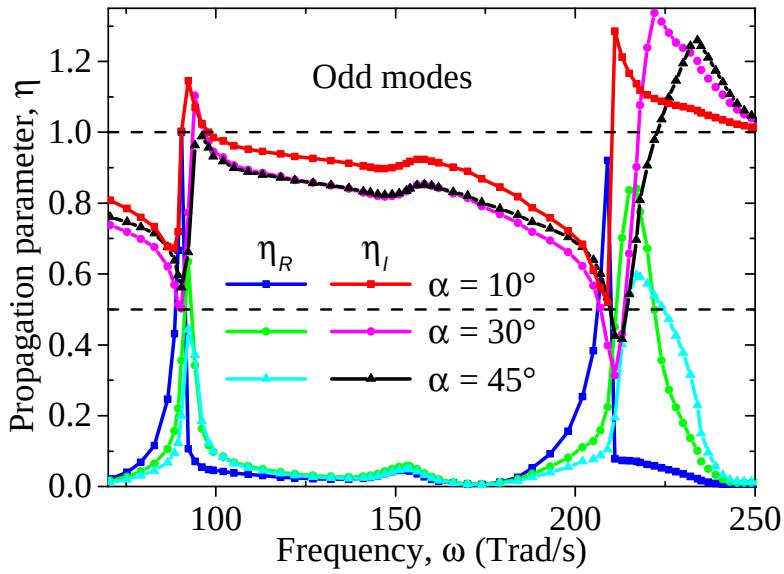

Figure 3: Propagation parameter (real and imaginary parts) as a function of frequency for the wedge structure for different aperture angles of the wedge.

observed only in the regions of frequencies where the real part of permittivity is negative, which corresponds to the results obtained for thin films and thin wires, reported in [1, 2, 4, 5]. According to

the energy conservation law, there are no SPPs in the regions of frequency where the imaginary part of the propagation parameter is greater than 0.5. Both real and imaginary parts of the propagation parameter should be positive in order to have propagation of the electro-magnetic field towards to the tip and to have focusing of the electro-magnetic field along the SiO_2–air interface. The focusing effect increases when the imaginary part of the propagation parameter decreases.

References:

[1] J. Ordonez-Miranda, L. Tranchant, T. Tokunaga, B. Kim, B. Palpant, Y. Chalopin, T. Antoni, S. Volz, "Anomalous thermal conductivity by surface phonon-polaritons of polar nano thin films due to their asymmetric surrounding media", *J. Appl. Phys.* **113**, 084311, 2013.

[2] J. Ordonez-Miranda, L. Tranchant, B. Kim, Y. Chalopin, T. Antoni, S. Volz, "Effects of anisotropy and size of polar nano thin films on their thermal conductivity due to surface phonon-polaritons ", Appl. Phys. Express. **7**, 035201, 2014.

[3] J. Ordonez-Miranda, L. Tranchant, Y. Chalopin, T. Antoni, S. Volz, "Thermal conductivity of nano-layered systems due to surface phonon-polaritons ", *J. Appl. Phys.* **115**, 054311, 2014.

[4] J. Ordonez-Miranda, L. Tranchant, T. Tokunaga, B. Kim, B. Palpant, Y. Chalopin, T. Antoni, S. Volz, "Anomalous thermal conductivity by surface phonon-polaritons of polar nano thin films due to their asymmetric surrounding media", *J. Appl. Phys.* **113**, 084311, 2013.

[5] J. Ordonez-Miranda, L. Tranchant, B. Kim, Y. Chalopin, T. Antoni, S. Volz, "Quantized Thermal Conductance of Nanowires at Room Temperature Due to Zenneck Surface-Phonon Polaritons ", *Phys. Rev. Lett.* **112**, 055901, 2014.

[6] D. Z. A. Chen, A. Narayanaswamy, G. Chen, "Surface phonon-polariton mediated thermal conductivity enhancement of amorphous thin films", *Phys. Rev.* B **72**, 155435, 2005.

[7] A. J. Huber, B. Deutsch, L. Novotny, R. Hillenbrand. "Focusing of surface phonon polaritons", *Appl. Phys. Lett.* **92**, 203104, 2008.

Modeling of heat transfer through gas molecules between a hot SThM probe and a cold sample surface

Jaona RANDRIANALISOA[a*] and Nathalie TRANNOY[a]

[a]*GRESPI, Université de Reims Champagne-Ardenne, EA 4694, Moulin de la Housse, F-51687 Reims, France*

**corresponding author: jaona.randrianalisoa@univ-reims.fr*

Keywords: Computational heat transfer, Monte Carlo simulation, gas molecules, SThM.

The knowledge of heat transfer at micro/nanoscale is essential for micro/nanotechnologies based on energy dissipation [1-3]. For the thermal studies at these scales, AFM-based techniques as Scanning Thermal Microscopes (SThM) have been developed to obtain information regarding thermal properties of materials with nanometer to micrometer resolution. [4-7]. This AFM-based technique requires a specific thermal probe, instead of conventional AFM tip, operating at ambient air and giving simultaneously topography and thermal property images of materials. When this microscope is equipped with a thermal-resistive probe, the interaction between the probe and the sample is ensured by the heat transfer. Thus, a better knowledge of heat transfer between the hot probe and the cold investigated sample is crucial for quantitative measurements.

When a hot probe-based Wollaston and a cold sample are in contact, heat can be exchanged through contact solid-solid (probe/sample) conduction, conduction (tip/holder), convection, water meniscus depending on ambient humidity [8]. Due to the probe shape, the probe is not a local heat point; thermal exchange through ambient air takes place along the probe filament. This contributes to the experimental measurement. So it is crucial to have a quantitative estimation of the heat transfer between the tip and the sample as heat transfer by air. This problem concerns also nanoscale device operating at high temperature or used for techniques of designing thermally storage data [9]. Investigation of 1 mm distances between the probe and the cold surface revealed a thermal resonance phenomenon of temperature field [10] which is independent of material properties but depends only on the distance between the probe and the sample. It can be interpreted as a resonance, with the behavior of thermal waves associated with the AC heat diffusion, due to the experimental geometry (probe/sample surface). In [10], the Finite Element method was used to study heat transfer through air between the probe and the sample and the heat transfer was assumed in the diffusion regime. In this paper, we report the development of a quantitative predicting tool of heat transfer through the fluid between SThM probe and sample at distances of nanometers as illustrated in figure 1. It is known that when the heat source and sink are separated by a distance comparable to the heat carrier mean-free-path (about tens of nanometers for the gas molecules composing the fluid medium), the classical macroscopic laws such as the Fourier law and Navier Stokes equations breakdown. In this case, advanced microscopic approaches have to be used. Regarding only the heat transfer through gas molecules, the problem can be modeled using the Boltzmann transport equation (BTE). We use direct Monte Carlo simulation (DMCS) for solving the BTE [11]. After the verification of model with classical cases of heat transfer between parallel plane surfaces, we discuss the effects of the separation distance and the size of the heating object on the temperature field within the fluid and heat flux transferred to the cold wall.

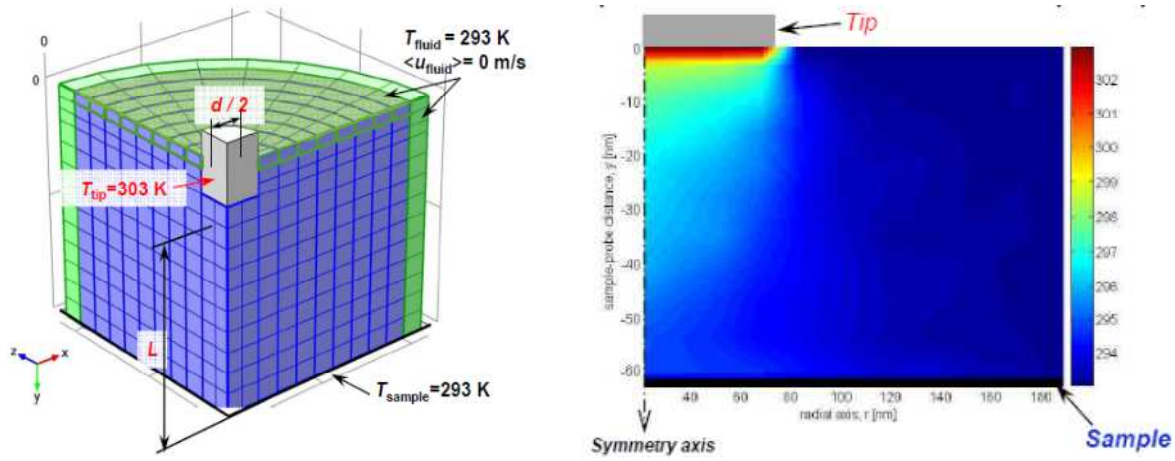

(a) (b)

Figure 1: (a) 3D geometry used to simulate the heat transfer through gas molecules (blue region) between a hot tip (gray cylinder) and a cold sample surface (black plane). (b) Typical 2D temperature distribution of the fluid phase for a tip located at 62.6nm above the sample surfaces

References

[1] D. G. Cahill *et al.*, "Nanoscale thermal transport", *J. Appl. Phys.*, **93**, pp. 793-818, 2003.

[2] E. Pop, "Energy Dissipation and Transport in Nanoscale", *Devices Nano Research*, **3**, pp. 147-169, 2010.

[3] A. B. A. Dow, K. Ivanova, T. Ivanov, I. Rangelow, "Design and fabrication of a horizontal thermal micro-actuator with integrated micro tweezers", CIMTEC 2008 - Proceedings of the 3rd International Conference on Smart Materials, Structures and Systems - Smart Materials and Micro/Nanosystems, **54**, pp. 378-383, 2008.

[4] A. Majumdar, "Scanning Thermal Microscopy", *Ann. Rev. Sci.*, **29**, pp. 505-585, 1999.

[5] E. Gmelin, R. Fischer and R. Stitzinger, "Sub-micrometer thermal physics - An overview on SThM Techniques", *Thermochimica Acta*, **310**, pp. 1-17, 1998.

[6] B. Cretin, S. Gomès, N. Trannoy, P. Vairac, "Scanning thermal microscopy", *Topics in Applied Physics*, **107**, pp. 181-238 (Springer 2006)

[7] F.A. Guo, N. Trannoy and J. Lu, "Characterization of the thermal properties by scanning thermal microscopy in ultrafine-grained iron surface layer produced by ultrasonic shot peening", *Materials Chemistry and Physics*, **96** (1), pp. 59-65, 2006.

[8] S. Gomès, N. Trannoy, F. Depasse, Ph. Grossel, C. Bainier, D. Charrault, "D.C. Scanning Thermal Microscopy: characterisation and interpretation of the measurement", *Int. J. Therm. Sci.*, **40**, pp. 949-958, 2001.

[9] P.-O. Chapuis, J.J. Greffet, K. Joulain, and S. Volz, "Heat transfer between a nano-tip and a surface", *Nanotechnology*, **17**, pp. 2978-2981, 2006.

[10] O. Raphael, N. Trannoy, P. Grossel, "Thermal Resonance at the Microscale in AC Scanning Thermal Microscopy with a Thermal-Resistive Probe", *Int. J. Thermophys.*, **33**, pp 1259-1269, 2012.

[11] G.A. Bird, "Molecular Gas Dynamics and the Direct Simulation of Gas Flows" (Clarendon, Oxford 1994).

Thermal conductances across silicon sub-mean free path sources measured with a four-probe electrical setup

Wassim JABER[1]*, Céline CHEVALIER[2] and P-Olivier CHAPUIS[1]

[1] *Université de Lyon, CNRS, INSA-Lyon, UCBL, CETHIL, UMR5008, F-69621, Villeurbanne*

[2] *UMI LN2 France-Sherbrooke, Grenoble and Ecole Centrale de Lyon, France*

** corresponding author: wassim.jaber@insa-lyon.fr, +33 4 72 43 73 53*

Keywords: Thermal conduction, four-probe electrical measurement, phonon heat transport, mean free path

The interest for the thermophysical properties of nanomaterials has grown in the past years. The reason behind this interest is related to many possible applications in various fields such as nanophononics [1] and thermoelectric [2]. There has been many works in the recent years that showed the large reduction of effective thermal conductivities in nanoscale samples compared to bulk materials, which results from phonon-boundary scattering, particularly at low temperatures. This phenomenon has been demonstrated in thin layers [3] and in nanowires [4-7], and the results can be reproduced with the phonon Boltzmann transport equation. In the samples, the mean free paths (MFP) of phonons, here denoted Λ, are controlled and are comparable to the geometric dimensions. The Knudsen number $Kn = \Lambda/D$ defines the ratio of the MFP Λ to the characteristic geometric length D (device size). We observe that, at room temperature, an estimation of the average MFP in silicon is close to 300 nm and that this value becomes larger when the substrate temperature decreases.

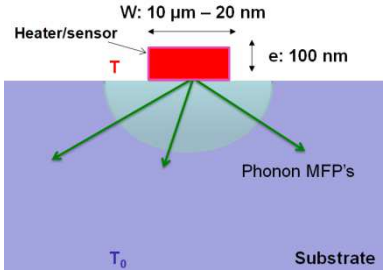

Figure 1: Geometry of the probed device: The heater (in red) is the deposited metallic wire on the top of a flat substrate (in blue).

The aim of our study is to investigate heat conduction different transport regimes. Here, we analyse the transition between two limit cases, when $Kn < 1$ (diffusive regime) and when $Kn > 1$ (ballistic regime). To do so, the measurements are performed at different levels of temperatures and for various heater sizes. This configuration provides various degrees of freedom that allow us to probe different ranges of Kn. Some optical measurements techniques [8, 9] have been introduced to probe this ranges of Kn and to measure the MFP distribution in silicon substrates. The principle of our technique is similar [10] but in our work, the measurements of the thermal conductance of silicon substrates are performed electrically using a four-probe electrical measurements technique [11] with small-scale devices.

The method consists in depositing a thin metallic wire on top of a flat silicon sample to be characterized. Figure 1 shows a schematic of the cross-section of the deposited device, which acts both as a heater and as a thermometer. The wire width ranges between 10 µm and 50 nm. The cross-section profile is controlled using both optical microscopy and atomic force microscopy (AFM) as exemplified in Figure 2. Two types of samples have been fabricated, by UV photolithography (largest widths) and by electron-beam lithography (smallest widths).

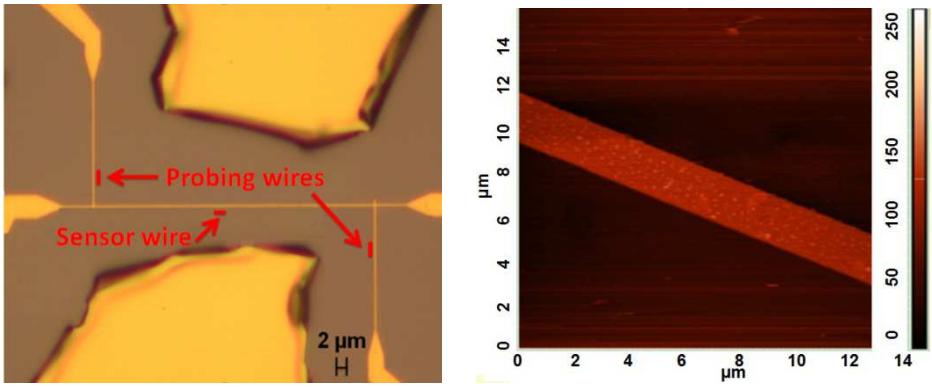

Figure 2: Representative optical and AFM images of the heater.

The measurements are performed by sending an ac current $I(t)=I_0 \cos(\omega t)$ through the metallic wire. By Joule heating, temperature oscillations at frequency 2ω are produced. Measuring the wire-voltage component (dc or ac) across the heater sensor, the electrical resistance and thus the temperature of the wire are determined. Four-probe electrical-transport measurement allows determining the thermal properties of different materials at room and cryogenic temperatures. The sample temperature was set and controlled in a liquid-helium cryostat, from room temperature down to ~10K.

Numerical simulations based on Finite Element Method with a commercial package (Comsol) were performed in order to estimate the temperature profile on the sample surface (see Figure 3).

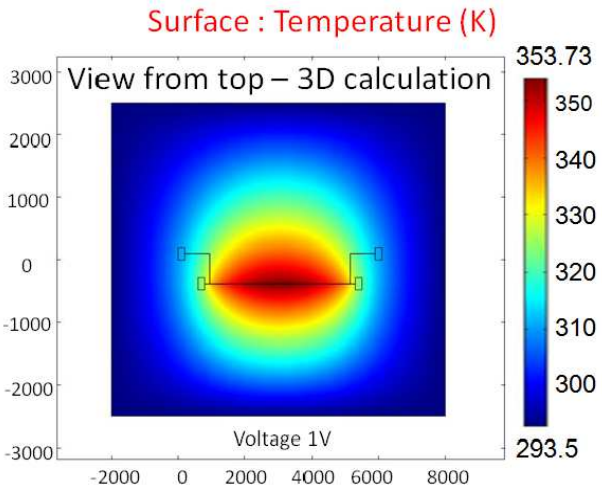

Figure 3: FEM-simulated profile around a Joule-heated deposited metallic wire on top of the substrate.

The obtained results are compared to previous experimental results with similar geometry [10] and also to numerical simulations based on FEM and on the Boltzmann transport equation (BTE) for phonons.

Acknowledgements

We warmly thank P. Bevilacqua (Lab. Ampère), P. Pittet, K. Ayadi, J. Grégoire, J.L. Leclercq (INL and NanoLyon) for their help during the fabrication of the samples. We thank M. Massoud and J.M. Bluet for discussions, and A. Shchepetov, M. Prunnila, C.M. Sotomayor Torres for continuous discussion and common work.

We acknowledge the support of INSA BQR MaNaTherm and ANR RPDOC project NanoHeat.

References

[1] D.G. Cahill,, W.K. Ford, K.E. Goodson, G.D. Mahan, A. Majumdar, H.J. Maris, R. Merlin, and S.R. Phillpot, "Nanoscale thermal transport", *Journal of Applied Physics*, **93**(2), 793-818, 2003..

[2] A. Shakouri and M. Zebarjadi, "Nanoengineered materials for thermoelectric energy conversion", in Thermal Nanosystems and Nanomaterials, Springer, 225-299, 2009.

[3] M. Asheghi, Y. Leung, S. Wong, and K. Goodson, "Phonon-boundary scattering in thin silicon layers", *Applied Physics Letters* **71**(13), 1798-1800, 1997.

[4] D. Li, Y. Wu, P. Kim, L. Shi, P. Yang, and A. Majumdar, "Thermal conductivity of individual silicon nanowires", *Applied Physics Letters*, **83**(14), 2934-2936, 2003.

[5] A.I. Hochbaum, R. Chen, R.D. Delgado, W. Liang, E.C. Garnett, M. Najarian, A. Majumdar, and P. Yang, "Enhanced thermoelectric performance of rough silicon nanowires", *Nature*, **451**(7175), 163-167, 2008.

[6] A.I. Boukai, Y. Bunimovich, J. Tahir-Kheli, J.-K. Yu, W.A. Goddard III, and J.R. Heath, "Silicon nanowires as efficient thermoelectric materials", *Nature*, **451**(7175), 168-171, 2008.

[7] J.-S. Heron, C. Bera, T. Fournier, N. Mingo, and O. Bourgeois, "Blocking phonons via nanoscale geometrical design", *Physical Review B*, **82**(15), 155458, 2010.

[8] K.T. Regner, D.P. Sellan, Z. Su, C.H. Amon, A.J. McGaughey, and J.A. Malen, "Broadband phonon mean free path contributions to thermal conductivity measured using frequency domain thermoreflectance", *Nature communications*, **4**, 1640, 2013.

[9] A.J. Minnich, J. Johnson, A. Schmidt, K. Esfarjani, M. Dresselhaus, K.A. Nelson, and G. Chen, "Thermal conductivity spectroscopy technique to measure phonon mean free paths", *Physical Review Letters*, **107**(9), 095901, 2011.

[10] P.-O. Chapuis, M. Prunnila, A. Shchepetov, L. Schneider, S. Laakso, J. Ahopelto, and C.M. Sotomayor Torres, "Effect of phonon confinement on heat dissipation in ridges", in *16th International Workshop on Thermal Investigations of ICs and Systems* (THERMINIC), 2010.

[11] W. Jaber, A. Assy, S. Lefevre, S. Gomes, and P.-O. Chapuis, "Thermal conductivity measurements with the 3ω method and scanning thermal microscopy", in *19th International Workshop on Thermal Investigations of ICs and Systems* (THERMINIC), 2013.

Thermal conductivity restoration by disulfide-based self-healing polymers

Nan ZHONG*, Santiago J. GARCIA and Sybrand VAN DER ZWAAG

Novel Aerospace Materials, Faculty of Aerospace Engineering, Delft University of Technology, Kluyverweg 1, 2629 HS, Delft, The Netherlands

**corresponding author: n.zhong@tudelft.nl*

Keywords: self-healing, thermal conductivity, mechanical properties.

Thermal Interface Materials (TIMs) are widely used as gap-filler materials to improve the heat dissipation of electronic devices such as light emitting diodes (LEDs). The aging of TIMs leading to cracks and delamination generally ends up with the loss of heat transfer and premature device failure. In this work we introduce a new concept to autonomously repair cracks and delamination ultimately leading to the recovery of the necessary heat dissipation for a proper device function. For the purpose we use intrinsic self-healing polymers. In these type of polymers covalent or non-covalent reversible bonds are included in the main network allowing, upon an external trigger, enough mobility to the networks so as to fully or partially restore damages [1].

In our previous work we introduced the concept of self-healing TIMs showing both adhesive and cohesive healing [2]. However there is no report on how filler size and surface treatment influence the healing ability. In the present work, we used a novel sol-gel based hybrid polymer as the self-healing matrix [3]. This polymer is a dual organic (epoxy-amine)-inorganic (siloxane) crosslinked network containing non-reversible crosslinks and reversible groups based on tetra-sulfides as explained in detail in [3]. The presence of the dynamic disulfide bonds allows for multiple healing events at relatively low temperatures (between 50 and 70ºC) [3]. In order to evaluate the effect of the particle size in the healing performance glass beads of different sizes were employed as fillers. The first results show how the cohesive healing efficiency increased with the particle size as well as with the healing time (Figure 1). The cohesive healing efficiency was calculated as follows:

$$\text{Healing efficiency} = \frac{\sigma_{Healed}}{\sigma_{virgin}} \times 100\% \quad (1)$$

where σ_{healed} and σ_{virgin} is the ultimate tensile strength of healed sample and virgin sample respectively.

In order to gain a major understanding of the role of the particle-matrix interface in the healing process several surface pre-treatments were implemented to the glass beads, namely (3-mercaptopropyl)-trimethoxysilane and bis-[γ-(triethoxysilyl)-propyl]-tetrasulfide, here on called -SH and -S-S- respectively. Figure 2 shows how the surface pretreatments by silane coupling agents increase the mechanical performance of the systems while at the same time allow for much higher healing efficiencies. The developed TIM films show on-demand restoration of the thermal conductivity as result of the recovery of the particle-matrix interface. In this work we will show the effect of the particle size and surface pretreatment in the healing performance as well as restoration of the thermal conductivity using good and poor thermally conductive particles in the same healing polymer matrix.

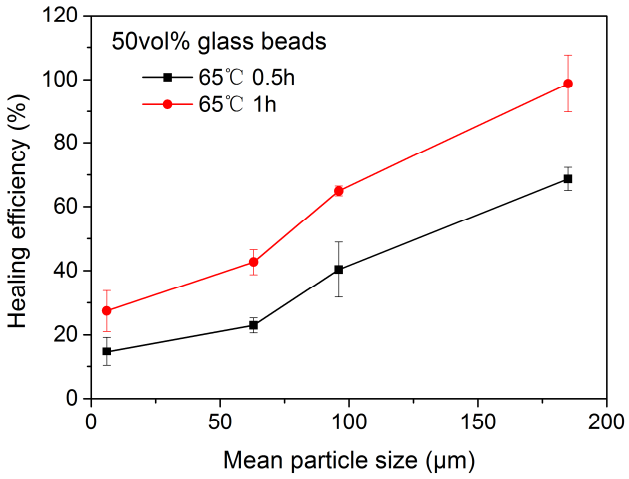

Figure 1: Effect of particle size and healing time on the healing efficiency of a self-healing polymer-based TIM containing 50% volume glass beads.

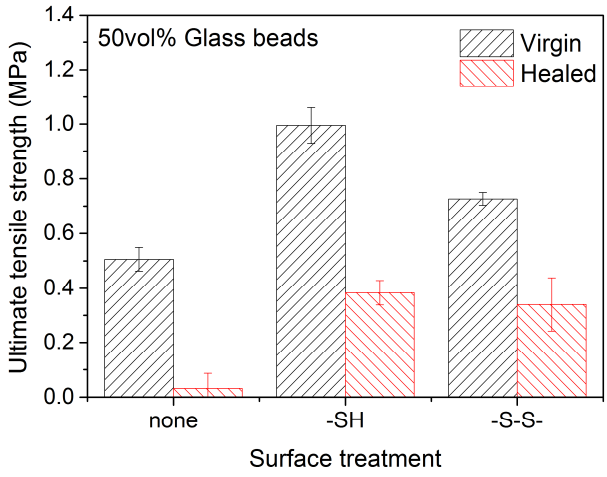

Figure 2: Effect on the mechanical properties and self-healing ability of a self-healing polymer-based TIM containing 50% volume glass beads with different surface treatments.

References

[1] S.J. Garcia, H. R. Fischer, S. van Der Zwaag, "A critical appraisal of the potential of self healing polymeric coatings", *Prog. Org. Coat.* **72**, 211, 2011.

[2] U. Lafont, C. Moreno-Belle, H. van Zeijl, S. van der Zwaag, "Self-healing thermally conductive adhesives", *J. Intell. Mater. Syst. Struct.* **25**, 67-74, 2014.

[3] M. AbdolahZadeh, C. Esteves, A. Catarina, S. van der Zwaag, S.J. Garcia, "Healable dual organic-inorganic crosslinked sol-gel based polymers: Crosslinking density and tetrasulfide content effect", *J. Polym. Sci., Part A: Polym. Chem.* **52**, 1953-1961, 2014.

Optimizing design of a thermal protection structure with PCs meta-material considering micro-scale transfer characteristics

Hao-Chun ZHANG[a*], Yang ZHAO[a], He-Ping TAN[a], Yao LI[b*] and Hai-Yan YU[a]

[a]*School of Energy Science and Engineering, Harbin Institute of Technology, Harbin, 150001, China*

[b]*Institute of Composite Material, Harbin Institute of Technology, Harbin,150001, China*

**corresponding author: zhc5@vip.163.com (Hao-Chun ZHANG); liyao@hit.edu.cn (Yao LI)*

Keywords: thermal protection structure, optimizing design, micro-scale transfer, photonic crystals.

Photonic Crystals (PCs) are kind of artificial material [1] which consist of different dielectrics periodically, and it has the ability to control propagation of electromagnetic transfer through photonic band gaps(PBG). Thermal control structure integrated with PCs become an emerging hot topic to protect the internal components of energy and power system from the damage caused by high temperature and heat flux, in view of effective reflection of electromagnetic energy through PCs band gap [2-5]. Through reasonable design, a kind of meta-material based on PCs can be developed with high emissivity and high reflectivity in the infrared region, which can modulate heat transfer. This paper demonstrates optimizing design of thermal protection structure with PCs meta-material considering micro-scale transfer characteristics.

In case of hypersonic aircraft, the main ways of heat transfer is aerodynamic heating [6], which is illustrated as objective of thermal protection by PCs coating in the current study. Through numerical simulation of aerodynamics and heat transfer [6-7], the following operation conditions are obtained for future consideration of thermal protection, including: flight speed 6 Ma, maximum aircraft surface temperature 1075.55 K, heat flux to aircraft substrate 97954.30W/m^2 as the worst flight environment, and so on.

There are several kinds of forms of PCs can be selected, in the current study, FCC lattice structure is considered, because it is the easiest way to form a complete band gap [8], without protrusion at the edge of the Brillouin zone. When the PCs are integrated to the thermal protection system, the reduced amount of energy flux to the aircraft substrate can be denoted by the following equation:

$$\Delta E = E_{all} - E_1 = (1+\eta)\varepsilon_2\sigma T^4 - \varepsilon_1\sigma T^4 = (\varepsilon_2 + \eta\varepsilon_2 - \varepsilon_1)\sigma T^4 \quad (1)$$

The optimal design of the thermal protection system is based on the simulation of 3D-PCs PBG, the preliminary equation is derived from vector Helmholtz equation [9-12], which can be expressed as the following:

$$\hat{L}\vec{u}_k = (ik+\nabla)\times\left(\frac{1}{\varepsilon(x)}(ik+\nabla)\right)\times\vec{u}_k = \tilde{\omega}^2\vec{u}_k \quad (2)$$

Simulation was carried out with RSoft software. With starting the CAD tool, a three-dimensional periodic structure was rendered, as shown in figure 1. The simulation was based on plane wave expansion (PWE) algorithm, with plane wavelength 2.5μm.

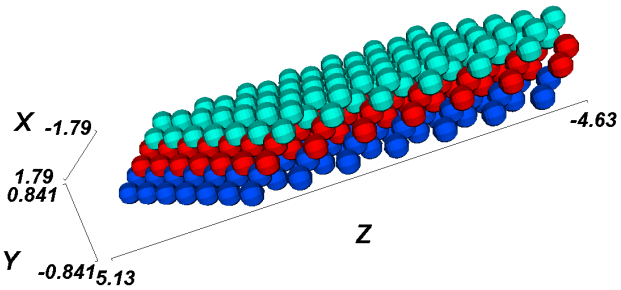

Figure 1: Three-dimensional periodic structure as diamond FCC lattice(a=1, 7×3×20)

The effect of dielectric sphere size on 3D-PCs band structure was simulated, with fixing refractive index 3.5 and the diamond lattice. The sphere radius are specified as 0.20μm, 0.22μm, 0.25μm, 0.26μm, 0.28μm and 0.29μm respectively, and the distribution of PBG center can be referred in Figure 2. It can be inferred that: with the increase of dielectric sphere radius, the PBG center appeared in a certain location; as the dielectric sphere radius continue to increase, the PBG center will gradually decrease and will eventually disappear.

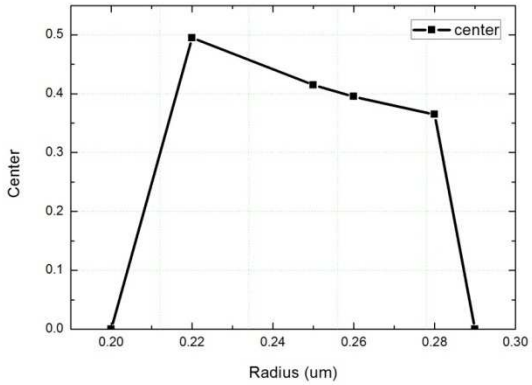

Figure 2: Distribution of the PBG center with varying sphere radius

The effect of dielectric sphere refractive index on 3D-PCs band structure was also simulated, which can be referred in Figure 3, which shows its effect on PBG center, with fixing sphere radius 0.22μm. It can be inferred that: with the increase of refractive index, the PBG center will reduce gradually and tends to disappear.

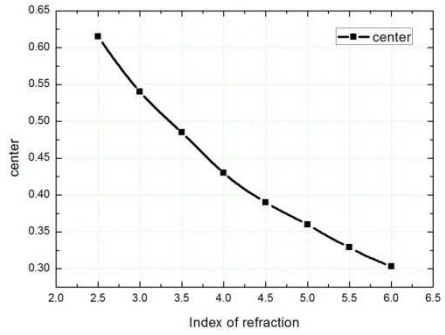

Figure 3: Distribution of the PBG center with varying refractive index of the dielectric sphere

The so-called “sphere radius optimization approach” is proposed to optimize the design of PCs structure by regulating dielectric sphere radius and refraction index simultaneously. Figure 4 shows

the ratio of the reflected energy by PCs to total blackbody radiation energy, and it can be inferred that the energy density entering into hypersonic vehicle substrate material can be reduced by 4.26 percent.

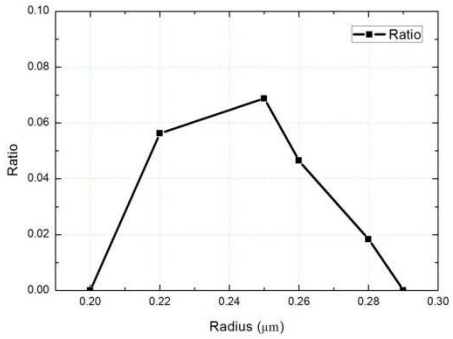

Figure 4: 3D-PCs radiation reflection ratio with the dielectric sphere radius

The so-called "refractive index optimization approach" is also proposed. Figure 5 shows the ratio of the reflected energy by PCs to total blackbody radiation energy, and it can be inferred that the energy density entering into hypersonic vehicle substrate material can be reduced by 7.68 percent.

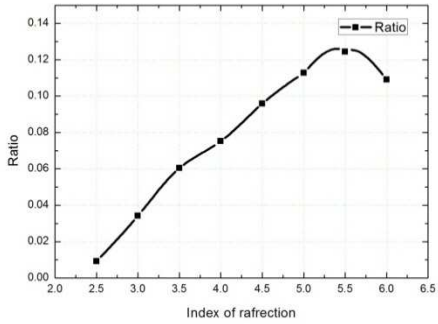

Figure 5: 3D-PCs radiation reflection ratio with the refraction index

Therefore, the above optimization approaches can be coupled together to improve the protection effect, and result of PBG band structure was shown in figure 6. It can be inferred that the energy density entering into hypersonic vehicle substrate material can be reduced by 7.99 percent.

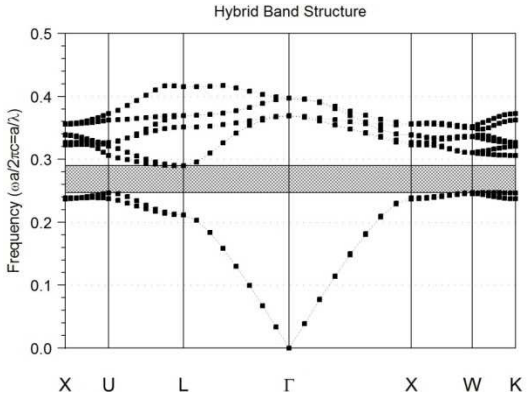

Figure 6: The optimization of three-dimensional PBG distribution

The PBG is free of scale, therefore, when the lattice constant is not a constant, the band structure will correspondingly changes. In this view, two design approaches were proposed, i.e., wavelength

approximation and lattice constants increasing, to reduce the energy density entering into hypersonic vehicle substrate material as 5.77 and 6.27 percent respectively.

This work demonstrates optimizing design of thermal protection structure with PCs meta-material considering micro-scale transfer characteristics, with 6Ma hypersonic aircraft aerodynamics heating conditions as objective for thermal protection structure design. The effect of dielectric sphere radius and refractive index on 3D-PCs band structure was simulated. Several optimization approaches were proposed, showing good effect on reducing the energy density entering into hypersonic vehicle substrate material.

Acknowledgment

This work is supported by the National Natural Science Foundation (91216123, 50930007) and Innovative Research Groups of the National Natural Science Foundation of China (Grant No. 51121004).

References

[1] J. D. Joannopoulos, S. G. Johnson, J. N. Winn, R. D. Meade, *Photonic Crystals: Molding the Flow of Light*, Princeton University Press, 2008.

[2] D. E. Wolfe, J. Singh, R. A. Miller, J. I. Eldridge, D. M. Zhu, "Tailored microstructure of EB-PVD 8YSZ thermal barrier coatings with low thermal conductivity and high thermal reflectivity for turbine applications", *Surface and Coatings Technology* **190**, 132-149, 2005.

[3] M. J. Kelly, D. E. Wolfe, J. Singh, J. Eldridge, D. M. Zhu, R. Miller, "Thermal barrier coatings design with increased reflectivity and lower thermal conductivity for high-temperature turbine applications", *International Journal of Applied Ceramic Technology* **3**, 81-93, 2006.

[4] V. Shklover, L. Braginsky, G. Witz, M. Mishrikey, C. Hafner, "High-temperature photonic structures. thermal barrier coatings, infrared sources and other applications", *Journal of Computational and Theoretical Nanoscience* **5**, 862–893, 2008.

[5] H. C. Zhang, X. Ben, Y. Li, Y.Y. Guo, "Heat transfer characteristics of an innovative thermal protection system based on photonic crystals," *Heat Transfer Engineering* **35**, 583-588, 2014.

[6] G. B. Cai, D. J. Xu, *Hypersonic Vehicle Technology*, Science Press, 2012.

[7] S. M. Yang, W. Q. Tao, *Heat Transfer*, 4th edition, Higher Education Press, 2006.

[8] K. M. Ho, C. T. Chan, C. M. Soukoulis, "Existence of a photonic gap in periodic dielectric structures", *Phys. Rev. Lett.* **65**, 3152-3155, 1990.

[9] E. Yablonovitch, "Inhibited spontaneous emission in solid-state physics and electronics", *Phys. Rev. Lett.* **58**, 2059-2061, 1987.

[10] S. John, J. Wang, "Quantum electrodynamics near a photonic band gap: Photon bound states and dressed atoms", *Phys. Rev. Lett.* **60**, 2418-2420, 1990.

[11] T. Ochiai, K. Sakoda, "Dispersion relation and optical transmittance of a hexagonal photonic crystal slab", *Phys. Rev. B* **63**, 125107, 2001.

[12] T. Ochiai, K. Sakoda, "Nearly free-photon approximation for two-dimensional photonic crystal slabs", *Phys. Rev. B* **64**, 045108, 2001.

Heat transfer through the water meniscus at the tip-sample contact investigated with Scanning Thermal Microscopy

Ali ASSY*, Stéphane LEFEVRE, Pierre-Olivier CHAPUIS and Séverine GOMES

Centre d'Energétique et de Thermique de Lyon (CETHIL), UMR CNRS 5008, INSA Lyon, UCBL, Université de Lyon, Villeurbanne, France

**corresponding author: ali.assy@insa-lyon.fr*

Keywords: Water meniscus, Capillary forces, Scanning Thermal microscopy, Thermal conductance.

Based on atomic force microscopy using a thermal sensor, Scanning Thermal Microscopy (SThM) is one of the key tools for performing micro/nano-scale heat transfer analysis. In this study, we focus on the heat transfer through the water meniscus at nanoscale contacts by using this method. Two facts have motivated this work. First of all, little information is available on this heat transfer and few results are subject to controversies. This heat transfer mechanism deserves to be analyzed more in depth for an improved use of quantitative SThM. Secondly, its understanding and management could support the design and optimization of new devices involving water meniscus. As an example, stiction remains an issue that can damage the performances of NEMS/MEMS devices. While working under ambient conditions, the main origin for stiction is the liquid meniscus that is formed at the small contacts due to capillary condensation. Stiction forces can be reduced by changing the surface properties or by reducing the contact area. Thermally-controlled devices may be another alternative that is not yet explored.

In order to investigate a large meniscus, a Wollaston wire SThM probe was used. The probe is made of a Pt 90%/ Rd 10% wire of diameter 5 µm and length 200 µm. The wire, bent in a V-shape with a curvature radius R_p of 15 µm, is obtained by electrochemical etching of the silver shell of a Wollaston wire of diameter 75 µm. In this study, we selected a germanium (Ge) sample of hydrophilic nature. The capillary forces are the dominant of the pull-off forces while working under ambient conditions [1, 2]. We investigated the meniscus at the tip-sample contact by performing pull-off forces measurements as a function of the probe mean temperature T_m (T_a=30 °C and relative humidity RH=40 %). Using Wheatstone bridge with a feedback circuit, the probe mean temperature was maintained constant during the measurements. Figure 1 shows the variation of the pull-off forces as a function of T_m. It is observed that the pull-off forces F_{po} decrease until reaching a certain temperature around T_t beyond which they become almost constant. It is observed that the pull-off forces F_{po} decrease until reaching a certain temperature around T_t where they become almost constant. The individual force-distance curve takes about 15 seconds. The contact time between the tip and the sample is larger than one second and we observed that there is no variation of the pull-off forces for larger contact times. This is in agreement with the study of study of Sirghi [3] where the meniscus reached the state of thermodynamic equilibrium after a certain limit of the contact time.

We noticed a hysteresis in the measurements while increasing T_m and decreasing T_m (see Figure 1). This could be related to the reported hysteresis during evaporation and the capillary condensation at the tip-sample contact as observed by Crassous *et al.* [4].

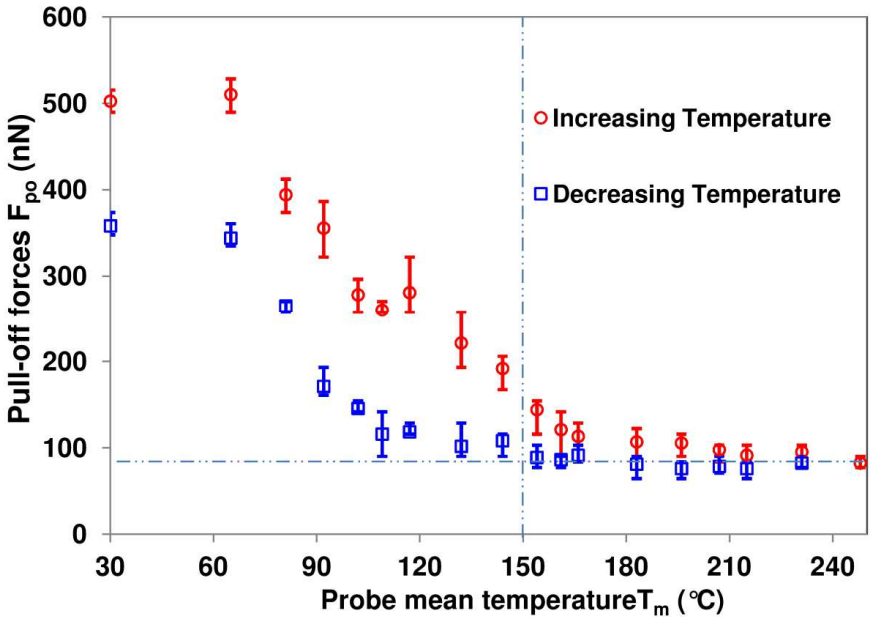

Figure 2: Variation of the pull-off forces F_{po} as a function of T_m for the sample of Ge.

Using the expressions of the Kelvin equation [5] and the meniscus radii of Crassous *et al*. [4] and Sirghi [3], the variation of the largest radius as a function of T_m was determined. Figure 2 represents a schematic of the probe apex in contact with the sample. The total thermal conductance of the meniscus G_{tot} can be determined taking into account the conductances at the interfaces of probe-meniscus and meniscus-sample [6]. The variations of the total thermal conductance of the meniscus as a function of T_m are shown in Figure 3. When the meniscus is large, the values of G_{tot} are at most one order of magnitude smaller than the values of the thermal conductance due to the heat transfer through air for the same probe [7, 8]). As a consequence, the thermal conductance through the water meniscus is not predominant in the thermal interaction between the probe and the sample [9].

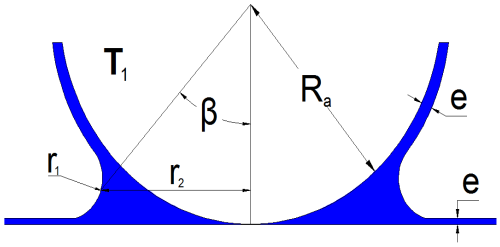

Figure 2: Schematic of the meniscus when the probe is in contact with the sample.

This work clarifies the role of the heat transfer through water meniscus in scanning thermal microscopy and will allow an improved use of quantitative SThM. We underline that our analysis justifies SThM calibration methods that have been developed previously with the same kind of microprobes at temperatures T_m larger than 100 °C. As the meniscus is almost evaporated at these relatively high temperatures, it has a smaller impact on the heat transfer to the sample and simplifies the analysis. The thermal conductance through the water meniscus is not predominant in the thermal interaction between the probe and the sample. It is striking that our findings are in accordance with the observations made with a nanoprobe, even though the tackled sizes are very different. The methodology used with the Wollaston probes in this paper can be extended later for the case of smaller probes and is one of the perspectives of this work [9].

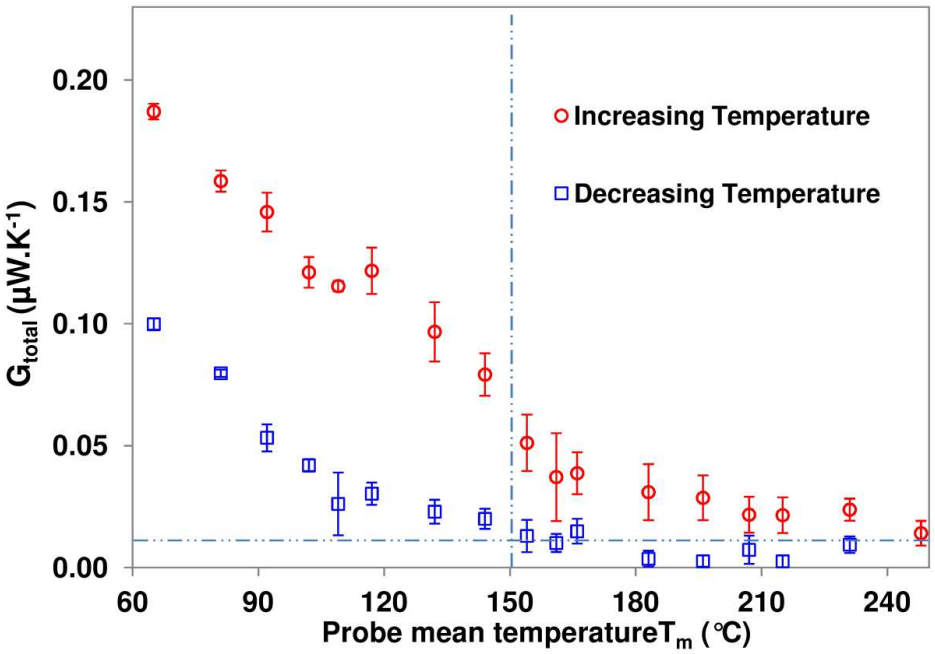

Figure 3: Total thermal conductance of the meniscus G_{total} as a function of the probe mean temperature T_m.

References

[1] B. Cappella, and G. Dietler, "Force-distance curves by atomic force microscopy", *Surface Science Reports*, **34**(1), 1-104, 1999.

[2] D. Maugis, and B. Gauthier-Manuel, "JKR-DMT transition in the presence of a liquid meniscus". *Journal of Adhesion Science and Technology*, **8**(11), 1311-1322, 1994.

[3] L. Sirghi, "Transport Mechanisms in Capillary Condensation of Water at a Single-Asperity Nanoscopic Contact". *Langmuir*, **28**(5), 2558-2566, 2012.

[4] J. Crassous, E. Charlaix, and J.-L. Loubet, "Capillary condensation between high-energy surfaces. An experimental study with a surface force apparatus", *EPL (Europhysics Letters)*, **28**(1), 37, 1994.

[5] J.N. Israelachvili, Intermolecular and surface forces (revised third edition), Academic press, 2011

[6] Z. Ge,, D.G. Cahill, and P.V. Braun, "Thermal conductance of hydrophilic and hydrophobic interfaces". *Physical review letters*, **96**(18), 186101, 2006.

[7] L. David, S. Gomes, and M. Raynaud, "Modelling for the thermal characterization of solid materials by dc scanning thermal microscopy. *Journal of Physics D: Applied Physics*, **40**(14), 4337, 2007.

[8] S. Lefèvre, S. Volz, and P.-O. Chapuis, "Nanoscale heat transfer at contact between a hot tip and a substrate", *International journal of heat and mass transfer*, **49**(1), 251-258, 2006.

[9] A. Assy, *et al.*, "Analysis of heat transfer in the water meniscus at the tip-sample contact in scanning thermal microscopy", *Journal of Physics D: Applied Physics* (accepted, 2014)

Thermoelectric coefficients: coupling transport equations and *ab initio* calculation

Gaston KANE*, Nathalie VAST and Jelena SJAKSTE

Ecole Polytechnique, Laboratoire des Solides Irradiés CEA-DSM-IRAMIS, CNRS UMR 7642, Palaiseau, France

**Corresponding author: gaston.kane@polytechnique.edu*

Keywords: thermoelectricity, electron-phonon coupling, Boltzmann transport equation

The search for materials that can produce electrical power from a temperature gradient - the Seebeck effect-, has gained significant interest in recent years. Indeed thermoelectric materials have proved to be viable solutions for the remote generation of electrical power in satellites [1]. The reverse (Peltier) effect allows to cool down electronic components in devices through a cold pole obtained with an electrical current passing through a junction of two conductors. The efficiency of a thermoelectric material is characterized by the figure of merit ZT [2], which is proportional to the electrical conductivity (σ) and to the square of the Seebeck coefficient (Q), and inversely proportional to the thermal conductivity (κ).

$$ZT = \frac{\sigma Q^2 T}{\kappa} \tag{1}$$

Improving the efficiency of thermoelectric devices requires an understanding of the mechanisms that control electronic transport. In particular, in semiconductors, the Seebeck coefficient increases drastically as the temperature decreases [3-4]. This is known as the phonon drag effect: phonons carrying a thermal current tend to drag the electrons with them from the hot side to the cold side of the sample. The phonon drag effect leads to the improvement of the figure of merit ZT. However, the phonon drag effect cannot be described in the framework of usual Boltzmann transport equations (BTE) [5-6]. In the first part of this presentation, we will present the approach to study the phonon-drag effect in materials [7].

At the same time, solving the transport equation for the electrons requires the knowledge of the electronic structure and of the carrier interactions (electron scattering on impurities and electron-phonon scattering). A good description of these physical mechanisms is achieved by parameter-free calculation in the framework of density functional theory (DFT) [8]. In a second part of the presentation, we will describe an approach based on the coupling of the Boltzmann transport equation with DFT calculations of the electronic structure and the electron-phonon coupling [6-7]. It has been successfully applied to the determination of the thermoelectric properties of bulk silicon [9]. This approach has the advantage of reducing the number of adjustable or *ad hoc* parameters in simulation of transport properties and thus leads to a better understanding of the underlying physical laws (in particular the phonon drag phenomenon), as shown in Ref. [8-9].

References

[1] A. Bulusu, D.G. Walker, *Superlattices and Microstructures* **44**, 2008.

[2] A. Shakouri, *Annu. Rev. Mater. Res.*. **41**, 399-431, 2011.

[3] T. Geballe and Hull, *Phys. Rev.* **98**, 940, 1955.

[4] C. Herring, *Phys. Rev.* **96**, 1163, 1953.

[5] M. Lundstrom, Fundamentals of Carrier Transport, *Cambridge University Press*, 2009.

[6] N. Vast, J. Sjakste, G. Kane and V. Trinité, "Simulation of transport in nanodevices", Ed. P. Dollfus and F. Triozon. Chaper 1 of volume 1*: Electrons, phonons, and their coupling within the density functional theory*, accepted (2014).

[7] J. Sjakste, I. Timrov, P. Gava, N. Mingo, N. Vast, "First-principles calculations of electron-phonon scattering", *Annual Reviews of Heat Transfer*, Begell House (in press, 2014*).*

[8] J. Sjakste, N. Vast and V. Tyuterev, *Phys. Rev. Lett*. **99**, 236405, 2007.

[9] Z. Wang, S. Wang, S. Obukhov, N. Vast, J. Sjakste, V. Tyuterev, and N. Mingo, *Phys. Rev. B.* **83**, 205208, 2011.

Thermal and electrical behavior of photon enhanced thermionic conversion

Mohamed AMARA[a] and Alexis VOSSIER[b]

[a]*Université de Lyon, CNRS, INSA-Lyon, UCBL, CETHIL, UMR5008, F-69621, Villeurbanne, France*

[b]*CNRS-PROMES, 7 Rue du Four Solaire, 66120 Odeillo, France*

**corresponding author: Mohamed.amara@insa-lyon.fr; alexis.vossier@promes-cnrs.fr*

Keywords: Photon Enhanced Thermionic Emission, Solar Energy Device.

Introduction

Thermionic emission is based on the ability of a material to emit electrons whose energy is greater than the work function of the material, which is defined as the difference between the vacuum energy level and the Fermi level. Basically, the thermionic converter material is made of a low work function metal, and requires a very high temperature (> 1000°C) in order to achieve high conversion efficiency. A new solar energy conversion concept, based on the combination of photon absorption using a semiconductor material and thermionic emission, was recently suggested [1]: Photon Enhanced Thermionic Emission (PETE).,

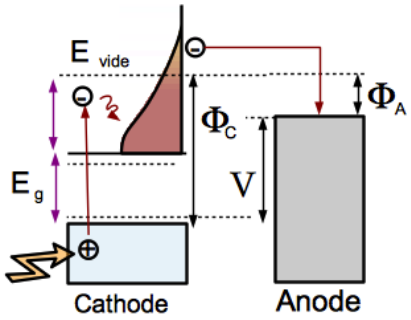

Figure 1: the energy diagram of the PETE energy conversion process

Absorption of solar photons leads to an increase in both the minority carrier concentration in the conduction band and the quasi-Fermi level splitting. As a result, the energy barrier between conduction band and vaccum is reduced and the temperature level required for the electrons to be emitted from the surface is dramatically lowered.

In this paper, we present a self-consistent model which predict the thermal and electrical behavior of the PETE diode cell.

Material and method

We present in this section the mathematical model of the PETE diode cell. Assuming a lumped-heat transfer model, the cathode energy balance is given by:

$$P_{sun} + J_A\left(\phi_A + 2kT_A\right) + R_{NRR}\left(E_g + 3kT_C\right) = \sigma T^4 + J_C\left(\phi_C + 2kT_C\right) + P_0\left[e^{\frac{E_{f,n}-E_{f,p}}{kTC}} - 1\right] \qquad (1)$$

where:

- $\phi_A + 2kT_A$ is the energy carried away by electron from the anode(heating process) [2]
- $\phi_C + 2kT_C$ is the energy carried away from cathode (cooling process)
- $R_{NRR}(E_g+3kT_C)$ is the energy supplied by the non-radiative recombination
- σT^4 is black body emission
- $P_0\left[e^{\frac{E_{f,n}-E_{f,p}}{kTC}}-1\right]$ is the no-equilibrium radiative recombination rate [3]

The cathode (J_C) and anode (J_A) currents are calculated as the difference between the cathode total optical generation (G) and recombination (R) rates, given by the equation:

$$L(G-R)=\frac{J_C-J_A}{q}$$

where *L* is the charge carriers diffusion length, assumed to be equal to the cathode thickness.

The cathode emission current is given by :

$$J_c=\int_{Eg+\chi}^{\infty} q\,v_x\,N(E)\,f(E)\,dE=q<v>n\exp(-\frac{\chi}{kT_c})$$

where Eg, χ and <v> are respectively the bandgap, the electrical affinity, and the thermal velocity of carriers. The anode current density is calculated using the standard expression of thermionic current for metals :

$$J_A=AT^2e^{\frac{-\phi_A}{kT_A}}$$

ϕ_A is the anode work function and A the Richardson-Dushman constant : 1.201×10^{-6} A m^{-2} K^{-2}

The generation rate is given by:

$$G=\frac{N\left(E>E_g\right)}{L}$$

where N(E> Eg) is the number of photons with energy above the band gap. The 3 main recombination processes (radiative, Auger and SRH) were accounted for in the model, as well as the thermal dependence of the main electrical parameters (E_g, n_i…) .

Results and discussion

Figure 2 depicts the variation of electrical conversion efficiency as a function of temperature for various values of the electrical affinity. It is shown that a high χ value leads to an increase in the diode voltage ($V=\chi+E_g-E_f-\phi_A$). As a consequence, the cathode work function rises and the

temperature required for the electrons to overcome such an energetic barrier by thermionic emission is increased

Figure 3 shows the different flux contributions for an illumination equivalent to 15 suns (where 1 sun = 1 mW/mm²) for both silicon and gallium arsenide semiconductors. At low applied voltage, the heat removed by the cathode electron emission and the thermal radiation applies a low temperature compared to high voltage.

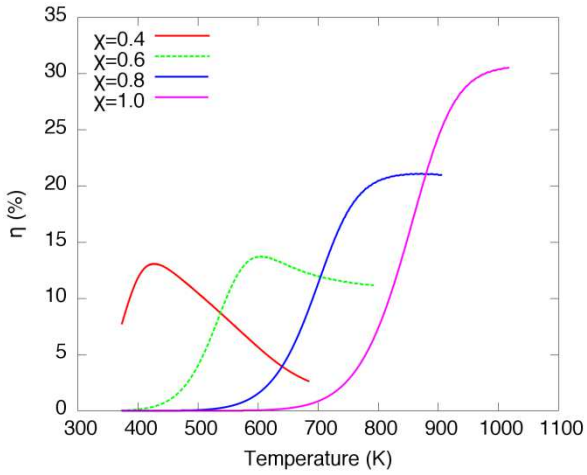

Figure 2: The contribution of power heat and power dissipation mechanisms.

Actually, for high voltage i.e., exceeding the limiting voltage V_{lim} for which $\phi_c = V_{lim} + \phi_a$, the cathode emission current drops, causing a temperature increase. Moreover, the rate of radiative and non-radiative recombination is enhanced. We then notice two different diode behaviours depending on the material considered. For Silicon (indirect band gap) PETE device, non-radiative recombination dominates over the radiative recombination, generating a supplemental source of heat,whereas in the GaAs, the radiative recombination, which removes heat, is enhanced. It should be noticed, that for an average concentration (X = 15), the temperature level of the cathode is ~ 700 K for silicon and 650 K for GaAs.

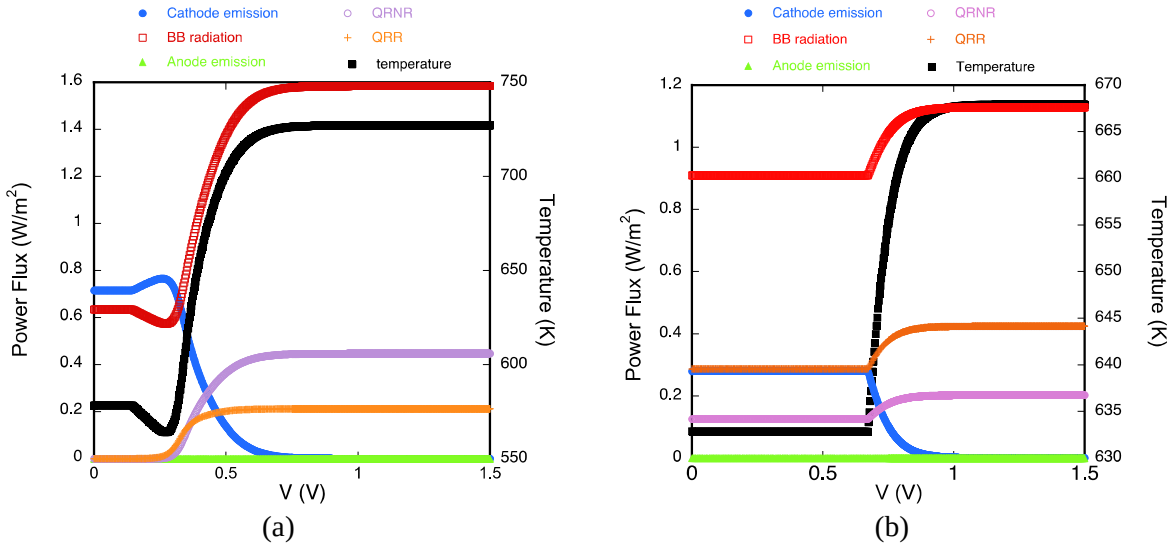

Figure 3: The contribution of power heat and power dissipation mechanisms.

Conclusion

In this paper a novel solar energy conversion process was presented. A self-consistent electrical and thermal model is developed and used to analyse the different heat generation mechanisms and the resulting electrical efficiency.

Acknowledgements

This work was supported by “cellule Energie” of CNRS-INSIS

References

[1] J. W. Schwede, I. Bargatin, D. C. Riley, B. E. Hardin, S. J. Rosenthal, Y. Sun, F. Schmitt, P. Pianetta, R. T. Howe, Z. Shen, and N. A. Melosh, “Photon-enhanced thermionic emission for solar concentrator systems,” *Nat. Mater.*, vol. **9**, no. 9, pp. 762–767, 2010.

[2] G. N. Hatsopoulos and E R. Gyftopoulos, *Thermionic Energy Conversion. Volume 1: Processes and Devices*, MIT, 1973.

[3] P. Würfel, *Physics of solar cells*, Wiley, 2005.

Thermal properties of a nanostructured Ge:Mn thin film for thermoelectricity

Yanqing LIU[a*], Dimitri TAINOFF[a], Mustapha BOUKHARI[b], Jacques RICHARD[a], André BARSKI[b], Pascale BAYLE-GUILLEMAUD[b], Emmanuel HADJI[b], Ali ASSY[c], Séverine GOMES[c] and Olivier BOURGEOIS[a]

[a]*University Grenoble Alpes, CNRS, Institut Néel, Grenoble F-38042, France*

[b]*Institut Nanosciences et Cryogénie, SP2M, CEA-UJF, 17 Rue des Martyrs, Grenoble 38054, France*

[c]*Centre de Thermique de Lyon, UMR 5008, 9 rue de la Physique, INSA de Lyon, Campus La Doua-LyonTech, 69621 Villeurbanne Cedex*

**corresponding author: yanqing.liu@neel.cnrs.fr*

Keywords: thermoelectricity, semiconductor thin film, nanoinclusion, thermal conductivity, 3-omega method.

1. Context and objectives

With the development of the nanotechnology, the domain of thermoelectricity has pushed itself to the frontiers of the global research on energy harvesting. Efforts are aimed at finding efficient thermoelectric materials under the idea of "electron crystal-phonon glass" material system [1]. The efficiency of a thermoelectric material is characterized by the dimensionless figure of merit (ZT value), which involves the Seebeck coefficient S, electrical conductivity σ and thermal conductivity κ through the formula of:

$$ZT = \frac{S^2 \sigma T}{\kappa}. \quad (1)$$

However, highly accurate measurements of the three concerned factors are required for a well determination of the ZT value. The measurement of thermal conductivity stays the greatest experimental challenge, especially for epitaxial thermal resistive thin films grown on electrical conductive substrates, which are the best material candidates for potential thermoelectric applications in microelectronics.

In this work we have developed an advanced experimental technique based on 3-omega method [2, 3, 4], for highly precise measurements of thermal conductivity of epitaxial semi-conductor thin films. Experiments have been done for the measurement of the thermal conductivity of a nanostructured Ge thin film. The results contribute to the investigation of the thermoelectric properties of this material, also importantly, help to achieve a complete comprehension of the thermal transport mechanism in nanostructured materials.

2. Originality of the research

For energy harvesting using thermoelectricity in the domain of microelectronics, the search of an efficient thermoelectric material stays the first challenge. It must be a semiconductor material and well compatible with the existing silicon based microelectronics platform.

Here we would like to present a work on the thermal characterization of nanostructured epitaxial Ge:Mn thin film, as a highly potential thermoelectric material for microelectronics. It is a thin film of a doped Ge matrix containing Ge_3Mn_5 nanoinclusions. The inclusions have a nearly isotrope distribution, and a diameter of 5 to 50 nm depending on the epitaxial conditions using MBE (Molecular Beam Epitaxy) [5, 6]. Being perfectly monocrystalline with a high doping level (p-type,

10^{18} cm^{-3}), the Ge matrix of the thin film possesses a high value of electrical conductivity, a low thermal conductivity is then expected for a high ZT value.
To achieve the most precise measurement of the thermal conductivity of this Ge:Mn thin film, which presents itself as a thin (generally 200 nm), epitaxial and electrical conductive layer, we have developed a highly sensitive experimental technique using the 3-omega method.

3. Method

3.1. The 3-omega method

To investigate the thermal properties of a thin film using the 3-omega method, a transducer metal line (role of both heater and thermometer, figure 1) is needed to be deposited on the film, in our case it is a 100 nm thick platinum transducer. For the case of an electrical conductive thin film, an isolating layer is required to isolate the transducer from the sample surface. A layer of 50 nm of aluminium oxide (Al_2O_3) (figure 2) is chosen to do the task in our work, deposited using the technique of ALD (Atomic Layer Deposition).

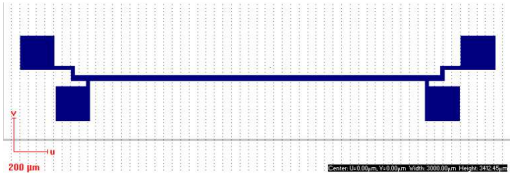

Figure 1: Designed motif in lithographic mask for the deposition of transducer.

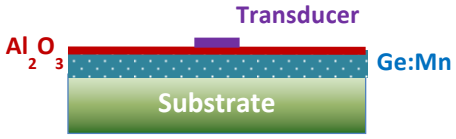

Figure 2: Schematic illustration of the sectional structure of a prepared sample for thermal measurement.

The 3-omega method concerns the measurement of the third harmonic part (3ω) of the voltage signal of the transducer after applying an alternating current (AC) of angular frequency ω. The frequency dependence of this $V_{3\omega}$ permits the extraction of the thermal conductivity of the substrate material. Here we have designed our measurement devices based on a differential geometry [2, 3, 7]. The sample is mounted inside a cryostat which ensures a large range of temperature environment from the temperature of helium liquid up to 400K.

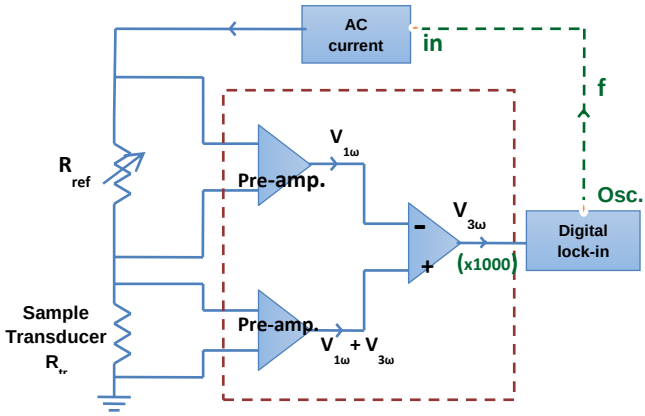

Figure 3: Schematic diagram of the electrical circuit for 3-omega measurement (the zone inside the dashed line represents a home-made electronic device).

3.2. 3-omega method for thin film

According to the principles of 3-omega method, for the case of a narrow transducer metal line on the surface of an infinite half-volume substrate, if the width of the line is largely small comparing to the thermal penetration depth (low frequency range), and the thickness of the transducer is negligible, an approximation of the temperature oscillation at the sample surface can be deduced [2]:

$$\Delta T = \frac{P_l}{\pi \cdot k_0}\left(-\frac{1}{2}\ln\frac{\omega}{\Omega}+\eta-i\frac{\pi}{4}\right) \qquad (P_l = \frac{R_{tr}I^2}{l}) \tag{2}$$

Where P_l is the linear heat dissipation with R_{tr} the electric resistance, I the applied AC current and l the length of the transducer; the thermal angular frequency $\omega = 4\pi f$, where f is the electric frequency of the AC current; $\Omega = \frac{k_0}{\rho C b^2}$ with k_0 the thermal conductivity of the substrate, ρ the density, C the specific heat, b the half width of the transducer and $\eta = 0.92$.

The Ge:Mn thin film (thickness t_1) is generally deposited on a thick substrate (Si or Ge, 300 µm thick). As long as t_1 is largely small comparing to the width $2b$ of the transducer, the heat transport is considered to be one-dimensional across the film and the heat flux conserved. This approximation brings a shift in the real part of the surface temperature oscillation:

$$\Delta T = \frac{P_l}{\pi \cdot k_0}\left(-\frac{1}{2}\ln\frac{\omega}{\Omega}+\eta-i\frac{\pi}{4}\right)+\frac{P_l \cdot R'}{2b} \tag{3}$$

$$\Delta\left\langle\frac{\Delta T_{real}}{P}\right\rangle = \frac{R'}{2bl} \tag{4}$$

The thin film represents itself only as a thermal barrier resistance R' for the heat flux, which is directly related with its thickness and thermal conductivity through:

$$R' = \frac{t_1}{k_1} + R_c \tag{5}$$

where R_c is the effective thermal resistance of interfaces, being the total interface thermal resistance of the thin film involved sample minus the total one for the case of the sample substrate.

4. Experimental results

The 3-omega measurements have been carried out on samples of Ge:Mn thin films (240 nm thick) grown on a n-type doped Ge substrate. As the Ge matrix of Ge:Mn thin film is perfectly crystalline and homoepitaxied on the Ge substract, the interface thermal resistance between the film and the substrate is neglected [8]. The Data of $V_{3\omega}$ signals as a function of frequency (here within 100 – 1000 Hz), from the sample and the reference Ge (n-type) substrate, at different temperature, are gathered and treated.

At one certain temperature, the comparison of the curves $\frac{\Delta T_{real}}{P}$ from the two samples reveal a clear shift as shown in figure 4, from the curve of reference sample to the Ge:Mn sample. For the case of 320K in the figure, the thermal conductivity of the Ge:Mn thin film is calculated to be 5.5 (±1) $Wm^{-1}K^{-1}$. The results have revealed a remarkably reduced thermal conductivity of this thin film by a factor of 10 at 320K, compared to the value for bulk Ge substrate (60W/mK).

5. Future works

To properly understand the physics of the involved phonon scattering mechanism introduced by the nanostructure, the 3-omega measurements will be continued on different samples of the Ge:Mn thin film, grown with different Mn concentration, at different annealing temperature. The measurement results will be evaluated together with further characterization results using TEM (Transmission Electron Microscopy), to finally identify the influence of the nano-inclusion, with its diameter and dispersion, on the heat transport inside the thin film. Meanwhile, experiments for a complete characterisation of the thin film's thermoelectric properties will also be carried out, mainly the measurements of its electrical conductivity and Seebeck coefficient, aiming at a final determination of the ZT value.

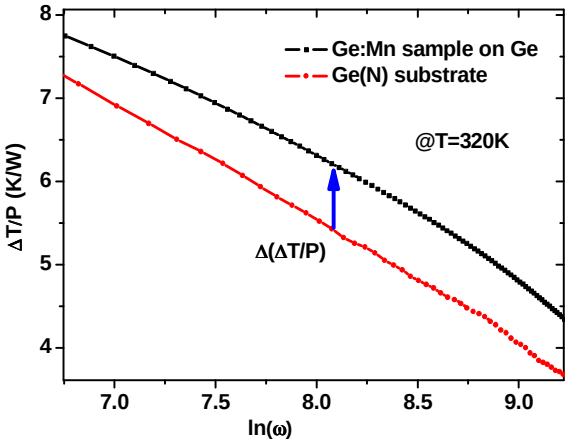

Figure 4: Comparison of the curves $\frac{\Delta T_{real}}{P}$ *from Ge:Mn sample and the Ge reference substrate sample at 320K.*

References

[1] G.A. Slack, *Handbook of Thermoelectrics*, CRS Press, 1995.

[2] D.G. Cahill, "Thermal conductivity measurement from 30 to 750 K: the 3ω method", *Rev. Sci. Instrum.* **61**, 802, 1990.

[3] D.G. Cahill, P.V. Braun, G. Chen, D.R. Clarke, S. Fan, K.E. Goodson, P. Keblinski, W.P. King, G.D. Mahan, A. Majumdar, H.J. Maris, S.R. Phillpot, E. Pop, L. Shi, "Nanoscale thermal transport II", *Appl. Phys. Rev.* **1**, 011305, 2014.

[4] A. Sikora, H. Ftouni, J. Richard, C. Hébert, D. Eon, F. Omnès, O. Bourgeois, "Highly sensitive thermal conductivity measurements of suspended membranes (SiN and diamond) using 3ω-Völklein method", *Rev. Sci. Instrum.* **83**, 054902, 2012.

[5] T. Devillers, *Ferromagnetic phases of Ge(1-x)Mn(x) for spintronics applications*, Ph.D. thesis, Grenoble, 2008.

[6] A. Jain, M. Jamet, A. Barski, T. Devillers, I.S. Yu, C. Porret, P. Bayle-Guillemaud, V. Favre-Nicolin, S. Gambarelli, V. Maurel, G. Desfonds, J.F. Jacquot, S. Tardif, "Structure and magnetism of Ge_3Mn_5 clusters", *J. Appl. Phys.* **109**, 013911, 2011.

[7] D.G. Cahill, M. Katiyar, J.R. Abelson, "Thermal conductivity of a-Si:H thin films", *Phys. Rev. B* **50**, 6077, 1994.

[8] R.M. Costescu, M.A. Wall and D.G. Cahill, "Thermal conductance of epitaxial interfaces", *Phys. Rev. B* **67**, 054302, 2003.

Heat transfer studies using Ln^{3+} based nanothermometers

Carlos D. S. BRITES[a], Patrícia P. LIMA[a], Nuno J. O. SILVA[a*], Angel MILAN[b], Vitor S. AMARAL[a], Fernando PALACIO[b] and Luís D. CARLOS[a*]

[a] *Departamento de Física & CICECO Universidade de Aveiro, Campus Santiago 3810-193, Aveiro, Portugal*

[b] *Departamento de Física de la Matéria Condensada & ICMA, Faculdad de Ciências, Universidad de Zaragoza, Calle Pedro Cerbuna, 50008, Zaragoza, Spain*

**corresponding author: carlos.brites @ua.pt*

Keywords: organic-inorganic hybrids, lanthanide ions, nanothermometry, heat transfer.

There is an increasing demand for accurate, non-invasive and self-reference temperature measurements as technology progresses into the nanoscale. This is particularly so in micro- and nanofluidics where the comprehension of heat transfer and thermal conductivity mechanisms can play a crucial role in areas as diverse as energy transfer and cell physiology [1,2].

In fact, the integration of optics and micro/nanofluidic devices to provide novel functionalities in nanosystems is stimulating a promising new area of optofuidics, for nanomedicine and energy. Despite promising progress precision control of fluid temperature by accounting for local temperature gradients, heat propagation and accurate temperature distributions have not yet been satisfactorily addressed, *e.g.*, investigating heat transfer mechanisms in nanofluids or mapping temperature distributions within living cells. The major obstacle for this has been the unavailability of a thermometer with the following requirements (that should be simultaneously satisfied): (i) high temperature resolution (<0.5 degree); (ii) ratiometric temperature output; (iii) high spatial resolution (<3 μm); (iv) functional independency of changes in pH, ionic strength and surrounding biomacromolecules; and (v) concentration-independent output. The most suitable class of thermometers to fulfil these requirements are the luminescent ones [3].

With the objective of investigate the heat transfer mechanisms in nanofluids and mapping temperature distributions we have focused in the development and characterization of nanothermometers that can be dispersed in different base fluids or incorporate organic-inorganic hybrid films [2,3]. The thermometers performance can be compared using the relative sensitivity (Eq. 1) , defined as the relative change on the thermometric parameter Δ (taken as a ratio of intensities, $\Delta = I_1/I_2$ to avoid any dependences of the temperature read on local concentration, fluctuations on excitation sources, etc.):

$$S_r = \frac{\partial \Delta / \Delta T}{\Delta} \tag{1}$$

Also the spatial resolution (δx) is defined as $\delta x = \delta T \Big/ \left|\vec{\nabla} T\right|_{\max}$, where δT is the temperature uncertainty and $\left|\vec{\nabla} T\right|_{\max} = \partial T / \partial x$ the largest temperature gradient that can be measured [4], and the temporal resolution defined as is defined as $\delta t = \delta T / \left(\partial T / \partial t\right)$,where $\left(\partial T / \partial t\right)$ the largest temporal temperature change measured.

In 2013 we reported the development of two luminescent ratiometric nanothermometers (**NP5-1.4**, spherical NPs, DLS diameter of 119.2 ± 11.6 nm and **NP4-1.3,** spherical NPs, DLS diameter of 40.2 ± 5.9 nm) based on a γ-Fe_2O_3 maghemite core coated with an organosilica shell co-doped with Eu^{3+} and Tb^{3+} β-diketonate chelates [2]. The design of either the siloxane-based hybrid host or the chelate ligands permits the nanothermometers to be used in nanofluids (*i.e.* water suspensions of the nanothermometers) at 293–320 K with an emission quantum yield between 0.24 ± 0.02 and 0.38 ± 0.04, a relative sensitivity of up to 1.5% K^{-1} (at 293 K), a spatiotemporal resolution (constrained by the experimental setup) of (64–65) μm/150 ms (to move out of the temperature uncertainty, δT, stated as 0.4 K).

The nanothermometers are easily dispersible in water forming transparent and stable nanofluids under day light illumination, making them ideal for temperature determination in micro- and nanofluidics using the temperature dependence of their emission properties. A demonstration of the use of these particles was performed by mapping the temperature of a glass tube with an inner diameter of 1 mm and a longitudinal length of 20 mm, filled with the nanothermometers nanofluids (1 g L^{-1}). A steady-state temperature gradient was induced in the nanofluids by an electrical current flowing in a coil-shaped resistance (**Fig. 1**a). The current was adjusted to produce the temperature gradient within the 293–320 K range. When illuminated with UV light, the nanofluids presented a blue-green (NP5-1.4) or a red-orange (NP4-1.3) emission (Fig. 1b and c) and an optical fiber was used to collect the emission spectra which were converted into absolute temperatures. Both nanothermometers gave analogous temperature values (temperature gradient along the capillary tube up to 3000 $K \cdot m^{-1}$), as shown in Fig. 1d. A temperature map recorded with a state-of-the-art commercial IR camera was used as a control measurement. The spatial resolutions of the nanothermometers and IR camera are 64 μm (NP4-1.3), 65 μm (NP5-1.4) and 160 μm, respectively, despite the optical fiber's inner diameter of 450 μm being ca. 1.5 times larger than the camera pixel field of view.

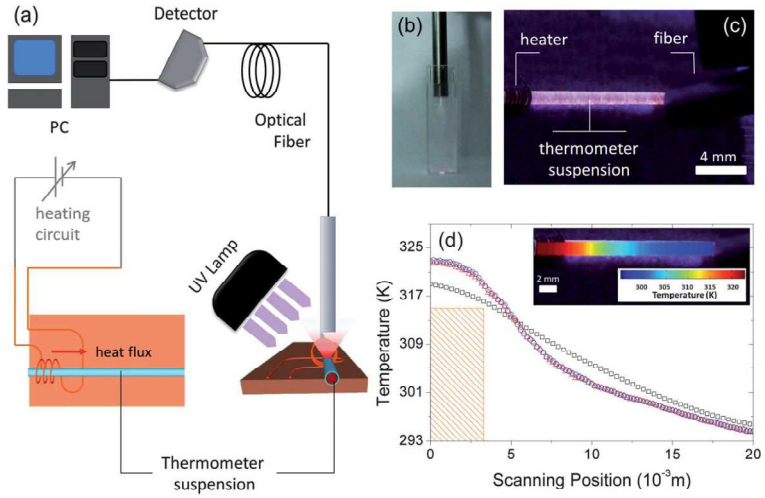

Figure 3: Temperature maping using Ln^{3+}-based nanothermometers. (a) Experimental setup used for temperature mapping in nanofluids. (b) Photograph of the NP5-1.4 suspension under UV irradiation (c) Photograph of the NP4-1.3 suspension under UV irradiation (handheld lamp). The heater, the capillary tube and the optical fibre are also visible. (d) Comparison of the temperature profile obtained with an IR camera (black squares) and with the light emission of NP4-1.3 (blue circles) and NP5-1.4 (red triangles). The shadowed area corresponds to the position of the heater. The pseudo-colour image of the NP4-1.3 suspension is represented in the inset.

None of the ratiometric luminescent and non-luminescent devices proposed so far can map the temperature in a micro/nanofluid in the 293–320 K range with such high emission quantum yields, relative sensitivity, temperature uncertainty, and spatio-temporal resolution values. Furthermore, a velocity in of heat traveling within the nanofluid, (2.2 ± 0.1) mm s^{-1}, was determined at 294 K simply using the Eu^{3+}/Tb^{3+} steady-state spectra of the nanothermometers (**Fig. 2**). There is no precedent of such an experimental measurement in a thermometric nanofluid, where the same nanoparticles constituting the nanofluid are used to measure the temperature and to study the heat transfer.

In this communication we will present our most recent heat transfer studies using Ln^{3+} based nanothermometers and compare the experimental values with the ones reported in the literature.

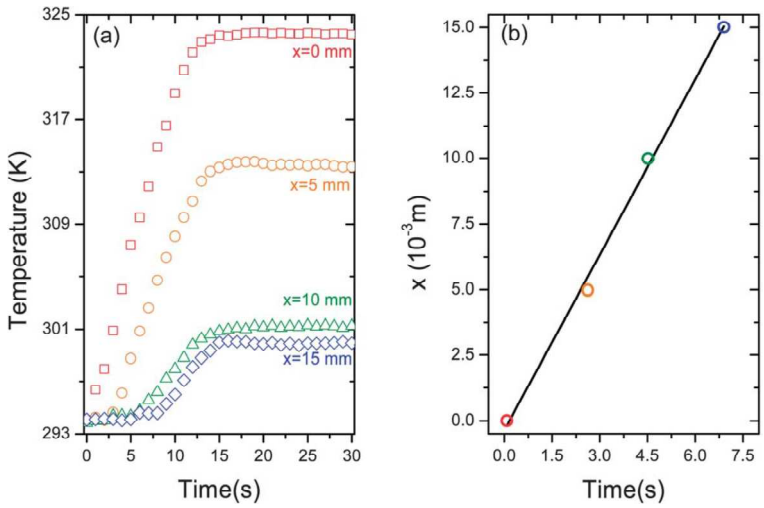

Figure 2 : Temperature dynamics on the capillary tube a) temperature dynamics monitored at different points x along the capillary tube using the NP5-1.4 thermometer . (b) linear relationship (r^2 = 0.996) between the distance x travelled by the thermal wave and the time instant t_0 for which the temperature starts to increase relative to the equilibrium value (294 K).

The work is partially supported by FCT Project RECI/CTM-CER/0336/2012 and FEDER, ref COMPETE: FCOMP-01-0124-FEDER-027465. CDSB tanks FCT (SFRH/BPD/ 89003/ 2012) for a grant.

References

[1] C.D.S. Brites, P.P. Lima, N.J.O. Silva, , A. Millan, V.S. Amaral, F. Palacio, , L.D. Carlos "Thermometry at the Nanoscale", *Nanoscale* **4**, 4799, 2012.

[2] C.D.S. Brites, P.P. Lima, N.J.O. Silva, , A. Millan, V.S. Amaral, F. Palacio, , L.D. Carlos " Ratiometric Highly Sensitive Luminescent Nanothermometers Working in the Room Temperature Range. Applications to Heat Propagation in Nanofluids", *Nanoscale* **5**, 7572, 2013.

[3] C.D.S. Brites, P.P. Lima, N.J.O. Silva, , A. Millan, V.S. Amaral, F. Palacio, , L.D. Carlos " A Luminescent Molecular Thermometer for Long-Term Absolute Temperature Measurements at the Nanoscale", *Adv. Mater*. **22**, 4499, 2010.

[4] K. Kim, W. H. Jeong, W. C. Lee and P. Reddy," Ultra-High Vacuum Scanning Thermal Microscopy for Nanometer Resolution Quantitative Thermometry" *ACS Nano*, **6**, 4248, 2012.

Xe-Arc Flash Lamp Crystallization of Amorphous Silicon Thin-Film for Large-Scale Displays

Seungho PARK

Hongik University, Seoul, Korea

**corresponding author: spark@hongik.ac.kr*

Keywords: Flash Lamp Annealing, Solid-Phase Crystallization, LTPS, Thermal Warpage, Large-Scale Display

The present study investigates the flash lamp annealing (FLA) process for fabrication of low-temperature poly-crystalline silicon (LTPS) as one of the most promising and economical candidate processes for large-scale windows of up to size of 2.2×2.5 m^2 [1]. Experimental and theoretical investigations on FLA of amorphous silicon (a-Si) film on glass were carried out in order to replacing excimer laser crystallization process. A Xe arc flash lamp of 950mm in length and 22mm in bore diameter was applied with nominal input voltage of 7kV and flash duration of 0.4ms.

Figure 1 shows the configuration of the FLA experimental setup, consisting of a lamp, a reflector, and a substrate. The radiation distribution incident on the substrate was simulated by the ray tracing method and compared with experimental measurements. To gain a better understanding of the detailed routes of phase-transformation, images of poly-Si microstructures after the process were observed by scanning electron microscopy (SEM), atomic force microscopy (AFM) and Raman Spectroscopy.

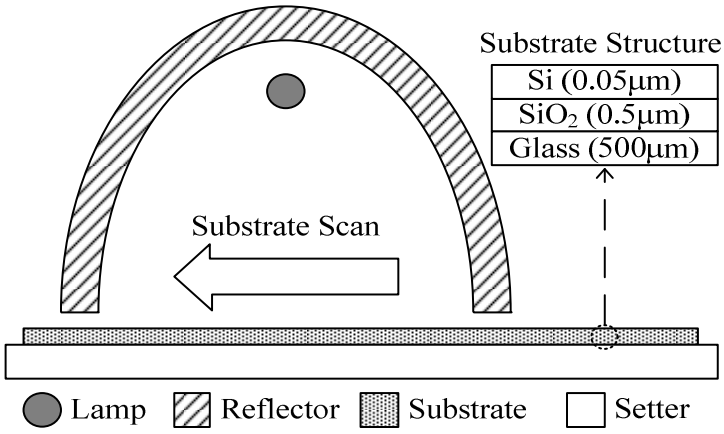

Figure 1: Schematic diagram of the flash lamp annealing system with a-Si substrate.

Prior to the annealing process, the specimen for FLA was preheated at 650°C, which was very close to the service temperature of the glass specimen used in this study. Crystallization of a-Si could be achieved in solid-phase by applying a flash beam with light density of at least 5J/cm^2, and its phase-transition characteristics that varied with energy densities could be explained by theoretically estimated temperature fields.

Since the major phase-transformation in the FLA process occurs during the lamp-flashing period of about tens or hundreds of microseconds with the heating rate in the order of 1~10 kW/cm^2 in general, convective and/or radiative heat losses in the order of 1~10 W/cm^2 can be considered negligible, compared with the conduction heat transfer. Based on this approximation, temperature fields inside the thin-film structure can be estimated by the one-dimensional heat conduction/radiation model. Here,

local radiation absorption rate was estimated from the distributions of electromagnetic fields and the resulting Poynting vectors. Since the temperature variation during the FLA process was extremely large and plays a critical role during the crystallization process, temperature dependencies of the physical properties for thin-film material were included in the present theoretical estimation.

Figure 2 describes temperature variations at the surface (solid line) as well as that at the region 15μm beneath the surface (dashed line), respectively for the experimental and electrical input conditions under the preheating at 650°C. While the glass backplane remains almost transparent to the flash light, the a-Si thin-film has a high value of imaginary refractive index in the visible wavelength range and absorbs major portion of the light energy. Therefore, the subsurface region of the glass adjacent to the a-Si film can be heated only by the thermal conduction from the a-Si.

Using a short duration heating, crystallization of a-Si usually requires temperatures around or beyond its melting point (higher than 1420 K), which is much larger than the glass softening point, T_{sp}, in general. The glass used in this study is Corning Eagle 2000, of which T_{sp} is 1258K. It could be assumed, therefore, that the glass softening cannot be avoided in the current FLA process. The peak temperature at the surface was about 1435 K, which was sufficient not only to crystallize a-Si, but also to soften the material. Furthermore, the peak temperature at the region 15□m beneath the surface reached T_{sp}, indicating a possibility that there occurred softening deep inside the backplane.

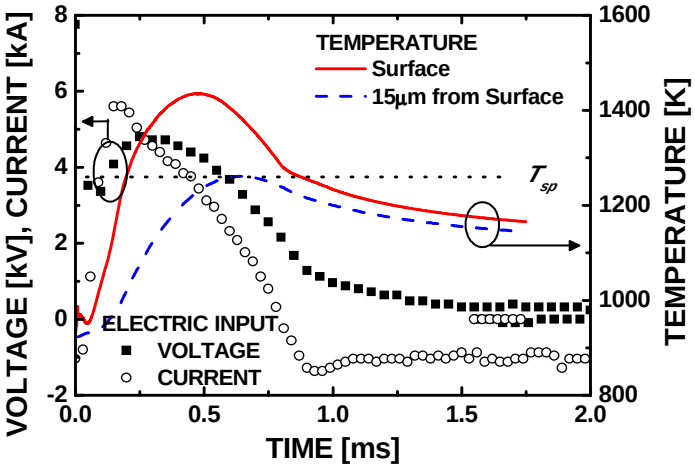

Figure 2: Experimental input voltages and currents and temperature predictions at surface and 15μm beneath the surface.

Through electron microscope observations Fig. 3 confirms that solid-phase crystallization preceded melting of a-Si due to relatively long flashing (heating) duration of 400μs, which was comparable to solid-phase crystal-growth times at elevated temperatures [2].

In addition, deformation of a large-window glass backplane during an in-line flash lamp annealing process for crystallization of amorphous silicon thin-film was investigated numerically using a viscoelastic model and experimentally, as shown in Fig. 4. This phenomenon is understood through the structural mismatching of hypothetical two-layers in a homogeneous glass structure [3]: thermally softened and uninfluenced, and is mechanistically different from that induced by the mismatch in coefficients of thermal expansions among heterogeneous thin-film structures [4].

Fig. 5 compares the various shapes of the glass deformations according to the specimen sizes, in case their center regions were exposed to a single flash under the conditions close to the experiments. The deformations were totally different after the final cooling stages, although the center regions were bulged up during the heating (flashing) stage regardless of the specimen lengths. Here, we could postulate that the critical mechanisms for deformations were structural shrinkage due to stress relaxations accompanied by glass softening and gravitational self-loading of the backplane, acting in the opposite way.

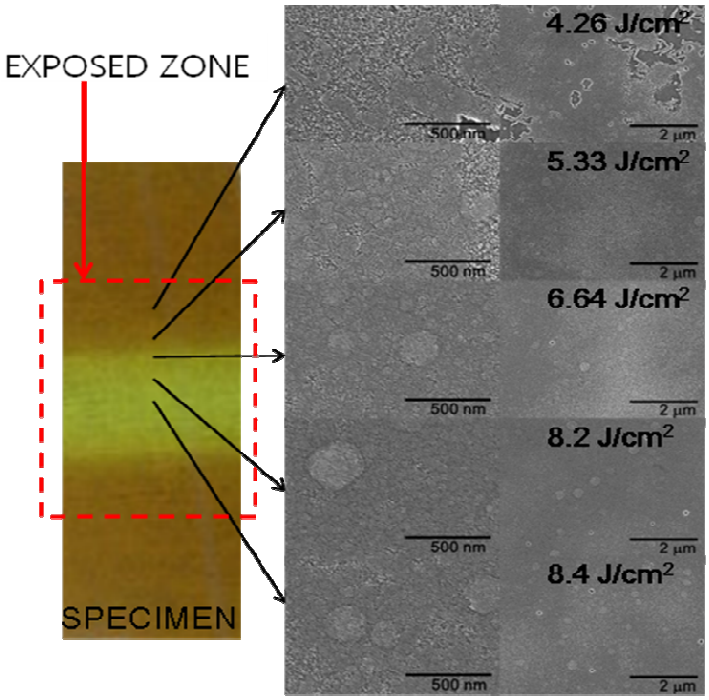

Figure 3: Picture of specimen exposed to flash beam and SEM images with respect to flash fluencies.

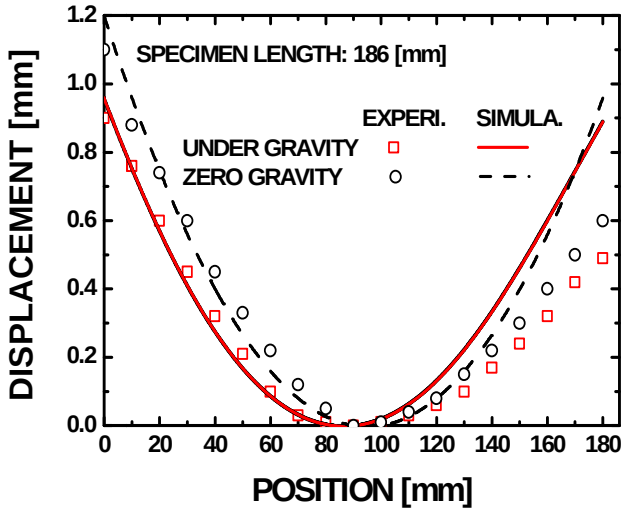

Figure 4: Comparisons between experimental and numerical deformations of the glass substrate after the FLA process of a single flash at the central zone of the specimen (length: 186 mm).

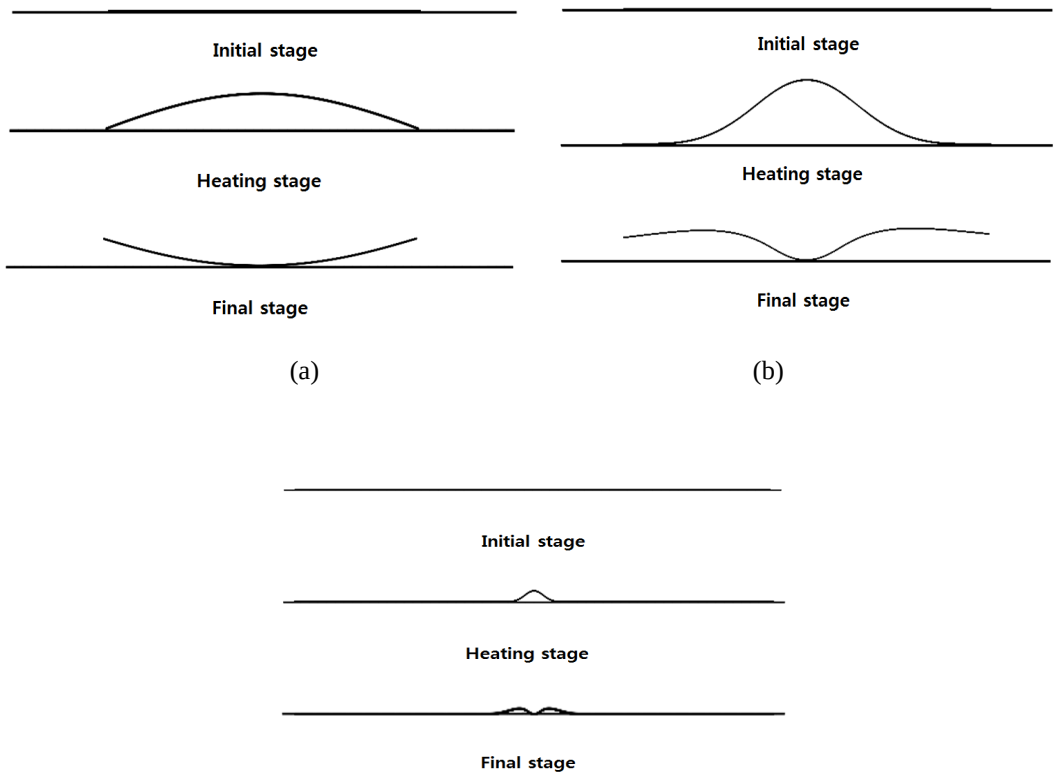

Figure 5: Thermal deformations of the glass substrates during the FLA process of a single flash at the central zone of the specimen: lengths and enlargements in vertical direction of (a) 186 mm, by 10 times, (b) 300 mm, by 100 times, and (c) 2200 mm, by 1500 times.

Acknowledgements

This work is supported by the National Research Foundation grant fund (No. 2009-0083510) through Multi-phenomena CFD Engineering Research Center and Basic Science Research Program funded by the Ministry of Education, Science and Technology (NRF-2012004364).

References

[1] D.H. Kim, B.K. Kim, H.J. Kim, and S. Park, "Crystallization of amorphous silicon thin-film on glass substrate preheated at 650℃ using Xe arc flash of 400μs", *Thin Solid Films* **520**, 6581, 2012.

[2] W.E. Hong, J.K. Chung, D.H. Kim, S. Park, J.S. Ro, "Supergrains Produced by Lateral Growth Using Joule-Heating Induced Crystallization without Artificial Control" *Appl Phys Lett*, **96**, 052105, 2010.

[3] W.B. Jin, Y. Park, B.K. Kim, H.J. Kim, J.H. Hwang, H. Chung, J.H. Park, D.H. Kim, and S. Park, " Thermal warpage of a glass substrate during Xe-arc flash lamp crystallization of amorphous silicon thin-film," *Int J Therm Sci*, **83**, 2532, 2014.

[4] H. Gleskova, I-C. Chen, S. Wagner, Z. Suo, "Mechanical Theory of the Film-on-Substrate-Foil Structure: Curvature and Overlay Alignment in Amorphous Silicon Thin-Film Devices Fabricated on Free-Standing Foil Substrates," in "Flexible Electronics: Materials and Applications" Edited by W.S. Wong, A. Salleo, Springer, New York, pp.29-51, 2009.

2ω/3ω SThM: improvements and perspectives

Alexia BONTEMPI, Laurent THIERY, Damien TEYSSIEUX and Pascal VAIRAC

FEMTO-ST, Université de Franche-Comté, ENSMM, UTBM, UMR6174, F-25044, Besançon, France

**corresponding author: laurent.thiery@univ-fcomte.fr*

Keywords: Scanning Thermal Microscope, 2ω/3ω techniques, thermoelectric probe, resistive probe.

Among available Scanning Thermal Microscopy techniques, the use of thermoelectric probes remains limited due to the difficulty to fabricate them. As a result, resistive probes represent the most wide-spread technique for which thorough theoretical and experimental studies have been performed [1-3]. The so-called Wollaston probe using a 5 µm wire and microfabricated cantilevered resistor tips represent the main active sensors for imaging substrate local apparent thermal conductivity. They also can be used in passive mode for temperature imaging of a surface.

Resistive probes differ from thermoelectric probes in terms of the measurement location. Unlike the mean temperature value derived from the probe resistor, a thermoelectric junction provides a direct thermoelectric voltage located at the junction. This should lead to a significant advantage of a thermoelectric probe in terms of dynamic range, and then on the expected image contrast. On the other hand, the need to increase the spatial resolution leads to reduce the tip size. However, this reduction contributes to degrade the tip-to-surface thermal admittance and subsequently the expected dynamic range of the probe.

To address these points, we have recently developed resistive and thermoelectric probes based on identical wires and different diameters. This should give the opportunity to explore the effects of dimension, shape and measurement methods on the spatial/thermal resolution and the sensitivity. The contact force mastering differs from usual cantilever technique since the principle is based on the use of a quartz tuning fork (QTF) on which the sensor is embedded (*Figure 1a*). During point contact scanning, a phase control of its resonant frequency insures a constant mechanical coupling between the tip and the sample surface [4].

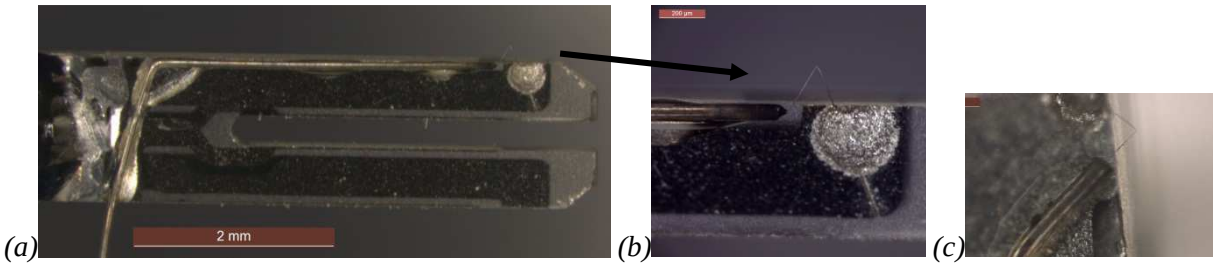

Figure 1: (a) QTF based resistive probe; (b) 5µm Pt-Rh10% resistive wire; (c) 1.3 µm Pt-Rh10% resistive wire.

An example of results is presented in Figure 2, obtained on a sample made of metal blocks separated by polymeric glue. Figure 2a corresponds to an AFM view whereas Figure 2b depicts the same area of the 3ω magnitude thermal image obtained with a 5µm wire probe supplied with an AC current of 12 mA. A single scan line is shown in Figure 2c-f, corresponding to the dotted line of Figure 2a.

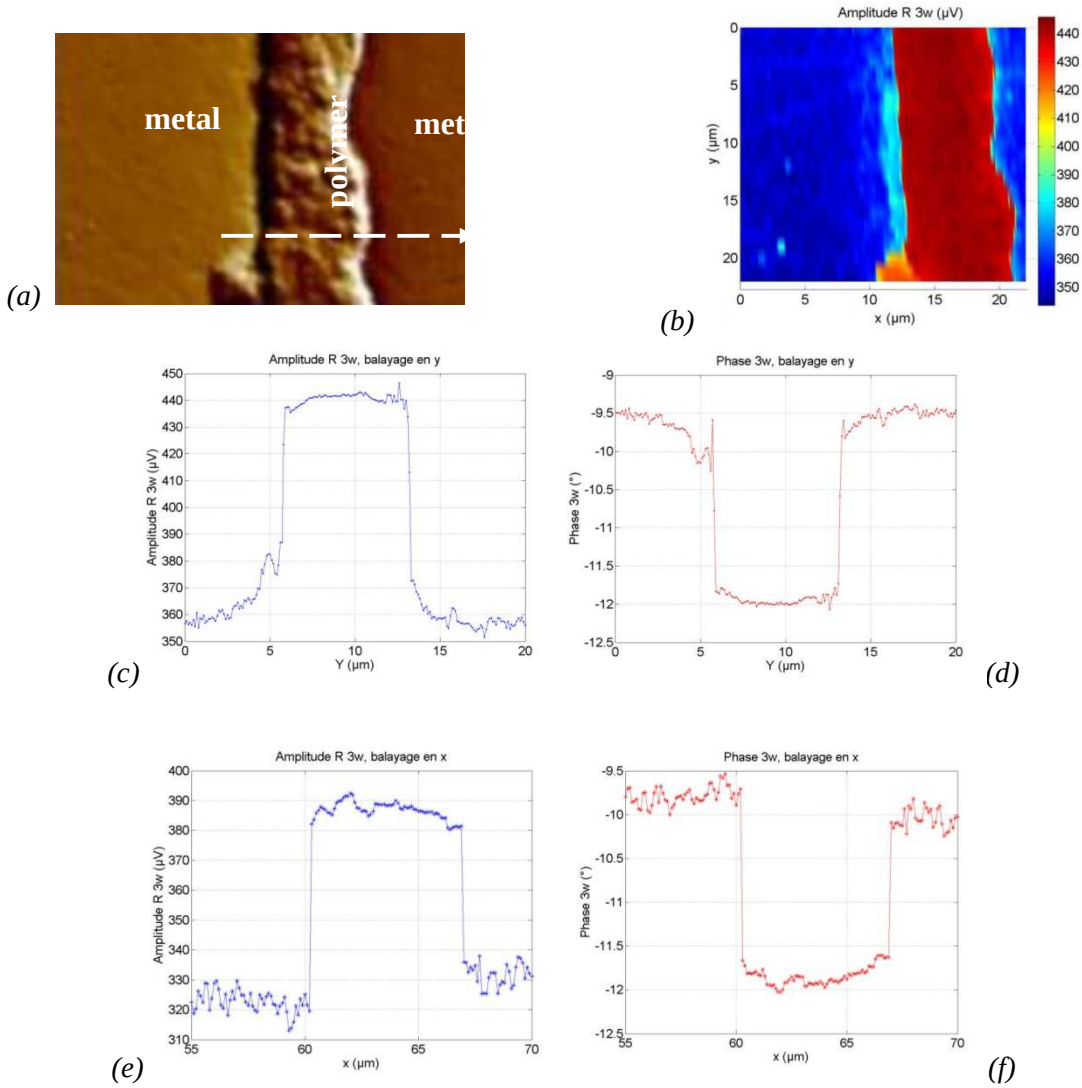

Figure 2: (a) AFM image of a metal-metal sample separated by polymeric glue; (b) 5µm resistive wire: 3ω magnitude image at f=17Hz; (c) 5µm resistive wire (f=17Hz, i=12mA RMS) 3ω magnitude and (d) phase (dotted line); (e) 1.3µm resistive wire (f=230Hz, i=2mA RMS) 3ω magnitude and (f) phase (dotted line).

These first results simply show that the sensitivity of both resistive probes seems to be comparable, and that more specific samples are needed to point out a significant effect of the wire diameter on the thermal spatial resolution.

A second example illustrates the interest of a thermoelectric probe used in active mode regarding to resistive wire probes [5]. Wollaston wires of platinum and platinum-10% rhodium have been used to produce S type thermoelectric probes which are also embedded on a QTF resonator (Figure 3a). To optimize the contact area, the junction is controlled and shaped by means of a focused ion beam (FIB) (Figure 3b).

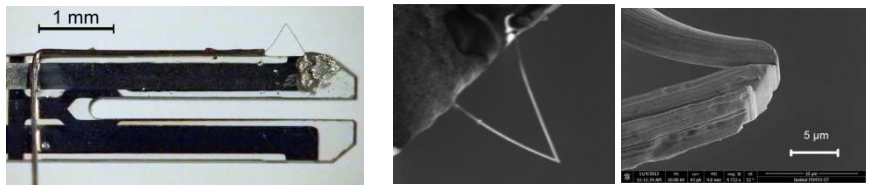

Figure 3: (a) QTF based 5µm wire thermocouple probe; (b) junction aspect after ion etching (FIB).

The following results have been obtained by using of a 5 µm wire thermocouple, similar to the configuration of the previous resistive probes. However, a thermoelectric probe which is supplied with a periodic current (AC) at f frequency provides simultaneously a 2f thermoelectric component (junction temperature) and a 3f component corresponding to the mean resistive value (mean temperature). Figure 4 depicts simultaneous images obtained by a scanning on a platinum layer (300 nm) deposited on a glass substrate and etched by means of FIB. Platinum has been removed so that the bottom of the etched letters corresponds to the glass substrate. A simple comparison of both 2f and 3f signals shows that the 2f images contrast (magnitude and phase) are four times higher than the 3f resistive images.

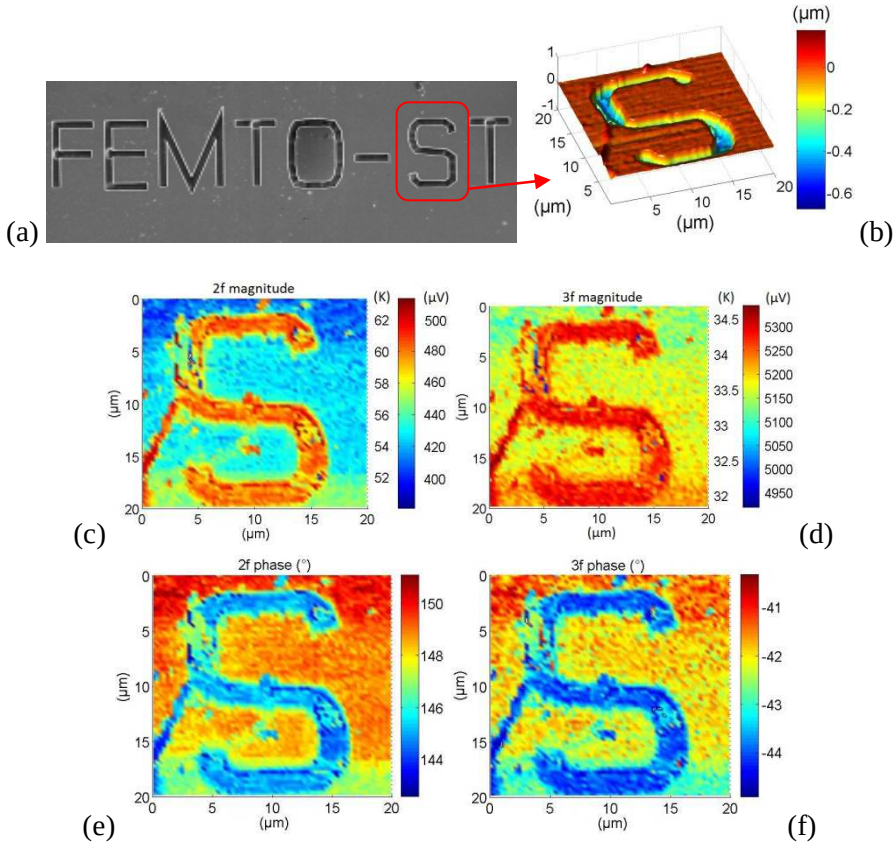

Figure 4: (a) FIB image of the sample surface; (b) topography given by the QTF resonance control (z table location); (c) 2ω magnitude; (d) 3ω magnitude; (e) 2ω phase; (f) 3ω phase. Frequency current f=270 Hz; RMS current i=22 mA.

These results have been obtained using a 3 axis NanoCube® piezo stage which is not optimized for a high resolution scanning purpose. Perspectives of this work include the use of specific AFM scanning piezo stages. In addition, the use of specific and well adapted samples are necessary to explore the effect of dimension and tip shapes.

References

[1] A. Majumdar, "Scanning thermal microscopy", *Annu. Rev. Mater. Sci.* **29**, 505-585, 1999.

[2] B. Cretin, S. Gomes, N. Trannoy, P. Vairac, in "Microscale and Nanoscale Heat Transfer", *Topics in Applied Physics Vol.107*, edited by S. Volz, (Springer, Heidelberg, 2007).

[3] S. Gomes, S. Lefevre, "Scanning thermal microscopy (SThM): Advances of the technique for the characterization of the thermo-physical properties of solid materials", J.L. Bubendorff and F.H. Lei (Eds.),

Advanced techniques and applications on scanning probe microscopy, Transworld Research Network, Trivandrum, Kerala, 2008.

[4] K. Karrai, R.D. Grober, "Piezoelectric tip-sample distance control for near field optical microscopes", *Applied Physics Letters*, **66**(14), 1842, 1995.

[5] L. Thiery, E. Gavignet and B. Cretin, "Two omega method for active thermocouple microscopy", *Rev. Sci. Instrum.* **80**, 034901, 2009.

SThM measurement of thermal conductivity of a nanowire Sb_2Te_3 crystal along the c-axis

Abdelhak SACI[a*], Jean-Luc BATTAGLIA[a], Andrzej KUSIAK[a],

Roberto FALLICA[b] and Massimo LONGO[b]

[a]*Laboratoire TREFLE, UMR 8508, Université de Bordeaux 33405 Talence Cedex France*

[b]*Laboratorio MDM, IMM-CNR, Unita di Agrate Brianza,Via C. Olivetti 2, 20864 Agrate Brianza, (MB), Italy*

**corresponding author: abdelhak.saci@u-bordeaux1.fr*

Keywords: thermal conductivity, nanowire, phase change, scanning thermal microcopy (SThM-3ω)

Phase change memories (PCMs) are the emerging non-volatile storage devices based on chalcogenide materials in which the programming function depends on the different electrical resistance offered by their amorphous and crystalline phases, reversibly induced by suitable current pulses [1, 2]. A very attractive option involves the use of chalcogenide nanowires (NWs) for highly scaled PCM devices and multilevel memory applications, since lowering active material volumes to be programmed requires shorter and less intense current pulses and implies higher cell density. In this paper we intend to measure the thermal conductivity of a Sb_2Te_3 nanowire using the scanning thermal microcopy (SThM) technique in the 3ω mode [3]. This well known contact method that allows reaching sub-micron spatial resolution [4]. In addition, the methodology we developed here does not require connecting the nanowire non handling it in a specific way.

The growth of the Sb_2Te_3 NW was performed in a MOCVD reactor on 4'' Si(100)/SiO_2 substrate. After the growth, some NWs were harvested on a new Si(100)/SiO_2 substrate e_{SiO2}=120 nm (thick thermal Si oxide) by mechanical rubbing. The NW is L_{NW}=3.5 μm long with a rectangular cross section area of height e_{NW}=150 nm and width l_{NW}=850 nm.

Our SThM is based on a silicon nitride (Si_3N_4) AFM tip on which is deposited a palladium (Pd) strip (1 μm thick and 10 μm long) that plays the role of the heater and the thermometer. A constant periodic current i_0 at angular frequency ω=2πf passes through the resistive strip, generating Joule's effect and thus a heat source at 2ω. The resulting temperature increase $\Delta T_{2\omega}$ leads to change the strip electrical resistance as: $R=R_0(1+\alpha_R \Delta T_{2\omega})$, where R_0 denotes the strip electrical resistance at ambient temperature and $\alpha_R = 1/ R_0 dR/dT$ is the thermal coefficient. It is easy to demonstrate that the voltage drop at the strip ends is expressed as a function of ω and 3ω. The third harmonic contribution $V_{3\omega}$ allows expressing the temperature increase as: $\Delta T_{2\omega}=2 V_{3\omega} / R_0 i_0 \alpha_R$ Therefore, measuring the third harmonic from a lock-in amplifier gives insight on the temperature increase of the palladium strip. The figures 1 a,b and c, respectively show the images obtained in mode AFM and SThM-3ω for the zone where the nanofil is deposited on the layer of SiO_2 for a frequency of 871 Hz. The images were carried out under a constant argon flow, for the goal was to reduce to the maximum conduction by the water meniscus.

The heat flux $\varphi_p(\omega)$ through the AFM tip is related to the measured temperature $T_{meas}(\omega)$ of the Pd strip through the thermal impedance $Z_p = (\omega)A_p(\omega)\exp(i\phi_p(\omega))/P_0$, where $P_0=R_0 i_0^2$. Facing the complexity of the tip, we proposed to obtain this thermal impedance from the measurement of the

amplitude $A_{p,mea}(\omega)$ and phase $\phi_{p,meas}$ (ω) in the contact-less mode. This obviously suggests that the heat transfer in the tip is not significantly influenced by the sample in the contact mode measurement. The procedure enabling us to measure the thermal conductivity of our nanofil in Sb_2Te_3, initially consists of carrying out cartographies varying thermals according to the frequency in a range from 871 to 3123 Hz. In the second phase, we compare this measurement with simulations of the model described in the previous section in the same frequency band.

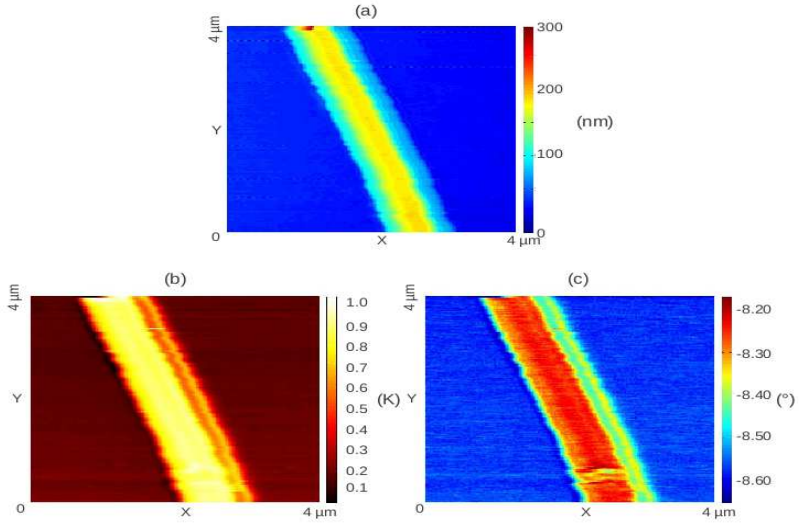

Figure 1: Experiment realized with 871 Hz: (a) topographic image, (b) amplitude of the temperature and (c) phase of the signal.

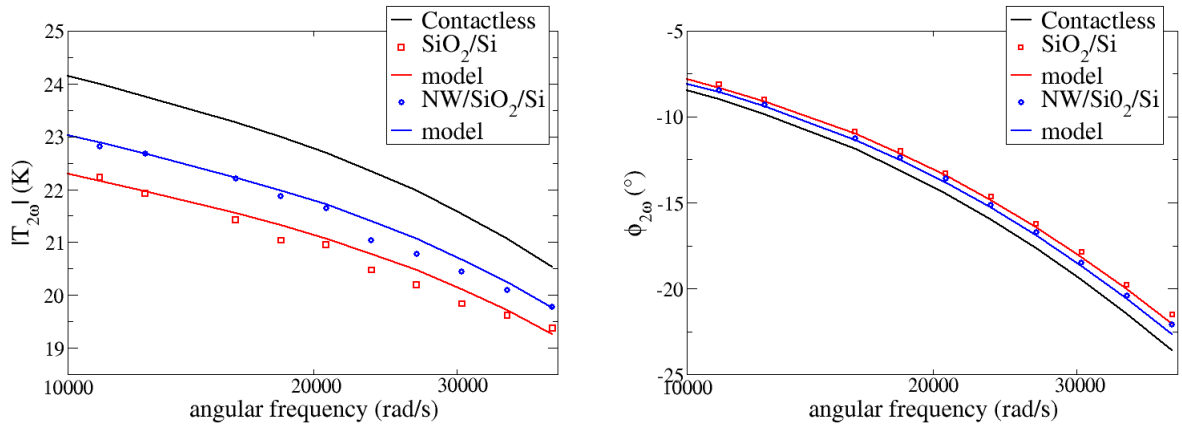

Figure 2: Amplitude and phase of the thrmal signal.

The figure 2 show the variation of the average temperature of the tip when this one is in contact with the layer of SiO_2 (red curve) for a frequency varying from 871 to 3123 Hz. This measurement enables us to estimate the value of the resistance of contact R_c between the probe and the sample. On the assumption that the speed of the probe remains low we suppose that the value of this resistance of contact remains constant during sweeping. By extrapolating the experimental points from the model given in the previous part and in fixing R_{NW}=$R_{NW/SiO2}$=0, $R_{SiO2/Si}$=4.5x10^{-9} K.m^2/W [5], we deduce from it a value of R_c equal to 3.87$\pm$0.2x10^6 K/W (either a resistance of 2.62$\pm$0.3x10^{-7} K.m^2/W). Minimization between the experimental points and the model was carried out using the algorithm of Levengerg-Marquardt. In the case of a measurement carried out under argon and with low power, the

resistance of contact is made up of several resistances [6]. The knowledge of the resistance in relation to the atmospheric condition, the radiation and the solide-solide contact needs further investigation. In case the probe is a wire of Wollaston and high power, the value of the resistance of contact is of the order $0.2x10^6$ K/W [7]. In the case of an experiment in carried out vacuum with a probe of the type Pd/SiO_2, the resistance of contact is estimated $4.09x10^6$ K/W [8]. The value of R_c estimated by the model is in agreement with that reached in the literature.

The value of the temperature according to the frequency on the figure 2 represents when the probe is in contact with the NW. It is noted that the influence of the NW adds an additional resistance to the measurement obtained previously for the probe in contact with the layer of SiO_2. By estimating the value of the resistance of contact (calculation is based on the model Diffuses Mismatch) $R_{NW/SiO2}$ at $1.061x10^5$ K/W [9] (i.e., $7.196\ x10^5$ K.m^2/W) and by considering that the value of Rc and r_0 remains unchanged, we deduce that R_{NW} equal to $2.351x10^6$ K/W. For dimensions of the NW, thermal conductivity k_{NW} is 0.93 ± 0.3 W.m^{-1}.K^{-1}. It is in a good agreement with value presented in the literature for the bulk ($k_{Sb2Te3,bulk}$=0.96 W.m^{-1}.K^{-1} [10]). This result is not surprising since the phonon mean free path is much less that the nanowire transverse characteristic dimension (width or heigh). However, the experimental method can be implemented with smaller dimension, leading to observe the phonon confinement along the nanowire transverse direction. The main drawback of the method is related to the contact zones between the AFM probe and the nanowire at one end and between the nanowire and the substrate on the other end. The thermal boundary resistance between the tip and the nanowire has been considered identical to that measured between the tip and the SiO_2 layer, whose properties are well known. This assumption seems realistic in the studied configuration, since Sb_2Te_3 and SiO_2 are expected to behave in a similar way considering the heat transfer diffusion. The thermal boundary resistance at the interface between the nanowire and the SiO_2 substrate has been estimated using the DMM theory. Although, this former approach seems leading to a consistent value, it could be more critical in the case of thermally conductive nanowires.

The authors would like to acknowledge Dr. Toni Stoycheva of CNR-IMM, for the MOCVD deposition and TXRF analysis of the Sb_2Te_3 NW.

References

[1] M. H. R. Lankhorst, B. W. S. M. M. Ketelaars, and R. A. M, *Nature Materials*, **1350**, 3347, 2005.

[2] M. Longo, R. Fallica, C. Wiemer, O. Salicio, M. Fanciulli, E. Rotunno, and L. Lazzarini: $Ge_1Sb_2Te_4$ Nanowires, *Nano Lett*, **12**, 1509–1515, 2012.

[3] D. G. Cahill: *Review of Scientific Instruments*, **61**, 802–808, 1990.

[4] A. Majumdar, J. P. Carrejo, and J. Lai, *Appl. Phys. Lett*., **62**, 2501, 1993.

[5] R. Kato and I. Hatta: *International Journal of Thermophysics*, **29**, 2062–2071, 2008.

[6] S. Gomes, N. Trannoy, P. Grossel, F. Depasse and C. Bainier, and Daniel Charraut, *International Journal of Thermal Sciences*, **40**, 948–958, 2001.

[7] L. David, S. Gomes, P. Galland, B. Vassort, and M. Raynaud: 17th European Congress on Thermophysical Properties (ECTP), Bratislava (Slovakia), p.87, 2005.

[8] E. Puyoo, S. Grauby, J.-M. Rampnoux, E. Rouvière, and St. Dilhaire: *J. Appl. Phys*., **109**, 024302, 2011.

[9] E. Swartz and R.O. Pohl, *Rev. Mod. Phys*., **61**, 605, 1989.

[10] R. Venkatasurbramanian, *Physical B*, **61**(4), 3091, 2000.

Poster session 2

Time-resolved measurements and quantitative analysis of the cooling dynamics of gold and gold-silica nanospheres in liquid environment

Tatjana STOLL*, Paolo MAIOLI, Aurélien CRUT, Natalia DEL FATTI and Fabrice VALLEE

FemtoNanoOptics group, Institut Lumière Matière, Université Lyon 1- CNRS, 43 Bd du 11 Novembre, 69622 Villeurbanne, France

**corresponding author: tatjana.stoll@univ-lyon1.fr*

Keywords: pump-probe spectroscopy, metal nanoparticles, thermal interface conductance.

With the development of devices in the nanometric size range, understanding and modelling thermal transport at the nanoscale are becoming key technological issues [1]. In particular, much attention is currently devoted to the increased role of thermal interfaces, characterized by a temperature discontinuity due to the so-called Kapitza resistance (or its inverse, the thermal interface conductance). In this context, cooling of bare gold and gold-silica core-shell nanospheres in solution was investigated using time-resolved spectroscopy. Here, we demonstrate a large contribution of the heated solvent to the pump-probe signals. Moreover, these data were quantitatively analyzed by modelling heat transfer in such systems and its impact on their optical properties. Using this approach, the thermal interface conductance at metal-liquid, metal-silica and silica-liquid interfaces could be estimated.

We performed measurements on bare 18 nm gold nanospheres in water and ethanol using optical pump-probe spectroscopy. Additionally, various samples obtained from the encapsulation of these nanospheres with 3 to 26 nm thick silica shells were considered. In such contact-free experiments, metal nanoparticles are selectively heated by a “pump” laser pulse. Their subsequent relaxation is then followed using a time-delayed “probe” pulse which monitors the change of the sample transmission induced by the pump beam. Typical signals consist of a large peak at short timescales, reflecting electronic excitation and internal thermalization of the nanoparticles, followed by a slower decay associated to nanoparticle cooling by energy transfer to their environment (Figure 1). For bare nanospheres in ethanol, relative probe beam transmission changes measured for different probe wavelengths close to their surface plasmon resonance (Figure 2) present different dynamics, with in particular modification of the amplitude and sign. This demonstrates that, in contrast to a frequent assumption of previous pump-probe studies, these signals are not directly proportional to the temperature of the metal nanoparticles (as this would lead to probe wavelength-independent signal shapes in Figure 2), but are also strongly affected by thermal kinetics in the liquid environment.

Cooling of an initially heated metal nanosphere and temperature evolution in its environment were modelled taking into account thermal resistance at the metal-liquid interface and heat diffusion in the liquid [2]. The resulting changes of the sample optical transmission were deduced by computing its sensitivity to changes of the nanoparticle/liquid dielectric functions, and using available measurements of the temperature derivatives of these functions. The temperature dependence of the refractive index of ethanol is particularly large, explaining the experimental observations described above by a large solvent contribution to pump-probe signals, even dominating that of gold for some wavelengths. Conversely, smaller environment impact is predicted for water, in agreement with experiments. For both liquids, time-resolved signals could be quantitatively reproduced using for all probe wavelengths

the same value of the metal-liquid thermal conductance, the only free parameter in the analysis. The deduced value for the gold-water interface (G≈110 $MW.m^{-2}.K^{-1}$) was similar to earlier experiments involving X-ray probe [3]. A smaller conductance (G≈40 $MW.m^{-2}.K^{-1}$) was obtained for the gold-ethanol interface, in agreement with recent measurements on gold nanorods [4].

Slight changes of the dynamics of pump-probe signals were observed for encapsulated nanoparticles. They were analyzed by extending the heat transfer model used for bare nanoparticles in order to include an additional interface. Estimations of the gold-silica and silica-liquid thermal interface conductances could thus be made, with however larger uncertainties due to limited knowledge of the characteristics of Stöber-synthesized silica shells such as porosity and possible solvent penetration (these parameters affecting the heat capacity and thermal conductance of silica shells). More precisely, a 2-step analysis was performed. First, samples involving the thickest silica shell (whose cooling kinetics can be approximated by that of nanospheres in an infinite glassy matrix) were used to estimate the thermal conductivity of the silica shell and the conductance at its interface with gold (G≈100 $MW.m^{-2}.K^{-1}$). In a second step, these parameters were used for analysis of thinner shell samples, enabling determination of a lower bound for the silica-liquid interface conductance.

In conclusion, optical pump-probe experiments on metal nanoparticles, bare and encapsulated, in ethanol and water, performed at different wavelengths, combined with a detailed model have permitted a quantitative analysis of heat transfer processes. This work could help interpretation of future optical experiments in temperature sensitive environments, allowing accurate estimation of interface conductances.

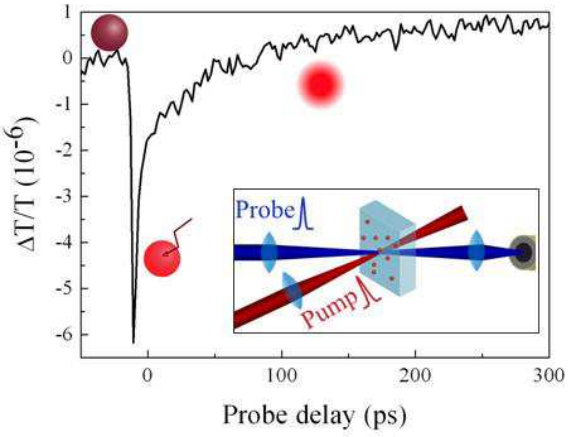

Figure 1: Normalized probe beam transmission change ΔT/T measured in 18 nm gold nanoparticles in ethanol (560 nm probe wavelength). The strong peak reflects particle heating and internal thermalization, heat dissipation to the environment dominating on longer timescales. Inset: principle of pump-probe experiments.

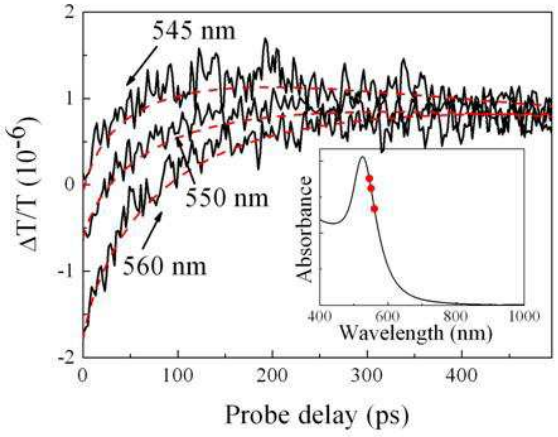

Figure 2: Long delay normalized transmission change for three different probe wavelengths (same sample as in Figure 1). The dashed lines indicate fits with the thermal interface conductance using the model described in the text. Inset: sample absorbance, with the three wavelengths indicated.

References

[1] D.G. Cahill, W.K. Ford, K.E. Goodson, G.D. Mahan, A. Majumdar, H.J. Marris, R. Merlin and S.R. Phillpot, "Nanoscale thermal transport ", *J. Appl. Phys* **93**, 793-818, 2003.

[2] V. Juvé, M. Scardamaglia, P. Maioli, A. Crut, S. Merabia, L. Joly, N. Del Fatti and F. Vallée, "Cooling dynamics and thermal interface resistance of glass-embedded metal nanoparticles", *Phys. Rev. B* **80**, 195406, 2009.

[3] A. Plech, V. Kotaidis, S. Grésillon, C. Dahmen and G. von Plessen, "Laser-induced heating and melting of gold nanoparticles studied by time-resolved x-ray scattering", *Phys. Rev. B* **70**, 195423, 2004.

[4] J. Huang, J. Park, W. Wang, C.J. Murphy and D.G. Cahill, "Ultrafast thermal analysis of surface functionalized gold nanorods in aqueous solution", *ACS Nano* **7**, 589-597, 2012.

Heat transfer through a triangular phononic crystal column

T. T. Trang NGHIEM[a*] and P.-Olivier CHAPUIS[a]

[a]*Université de Lyon, CNRS, INSA-Lyon, UCBL, CETHIL, UMR5008, F-69621, Villeurbanne, France*

**corresponding author: trang.nghiem@insa-lyon.fr*

Keywords: acoustic phonon, elastic equation, phononic crystal, heat transmission, spatio-temporal Fourier transform.

Phononic materials have been shown to possess interesting physical properties and provide new ideas for devices controlling both sound and heat [1]. The development of material design and fabrication capabilities has allowed to study the impact on sound in phononic crystals [2-3], which are artificial periodic structures made of two elastic materials. Proposals involving the use of such crystals to control heat have been highlighted in recent years [1, 6]. One ambition is to create thermal devices such as electronic diode/rectifier and transistor, which could lead to a revolution similar to the one acknowledged by electronics since the 1950s. Some nonlinear effects, such as non-uniform mass [7-8] and geometry [7, 9] or nonlinear acoustic response [10] have been used for the rectification.

It is interesting to note that acoustic waves sent perpendicularly to the sides of a periodic column of triangles can be reflected in a stronger way than the wave sent to the vertices [4], which leads to the fact that the transmittivity is quite different in these two cases. A. A. Maznev *et al*. [5] have pointed out that the matrix of coefficients of reflection-transmission (R-T) is symmetric ($S_{ij} = S_{ji}$), so that this is essentially a "*filtering effect*" in linear systems. Hence, if we excite all angles of incidence, the components of the wave are diffracted at different angles and reciprocity is fulfilled.

Here, we do not consider the nonlinear effects and do not investigate rectification effects. Instead, we analyze how a column of periodic objects set perpendicularly to the heat flux direction can be considered as a thermal barrier associated to a thermal resistance. We study numerically the transmission of the phonons through crystals with various geometries, including triangular-hole based crystals (see Fig. 1). This is realized by solving the elastic equation in 2D by a Finite Element Method technique with a commercial package (COMSOL):

$$\rho \frac{\partial^2 u}{\partial t^2} + \nabla \sigma = 0 , \qquad (1)$$

where ρ is the density, u is displacement field and σ is the strain tensor. Results are presented for silicon (Si) in the isotropic approach: knowing the longitudinal and transverse elastic constants C_{11} and C_{44} (C_{11} = 16,57×10^{10} Nm^{-2}, C_{44} = 7.692×10^{10} Nm^{-2} [11]), the constant C_{12} is defined as in [11] by $C_{11} - 2C_{44}$. Perfectly-Matching Layers are implemented at left and at right in the computational domain while periodic conditions are set at the top and bottom (see Fig. 1).

In contrast to previous acoustic works, we excite not only the acoustic waves that are perpendicular to the periodic direction, but also oblique waves. In Fig. 1, a longitudinal wave is excited and propagates towards the triangle-based crystal column with the initial following components: $u_x = \cos(\omega t)$, $u_y = 0$,

where ω is the circular frequency. The wavelength $\lambda = \frac{2\pi v}{\omega}$, where v is the acoustic velocity of the material, is compared to the crystal periodicity a with the non-dimensioned number $N_\omega = \frac{\lambda}{2a}$. Fig. 1 illustrates the displacement fields after reaching the stationary regime with N_ω = 5 for normal and oblique incidences.

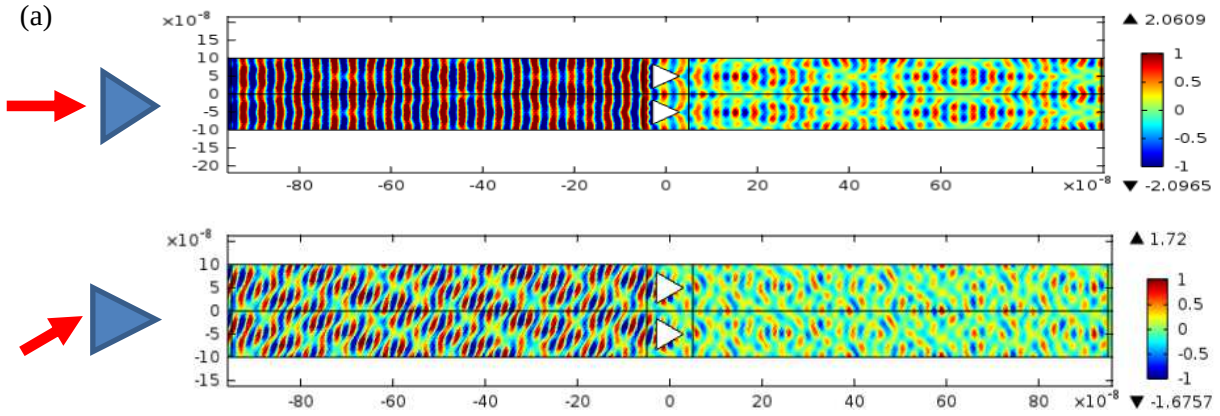

Figure 1. Displacement field u_x after reaching the stationary regime for (a) normal incidence and (b) oblique incidence.

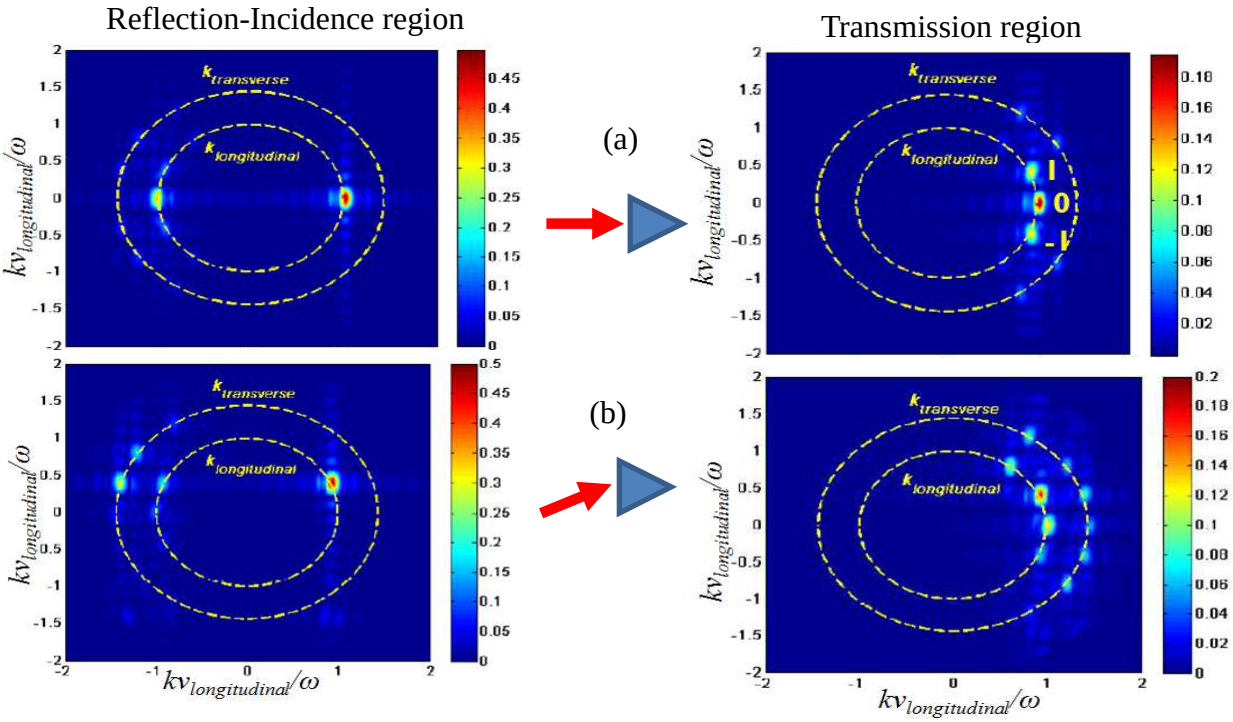

Figure 2. Spatio-temporal Fourier transform of the displacement fields in the reflection-incidence region (left column) and transmission region (right column) for (a) normal incidence and (b) oblique incidence.

It is well known that when waves are transmitted through a periodic lattice, they can be diffracted according to the Bragg's law: $a\sin\theta = n\lambda$, where *n* is an integral number. Hence, in the case of N_ω = 5, two diffraction angles appear, at $\theta_1 \approx 23{,}6°$ and $\theta_2 \approx 53{,}1°$. By employing the spatio-temporal Fourier transform, we verify that transmitted waves follow the Bragg's law whatever the wave's initial polarization. In addition, we observe the generation of a transverse wave after the lattice when the crystal is excited with a longitudinal wave; both transmitted waves have the same k_y component, as predicted by acoustic Snell's laws.

The same calculations can be made for the acoustic Poynting vector $\vec{P} = -\frac{1}{2}\vec{v}\hat{\sigma}$, which carries the energy associated with the wave. The energy reflection and transmission coefficients in the direction of the scattered angle θ_t are then computed for each incident angle θ_i and for each frequency ω:

$$\tau(\omega,\theta_i,\theta_t) = \frac{P_{\theta_t}(\omega)}{P_{\theta_i}(\omega)} \ . \qquad (2)$$

The total transmission coefficients can be calculated for the two following cases: (i) the wave is sent to the bases and (ii) to the vertices of triangle crystals. These transmissions allow defining the thermal conductance of various crystals. We vary the shapes of triangle and circular hole-based periodic column and compare the effects on the thermal conductances associated to these crystals.

Acknowledgements

We acknowledge the support of ANR project RPDOC NanoHeat and INSA BQR MaNaTherm.

References

[1] M. Maldovan, " Sound and heat revolutions in phononics", *Nature* **503**, 209-217, 2013.

[2] A. Khelif, B. Djafari-Rouhani, J.O. Vasseur, J. O., P.A. Deymier, P. Lambin, L. Dobrzynski, "Transmittivity through straight and stublike waveguides in a two-dimensional phononic crystal", *Physical Review B* **65**, 174308, 2002.

[3] Ramya Krishnan, S. Shirota,Y. Tanaka and N. Nishiguchi, B. Gotsmann, M.A. Lantz, "Highly-efficient acoustic wave rectifier", *Solid State Comm.* **144**, 194-197, 2007.

[4] Y. Tanaka, T. Murai, N. Nishiguchi, "Rectification of elastic waves in a thin plate", *Journal of Applied Physics* **111**, 024507, 2012.

[5] A.A. Maznev, A.G., Every, O.B. Wright, "Reciprocity in reflection and transmission: what is a 'phonon diode?", *Wave Motion*, **50**, 776-784, 2013.

[6] N. Li, J. Ren, L. Wang, G. Zhang, P. Hänggi, B. Li, "Phoninics: Manupulating heat flow with electronic analogues and beyond", *Review of Modern Physics* **84**, p. 1045-1066, 2012,).

[7] C. W. Chang, D. Okawa, A. Majumdar and A. Zettl, "Solid-state thermal rectifier", *Science* **314**, 1121, 2006.

[8] N. Yang, N. Li, L. Wang and B. Li, "Thermal rectification and negative differential thermal resistance in lattices with mass gradient", *Phys. Rev. Let.* B **76**, 020301, 2007.

[9] N. Yang, G. Zhang abd B. Li, "Thermal rectification in asymmetric grapheme ribbons", *Appl. Phys. Let.* **95**, 033107, 2009.

[10] B. Liang, X. S. Guo, J. Tu, D. Zhang and J. C. Cheng, "An acoustic rectifier", *Nature Mat.* **9**, 989, 2010.

[11] B.A. Auld, Acoustic fields and waves in solids (Vol. 1, p. 423). New York: Wiley, 1973.

Morphologies and radiative properties of soot particles issued from partial oxidation combustions

Gizem OKYAY[a,b*], Youssef JOUMANI[c], Caroline BERTAIL[c] and Franck ENGUEHARD[a,b]

[a]*CNRS, UPR 288 Laboratoire d'Energétique Moléculaire et Macroscopique, Combustion (EM2C), Grande Voie des Vignes, 92295 Châtenay-Malabry, France*

[b]*Ecole Centrale Paris, Grande Voie des Vignes, 92295 Châtenay-Malabry, France*

[c]*Air Liquide R&D Centre Paris-Saclay, 78356 Jouy-en-Josas, France*

**Corresponding author: gizem.okyay@ecp.fr*

Keywords: soot morphology, electron microscopy, fractal aggregates, DDA, Mie theory

1. Scope of work

Hydrogen production is seen today as a route for reducing greenhouse gases emissions in the atmosphere. These molecules can be produced by steam reformers, water electrolysis or by gasification processes. In this last process, fuels are pressurized up to 70 bars: natural gas, fuel-oil or coal are introduced with pure oxygen for making a mixture of CO/H_2. Heat transfer in partial oxidation chambers is dominated by radiation and more specifically by CO, CO_2 and H_2O molecules. Evaluating radiation levels is necessary to understand the flame behavior and to predict potential hot spots that could damage the combustion chamber or the burner. In traditional lean combustion oxygen flame, such as glass furnaces and steelmaking furnaces, soot produced by the gaseous combustion can be neglected because they are destroyed as soon as they are formed. Ammouri *et al.* [1] have measured soot volume fractions of $0.5*10^{-6}$: they assumed a refractive index of $1.55 - 0.56i$ for the soot and used the Rayleigh approximation to calculate the absorption coefficient of the mixture. In such flames, the residence time of soot is very short and their trajectory meets oxygen molecules very quickly (for example, 5% of oxygen in flue gases represents 100000 times more oxygen molecules than soot aggregates). In order to evaluate the radiative properties of the soot in this type of combustion, the Mie theory has been widely used assuming that they behave as homogeneous spheres.

The results presented above are based on data obtained on lean combustion and must be reconsidered in the case of partial oxidation conditions. In rich flames, the residence time of soot and the concentration of carbon atoms are much higher than in full oxycombustion flames; therefore the contribution of soot and of its morphology to the radiative transfer becomes important. This research aims to build a complete methodology from the description of the morphology of soot to the derivation of its radiative properties and its possible effects in rich flame conditions on the radiative heat transfer in a combustion chamber by use of experimental (microscopy) and computational tools.

The morphology of hydrocarbon soot is investigated by TEM (Transmission Electron Microscopy) and SEM (Scanning Electron Microscopy) images and by associated tomography techniques in parallel with the data gathered from the literature. The state of the art work on heat transfer simulations including combustion soot [2,3] and the studies on the effect of soot morphology (Oh and Sorensen 1997, Skorupski *et al*. 2013) rely on numerically generated geometries. In parallel with the classical aggregate numerical generation techniques, this study proposes SEM image reconstruction to

describe actual aggregate morphologies and considers the implementation of multiple scattering from complex shaped aggregates in the computation of thermal radiative properties and radiation heat fluxes. Soot radiative property spectra obtained by the DDA (Discrete Dipole Approximation) are coupled to non-gray gas properties which are then inserted in the radiation simulation of a simplified representative case of the combustion environment by discrete ordinates method.

2. Microscopy studies on soot morphology and numerical aggregate generation

The size of soot aggregates being susceptible to reach 1µm, i.e. the order of magnitude of the incident wavelengths in the visible and near IR, the necessary input throughout this research is the complete description of the soot morphology. Furthermore, our modeling approach (DDA) accounts for the complex geometry of the target in the computing of the radiative properties.

The early researches on soot morphology and later experimental works are based on a fractal description of the aggregates [4,5]. In order to better predict the radiative properties, Talbaut *et al*. [5] have measured real *n* and imaginary *k* components of the optical index indirectly from the extinction coefficient of an oxygen flame by assuming a fractal shape of soot:

$$N_p = k_f (R_g / d_p)^{D_f} \tag{1}$$

where N_p is the number of monomers in the aggregate, D_f is the fractal dimension, k_f is the prefactor, d_p is the monomer diameter and R_g is the radius of gyration of the aggregate. The characteristic sizes of aggregates are deduced from experimental observations. The fractal definition remains valid according to up-to-date information provided by other researchers [1,2,7] defining the fractal geometry of soot from combustion of hydrocarbon fuels. As methane combustion is of primary concern, D_f varies in a narrow range of 1.60-1.75 whereas k_f varies in a larger range of 1.2-7.9, N_p in an aggregate varies from 100 to 500, and d_p is around 20 nm according to the literature data gathered in our previous work [6] retrieved mainly from the studies of Köylü, Farias, Sorensen, Cai, Zhang and Lee. The DLCCA (Diffusion Limited Cluster-Cluster Aggregation) algorithm [7] is selected for $D_f < 1.9$; the fractal parameters of the generated aggregate in Figure 1 are $D_f = 1.7$, $k_f = 2.0$, $N_p = 500$.

Figure 4: Methane soot aggregate generated by DLCCA algorithm.

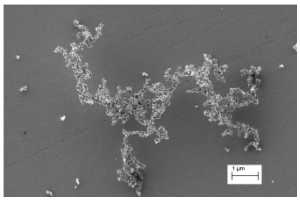

Figure 2: SEM image of soot indicating fractal agglomerate.

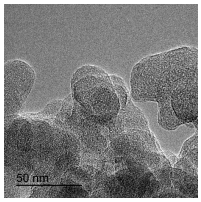

Figure 3: TEM image of soot monomers.

In parallel with the above-mentioned numerical approach, a soot deposit is extracted from a laboratory scale propane flame and the aggregation pattern is examined by SEM (see Figure 2). Some of the collected soot is deposited on a TEM membrane: monomers are correctly represented by 20 nm diameter spheroids as shown in Figure 3. First EDX experiments indicate that the monomers are amorphous and mostly composed of carbon. It is not yet possible to distinguish between the agglomerates and the individual aggregates; nevertheless one can say that the fractal theory seems to hold because soot has the same geometry pattern regardless of the size of the aggregate/agglomerate. The fractal nature of the aggregates is also examined by SEM: a series of images is obtained for subsequent 3D geometry reconstruction from a 100° rotation of the soot sample around a tilt axis

within the microscope as shown in Figure 4. These microscopy results will allow us to test the fractal morphology assumption, to validate the literature values extracted for the fractal parameters.

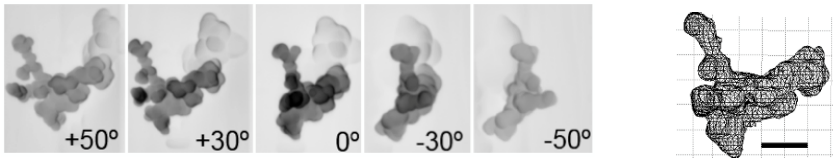

Figure 4: Left: Examples of SEM images of a soot aggregate obtained with tilt angles from -50° to +50° for 3D image reconstruction. Right: Reconstructed 3D geometry; scale bar corresponds to 100 nm.

3. Computation of radiative properties of soot by DDA for radiative transfer simulations

DDA is chosen for the simulation of the radiative properties of soot aggregates between different other methods such as the Mie solution, RDG-FA, the T-matrix method, GMM and FDTD due to its applicability to complex shaped aggregates not limited to spherical monomers and due to its advantage in terms of discretization effort, computation time and solution techniques as mentioned in our previous study [7]. The target is discretized into a sufficient number of dipoles satisfying Draine's condition $|m|k\delta < 1$ where m is the complex optical index of the material, k is the wavenumber and δ is the characteristic size of the discretization [8]. Each dipole is polarized under the effect of the incident light and contributes to material-light interaction depending on its composition and its position. The whole set of oscillating dipole moments are determined under two orthogonal polarization directions, from which the radiative properties of the set of dipoles are deduced [9].

Our research being focused on radiation in combustion chambers at high temperatures of 1500K-2000K, the relevant radiation spectrum ranges from 0.5µm to 20µm. In this wavelength range, the applicability limits of the DDA are checked and the radiation spectra of soot are obtained as shown in Figure 5. The calculations are performed by our in-house developed DDA code which has been validated with analytical results and tested for its applicability to highly absorbing materials [7]. The aggregate fractal parameters and the number and size of the monomers are fixed to the values presented in Section 2. It is worth to mention here the low sensitivity of soot radiative properties to the fractal parameters around the selected values, as demonstrated in our previous research [10].

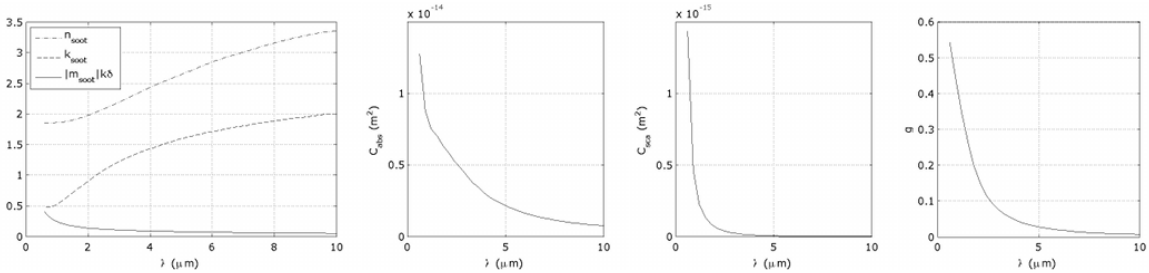

(a) *(b)* *(c)* *(d)*

Figure 5: (a) One dipole per monomer satisfies the Draine's condition based on the complex optical index of soot reproduced from Dalzell and Sarofim (1969); Soot absorption (b), scattering (c) cross-sections and asymmetry parameter (d) computed by DDA over the wavelength range of interest.

4. Effect of soot on radiation heat transfer in combustion chambers and future works

In order to account for the non-gray properties of gases and for the scattering from soot, the discrete ordinate method is selected for the resolution of the radiative transfer equation. One advantage is that

the problem of selection of the proper quadrature for directional integration/averaging has already been treated in the course of the development of our DDA code [6]. Soot spectra obtained by DDA will be coupled to combustion gas properties obtained from the HITRAN/HITEMP database through Equation (2) written for extinction, where $\beta_{\{gas\ +\ soot\}}$ stands for the extinction coefficient of the mixture {gas + soot} and the notations *C* and *n* refer respectively to individual extinction cross-sections (of one gas molecule or one soot aggregate) and to volume number densities (of gas molecules or soot aggregates):

$$\beta_{\{gas\ +\ soot\}} = n_{gas} C_{gas} + n_{soot}\ C_{soot} \tag{2}$$

Results of radiative transfer simulations will be presented between two infinite walls at controlled temperatures in order to quantify the effect of different soot concentrations on heat flux rates. Low heat flux sensitivity to soot morphology is expected at high concentrations. On the other hand, better sampling techniques regarding partial combustion need to be developed for more representative morphology analysis of soot in flames.

Acknowledgement

This work is supported by the Air Liquide chair on oxycombustion and heat transfer for energy and environment and by OXYTEC ANR program. Authors would like to thank Thierry Auger, Eva Héripré, Thomas Reiss and Paul Haghi of the MSSMat Laboratory of CNRS and Ecole Centrale Paris for giving access to the microscopy facilities and for their help in microscopy analyses.

References

[1] F. Ammouri, B. Labégorre, J-M. Samaniego, A. Coppalle, M. Talbaut-Haudiquert, "Soot effects on heat transfer and NOx formation in industrial scale furnace – Experimental study on turbulent diffusion oxygen gas flames", in: *Proceedings of 5th International Conference on Technologies and Combustion for a clean Environment*, 1097-1100, Lisbon, Portugal, July 12-15, 1999.

[2] V. Eymet, A.M Brasil, M. El Hafi, T.L. Farias, P.J. Coelho, "Numerical investigation of the effect of soot aggregation on the radiative properties in the infrared region and radiative heat transfer", *J. Quant. Spectrosc. Radiat. Transfer* **74**, 697-718, 2002.

[3] L. H. Dorey, "*Modélisation des phénomènes couplés combustion – formation des suies – transferts radiatifs dans les chambres de combustion de turbine à gaz*", PhD Thesis, Ecole Centrale Paris, 2012.

[4] C.M. Megaridis, R.A. Dobbins, "Morphological Description of Flame-Generated Materials", *Combustion Science and Technology* **71**, 95-109, 1990.

[5] M. Talbaut, P. Van-Hulle, A. Coppalle, M. Weil, F. Ammouri, "Determination of soot refractive index in turbulent diffusion oxygen gas flame", in: *Proceedings of 6th International Conference on Technologies and Combustion for a clean Environment*, 1501-1506, Porto, Portugal, July 9-12, 2001.

[6] G. Okyay, F. Enguehard, "Modélisation des proprieties radiatives des suies issues de combustions incomplètes au moyen de l'approximation dipolaire discrète", in: *Actes du Congrès Français de Thermique*, Lyon, France, June 3-6, 2014.

[7] D.W. Mackowski, "A simplified model to predict the effects of aggregation on the absorption properties of soot particles", *J. Quant. Spectrosc. Radiat. Transfer* **100**, 237-249, 2006.

[8] B. T. Draine, The Discrete Dipole Approximation and Its Application to Interstellar Graphite Grains, Astrophys. J. **333**, 848-872, 1988.

[9] F. Enguehard, "Mie Theory and the Discrete Dipole Approximation. Calculating Radiative Properties of Particulate Media, with Application to Nanostructured Materials", in S. Volz, *Thermal Nanosystems and Nanomaterials, Topics in Applied Physics*, **118**, 151-212, Springer Verlag Berlin Heidelberg, 2009.

[10] G. Okyay, F. Enguehard, "Effect of Fractal Parameters of Soot Aggregates on Their Absorption and Scattering Properties Simulated by Discrete Dipole Approximation", in: *Proceedings of 10th International Conference on Laser-Light and Interactions with Particles*, Marseille, France, August 25-29, 2014.

Thermal properties of chirped superlattice structures through molecular dynamics and photothermal radiometry

Kyle HORNE[a,c], Mihai CHIRTOC[b*], Nicolas HORNY[b], Thomas ANTONI[a], Sebastian VOLZ[a] and Heng BAN[c]

1. [a]*Lab. EM2C, Ecole Centrale Paris, Building PECLET, Grande Voie des Vignes, Chatenay-Malabry, 92295, France*

2. [b]*Lab. GRESPI, Université de Reims Champagne Ardenne URCA, Moulin de la Housse BP 1039, Reims, 51687, France*

3. [c]*Department of Mechanical & Aerospace Engineering, Utah State University, Logan, 84322, USA*

**corresponding author: mihai.chirtoc@univ-reims.fr*

Keywords: computational and experimental sciences, molecular dynamics, phonon heat transport, photothermal methods, photothernal radiometry.

Superlattice structures are increasingly common in solid state applications, primarily to manipulate electrical properties of the device in order to optimize performance; specific applications of these devices include quantum-well laser diodes. As the scale of the system approaches the phonon mean free path and then the phonon wavelength, Fourier's law fails to correctly predict the heat flux and more sophisticated treatments are required. Molecular Dynamics (MD) can be used to compute the thermal properties as emergent behaviors. While this requires considerably more computing power than solving the well known diffusion equation for macro-scale heat transfer, modern computers have brought such calculations within reach for many practical problems using standard hardware.

The Green-Kubo method has previously been successfully applied to molecular dynamics results to compute the thermal conductivity of layered structures, and the size effects that complicate its use have been considered carefully[1, 2]. Quantum cascade lasers (QCLs) have been developed since the mid-1990's and are constructed from superlattices of semiconductors which produce inter-sub band energy levels enabling a single electron to emit multiple photons as it passes through the device under bias [3]. Like many such devices, increased temperatures impede their operation, so some care has been taken to characterize their thermal properties [4, 5]. These efforts have yet been unable to directly measure QCL thermal conductivity, but rather have developed it through fitting finite element simulations to steady-state power and temperature measurements.

This work is divided into both modeling and experimental validation: the former accomplished through a combination of MD simulation and classical methods, and the latter being implemented using Photothermal Radiometry (PTR) [6-9]. The simulations provide effective bulk properties of a single period within the superlattice. These results are compared with the PTR measurements of similarly structured samples. Note that the amplitude and phase response of the superlattice sample were both measured, but that the phase is typically more sensitive to thermophysical parameters, and less sensitive to fluctuations in laser power.

The results of the MD simulations are summarized below. By comparison between experimental values for bulk materials and simulation results, the ratios between the two can be used to project the QCL simulation results to an expected range of true values.

Material	Thermal Conductivity (k) [W/m.K]		Ratio (Sim/Exp)
	Simulation	Experiment	
AlInAs (Experiment)	10.29	3.5	2.94
GaInAs (Experiment)	6.27	5	1.25
QCL (Simulation)	5.37		
QCL (Expected)	1.8-4.3		

The MD simulations are used to compute the thermal conductivity through the Green-Kubo method, which takes the equilibrium heat flux variations within the system as input. The system heat flux is autocorrelated and then integrated; the result of integration is proportional to the thermal conductivity through the volume and temperature squared, as well as the Boltzman constant. Figure 1 shows the QCL system heat flux autocorrelation and its integral.

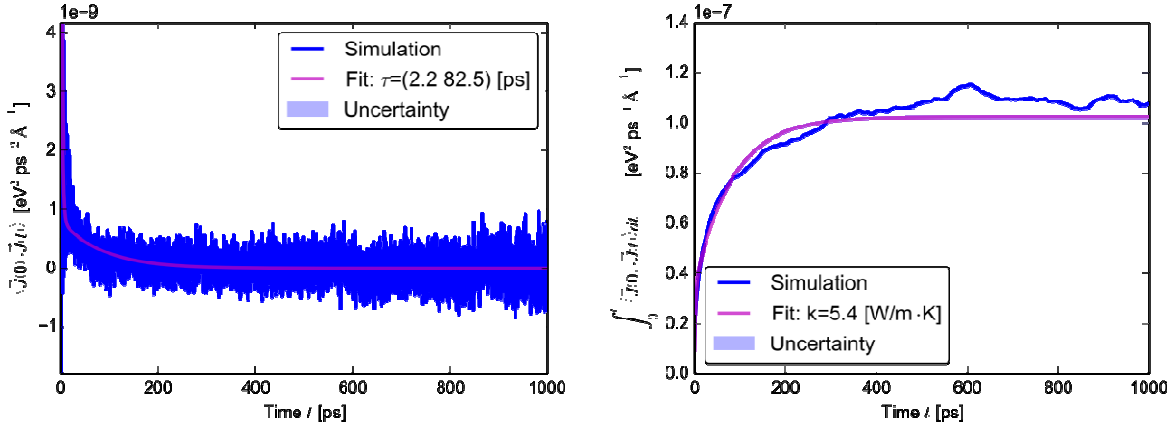

Figure 1: Heat flux autocorrelation function (left) and its integral (right) as well as a line of best fit for the QCL diode simulation results.

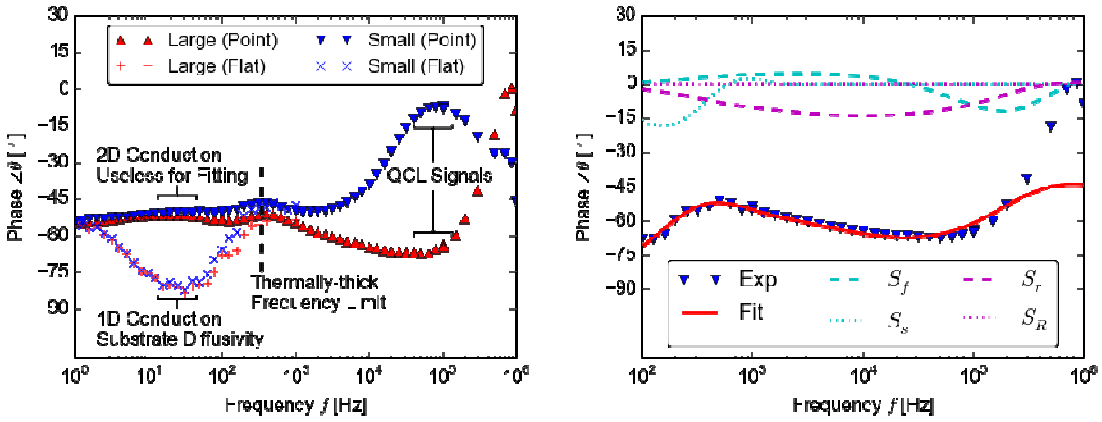

Figure 2: Comparison between SIM and EXP in same parameter space

The PTR raw data and preliminary fitting results are shown in Figure 2. While the effects of the superlattice film on the InP substrate can clearly be seen in the higher frequencies, it is observed that the line of best fit cannot duplicate the system's phase response at these frequencies adequately. It is possible that more complex physics are involved than the simple 1D heat transfer models used as the functional family for the fitting process.

From the MD simulations the predicted thermal diffusivity of the QCL strucure should 1.77×10^{-6} m^2/s, while the fitting for the PTR results measures as value of 4.70×10^{-7} m^2/s: a value nearly four times lower. Further work must be done to reconcile this discrepancy; this will likely include additional simulations and PTR frequency scans with new fits.

References

[1] Y. Chalopin, K. Esfarjani, A. Henry, S Volz, and G. Chen, "Thermal interface conductance in Si/Ge superlattices by equilibrium molecular dynamics", *Phy. Rev. B* **85**, 195302, 2012.

[2] D.P. Sellan, E.S. Landry, J.E. Turney, A.J.H. McGaughey, and C.H. Amon, "Size effects in molecular dynamics thermal conductivity predictions", *Phy. Rev. B* **81**, 214305, 2010.

[3] F. Capasso, A. Tredicucci, C. Gmachl, D.L. Sivco, A.L. Hutchinson, A.Y. Cho, and G. Scamarcio, "High-performance superlattice quantum cascade lasers", *IEEE Journal of Selected Topics in Quantum Electronics*, **5** 792, 1999.

[4] G. Scamarcio, M.S. Vitiello, V. Spagnolo, S. Kumar, B. Williams, and Q. Hu, "Nanoscale heat transfer in quantum cascade lasers", *Physica E: Low-dimensional Systems and Nanostructures*, **40** 1780, 2008.

[5] M.S. Vitiello, T. Gresch, A. Lops, V. Spagnolo, G. Scamarcio, N. Hoyler, M. Giovannini, and J. Faist, "Influence of InAs, AlAs δ layers on the optical, electronic, and thermal characteristics of strain-compensated GaInAs/AlInAs quantum-cascade lasers", *Appl. Phys. Lett*., **91** 161111, 2007.

[6] P.-E. Nordal and S. O. Kanstad, *Phys. Scr*. **20**, 659, 1979.

[7] R. Santos, and L.C.M. Miranda, J. Appl. Phys. **52**, 4194, 1981.

[8] R.D. Tom, and E.P.J. O'Hara, Appl. Phys. **53,** 5392, 1982.

[9] M. Chirtoc, "Thermal Wave Physics and Related Photothermal Techniques", in *"Basic Principles and Recent Developments"*, Ed. E.M. Moares, Transworld Research Network, Kerala, India, 2009, pp. 29–63.

Vacuum phonon coupling through Casimir force between two solid dielectric materials

Younès EZZAHRI* and Karl JOULAIN

Institut Pprime, Université de Poitiers-CNRS-ENSMA
2, Rue Pierre Brousse Bâtiment B25, TSA 41105
86073 Poitiers Cedex 9 France

**corresponding author: younes.ezzahri@univ-poitiers.fr*

Keywords: Dielectric materials, Casimir force, Scattering Boundary Method, Interface phonon thermal conductance, Near field radiative heat transfer coefficient.

One expects a natural transition from the near field radiative regime to the conductive regime of heat transfer to occur when the separation distance between two solid materials tends to zero. The occurrence of such a transition regime in heat transfer between two solid materials has raised a very fundamental question regarding the possibility of induced phonon transfer through the separation gap between the two solids when the latter become very close to each other. We investigate here the possibility of such a mechanism mediated through Casimir force. The latter depends on the gap distance between the two solids, hence a local change of this distance due to any displacement of one side of the gap in the acoustic wave causes an excess pressure on the opposite side of the gap. This work will be a generalization of the approach recently presented by Budaev and Bogy [1].
A sketch of the situation under study is illustrated in Fig. 1. For simplicity sake, and without loss of generality, we will consider two identical nonmagnetic isotropic semi-infinite parallel plane solid materials both in a thermal equilibrium state at different temperatures, to be put in vacuum and separated by a gap distance *d*. The situation corresponds to a point junction case, through which the transport of phonons may be regarded as ballistic [2]. Each solid material is characterized by: (i) an atomic mass *m*, (ii) a hamornic spring constant *k* and (iii) a dielectric permittivity function ε. The two solids are then connected through a Casimir spring coupling constant $k_{Casimir}$ that we assume to be harmonic.

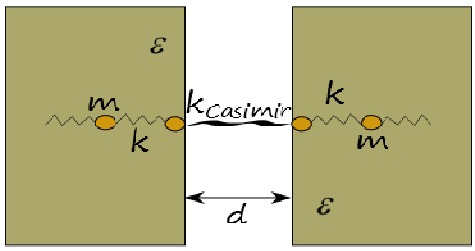

Figure 1: Schematic illustration of the studied structure.

We carry out the calculation of the phonon heat flux density through the interface using the Scattering Boundary Method (SBM) [2] within a Landauer formalism. The phononic thermal conductance through the interface takes the expression:

$$\sigma_{Ph}(T)=\frac{1}{2\pi}\int_0^{\omega_C}\tau_{3D}\left(\omega^2,\omega_C^2,k,k_{Casimir}\right)C_{Ph}(\omega,T)\,d\omega \qquad (1)$$

where $\omega_C = 2\sqrt{k/m}$ is the cutoff frequency in the phonon dispersion relation inside each material, $C_{Ph}(\omega,T) = \hbar\omega\left[\partial n_0(\omega,T)/\partial T\right]$ represents the specific heat per normal phonon mode and $n_0(\omega,T) = \left[\exp(\hbar\omega/K_B T) - 1\right]^{-1}$ is the Planck equilibrium phonon distribution function.

The key step for the calculation of $\sigma_{Ph}(T)$ is the determination of the frequency dependent transmission function for the 3D configuration we are considering $\tau_{3D}\left(\omega^2, \omega_C^2, k, k_{Casimir}\right)$. The latter gathers all the information about the nature of the phonon transport mechanisms.

Taking into consideration the isotropy of the solid media and the conservation of the parallel momentum relative to the phonon dispersion within the frame work of Debye theory [3], one can show that the transmission function can be written as:

$$\begin{aligned}\tau_{3D}\left(\omega^2, \omega_C^2, k, k_{Casimir}\right) &= \frac{1}{2\pi}\int_0^{\omega/v} \tau_{1D}\left(\omega^2 - v^2 q^2, \omega_C^2, k, k_{Casimir}\right) q\,dq \\ &= \frac{k_{Casimir}^2 \omega_C^2}{4\pi k^2 \left(k - 2k_{Casimir}\right)^2 v^2}\left\{\begin{array}{l}\left(k - k_{Casimir}\right)^2 \log\left[1 + \dfrac{k\left(k - 2k_{Casimir}\right)}{k_{Casimir}^2}\left(\dfrac{\omega}{\omega_C}\right)^2\right] \\ -k\left(k - 2k_{Casimir}\right)\left(\dfrac{\omega}{\omega_C}\right)^2\end{array}\right\}\end{aligned} \quad (2)$$

where q is the parallel wavevector and v represents an average sound velocity that takes into account both longitudinal and transverse phonon polarizations $3/v^2 = 1/v_L^2 + 2/v_T^2$.

Inserting Eq. (1) into Eq. (2), allows obtaining the final expression of the phononic thermal conductance $\sigma_{Ph}(T)$ through the point junction between two identical semi-infinite parallel plane solid materials coupled via Casimir force.

We shall now compare this thermal conductance to the Near Field Radiative Heat Transfer (NFRHT) coefficient $h_r(d,T)$ due to the contribution of the dominant evanescent waves of the P-polarized electromagnetic (EM) field within the framework of a local dielectric permittivity function theory. In the small gap distance regime, one can assume the electrostatic limit to be valid. In this case, it is easy to show that $h_r(d,T)$ takes a closed-form expression using the polylogarithm function of second order [4]:

$$\left\{\begin{array}{l} h_r(d,T) = \dfrac{\delta G(T)}{d^2} \\ \delta G(T) = \dfrac{3}{2\pi^3} g_0 \displaystyle\int_0^{\infty} h^0(u) \frac{\mathrm{Im}^2\left[r_P(u)\right]}{\mathrm{Im}\left[r_P^2(u)\right]} \mathrm{Im}\left\{Li_2\left[r_P^2(u)\right]\right\} du \end{array}\right. \quad (3)$$

In Eq. (3), $g_0 = \pi^2 K_B^2 T/3h$ is the quantum of thermal conductance, $h^0(u) = u^2 e^u \Big/ \left(e^u - 1\right)^2$ and $r_P(u) = \left[\varepsilon(u) - 1\right]/\left[\varepsilon(u) + 1\right]$ represents the Fresnel reflection coefficient of the P-polarized evanescent EM wave in the electrostatic limit [4].

According to Lifshitz theory of Casimir force [5], the latter is temperature dependent in general, but as affirmed by many studies, the explicit thermal corrections, even in the high temperature regime, can be neglected when the separation distance d is very small in comparison to the dominant thermal wavelength $\lambda_T = \hbar c/K_B T$ [6]. Since this is the d-regime, we are interested to in our study, we will therefore use the zero-temperature expression of Casimir force in the small separation regime [5]. The Casimir string coupling constant is defined as the absolute value of the derivative of Casimir force per

unit area with respect to the separation distance *d*, multiplied by the lattice constant squared. Thus, we get:

$$k_{Casimir}(d)=\left|\frac{\partial F_{Casimir}}{\partial d}\right|a^2=\frac{3\hbar a^2}{8\pi^2 d^4}\int_0^{\infty}Li_3\left[r_P^2(iy)\right]dy \qquad (4)$$

where Li_3 is the polylogarithm function of order 3, a denotes the lattice constant and r_p is Fresnel reflection coefficient of the P-polarized EM wave in the electrostatic limit as introduced in the expression of $h_r(d,T)$ in Eq. (3). One should note here that there still is an implicit temperature dependence of Casimir force through r_p.

In order to illustrate our results, we consider two dielectrics (Si and SiC) as typical materials. In addition, SiC is assumed to be in a cubic crystallographic configuration (3C-SiC). We will consider the temperature to range from 300 K to 800 K. Si will be assumed to be highly n-doped with a doping level ranging from 10^{18}cm^{-3} to 10^{21}cm^{-3}. The dielectric permittivity function of Si is described using Drude model while the one of SiC is modeled using Lorentz-Drude Model [7]:

We neglect the temperature dependence of the intrinsic string coupling constant *k*. In addition, we can easily check that the equivalent Debye-like temperatures ($\theta_C^D=\hbar\omega_C/K_B$) corresponding to the phonon cutoff frequencies of the two materials (~176 K for Si) and (~168 K for 3C-SiC) are almost half the room temperature (300 K). Hence, one can even simplify the expression of $\sigma_{Ph}(T)$ by using the high temperature expression of $C_{Ph}(\omega,T)\simeq K_B$ where all phonon modes will be in a highly thermally excited state. In this case, it is straightforward to show that the final expression of $\sigma_{Ph}(d,T)$ is given by:

$$\sigma_{Ph}(d,T)=\frac{K_B\omega_C^3}{8\pi^2v^2}\frac{\kappa^2}{(2\kappa-1)^2}\left\{\frac{2\kappa-1}{3}+(\kappa-1)^2\left[\begin{array}{l}\dfrac{2\kappa\,ArcCoth\left[\dfrac{\kappa}{\sqrt{2\kappa-1}}\right]}{\sqrt{2\kappa-1}}\\ +\log\left[(\kappa-1)^2\right]-2(\log\kappa+1)\end{array}\right]\right\} \qquad (5)$$

$$\kappa\equiv\kappa(d,T)=k_{Casimir}(d,T)/k$$

Figures 2(a) and 2(b) illustrate a comparison between the calculated $\sigma_{Ph}(d,T)$ and the NFRHT coefficient $h_r(d,T)$ through a point junction between two identical isotropic semi-infinite parallel plane solid media of highly n-doped Si and 3C-SiC, respectively. For both materials, $\sigma_{Ph}(d,T)$ turns out to be less sensitive to temperature T and doping concentration N for the values considered above for highly n-doped Si. On the other hand, $h_r(d,T)$ appears to be sensitive to both T and N for Si and to T for SiC. In addition, in the case of highly n-doped Si, the sensitivity of $h_r(d,T)$ to T seems to be dependent on N. Thus only the room temperature $\sigma_{Ph}(d,T=300K)$ is represented for both dielectrics.

Starting from Eq. (5), one can straightforwardly check that the ratio between the maximum and the saturation values of $\sigma_{Ph}(d,T=300K)$ is exactly $R=\sigma_{Ph}^{Max}/\sigma_{Ph}^{Sat}=10/7$.

From figures 2, we see that the NFRHT dominates heat transfer in the case of 3C-SiC. In the case of highly n-doped Si, we found that the interplay between induced phonon transfer through Casimir force (IPTTCF) and NFRHT depends primarily on the doping level N then secondarily on T. IPTTCF starts to dominate the heat transfer as the doping level increases. One can see that for $N=10^{21}cm^{-3}$, the transition distance lies around the lattice constant at room temperature and tends to decrease by increasing the ambient temperature.

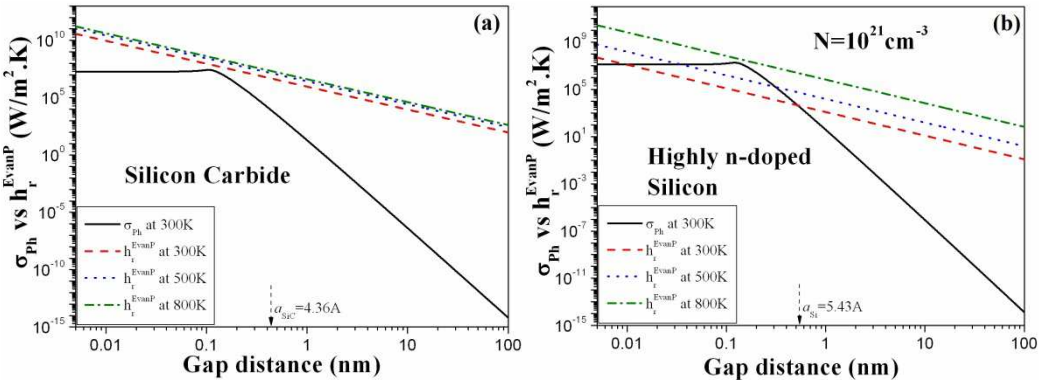

Figure 2: Behavior of $\sigma_{Ph}(d,T)$ and $h_r(d,T)$ as functions of the gap distance through a point junction between two identical isotropic semi-infinite parallel plane solid media of 3C-SiC (a) and highly n-doped Si (b).

It is true that because the transition distance below which IPTTCF dominates NFRHT is of the order or smaller than the lattice constant, the domain of validity of our herein presented approach is undoubtedly questionable and might even be invalid to some extent. It however and certainly shows that IPTTCF constitutes a plausible and a very potential mechanism to capture and describe the natural transition from the radiative regime to the conductive regime of heat transfer. The IPTTCF mechanism would even be enhanced if combined to other potential coupling mechanisms such as piezoelectricity that was recently analyzed by Prunnila and Meltaus [8].

For gap distances of the same order or less than the lattice constant *($d \leq a$)*, the microscopic variation and the discrete character of the matter will take over the continuum approximation. Thus, one expects other additional effects to come into play and even to be more dominant, mainly nonlocal effects of the dielectric permittivity function [9] as well as quantum electronic coupling effects [10].

References

[1] B. V. Budaev and D. B. Bogy, "On the role of acoustic waves (phonons) in equilibrium heat exchange across a vacuum gap", *Appl. Phys. Lett.* **99**, 053109, 2011.

[2] L. Zhang, P. Keblinski, J. S. Wang and B. Li, "Interfacial thermal transport in atomic junctions", *Phys. Rev. B* **83**, 064303, 2011.

[3] N. Mingo, "Green's Function Methods for Phonon Transport Through Nano-Contacts", Chapter 3 in "Thermal Nanosystems and Nanomaterials", edited by S. Volz, Springer, Berlin, 2009.

[4] E. Rousseau, M. Laroche and J. J. Greffet, "Asymptotic expressions describing radiative heat transfer between polar materials from the far-field regime to the nanoscale regime", *J. Appl. Phys.* **111**, 014311, 2012.

[5] E. M. Lifshitz, "The theory of molecular attractive forces between solids", *Soviet Phys. JETP* **2**, 73, 1956.

[6] G. L. Klimchitskaya, U. Mohideen and V. M. Mostepanenko, "The Casimir force between real materials: Experiment and theory", *Rev. Mod. Phys.* **81**, 1827, 2009.

[7] K. Joulain, J. P. Mulet, F. Marquier, R. Carminati and J. J. Greffet, "Surface electromagnetic waves thermally excited: Radiative heat transfer, coherence properties and Casimir forces revisited in the near field", *Surf. Sci. Rep*. **57**, 59, 2005.

[8] M. Prunnila and J. Meltaus, "Acoustic phonon tunneling and heat transport due to evanescent electric fields", *Phys. Rev. Lett.* **105**, 125501, 2010.

[9] P.-O. Chapuis, S. Volz, C. Henkel, K. Joulain and J. J. Greffet, "Effects of spatial dispersion in near-field radiative heat transfer between two parallel metallic surfaces", *Phys. Rev. B* **77**, 035431, 2008.

[10] S. Xiong, K. Yang, Y. A. Kosevich, Y. Chalopin, R. D'Agosta, P. Cortona and S. Volz, "Classical to quantum transition of heat transfer between two silica clusters", *Phys. Rev. Lett.* **112**, 114301, 2014.

Submicrometric scale thermometry: coupling of a thermal-resistive probe and a photoluminescent microcrystal

Gary DEGLIAME[a*], Nathalie TRANNOY[a*], Jean-Pierre JOUART[a], Madjid DIAF[b], Thierry DUVAUT[a] and Didier CARON[a]

[a] *Université de Reims Champagne-Ardenne, GRESPI/CATHERM EA4694 Moulin de la Housse, BP 1039, 51687 Reims Cedex 2, France*

[b] *Université Badji MokhtarAnnaba, Laboratoire de Physique des Lasers, de Spectroscopie Optique et d'Opto-électronique, LAPLASO, BP 12, 23000 Annaba, Algérie*

[*] *corresponding authors: gary.degliame@univ-reims.fr, nathalie.trannoy@univ-reims.fr*

Keywords: Temperature sensor, Thermal probe, Erbium, Photoluminescence, AFM, microcrystal

The determination of the thermal properties of sub-micron scale material is a major challenge for the electronics industry. This type of investigation requires scanning probe microscopes, but the temperature calibration is still difficult.

To overcome this problem, we propose to couple thermal-resistive probe with a photoluminescent microcrystal of $Cd_{0.7}Sr_{0.3}F_2$: Er^{3+} (4%)-Yb^{3+} (6%). Such crystal has luminescence lines sensitive to temperature. The application of the technique of fluorescence Intensity Ratio (FIR) allows us to estimate the microcrystal temperature , then corresponding to the apex probe temperature. According to the Boltzmann's law, the temperature can be assessed by the following formulation on line intensity ratio at wave-lenghts mentionned [1,2].

$$\frac{I_{522}}{I_{549}} = C\, e^{-\frac{\Delta E}{kT}} \quad (1)$$

$$\frac{I_{522}}{I_{540}} = C'\, e^{-\frac{\Delta E'}{kT'}} \quad (2)$$

where C and C' are experimentals constants, ΔE and ΔE', the energetics gaps between emitting levels, k is the Boltzmann's constant, T and T' correspond to temperature, I_n is intensity line at wave-length n= 522, 540 and 549 nm.

The temperature sensor used is a thermoresistive probe Wollaston whose sensing element is platinum/rhodium heat probe commonly used in scanning probe microscopy (SThM). A few micrometers microcrystal was glued at its apex [3].

The experimental set-up is described in figure 1. The first stage is to compare the temperature estimated from the luminescence and the thermal probe temperature. For this, an electrical current is used to induce a Joule effect heating allowing a simultaneous heating of the probe and of the microcrystal. To start Anti-Stokes mechanism, the microcristal is irradiated with a laser at 652 nm. We collect the luminescence photon by an optic fiber to a spectrometer.

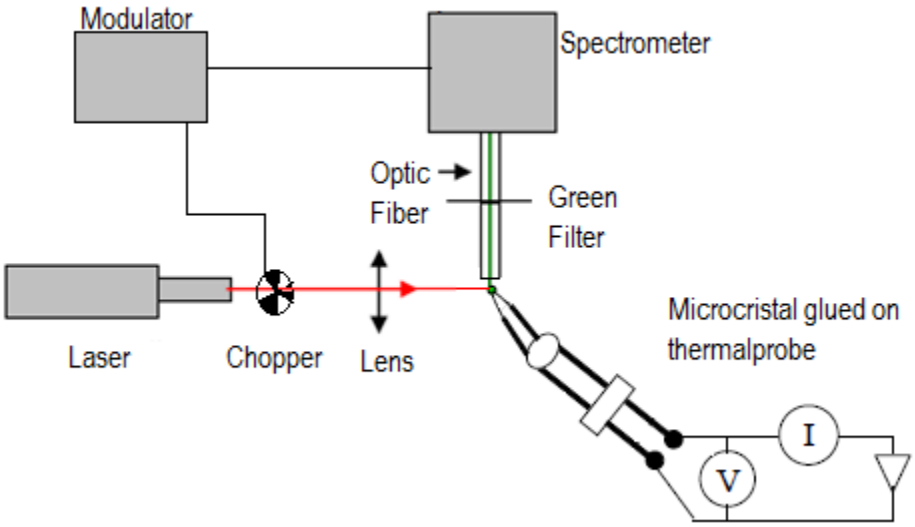

Figure 5 : Experimental set-up.

This technique aims to be able to determine system temperature that obtained by circuit components and that obtained from FIR technique. In this work, we suggest a thermal behavior study of crystal depending on crystal size. This has an impact on the temperature measurements. We present a physical model for explaining such behavior.

References:

[1] S.A. Wade, S.F. Collins, G.W. Baxter, "Fluorescence intensity ratio technique for optical fiber point temperature sensing", *Journal of Applied Physics*, **94** (8), 4743-4754, 2003.

[2] A. Sayoud, J.P. Jouart, N. Trannoy, M. Diaf, T. Duvaut, "Temperature measurements inside an Er^{3+}–Yb^{3+} co-doped fluoride crystal heated by a NIR laser diode and probed by red-to-green upconversion", *Journal of Luminescence*, **132**, 566–569, 2012.

[3] A. Sayoud, N. Trannoy, J-P. Jouart, P. Grossel, M. Diaf, T. Duvaut, "Temperature sensor for scanning thermal microscopy based on photoluminescence of microcrystal", *Proc. SPIE* **8154**, 815408, 2011.

Coherent acoustic phonons in thin films of $CoSb_3$ and partially filled $Yb_xCo_4Sb_{12}$ skutterudites

Chuan HE[a*], Marcus DANIEL[b], Martin GROSSMANN[a], Oliver RISTOW[a], Delia BRICK[a], Martin SCHUBERT[a], Manfred ALBRECHT[b,c] and Thomas DEKORSY[a]

[a]*University of Konstanz, 78457 Konstanz, Germany*

[b]*Chemnitz University of Technology, 09107 Chemnitz, Germany*

[c]*Present address: University of Augsburg, Universitätsstr. 1, 86159 Augsburg, Germany*

**corresponding author: chuan.he@uni-konstanz.de*

Keywords: coherent acoustic phonon, femtosecond pump-probe spectroscopy, phonon scattering process, thermal conductivity, skutterudite.

Skutterudites are interesting materials for thermoelectric applications. Filling foreign atoms into the cagelike structure of a $CoSb_3$ skutterudite is beneficial to its thermoelectric properties [1-2]. Here we demonstrate the generation and detection of coherent acoustic phonons in thin films of $CoSb_3$ and partially filled $Yb_xCo_4Sb_{12}$ skutterudites [3] using high-speed asynchronous optical sampling (ASOPS) [4]. ASOPS is a femtosecond pump-probe technique that uses two mode-locked Ti:sapphire lasers operating at ~800 MHz. A stabilized frequency offset between the two lasers allows the ASOPS system to scan the ultrafast dynamic processes in a measurement of ~1.25 ns.

We have measured the as-deposited and annealed $CoSb_3$ samples using a high-speed ASOPS system. By using a pulse echo method, the longitudinal sound velocities of as-deposited and annealed $CoSb_3$ films are calculated to be $(3.39\pm0.01)\times10^3$ m/s and $(4.05\pm0.11)\times10^3$ m/s, respectively. In order to study the effect of foreign atoms on the heat transport in $CoSb_3$ skutterudite, $Yb_xCo_4Sb_{12}$ thin films with different filling fraction x were also investigated. For the film samples annealed at 300 ºC, x = 0, 0.08, 0.27, 0.68; the film samples annealed at 500 ºC, x = 0, 0.05, 0.12, 0.57. The confinement of acoustical vibrations in the $Yb_xCo_4Sb_{12}$ films is observed [5]. As the Yb filling increases, the high frequency phonon modes are strongly suppressed, which gives evidence of the scattering of acoustic phonons in the presence of Yb atoms.

The relationship between the discrete frequency f_m and the film thickness d is $f_m = m\upsilon/2d$. The frequency of the peaks f_m is plotted over the mode number m in Fig. 1(a). Provided the thicknesses d, the longitudinal sound velocities υ of the $Yb_xCo_4Sb_{12}$ films are obtained and plotted in Fig. 1(b), in which the value of υ of as-deposited and annealed $CoSb_3$ films are also given for comparison. As the filling fraction x increases, an obvious decrease of υ is observed. Since the structure of skutterudites is well maintained after filling, the decrease of υ is primarily ascribed to the presence of Yb atoms.

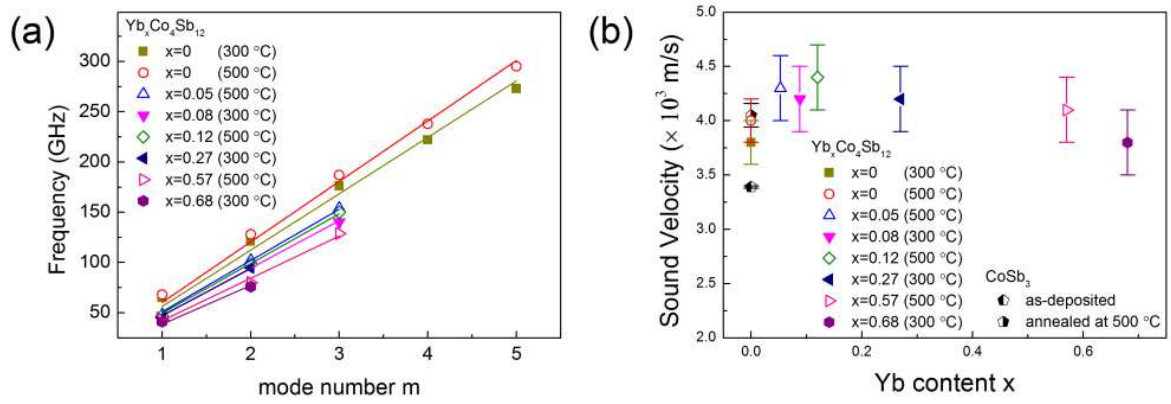

Figure 1: (a) The frequency of the phonons is plotted over mode number m. The linear fits for $Yb_xCo_4Sb_{12}$ film samples are also shown. (b) Plot of calculated sound velocity over Yb content x. The sound velocities of $CoSb_3$ films are depicted for comparison. Filled and open symbols represent $Yb_xCo_4Sb_{12}$ film samples annealed at 300 °C and 500 °C, respectively.

The lattice thermal conductivity κ can be estimated using the kinetic theory of gases [6]:

$$\kappa = (1/3)\, C_V\, \upsilon_m^{\,2}\, \tau, \qquad (1)$$

where C_V is the heat capacity per unit volume, υ_m the mean sound velocity of the phonons, τ the phonon relaxation time. It has been experimentally confirmed that the κ of $CoSb_3$ decreases upon Yb filling [1]. In the low filling fraction region ($0<x<0.3$), an increase of υ is observed, and the reduction of κ is mainly achieved by the strong scattering of the high frequency acoustic phonons. At high filling fractions of x = 0.57 and 0.68, the significant drop of υ, together with the strong scattering of acoustic phonons, could lead to a further reduction of κ. But even at x = 0.68, υ is still comparable to that of polycrystalline $CoSb_3$, so despite the drop of υ at high filling fractions, the dominant mechanism in the reduction of κ after filling is the stronger scattering of acoustic phonons, which shortens the phonon relaxation time.

References

[1] G. S. Nolas, M. Kaeser, R. T. Littleton IV, T. M. Tritt, "High figure of merit in partially filled ytterbium skutterudite materials", *Appl. Phys. Lett.* **77**, 1855-1857, 2000.

[2] G. S. Nolas, D. T. Morelli, T. M. Tritt, "Skutterudites: A phonon-glass-electron crystal approach to advanced thermoelectric energy conversion applications", *Annu. Rev. Mater. Sci.* **29**, 89-116, 1999.

[3] C. He, M. Daniel, M. Grossmann, O. Ristow, D. Brick, M. Schubert, M. Albrecht, and T. Dekorsy, "Dynamics of coherent acoustic phonons in thin films of $CoSb_3$ and partially filled $Yb_xCo_4Sb_{12}$ skutterudites", *Phys. Rev. B* **89**, 174303 (2014).

[4] R. Gebs, G. Klatt, C. Janke, T. Dekorsy, A. Bartels, "High-speed asynchronous optical sampling with sub-50fs time resolution", *Opt. Express* **18**, 5974-5983, 2010.

[5] F. Hudert, A. Bruchhausen, D. Issenmann, O. Schecker, R. Waitz, A. Erbe, E. Scheer, T. Dekorsy, A. Mlayah, J.-R. Huntzinger, "Confined longitudinal acoustic phonon modes in free-standing Si membranes coherently excited by femtosecond laser pulses", *Phys. Rev. B* **79**, 201307(R), 2009.

[6] E. S. Toberer, A. Zevalkink, G. J. Snyder, "Phonon engineering through crystal chemistry", *J. Mater. Chem.* **21**, 15843-15852, 2011.

A comparative study of different numerical approaches to the Boltzmann Transport Equation for phonons

Elyes NEFZAOUI* and P-Olivier CHAPUIS

Université de Lyon, CNRS, INSA-Lyon, UCBL, CETHIL, UMR5008, F-69621, Villeurbanne, France

**corresponding author: elyes.nefzaoui@univ-poitiers.fr*

Keywords: Computational heat conduction, Phonon heat transport, Boltzmann Transport Equation (BTE), Equation of Phonon Radiative Transfer (EPRT), Ballistic Diffusive

The Boltzmann Transport Equation (BTE) can be used to describe phonon transport in solids and predict the resulting conductive heat transfer [1]. Its complete resolution can be cumbersome without simplifying approximations. The commonly-used single-mode relaxation time approximation [2] leads to the following expression of the BTE:

$$\frac{\partial f}{\partial t} + \mathrm{v} \cdot \nabla f = \left(\frac{\partial f}{\partial t} \right)_{scatt} = \frac{f^0 - f(t)}{\tau} \tag{1}$$

where f is the phonons distribution function, v is the heat carrier group velocity, f^0 is the distribution function at equilibrium and τ is the relaxation time of the considered phonon due to all scattering phenomena.Even with this strong assumption, and assuming the phonon relaxation times are known, the BTE resolution is still very resource-consuming since it requires the integration over all frequencies and wave vectors for all branches of the phonons dispersion relations. Besides, phonons of different branches can interact through phonon-phonon scattering events and a treatment of all branches leads to a system of coupled BTEs. The approach accounting for full dispersion has already been implemented, and the BTE has been solved by different deterministic methods such as the Discrete Ordinates Method (DOM) considered in this work or by Monte Carlo (MC) statistical sampling [3][4][5]. A similar equation known as the Equation of Phonon Radiative Transfer (EPRT) where f is replaced by the phonon equivalent of the specific intensity $I_\omega(\theta,\phi,x,t) = \sum_p v(\theta,\phi)\, f_\omega(x,t) \hbar\omega \mathcal{D}(\omega)$ where $v(\theta,\phi)$ is the velocity in the direction (θ,ϕ) in a solid angle unit and $\mathcal{D}(\omega)$ is the density of states, has been also used [6][7].

In order to avoid the numerical cost of such a complete treatment, some authors proposed simplifications that model separately different regions of the considered medium (surface boundaries and sources, volume far from these surfaces) accounting for the particular features of heat transfer in each region [8][9]. Here we also consider the Ballistic-Diffusive Equations (BDE), which are obtained by splitting the distribution function into a nonlocal component due to the surface boundaries and the heat sources and a local one due to the heat exchange inside the volume, assumed to be more isotropic. One can derive a set of two equations which involve two temperatures: a temperature assigned to the nonlocal ballistic heat flux and another one assigned to a more diffusive heat flux.

We present in particular a comparative study of steady-state conductive heat transfer in a one-dimensional thin film (Figure 1.a) computed by the EPRT solved by the DOM, and the BDE. For the gray case (single mean free path (MFP)), the comparison emphasizes some weaknesses of the BDE which fails in predicting accurately the temperatures near the boundaries while succeeding in predicting the effective thermal conductivity derived from the mean slope of the temperature profile (Figure 1.b).

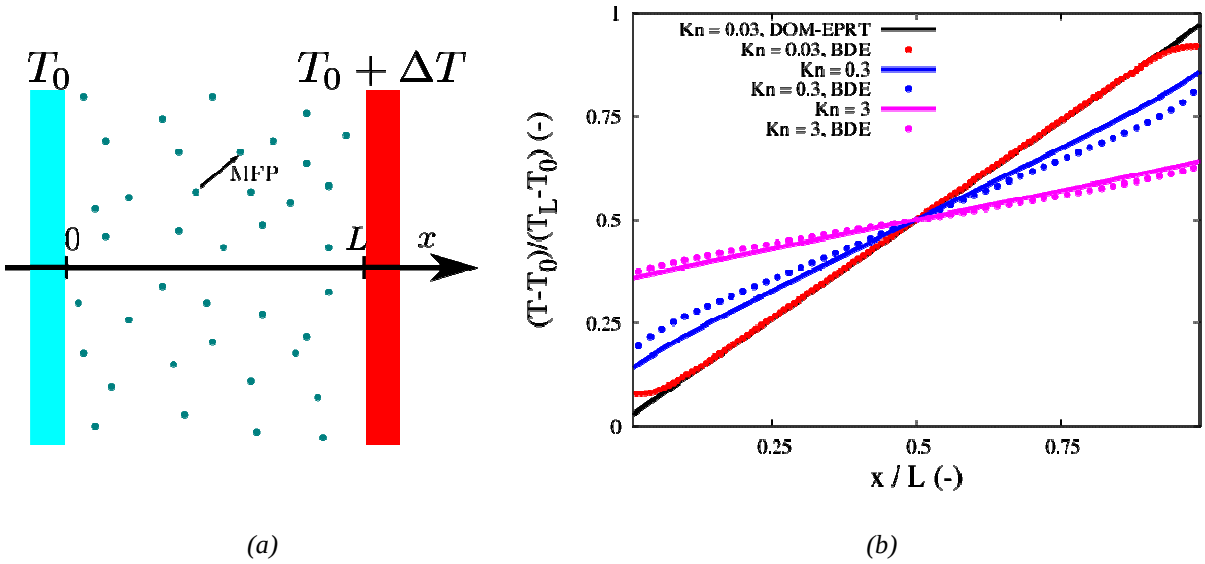

(a) *(b)*

Figure 1: (a) A one-dimensional thin film of thickness L *with walls at given temperatures* T_0 *and* $T_L = T_0 + \Delta T > T_0$. *(b) Normalized temperature profiles in the slab for various gray MFPs. The lowest temperature is* $T_0 = 295$ *K and a temperature difference* $\Delta T = 10$ *K is set between the two boundaries. Profiles are obtained by solving the EPRT by the DOM (lines) and the BDE (plain circles).*

We then extend the EPRT beyond the simple gray situation. Instead of the familiar description of phonon populations through the dispersion relations in the (ω, k) space, we use a description as a function of the distribution of MFPs. The aim of this section is to determine a MFP distribution that can lead to accurate results while avoiding the complexity induced by a more complete treatment involving dispersion relations. Such line of research has been highlighted in particular by [10] and [11].

Finally, the boundaries effects are investigated for the simple gray medium case by solving the EPRT with DOM. Specular and diffusive reflections at the boundaries are considered and different effects on the carriers MFP are observed. An analytical expression of the resulting effective MFP, equivalent to the MFP with black walls which leads to the same thermal conductivity, is analyzed and compared to a simple Matthiessen's rule.

Acknowledgments

The authors acknowledge the support of ANR through the nanoHEAT project (ANR-11-PDOC-0024) and EU FP7-NMP-2013-LARGE-7 project QuantiHeat (GA n°604668). They also acknowledge the sustained help of Dr S. Gomes, as well as Drs. D. Lemonnier, M. Roger, and R. Vaillon for fruitful discussions.

References

[1] J. M. Ziman, *Electrons and Phonons*, Clarendon Press, 1960.

[2] P. G. Klemens, "The Thermal Conductivity of Dielectric Solids at Low Temperatures (Theoretical)", *Proc. R. Soc. Lond. Ser. Math. Phys. Sci.*, **208**, 108–133, 1951.

[3] D. Lacroix, K. Joulain, and D. Lemonnier, "Monte Carlo transient phonon transport in silicon and germanium at nanoscales", *Phys. Rev. B*, **72**, 064305, 2005.

[4] D. Terris, K. Joulain, D. Lemonnier, and D. Lacroix, "Modeling semiconductor nanostructures thermal properties: The dispersion role", *J. Appl. Phys.*, **105**, 073516, 2009.

[5] J. Y. Murthy, S. V. J. Narumanchi, J. A. Pascual-Gutierrez, T. Wang, C. Ni, and S. R. Mathur, "Review of Multiscale Simulation in Submicron Heat Transfer", *Int. J. Multiscale Comput. Eng.*, **3**, 5–32, 2005.

[6] A. Majumdar, "Microscale Heat Conduction in Dielectric Thin Films", *J. Heat Transf.*, **115**, 7–16, 1993.

[7] R. Prasher, "Generalized equation of phonon radiative transport", *Appl. Phys. Lett.*, **83**, 48–50, 2003.

[8] G. Chen, "Ballistic-Diffusive Heat-Conduction Equations", *Phys. Rev. Lett.*, **86**, 2297–2300, 2001.

[9] N. Donmezer and S. Graham, "A multiscale thermal modeling approach for ballistic and diffusive heat transport in two dimensional domains", *Int. J. Therm. Sci.*, **76**, 235–244, 2014.

[10] A.J. Minnich, J.A. Johnson, A.J. Schmidt, K. Esfarjani, M.S. Dresselhaus, K.A. Nelson, and G. Chen, "Thermal Conductivity Spectroscopy Technique to Measure Phonon Mean Free Paths", *Phys. Rev. Lett.*, **107**, 095901, 2011.

[11] K.T. Regner, D.P. Sellan, Z. Su, C.H. Amon, A.J.H. McGaughey, J.A. Malen, "Broadband mean free path contribution to thermal conductivity measured using frequency domain thermoreflectance", *Nature Com.*, **4**, 1640, 2013.

Index of authors

AHOPELTO	147
ALBRECHT	220
ALKURDI	55
AL-OTAIBI	61
ALZINA	139, 147
AMARA	112, 178
AMARAL	186
ANOMA	7
ANTONI	83, 126, 159, 211
ASSY	173, 182
BAN	211
BARSKI	182
BATTAGLIA	197
BAYLE-GUILLEMAUD	182
BEN ABDALLAH	25, 80, 129
BENENTI	107
BENISTY	36
BERGAUD	47
BERTAIL	207
BIBEN	55
BIEHS	25, 80, 129
BLANDRE	32
BLUET	39
BODZENTA	90
BONTEMPI	193
BOUKHARI	182
BOURGEOIS	182
BRICK	220
BRITES	186
BRUCHHAUSEN	145
BRUCOLI	36
CAHILL	3
CANUT	39
CARCENAC	47
CARLOS	186
CARON	218
CASATI	107
CHAPUIS	32, 39, 121, 164, 173, 204, 222
CHAUDHURI	42
CHAVEZ-ANGEL	139
CHEVALIER	164
CHIRTOC	90, 211
CHOI	3
CLERI	18
COSTANTINI	36
COUDERC	112
CROCOMBETTE	98
CRUT	201
DANIEL	220
DAVOYAN	21
DE BOISSIEU	143
DEBORD	143
DEGLIAME	218
DEKORSY	145, 220
DEL FATTI	201
DIAF	218
DIDARI	28
DILHAIRE	77
DOLLFUS	72, 155
DREVILLON	132, 151
DUBOIS	44
DUVAUT	218
EA-KIM	77
EICH	80
EMIG	124
ENGHETA	21
ENGUEHARD	207
EUCHNER	143
EZZAHRI	132, 151, 214
FALLICA	197
FAN	7
FRANCIOSO	18
FRANCOEUR	32
FRECHETTE	39

FUMERON	65
GARCIA	167
GIORDANO	143
GLUCHKO	159
GOMES	173, 182
GOMIS-BRESCO	139, 147
GOTSMANN	9
GRACZYKOWSKI	147
GREFFET	36
GROSSMANN	145, 220
GUSEV	145
HADJI	182
HAN	102
HARAS	44
HE	145, 220
HENKEL	25
HERNANDEZ	47
HETTICH	145
HOHENSEE	3
HORNE	211
HORNY	211
IGUCHI	116
INCARDONE	124
ISOTALO	42
JABER	164
JARAMILLO-FERNANDEZ	93
JEAN	65
JOUART	218
JOULAIN	25, 132, 151, 214
JOUMANI	207
JUSZCZYK	90
KANE	176
KARG	9
KASSEM	93
KITTEL	87, 137
KLINGELE	145
KLOPPSTECH	87, 137
KOHIYAMA	116
KOMIYA	121
KÖNNE	87, 137
KOSEVICH	15, 102
KRAIEVA	47
KRÜGER	124
KUBYTSKYI	129
KUSIAK	197
LACATENA	44
LACROIX	59, 65
LAGRANGE	47
LALANNE	77
LAMPIN	18
LANG	80
LAPAS	109
LARROQUE	72
LATELLA	109
LEFEVRE	173
LEMITI	112
LI	169
LIMA	186
LIU	182
LOMBARD	55
LONGO	197
LOZAN	77
LUKES	21
MAASILTA	42, 52
MAHMOUD	21
MAIOLI	201
MARQUIER	36
MARUYAMA	121
MASSOUD	39
MAYO	121
MENGES	9
MENGÜÇ	28
MENSCH	9
MERABIA	55
MILAN	186
MOLNAR	47
MONFRAY	44
NARAYANASWAMY	121
NAVARRO-URIOS	139
NEFZAOUI	151, 222

Newby	39
Nghiem	155, 204
Ni	15
Okajima	121
Okyay	207
Ollier	93
Ordonez-Miranda	83, 126, 159
Pailhes	143
Palacio	186
Palla	18
Park	189
Perez-Madrid	109
Perrin	77
Petrov	80
Prunnila	147
Puurtinen	42, 52
Quintero	47
Raman	7
Rampnoux	77
Randrianalisoa	162
Remondiere	93
Reparaz	147
Rephaeli	7
Richard	182
Riel	9
Ristow	145, 220
Robillard	44
Rubi	109
Sääkilahti	15
Saci	197
Saint-Martin	72, 155
Scheel	145
Scheer	145
Schubert	145, 220
Shchepetov	147
Shimizu	116
Silva	186
Sjakste	176
Skotnicki	44
Sotomayor Torres	139, 147
Soupremanien	93
Srivastava	61
Stemmer	9
Stoll	201
Tan	169
Termentzidis	59, 65
Teyssieux	193
Thiery	193
Tranchant	83, 126, 159
Trannoy	162, 218
Tschikin	80
Tsurimaki	121
Vaillon	32, 121
Vairac	193
Vallee	201
Van Der Zwaag	167
Vast	176
Volz	15, 83, 93, 102, 126, 159, 211
Vossier	178
Waitz	145
Xiong	15
Yu	169
Yugami	116
Zanjani	21
Zarate	139
Zen	42
Zhang	169
Zhao	169
Zhong	167
Zhu	7
Zianni	68